UNIVERSITY OF KENT

DOCTORAL THESIS

Quantum Free Particle Superoscillations in $1+1$ Dimensions: A First-Quantised Approach

---

Author:
Jack Richard HERKLOTS

Supervisor:
Professor Paul STRANGE

A thesis submitted in fulfillment of the requirements

for the degree of Doctor of Philosophy

in the

Functional Materials Group

School of Physical Sciences

2019

Declaration of Authorship

I, Jack Richard HERKLOTS, declare that this thesis titled, "Quantum Free Particle Superoscillations in $\mathbf{1}+\mathbf{1}$ Dimensions: A First-Quantised Approach" and the work presented in it are my own. I confirm that:

- This work was done wholly or mainly while in candidature for a research degree at this University.
- Where any part of this thesis has previously been submitted for a degree or any other qualification at this University or any other institution, this has been clearly stated.
- Where I have consulted the published work of others, this is always clearly attributed.
- Where I have quoted from the work of others, the source is always given. With the exception of such quotations, this thesis is entirely my own work.
- I have acknowledged all main sources of help.
- Where the thesis is based on work done by myself jointly with others, I have made clear exactly what was done by others and what I have contributed myself.

Signed:

_____

Date:

_____

"We live lives that are waveforms constantly changing with time, now positive, now negative. Only at moments of great serenity is it possible to find the pure, the informationless state of signal zero. "

Thomas Pynchon, Gravity's Rainbow (1973)

UNIVERSITY OF KENT

Abstract

Faculty of Sciences

School of Physical Sciences

Doctor of Philosophy

Quantum Free Particle Superoscillations in $1+1$ Dimensions: A First-Quantised Approach

by Jack Richard HERKLOTS

The principal differences between non-relativistic and relativistic quantum mechanics are: the existence of negative energy states, and the natural emergence of spin within a relativistic framework. We consider both these effects in the creation and evolution of superoscillating wavepackets.

Superoscillations are a phenomena in which a function can oscillate faster than it's fastest Fourier component. As a trade-off they suffer by being exponentially smaller than conventional oscillations. Previous studies of superoscillations within the construct of the Schrödinger equation have identified two key features: disappearance after a time, t_d, and an asymmetrical evolution either side of a line in space (the wall effect).

In this thesis, we expand this work into a relativistic framework by applying it to the Klein-Gordon and Dirac equations, to do this we require a thorough examination of $1+1$ dimensional relativistic propagators. Although initially derived in terms of Bessel functions, these have two key limits which allow for simpler calculation: the light-cone limit ($x \to x_0 + ct$) and the WKB limit ($\hbar \to 0$).

Positive and negative energy superoscillations are best described in the WKB limit. Through application of asymptotic integration, we find that both positive and negative energy superoscillations possess a disappearance time and wall effect. For both Klein Gordon and Dirac equations, t_d is equal. This implies, in terms of disappearance spin has no effect on the evolution of a superoscillatory, relativistic wavefunction of positive or negative energy. However, relativistic superoscillations disappear faster than non-relativistic superoscillations. and in each case, the disappearance time tends to a finite value as a superoscillatory parameter is increased. For non-relativistic superoscillations $t_d \to 1/2$ compared to $t_d \to 0.3715$ for the relativistic case.

The wall effect is also noticeably different in relativistic and non-relativistic contexts. The walls appear at different points in space and, despite the relativistic wall effect being evident from $t = 0$, within the Schrödinger equation, it doesn't appear until a time of $t = 1/32$. This contrast in the wall effects of both cases is the leading cause of the inequality of the disappearance times.

The asymmetries between the wall effects are caused by differences in the behaviour of saddles (complex momenta) found when evaluating the wavefunction as an integral over the propagator. Again, there is no disparity between the walls of the Klein-Gordon or Dirac equation; spin does not affect the evolution of positive or negative energy superoscillations.

Where positive and negative energy wavefunctions appear as $\hbar \to 0$, mixed energy superoscillations appear at the light-cone. Mixed energy superoscillations do not exhibit the wall effect and neither do they exist in a non-relativistic description. However, they do have a disappearance time. In contrast to the positive and negative energy states, $t_d \to 0$ as a superoscillatory parameter is increased. It is within a mixed energy construct that the effect of spin on the evolution of relativistic superoscillations appears; one of the components of the Dirac equation does not superoscillate. This is caused by this term existing at the WKB limit as opposed to the light-cone.

Acknowledgements

First thanks deservedly go to my supervisor Professor Paul Strange; without his initial suggestion of the project and many insightful conversations since, this thesis would not have been possible. The support he provided throughout and discussions about our love of cricket helped to make studying for a PhD the most enjoyable period of my time at university. To have been granted the opportunity to undertake research in an area which, even before my time as a physics undergraduate, has fascinated me is something I will never forget.

I would also like to thank my fellow graduate students: Greg Smith, Sharif Alkass and Max Bussel. I couldn't have asked for better people with which to share an office. As well as directly helping with my doctorate, they provided welcome distraction and vital encouragement when I needed it most.

Throughout my seven years of university life, the friendships I made during my PhD are by far my strongest and I would not have been able to complete this thesis without them. Thanks, in particular, goes to: my house-mates from 90 Bingley Court, the University of Kent Cricket Club and the pub quiz team.

Midway through writing, I took on full time employment at AA Underwriting Insurance Company Limited. This was without doubt a risk, but thanks to the encouragement and interest shown by my colleagues, in particular my boss Paul Frith, I have not only been able to balance finishing my PhD with starting a new job, but have found the time both enjoyable and immensely rewarding.

As a part of my undergraduate, I spent a year studying abroad at the State University of New York, University at Buffalo. This experience, more than any other in my life, allowed me to grow both as a person and a physicist; I wouldn't have had the confidence to apply for a PhD without it. It would not have been possible without the extremely generous help from my relatives: Mum and Dad; Grandad; Granny Leila; Uncle Radu and Auntie Lucinda; Auntie Heléna and Uncle Ade.

Lastly, I thank my family - for everything. Throughout my life I have received nothing but loving support and guidance; with this I have been lucky enough to attend university, spend a year studying in the USA and both undertake and finish this thesis. My parents: Annie and Lawrence, my brothers: Billy, Paddy and Henry; my Grandparents; my Aunties and Uncles, I thank you all not only for your encouragement throughout my doctorate but for all you have given me in the past twenty six years.

Contents

List of Figures

For my Grandparents

Chapter 1

Introduction

Is it possible for a band-limited function to oscillate faster than its fastest Fourier component? Initially, one may tempted to say it is not; some could go as far to declare it a paradox[1]. However, in the late 1980s and early 90s [27], [6], [8] it was shown that it was not the paradox it first seemed as the uncertainty relation between the variances of a function and its Fourier transform is obeyed[9]. This phenomena was given the title 'Superoscillation' [13].

Superoscillations were first realised following Yakir Aharonov's re-formulation of quantum mechanics as a time-symmetric theory [4] that produced the concept of the weak value [3]. It was shown that by taking careful selections from the quantum state both before and after measurement, quantities such as the spin eigenvalue of a spin half particle could attain values far larger than conventionally expected. Superoscillation was found when taking a weak measurement of the frequency of an oscillating wavefunction. Despite their classification in the 1900s, the observation of superoscillation and antenna-superdirectivity being a dual phenomenon [113], superoscillations can be traced back as far back as 1956 [52].

Following from discussions with Aharonov, Berry defined a large class of superoscillating functions [27]. Mathematical superoscillations have since been of interest to physicists and mathematicians studying their properties [2], [64], [38] and relationships to other functions [15], [24], [7].

[1] How can a function, built from a series of oscillating contributary functions oscillate faster than any of its constituent components?

It has been shown that superoscillations can be formed naturally, as a consequence of near-perfect destructive interference in random wave fields [45]. In fact, the probability of a region of such a field being superoscillatory is remarkably high; for a monochromatic super-position of waves with random direction in two dimensions, the probability was found to be $1/3$ [44].

Superoscillatory waves gained the attention of experimentalists when, in 2006, Michael Berry and Sandu Popescu showed that an initial superoscillatory wave is a solution to the free-particle Schrödinger equation and hence, the paraxial wave equation [30]. By passing such a wave through a complex diffraction grating, it was shown that superoscillations produce sub-wavelength detail that remained at a considerable distance from that grating. From this, it was concluded that superoscillation could hold the key for far-field imaging beyond the diffraction limit. Since this, there have been significant advancements in developing optical superoscillations from nano-hole arrays [121] [120], superoscillatory lenses [90] [91] and antenna arrays [111] [112].

In this introductory chapter, we aim to explain some of the key features of superoscillation mentioned in a little more detail, such that the reader has an appreciation for the subject as a whole. We then consider the specific aims of this thesis and discuss its structure.

1.1 Mathematical Superoscillations

1.1.1 Superoscillations in A Fourier Series

As superoscillations are defined in terms of their Fourier spectrum, an instructive place to begin a mathematical description is by observing how they can occur in a simple Fourier series [120]:

$$f(x) = \sum_{n=0}^{5} a_n \cos(2\pi n x) \tag{1.1}$$

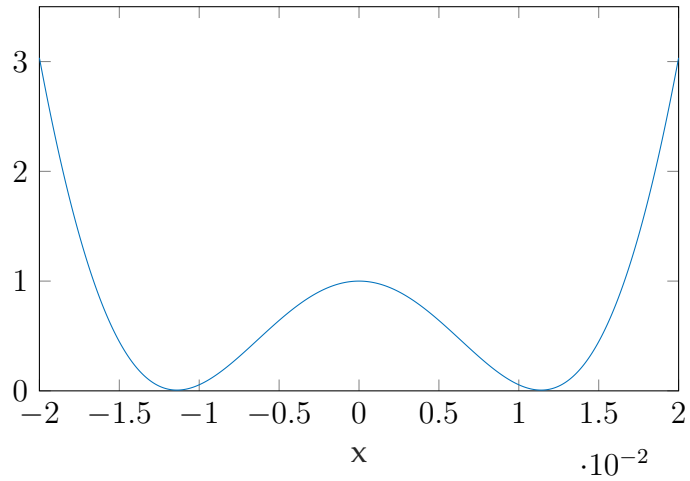

FIGURE 1.1: (1.1) in the range $-0.02 \leq x \leq 0.02$

where:

$$a_0 = 1,\ a_1 = 13295000,\ a_2 = -30802818,\ a_3 = 26581909, \tag{1.2}$$

$$a_4 = -10836909,\ a_5 = 1762818$$

In (1.1), the fastest Fourier component corresponds to $n = 5$ and therefore it would be expected that the function would oscillate with a frequency no larger than $\frac{2}{5}\pi$. Figure 1.1 shows (1.1) oscillating with a frequency far larger than the fastest Fourier component and shows that, in this region, $f(x)$ is superoscillating.

This example highlights a key feature of superoscillation; superoscillations are caused by almost-perfect destructive interference[44]. We shall now explain how this occurs. Studying figure 1.1, it is clear that the superoscillation attains its highest magnitude at $x = 0$. Evaluating (1.1) at this point, all the terms of the series cancel except for $n = 0$. Given that the other five terms in the series are many orders of magnitude larger than this (outside the region shown in figure 1.1) the function, at $x \approx 0$, is approximately zero, this is shown in figure 1.2. Superoscillation in (1.1) is caused as the other 'conventionally oscillating' terms enter in at $x \approx 0$. The superoscillations are quickly destroyed as the larger terms begin to dominate.

Clearly, superoscillation comes at a price: superoscillations are considerably smaller

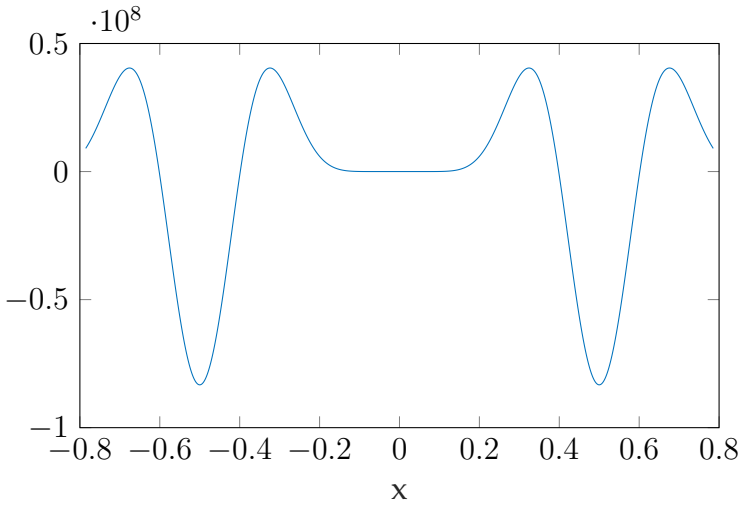

FIGURE 1.2: (1.1) in the range $-\pi/4 \leq x \leq \pi/4$

than their function's conventional oscillations and exist in a far smaller space. However, (1.1) can only allude to those facts, in order to quantify the relative sizes of superoscillations and the regions in which they exist, a different example function is required.

1.1.2 Superoscillatory Asymptotics

To understand more about the cost of superoscillations we follow an example given in Michael Berry's much celebrated paper *Faster Than Fourier*[27] which, begins with the function:

$$f(x, A, \delta) = \frac{1}{\delta\sqrt{2\pi}} \int_{-\infty}^{\infty} e^{ik(u)} e^{-\frac{1}{2\delta^2}(u-iA)^2} du, \tag{1.3}$$

where $k(u)$ is even, $k(0) = k$ and $|k(u)| \leq k$ for real u, A is real and positive and δ is real and small. In order to have (1.3) superoscillating, the spectrum of the function's frequencies must be band-limited (in this case we will take $|k| \leq 1$) such that, conventionally, we would not expect oscillations with frequencies larger than $\cos(x)$. To achieve this, $k(u)$ must be specified so that the requirements, previously mentioned are satisfied, examples are:

$$k_1 = \frac{1}{1 + \frac{1}{2}u^2},\ k_2 = \operatorname{sech}(u),\ k_3 \exp\left[-\frac{1}{2}u^2\right],\ k_4 = \cos(u) \tag{1.4}$$

Before moving onto to analysing the integral in (1.3) in detail, we will look at the features that cause it to superoscillate. By taking δ to be small, the second integral acts as a complex-delta function:

$$e^{-\frac{1}{2\delta^2}(u-iA)^2} \rightarrow \delta(iA)|_{\delta\rightarrow 0}, \tag{1.5}$$

this will project the value of the first exponential in (1.3) at $u = iA$. Therefore, under integration, the argument of (1.5) is projected onto the first exponential giving:

$$f(x, A, \delta) = \frac{1}{\delta\sqrt{2\pi}} e^{ik(iA)} \tag{1.6}$$

When substituting k_4 into (1.6), the resultant function will be oscillating with a wavenumber much larger than $k = 1$, it's fastest Fourier component; (1.3) is therefore a superoscillatory function.

We now wish to look at how the function (1.3) behaves in the superoscillatory region as opposed to the space where it oscillates conventionally. This allows us to study what happens to the conventional oscillations as the superoscillatory region is increased. A condition of (1.3) is that δ is small, to highlight this, we make the substitution:

$$\xi = x\delta^2 \tag{1.7}$$

giving:

$$f\Big(\frac{\xi}{\delta^2}, A, \delta\Big) = \int_{-\infty}^{\infty} \exp\left[-\frac{1}{\delta^2}\Phi(u, \xi, A)du\right], \tag{1.8}$$

where:

$$\Phi \equiv \frac{1}{2}(u - iA)^2 - i\xi k(u). \tag{1.9}$$

As $\delta \rightarrow 0$, the prefactor in front of Φ in the exponential tends to infinity. This allows the integral in (1.8) to be evaluated by the saddle point method[43]. This method is

described in detail in appendix B but, in essence, an integral of the form:

$$I = \int_{-\infty}^{\infty} g(z) e^{\nu w(z)} dz \tag{1.10}$$

where $\nu \gg 1$ is solved through contributions from saddles in the phase $w(z)$, giving solutions:

$$I = \sum_j \sqrt{\frac{-2\pi}{\nu w''(z_j)}} g(z_j) e^{\nu w(z_j)} \tag{1.11}$$

where z_j are the saddles of $w(z_j)$.

Therefore, to solve (1.8) , the saddles of (1.9) must be determined:

$$\frac{d\Phi}{du} = 0 \tag{1.12}$$

$$\Rightarrow \frac{\partial}{\partial u}\left[\frac{1}{2}(u - iA)^2 - i\xi k'(u)\right] = 0 \tag{1.13}$$

$$\therefore u_s = i(\xi k'(u) + A) \tag{1.14}$$

From (1.14) and (1.10) the asymptotic approximation to (1.8) is:

$$f(x, A, \delta) = \frac{\exp[\frac{1}{2\delta^2}(u_s - iA^2) - ixk(u_s)]}{\sqrt{1 - ix\delta^2 k''(u_s)}} \tag{1.15}$$

To understand how (1.15) behaves in the superoscillatory region, we take $\xi \gg 1$ i.e. $x \gg \delta^{-2}$. In this limit, $u_s \to iA$, which gives (1.15) as:

$$f(x, A, \delta) \approx \exp[-ixk(iA)] \tag{1.16}$$

This is the same form found when discussing the superoscillatory region and hence, the saddle point approximation retains the superoscillatory nature of (1.8).

We now take $\xi \gg 1$, in this limit, the saddle point approximation to the integral

gives:

$$f(x, A, \delta) \approx \frac{1}{\delta\sqrt{xk''(0)}} e^{i(x+\frac{1}{4}\pi)} e^{\frac{A^2}{2\delta^2}} \tag{1.17}$$

This is the regime of conventional oscillations. The function (1.17) is $\mathcal{O}(\exp[\frac{A^2}{2\delta^2}])$ and hence the region of conventional oscillation is exponentially amplified relative to the superoscillatory space (this behaviour is proved explicitly in [64]). Similarly, if we wish to see a large number of superoscillations, the range of x through which the function is superoscillatory must be increased. As a trade-off, to allow x to be larger and the function to still superoscillate, δ must be smaller such that the limit $\xi \gg 1$ is still stipulated. However, from (1.17), as δ becomes smaller the conventional oscillations become exponentially larger.

The superoscillatory function presented here is quite general and one can create a wide variety of superoscillatory functions from it [86]. However, clearly these come at a cost; a function's superoscillations are exponentially smaller than its conventional oscillations. It is therefore quite difficult to spot when a band-limited function is superoscillating. An easy way to see when a function is superoscillatory is to look at the local wavenumber [29], [55] given by:

$$q(\xi) = -\Im m\left[\frac{\partial \Phi(u_s(\xi), \xi, A)}{\partial \xi}\right] = \Re e[k(u_s)] \tag{1.18}$$

To see how this works we use a different $k(u)$ from those shown in (1.4), instead we take:

$$k_5(u) = 1 - \frac{1}{2}u^2 \tag{1.19}$$

From (1.18) we can plot the local wavenumber alongside the fastest Fourier component ($|k| = 1$). As we see from figure 1.3, for small ξ, the local wavenumber, $q(\xi)$ is larger than the fastest Fourier component. As ξ increases, the local wavenumber decreases such that it becomes smaller than the faster Fourier component. This is not a surprising result considering that the local wavenumber gives information about the wavelength as a function of position. In fact, we can define superoscillations in

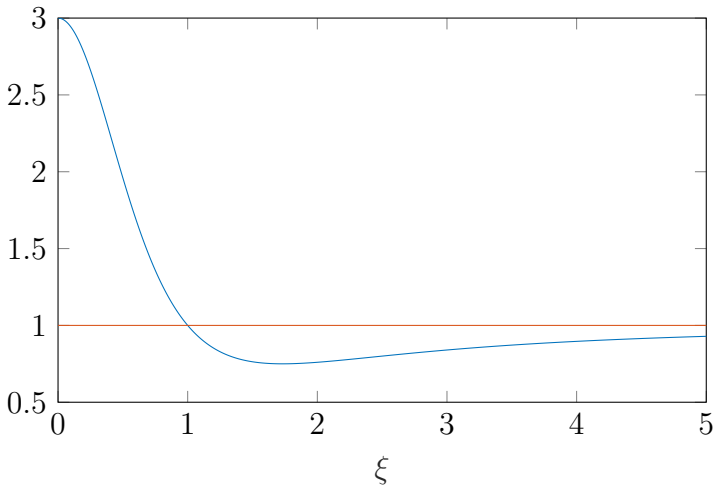

FIGURE 1.3: $q(\xi)$ caluclated from (1.18) and (1.19) for $A = 2$ (blue line) and the fastest Fourier component of the superoscillatory function (1.3) with (1.18) (orange line).

terms of the local wavenumber: A function is superoscillatory at a point in space ξ if the function's local wavenumber is larger in magnitude that it's fastest Fourier component. This definition, although very similar to the one previously used, is a more rigorous statement as it compares two quantifiable properties of the function.

1.2 Weak Values

Weak values emerged following a re-formulation of quantum mechanics by Aharonov, Alber and Vaidmen [3] which determined quantum measurements through pre- and post-selection[66]. Traditionally, up to 1964 [10], quantum measurements were taken entirely through pre-selection; a system $|\Psi\rangle$ is prepared, it is operated upon and measurements are taken. In classical mechanics, this is a very straightforward procedure; provided the initial conditions and dynamics (e.g. the Hamiltonian) of the system are known beforehand, all the information of the system for all time is available [51]. However, in a quantum mechanical system, this is not the case. Even if the entire initial wavefunction i.e. $(t = t_0)$ of a system is determined alongside its Hamiltonian (for all time), one can only calculate the probability of a specific measurement being taken at a later time $(t = t_1)$ [76].

In Aharonov's re-formulation, it was found that if one were to take a subsequent measurement, it would not only have implications for what happens at times $t > t_1$ but also for time $t < t_1$. To show this, an ensemble of particles is prepared in the initial state, $|\Psi\rangle$. A measurement is then taken on each particle at an intermediate time between t_0 and t_1, a final measurement is then taken of the system at t_1. Following the result of the final measurement, the original ensemble is then split into sub-ensembles accordingly. The statistical distribution of results from the intermediate measurement is different for each post- and pre-selected sub-ensemble and also different from the statistical distribution over the whole initial ensemble, which was only subject to pre-selection. Therefore, in the time-symmetric formulation of quantum mechanics, the results of a measurement at a time t depend not only on what happened before the measurement was taken but also on what happens after the measurement is taken [105].

It is from the time-symmetric formalism of quantum mechanics that weak values emerge [12]. A typical quantum measurement is that of the expectation value:

$$\langle A \rangle = \langle \psi_{pre} | \hat{A} | \psi_{pre} \rangle \tag{1.20}$$

If all eigenvalues of the operator, $\hat{A}$, are in the range $A_{min} \leq A_n \leq A_{max}$, in the familiar asymmetric formalism of quantum mechanics, $\langle A \rangle$ can never lie outside this range. However, in the symmetric formalism, where a different state, ψ_{post} is post-selected, the expectation value gives the weak value [108]:

$$A_{weak} = \frac{\langle \psi_{post} | \hat{A} | \psi_{pre} \rangle}{\langle \psi_{post} | \psi_{pre} \rangle} \equiv A + iA' \tag{1.21}$$

The result of this weak measurement is often a complex value, the consequences of this are discussed in the following articles [100], [42], [78]. However, if the initial wave function is real, the resulting expectation value is replaced by $\Re e[A_{weak}]$. In fact, $\Re e[A_{weak}]$ can lie outside the range $A_{min} \leq A_n \leq A_{max}$ (such values are called

superweak) [98] [53].

1.2.1 Superoscillations as Weak Values

Superoscillations can emerge from the study of weak values by looking at the case of a spin-$\frac{1}{2}$ wavefunction [3]. We pre-select a spin-half particle with the x-component of spin pointing up (its eigenvalue, $\sigma_x = 1$) and post select states which correspond to the y-component of spin pointing up ($\sigma_y = 1$). To investigate weak values we then take the measurement of the spin at an angle of 45^o to the $x-y$ which gives our operator spin-operator as:

$$\sigma_{x-y} = \cos(45^\circ)\hat{\sigma_x} + \sin(45^\circ)\hat{\sigma_y} = \frac{\hat{\sigma_x} + \hat{\sigma_y}}{\sqrt{2}} = \sqrt{2} \tag{1.22}$$

This can be achieved through a weak measurement of the system in which the interaction between the measuring device and the ensemble of particles weakens and produces unexpected results akin to those of the weak values previously discussed[104]. This result of $\sqrt{2}$ is unexpected as it lies outside the range of eigenvalues for a spin-half particle $-\frac{1}{2} \leq A_n \leq \frac{1}{2}$.

By performing this weak measurement on an ensemble of N spins it is shown in [107] that the final result of the weak measurement is given as:

$$|\Phi_{final}\rangle = \langle\uparrow_y \mid \uparrow_x\rangle \Big(\cos\Big(\frac{\lambda Q_{md}}{N}\Big) - iA_{weak} \sin\Big(\frac{\lambda Q_{md}}{N}\Big)\Big)^N |\Phi_{initial}\rangle, \tag{1.23}$$

in which Q_{md} is an observable of the measuring device (e.g. the position of pointer). As both $\langle\uparrow_y \mid \uparrow_x\rangle$ and $|\Phi_{initial}\rangle$ are trivial, the important part of (1.23) is:

$$\psi = \left(\cos\Big(\frac{\lambda Q_{md}}{N}\Big) - iA_{weak} \sin\Big(\frac{\lambda Q_{md}}{N}\Big)\right)^N \tag{1.24}$$

Using the exponential forms of $\sin$ and $\cos$, (1.24) becomes:

$$\psi = \left[\frac{1}{2}(1 + A_{weak})e^{i\frac{\lambda Q_{md}}{N}} + \frac{1}{2}(1 - A_{weak})e^{-i\frac{\lambda Q_{md}}{N}}\right]^N \tag{1.25}$$

Through a binomial expansion of (1.25), we get ψ as a Fourier series:

$$\psi = \sum_{m=0}^{N} c_m \exp\left[i\frac{\lambda \kappa_m Q_{md}}{N}\right] \tag{1.26}$$

where

$$c_m = \frac{(1 + A_{weak})^m (1 - A_{weak})^{N-m}}{2^N m!(N-m)!}, \;\; \kappa_m = 1 - \frac{2m - N}{N} \tag{1.27}$$

As seen in (1.25), ψ is band-limited ($|\kappa_m| \leq 1$). By taking a small Q_{md} approximation to (1.24), one gets:

$$\psi \approx \left(1 - iA_{weak}\frac{\lambda Q_{md}}{N}\right)^N \tag{1.28}$$

$$= \exp\left[N \log\left((1 - iA_{weak}\frac{\lambda Q_{md}}{N}\right)\right] \approx \exp\left[iA_{weak}\frac{\lambda Q_{md}}{N}\right] \tag{1.29}$$

As we have seen, taking the weak value for a spin-$\frac{1}{2}$ particle (when the measurement is taken at a 45^o angle to the $x - y$ plane) is $A_{weak} = \sqrt{2}$. Clearly then, the frequency with which is dependent on the weak value A_{weak}. As this can exceed the fastest Fourier component in (1.26), ψ can superoscillate; its degree of superoscillation is proportional to its weak value [25].

As will be seen later, (1.24) is a very important equation in the context of superoscillations; it is referred to by Berry and Fishman as '*the standard superoscillatory function*' [21].

1.3 Quantum Superoscillations

The study of the weak value of an ensemble of spin-$\frac{1}{2}$ particles is an example of one of many cases of the theory of superoscillations coalescing with the theory of

quantum mechanics. In this section, we will discuss some of the key discoveries in this area [11] [2].

Q_{md} represents the position of the measuring device (e.g. the position in a Sern-Gerlach experiment) replacing this with x (also, a spatial variable) in (1.26), one is left with a superposition of plane-waves:

$$\psi = \sum_{m=0}^{N} c_m \exp\left[i\frac{\lambda\kappa_m x}{N}\right]. \tag{1.30}$$

This superposition, or one very similar to it, was used by Berry and Popescu to describe how a superoscillatory function would evolve according to the free-particle Schrödinger equation [30]. It was found that, using the 'standard superoscillatory function' as the initial wavefunction, the superoscillations persist for a far longer time than expected - noticeably longer than exponentially decaying evanescent waves and depend on a superoscillatory parameter, akin to the weak value in (1.25). This behaviour was explained through the interaction of contributions to the wavefunction appearing as complex momenta in the phase.

It is this persistence of superoscillations that has been of most interest in the area of quantum superoscillations with the case of the harmonic oscillator [37], [36], a uniform magnetic field [41] and a uniform electric field [5] all being studied.

In the case of the harmonic oscillator another control parameter, the frequency of the harmonic potential, is added to the evolution of the superoscillations; a 'critical harmonic frequency' exists for which superoscillations can only be found if their harmonic frequency is less than than the critical value. The strength of superoscillations gets larger as the harmonic frequency gets smaller suggesting that the free-particle is somehow 'maximally superoscillating'. It is also found that for the case of the harmonic oscillator, the superoscillations disappear much in the same way as they do for the free particle but reform periodically.

For the case of the electric field, it is found that the superoscillations disappear on a time scale identical to that of the free-particle. However, in this interpretation and

others [9], [7], a more general case of the Hamiltonian was used and, consequently, it was found that the time in which superoscillations exist for is dependent on N (1.30) as well as the superoscillatory parameter and such, as $N \to \infty$ so will the time in which superoscillations persist. A method for creating non-singular Schrödinger potentials in which the corresponding ground-state wavefunction is a superoscillating wavefunction have been developed [40].

It has also been show that superoscillations can exist in a quantum-mechanical, non-commucative phase space through the study of Wigner and Husimi functions [23]. This is of particular interest as quantum superoscillations are often explained in terms of their complex-momenta. However, the way superoscillations evolve in phase space is yet to be considered.

1.4 Natural Superoscillations

Up to this point, superoscillations have so far been treated as a fairly exotic phenomenon which only belong to a certain group of functions [9]. In this section, we discuss some of the research that has been undertaken that suggests superoscillation is not restricted to functions in which the superoscillatory properties have been prefabricated but can occur as the result of destructive interference in a superposition of random waves. This also highlights the relationship between superoscillations and vortices in random waves [20].

As discussed previously, superoscillations within a function can be detected by analysing the local wave number (phase gradient) of the function; superoscillations occur at points at which the local wavenumber is larger than the fastest Fourier component. It is through this method that Dennis, Hamilton and Courtial explained how superoscillations occur in optical speckle patterns [44]. By setting up a superposition of waves, in a two-dimensional plane, in which the direction and phase are uniformly distributed random variables, the regions of superoscillation can be

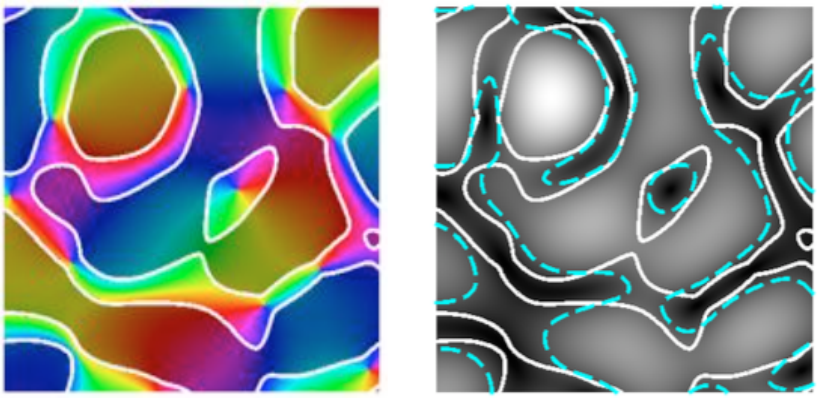

FIGURE 1.4: c.f. Fig.2 in [44]. A random superposition of 100 two dimensional plane-waves each with the same wavenumber. (a) phase pattern; (b) intensity pattern. The white contour denotes the line in which the local wavenumber is equal to the fastest Fourier component ($|q(x,y)| = k_{max}$). In (a) the region of conventional oscillation is shaded, several phase singularities are seen. In (b) the dashed-cyan contour encloses the lowest $1/3$ of the intensity. The area plotted is $(4\pi/k)^2$

determined through:

$$|q(x,y)|^2 - k_{max}^2 > 0, \tag{1.31}$$

in which $q(x)$ is the local wavenumber and k_{max} is the fastest Fourier component. For this situation, the question can then be asked: given a point $r = (x,y)$ what is the probability that the superposition of random waves is superoscillating at this point? Surprisingly, it is found that, for a superposition in which all the contributing waves have the same wavenumber, the fraction of the overall function that is superoscillatory is $1/3$. This is shown in figure 1.4 in which the regions where (1.31) is valid are highlighted in (a). (b) shows the intensity as a function of x and y for the superposition, the points at which the intensity falls within the lowest $1/3$ of the whole wave are enclosed by the cyan line. It is clear that there is significant overlap between the superoscillatory regions and regions of low intensity. This is expected from our previous discussion of superoscillations in which we showed that superoscillations are formed from almost-perfect destructive interference. It is also shown that the superoscillations in these regions have a far smaller local wave number than

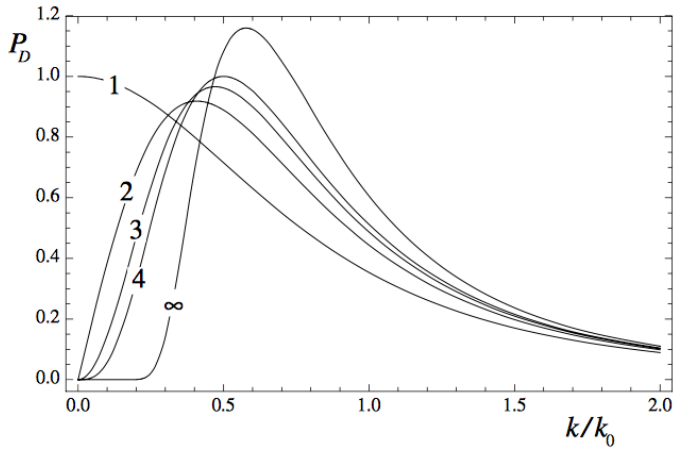

FIGURE 1.5: c.f. Figure 3 in [19]. Probability distributions P_D as a function of the local wavenumber k and scaled by the free space wavenumber k_0 for indicated values of dimension D.

those created from the standard superoscillatory function; natural superoscillations are far less extreme than the tailor made examples seen previously.

Another interesting feature of figure 1.4 is that all of the phase singularities (points of zero intensity) are contained within the superoscillatory regions. These phase singularities can be thought of as the extremes of superoscillation [18].

The case where all the wavenumbers in the random superposition are equal will give the most amount of superoscillation; a monochromatic superposition would 'wash out' most of the almost perfect destructive interference. It is shown in [44] that, for a disk-spectrum, the probability of superoscillation is $1/5$.

The concept of natural superoscillation has also been developed into other dimensions than just the two spatial ones discussed here [19], [45], where it was shown that the the probability of superoscillation increases from 0.293 to 0.394 as the number of dimensions, D, increases from 1 to ∞. It is also shown that, in the case $D = 1$, that the probability, as a function of the local wavenumber, behaves in a peculiar fashion relative to the cases $D > 1$.

1.5 Numerical Superoscillations

As with any novel physical phenomenon, as many questions will asked about its application as well as its nature. Superoscillations are no different in this respect and, by 1994 [27], Michael Berry had already selected them as a possible candidate for optical superresolution.

We look at a method of creating superoscillations, not through the Fourier based methods previously discussed but by taking a series of band-limited signals and imposing upon them specific values in the superoscillatory window. In an imaging context, this means making the signal, $f(\xi)$, coincide with a target image which contains details smaller than that of the wavelength of the interrogating signal [80], [35], [83]. This gives an example of how superoscillations may be numerically generated as well as how they hold up as a candidate for superresolution [77]

In general, consider a wave, $\Psi(x)$, constructed from a series of plane-waves, $\psi_m(x)$:

$$\Psi(x) = \sum_{m=1}^{N} c_m \psi_m(x) \tag{1.32}$$

To recreate an image ($F(x)$), we specify that at certain points, x_i :

$$\Psi(x_i) = \sum_{m=1}^{N} c_m \psi_m(x_i) = F(x_i) \tag{1.33}$$

where i is found in the range: $1 \leq i \leq I^2$. This is then a matrix eigenvalue problem:

$$\Psi(x_i) = \sum_{m=1}^{N} M_{m,i} c_m \tag{1.34}$$

[2] I represents the number of points in space for which we require our wave, $\Psi(x)$ to coincide with the target image $F(x)$, their distribution of can then be determined accordingly. Making I very large will increase the accuracy of the image within the sampled space however, this comes at the cost of computational expense.

In which $M_{m,i}$ is an $I \times N$ matrix. (1.34) can be inverted to give the coefficients, c_m:

$$c_m = \sum_{i=1}^{I} (M_{i,m})^{-1} F(x_i) \tag{1.35}$$

The recreated image can the be determined by substituting the results of (1.35) into (1.32). In order to ensure that the resultant wave function is superoscillatory, the interpolation points, x_i, are chosen so that the two furthest points lie within one wavelength of each other. Therefore, the function has to display superoscillatory properties. The connection with this superoscillatory rendering of an image and oversampling has been discussed [50].

To demonstrate how this works, we show an example from Berry [16] through which this concept was applied to a beam in which the details are reproduced periodically in the far field [82][3].

In his paper, Berry attempted to recreate a target image (a double Gaussian) which contained detail on the scale of $\lambda/20$ of the interrogating wave:

As seen in figure 1.6, as the distance from the sampled interval increases, the function $\Psi(x)$ diverges rapidly from the target image; it is 40 magnitudes larger in some points. This is not a surprising result considering previous discussions and has consequences for the energy of the system [49]. However, in the context of creating superoscillations, there is another major issue; the conditioning of the matrix. The eigenvalues, c_m are very small and hence the matrix, $M_{i,x}$ is ill-conditioned. This is problematic as the solution becomes numerically unstable, in order to produce the results in figure 1.6, computations with an accuracy of > 50 digits were required. The ill-conditioned matrix in (1.35) gives a superoscillatory wave an inherent susceptibility to noise. This is discussed in [29] where it was shown that superoscillations can be suppressed by random phases with small rms strengths,

[3]The optical effect here is not the Talbot effect [22] but the Montgommery effect. Relationships between the two are well understood [79]; the reason for not using the Talbot effect is that it blurs details far larger than the sub-wavelength structure [88]. This is why it was found in [30] that although the wave passing through the diffraction grating exhibited the Talbot effect, the superoscillatory data was lost upon repetition.

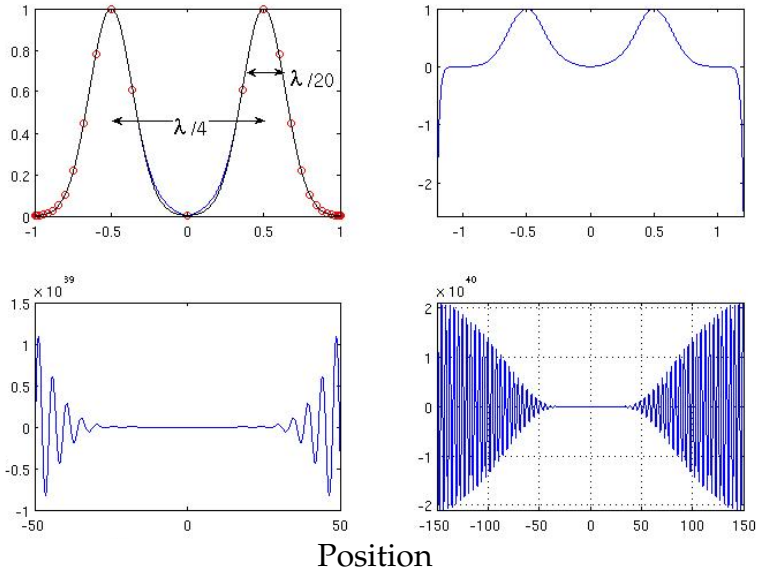

FIGURE 1.6: Top left: showing the target image (black line) the recreated image (blue line) and the interpolation points (red circles). In the other three diagrams the distance from the interpolation window is increased showing how the function becomes orders of magnitude larger outside the sampled interval.

very close to the strength of the superoscillations.

Here we have described just one way of numerically generating superoscillations; many more exist. Lee and Ferrieria devised a method, similar to the one described here in which values were prescribed onto a grid (which is not necessarily uniform) arbitrarily finer than the reference grid. Therefore, as the grid to which the beam is interloped becomes finer, the degree of superoscillation becomes greater [71]. Recently, a new method has been developed which creates superoscillations multiplicatively [40]. By multiplying functions whose zeros lie closer together than their respective wavelengths, an overall superoscillatory wave is created, this allows for computation of superoscillations that have both arbitrarily long duration and high frequency.

1.6 Optimising Superoscillations

In the previous section, it was shown that superoscillations are capable of constructing images with sub-wavelength detail. However, due to the exponential disparity between the superoscillatory region and conventional oscillations, any superoscillatory beam will have to be carefully managed in order to make it a viable tool for imaging. In this section, we show how this is handled; successful research in this area would greatly improve the chances of using superoscillation as a tool for imaging below the diffraction limit.

It is known that the creation of a superoscillatory beam comes at the expense of the energy of the region outside the sample interval. Therefore, it is intuitive to design a minimum energy superoscillatory wave [50]. Such minimum energy solutions are beneficial as they come at a low energy cost and and have the smallest overall amplitude. However, such signals are very dependent on cancellation which gives rise to the ill-conditioned matrix problem seen earlier. A recent development on this method drops the concept of determining the minimum energy superoscillations. Instead it constructs superoscillations through orthonormal functions that would have previously created an ill-condition matrix but now recover the identity matrix [73]. It has also been shown that by placing constraints upon the amplitude and the derivative of the superoscillatory wave and manipulating the combinations of the constraints, the minimum energy required for the superoscillatory signal can change by as much as an order of magnitude [72].

Optimisation of the yield of superoscillations has provided a potentially viable method of augmenting superoscillations [63]. By yield we refer to the ratio:

$$Y = \frac{\int_{-a}^{a} f^2(x)dx}{\int_{-\infty}^{\infty} f^2(x)dx}, \tag{1.36}$$

in which $f(x)$ is a function that is superoscillatory in the region $-a \leq x \leq a$. A constrained optimisation approach to this leads to an eigenvalue problem which is solved numerically. This method creates superoscillations which have a trade-off of

superoscillatory yield and signal quality. The susceptibility of noise to this method has been considered [97]; it was found that the deviation from the yield to its maximum value in the presence of random errors in the Fourier coefficients was not considerable if an absolute minimum error could be established. The deviation increased upon only being able to determine a relative minimum error. Furthermore, by varying the 'strictness' of the interpolation requirement (how many of the prescribed points pass through the superoscillatory region) it was found that, although high machine precision was still required, storing and using yield-optimised superoscillations does not pose a technical problem [62].

1.7 Optical Superoscillation

In recent years, interest in optical superoscillation has grown considerably due to the potential of superoscillations as a way of probing details below the diffraction limit. We have discussed how superoscillation can be generated numerically and how the initially troubling high-magnitude side-bands can be controlled so that the superoscillations are more prominent. In this section, we examine how superoscillations can be created optically and how optical superoscillations can be used in superresolution.

Optical superoscillations, in a controlled fashion[4], were first created in 2007 by attempting to focus light through a quasi crystal nano-hole array (QNA) in the far-field [59]. The resultant diffraction pattern created optical hotspots (high intensity regions) less than half a wavelength in diameter, these were attributed to superoscillations. A quasi-periodic mask, such as this, is a good candidate for optical superoscillation as it has a continuous Fourier spectrum and can create complex field patterns [74] [75].

The schematic shown in figure 1.7 shows how a nano-hole array superoscillatory lens can create point to point imaging as well as the focusing mentioned previously.

[4]From earlier discussion, as any speckle pattern could create superoscillations which dates their creation (in an uncontroled way) back to the 1940s.

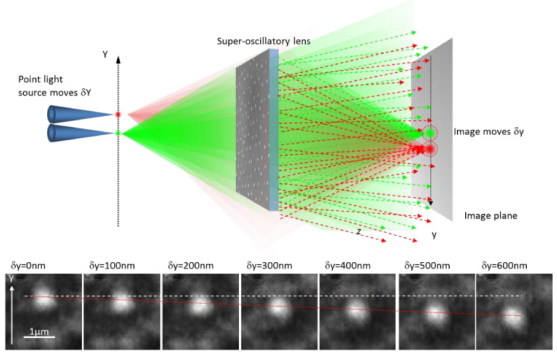

FIGURE 1.7: c.f. figure 11 in [48] adapted from figure 1 in [58]. Top: A schematic of quasi-crystalline imaging. Bottom: Showing movement as the sources moves by upto 600nm.

In figure 1.7, a point light source is created by a scanning near-field optical microscope (SNOM) by emitting light of wavelength 635nm. The array is then used as a superoscillatory lens to image the point light source on the other side. As the source is moved in one direction, its image moves in the opposite direction as is normal for a glass lens. It is shown in [121] that multiple images of the same image are created in the same focal plane. Despite its low throughput efficiency, complex objects containing multiple points can be imaged using this method [61].

Building from the work on quasi-crystal nanohole arrays , a number of binary superoscillatory lenses have been considered. The lens in figure 1.8 (a) is created by projecting a 27-dimensional hypercubic lattice onto a plane. A well defined centre of rotation can then be determined by requiring that the projection plane passes through a specific point on the hypercubic lattice [68]. This creates the optical axis upon which focal spots are formed. By randomly placing holes on spiral arms around a central point, the lens in figure 1.8 (b) is created, with the number of arms determining the the order of rotational symmetry. In [94] the 40 fold symmetric example is created and superfocusing (focsing beyond the conventional diffraction limit [117]) is observed.

As seen in figure 1.8, the lens which creates the most pronounced hotspot is the optimised binary ring mask shown in (c), which generates a far larger throughput efficiency than the the other two examples. These ring masks are optimised through

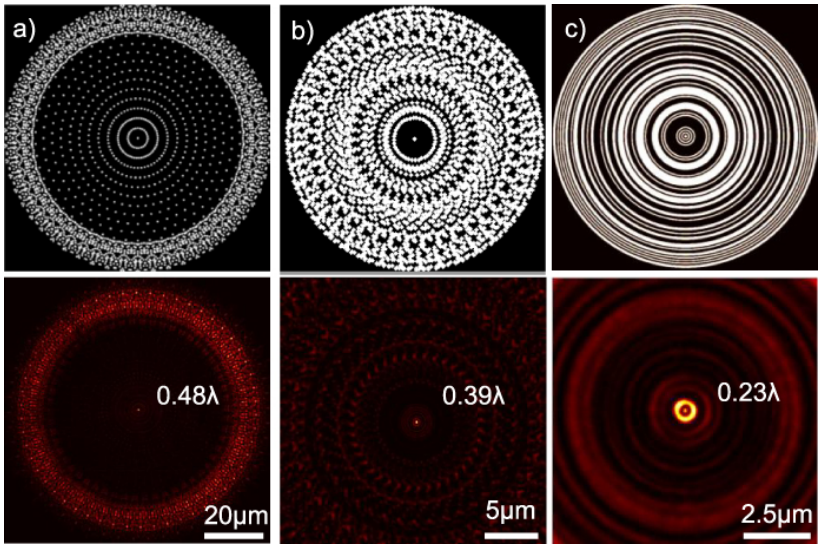

FIGURE 1.8: c.f. figure 12 in [48] Examples of superoscillatory lenses and their respective focal spots. (a) A 27-fold symmetric QNA forming a 048λ focal spot. (b) A semi-random spiral hole array forming a 0.39λ focal spot. (c) A ring mask superoscillatory lens forming a 0.23λ spot in immersion oil.

an algorithm called binary particle swarm optimisation (BPSO) which is described in [65], [89] and [60] and a schematic is given in figure 13 in [48]. An example of a lens created using this method is given in [90], where it was employed using a modification to a conventional microscope, and produced resolution better than $\lambda/6$. Using the principles of BPSO, superoscillatory lenses in which it is possible to focus light of different colours into the same hotspot have been developed [118]. As is shown in figure 1.9, slits of width $> \lambda/6$ were imaged using a scanning electron microscope (SEM), a superoscillatory lens (SOL) and, for two-slits a conventional lens of numerical aperture 1.4. The key difference between the SOL and a conventional lens is seen when comparing the images of two slits; only the SOL picks up the presence of both slits whereas the conventional lens renders them as a single object.

Dynamic SOLs have been created using spatial light modulators (SLMs) and a conventional microscope objective that focuses a beam whose interference pattern is designed by careful selection of the amplitude and phase profile. This builds upon work on superfocusing with pupil filters first discussed in 1957 [52] and has since

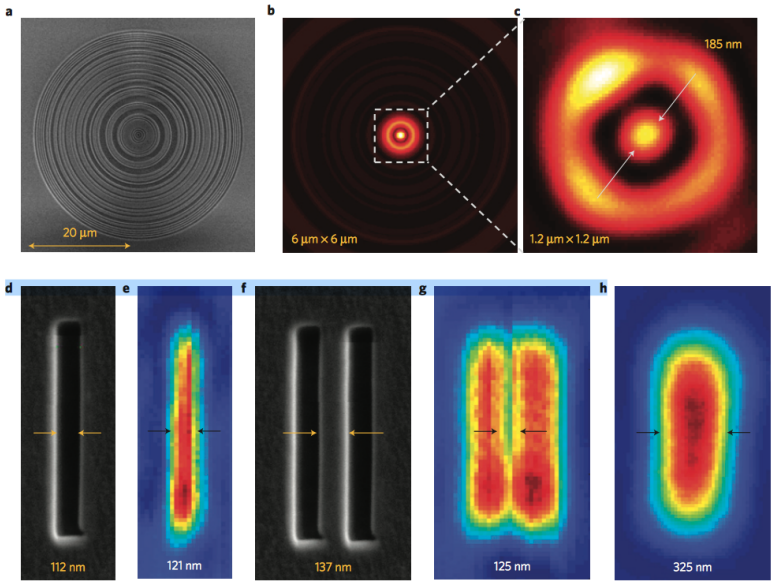

FIGURE 1.9: c.f. figure 1 in [90]. Subwavelength imaging with a superoscillatory lens (SOL). (a) A scanning electron microscope image of the SOL. (b) Calculated energy distribution of the SOL at 10.4μm from the lens. (c) The actual focal point for $\lambda = 640$nm. (d) SEM image of a 112nm slit, (e) the SOL image of the slit, (f) a double slit, separated by 137 nm, (g) the SOL image of the double slit and (h) the image of the double slit using a conventional lens of NA $= 1.4$.

been developed [57], [93]. In order to create a dynamic SOL, the desired focal spot is created by determining the amplitude and phase incident on the objective. This has been shown to be well suited to the optical eigenmode method, described in [81] and [85]. In essence, this method works through the probing of the lenses, free-space and microscope objective between the SLM and the focal plane. This gives the spot size matrix operators from which, the eigenvectors give the eigenmodes of the system and the eigenvalues give the respective spot size of the system. This method has been deployed in [14] in which a spot of 0.35λ was generated and [69] in which resolution was achieved 1.3 times that of the system's theoretical limit.

It is clear from figures 1.8 and 1.9 that high amplitude side bands are intrinsic to the fields generated by a SOL[5]. A class of SOL has since been developed which pushes these far away from the optical axis. This is done by focusing the light into a subwavelength needle as opposed to a spot. These optical needle superoscillatory

[5]This is not a suprising result considering many, if not all, of the superoscillatory waves so far discussed have contained similar high amplitude regions.

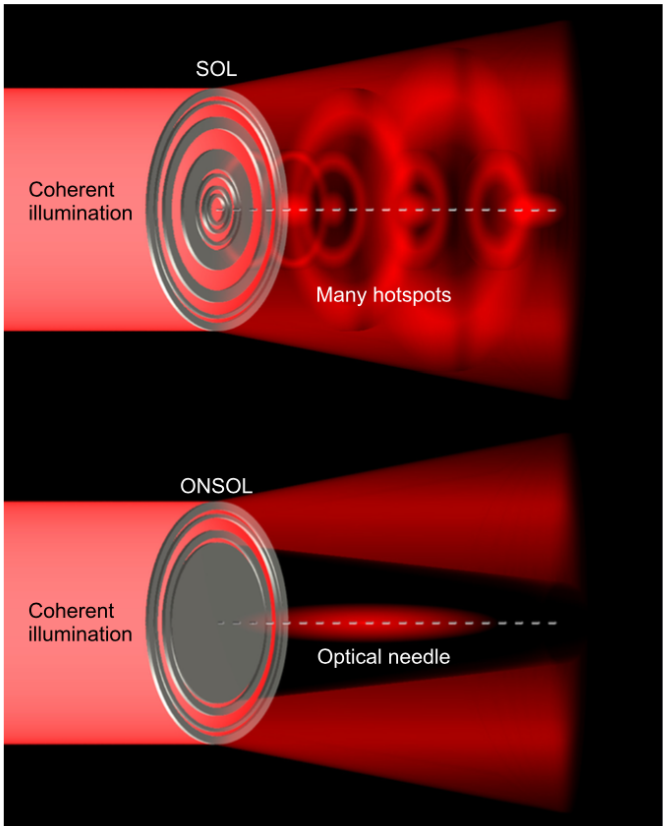

FIGURE 1.10: c.f. Figure 1 [91]. The difference between a SOL and an ONSOL: The SOL produces a complex pattern of subwavelength spots and high amplitude sidebands. The diffraction pattern created by the ONSOL is far simpler with a subwavelength needle and sidebands far from the axis.

lenses (ONSOLs)[91] are created in much the same way as the SOLs previously discussed except that the centre of is always opaque, this blocks any incident light to this region and the needle is created in the resulting 'shadow region'. The ONSOL has a very long focal length with lengths of 11λ [91], 15λ [116] and 300λ [39].

Optical superoscillations have been created by building upon the well known work on antenna pattern synthesis[95] and the relationship between superoscillation and antenna superdirectivity [113] , [112], [111]. From this method a way of handling the sidebands is proposed in which the side bands are removed by a cavity [114]. A new type of superoscillatory wave is also created which contains a diffraction limited spot surrounded by superoscillatory ripples which does not suffer as greatly from the trade-off between resolution, viewing area and the sensitivity of the device [47].

Material presented in this introduction represents but a fraction of what is now a very rich field of scientific interest. In order to gain further understanding of superoscillations and their surrounding phenomena (principally weak values and superresolution), the reader is directed to the following review articles:

- *The Mathematics of Superoscillations* [2]. Discusses mathematical and quantum superoscillations with an emphasis on their relationship to weak values.
- *Mathematical Concepts of Superresolution* [77]. Discusses the theory of superresolution as a whole, with a section on superoscillations.
- *Optical Superoscillations: Sub-Wavelength Light Focusing and Superresolution Imaging* [48]. Discusses the development of optical superoscillations and their implementation into sub-wavelength imaging.

1.8 Overview of the Thesis

As we have seen, despite quantum mechanics being the first area in which superoscillations were studied in earnest, they are still of much interest today with their behaviour being investigated in many different quantum systems [41], [5]. This thesis hopes to build upon this work by considering free-particle quantum superoscillation in relativistic space; where time and space must be treated on an equal footing. Superoscillations in a relativistic setting have been considered [21], [17], their existence being attributed to a superluminal group velocity. However a rigorous description of their nature in relativistic quantum mechanics is yet to be provided. We consider superoscillations in $1+1$ dimensions and study how the initial superoscillatory function evolves according to both the Klein-Gordon and Dirac equation in their first-quantised configurations.

In order to evaluate the evolution free-particle quantum superoscillations, it has been shown in [30], that an eigenfunction expansion of the initial wavefunction (as shown in 1.30) does not provide a clear enough description of the wavefunction to

analyse a phenomena as subtle as superoscillation. To explain quantum superoscillation, the integral over a propagator formulation of the wavefunction is required. In chapter 2, we derive the relativistic propagators and study their behaviours near the light cone and at the $\hbar \to 0$ (WKB) limit.

In chapter 3, we review Michael Berry and Sandu Popescu's paper *Evolution of Quantum Superoscillations and Optical Superresolution Without Evanescent Waves* [30]. This paper forms the basis of how we investigate superoscillations in the relativistic limit. As it is written in terms of the Schrödinger equation, it allows us to scrutinise any calculations used in the relativistic quantum wave equations as they should all produce the results of Berry's paper as $c \to \infty$.

In chapter 4, we begin our work on quantum superoscillations in earnest. Considered first is the free-particle Klein-Gordon equation: the description of a spin-zero relativistic quantum wavefunction. We first produce an eigenvalue solution to the Klein-Gordon equation with an initial superoscillatory wavepacket: this provides a good way of making sure any approximations subsequently made still preserve the essential structure of the superoscillatory evolution. Using the propagators derived in chapter 2, we then analyse the way in which the initial wavefunction evolves according to the Klein-Gordon equation and compare the results with the Schrödinger superoscillations seen in the previous chapter.

Using the Klein-Gordon equation, we get results for a spin-zero relativistic wavefunction. In order to analyse how an initial superoscillatory wavefunction of spin-half evolves in the relativistic limit, we use the Dirac equation. To begin chapter 5, we discuss the results of [33] in which a method of producing spin-half wavefuncitons by starting with one of spin-zero. We then apply this to the results of chapter 4 and compare the two, showing whether or not spin affects the evolution of a relativistic free-particle superoscillatory wavefunction.

Lastly, we conclude the findings of each chapter and discuss where this research can go in the future.

Chapter 2

The Dynamics of a Klein-Gordon Free Particle in 1+1 Dimensions

As discussed in the introductory chapter, superoscillatory waves are the product of almost perfect destructive interference between contributing plane waves. It has been shown that investigation of the evolution of these waves requires subtle mathematical analysis [30] [36]. In this situation, the standard method of studying the time dependence of a quantum wavefunction; evaluation of the interference between eigenfunctions does not give much insight for a superoscillatory wavefunction.

In this chapter, we discuss the tools required to calculate free particle, time dependent, spin-zero, massive, relativistic quantum wavefunctions[1]. Such tools (time evolution operators and propagators) are well known for non-relativistic quantum wavefunctions and have been used in the study of superoscillations [30], [37]. It is therefore the relativistic nature of these methods which will be of most importance to the problems we wish to solve in this thesis.

Beginning with standard plane-wave solutions then moving onto creating wavepackets for an arbitrary initial wavefunction, features of relativistic quantum evolution, such as causality and the occurrence of negative energy states, are considered.

The main emphasis of this chapter is the derivation and limits of the free-particle

[1]The case for a spin-half wavefunction is considered in chapter 5

Klein-Gordon propagator, which allows us to analyse superoscillatory wavefunctions. Derivations for propagators of positive, negative and mixed energy are presented as well as their 'light-cone' and WKB limits. Lastly, example calculations are provided.

2.1 The Free Particle Klein-Gordon Equation

The free particle Klein-Gordon equation is given, in 1+1 dimensions, as:

$$\left(\frac{\partial^2}{\partial x^2} - \frac{1}{c^2}\frac{\partial^2}{\partial t^2} - \frac{m^2c^2}{\hbar^2}\right)\Psi(x,t) = 0 \tag{2.1}$$

Solving (2.1) directly obtains the following plane wave solution:

$$\psi_{\pm}(x,t) = \frac{1}{\sqrt{V}}\exp\left[i\left(kx \mp \frac{W(k)}{\hbar}t\right)\right], \tag{2.2}$$

where the ratio $\frac{1}{\sqrt{V}}$ is a normalisation constant. (2.2) has energy eigenvalues,

$$W(k) = \sqrt{\hbar^2c^2k^2 + m^2c^4} \tag{2.3}$$

In this section we look at the properties of these solutions before showing how arbitrary wave-packet solutions can be created.

2.1.1 Positive/Negative Energy Eigenstates

A notable feature of (2.2) is the presence of the $\mp$ sign in front of the energy, $W(k)$. In relativistic quantum mechanics, eigenfunctions can have either positive or negative energy. These emerge from the fact that to ensure the energy-momentum relationship is scalar, it must be quadratic in both energy and momentum. Hence, when taking the square root of $W(k)^2$, both positive and negative energy solutions are

present.

Such negative energies are intrinsically related to anti-particles. When formulating his eponymous equation in 1930, Paul Dirac theorized that a vacuum is a state in which all negative energy levels are filled and all positive levels, empty[46]. From this theory (entitled the 'Dirac Sea') anti-particles emerge when one of the negative energy states in the Dirac Sea is unfilled.

The time dependence of negative energy states can be viewed as a wavefunction of positive energy moving backwards in time[102]. This can be seen quite clearly from (2.2) where, taking an initial positive energy state and, making the transformation $t \to -t$, a negative energy state is produced. We show this in figure 2.1 where, as t is increased, the two waves move in opposite directions.

2.1.2 Wave-Packet Solutions

Through application of Fourier's theorem to (2.2), any arbitrary wave packet can be created using the following equation:

$$\Psi(x,t) = \int_{-\infty}^{\infty} \phi(k) \exp\left[i\left(kx \mp \frac{W(k)}{\hbar}t\right)\right] dk \tag{2.4}$$

where:

$$\phi(k) = \frac{1}{2\pi}\int_{-\infty}^{\infty} \Psi(x,0)e^{ikx}dx. \tag{2.5}$$

in which, $\Psi(x,0)$ is the initial wave packet. (2.4) allows one to study how any initial wave packet evolves according to the Klein-Gordon equation.

2.2 Klein-Gordon Wave Packets and Causality

Given these basic features of Klein-Gordon wave packets, we consider a fundamental property in relativity: causality and how this plays a part in their creation. We also consider what effect negative energy states have in these calculations.

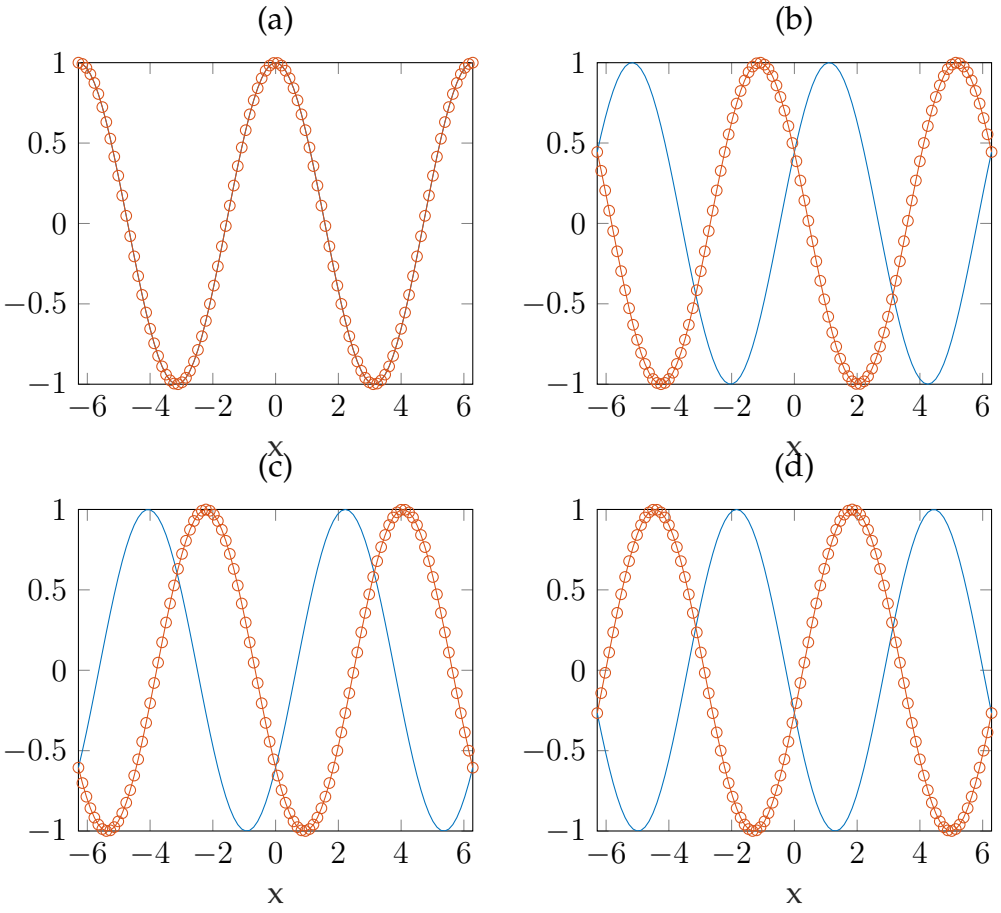

FIGURE 2.1: Time evolution of $\Re e(\Psi(x,t))$ (2.2) positive energy states (blue lines) and negative energy states (orange circled lines) for (a) $t = 0$, (b) $t = \pi/4$, (c) $t = \pi/2$ and (d) $t = \pi$. In all diagrams $-2\pi \leq x \leq 2\pi$, $m = c = k = \hbar = 1$. As t increases, the two wavefunctions move in opposite directions.

2.2.1 Causality

In essence, causality relates a cause to its effect; it states that cause must precede the effect. Take the point, in $1+1$ dimensional space-time, $r(x_0, t_0)$. In relativistic theory, causality requires that no event taking place at a distance further away (in either direction) than $x_0 + ct_0$ can affect $r(x_0, t_0)$; event A can cause event B if A lies in B's past light cone.

Using this definition of relativistic causality, we construct a one-dimensional light-cone with boundaries at $x + ct$ and $x - ct$. If a path between two events $r(x,t)$ and $r'(x',t')$ has an angle (with respect to the x-axis) smaller than that of the light-cone, it is an acausal path. This is shown, for $x > 0$, in figure 2.2.

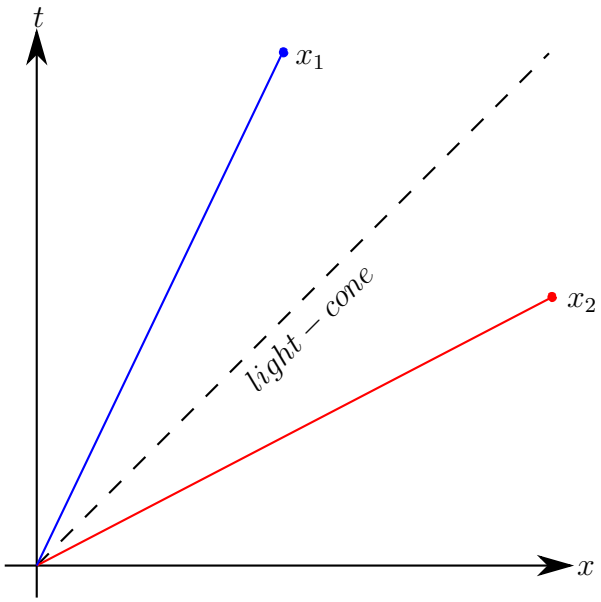

FIGURE 2.2: Showing two space-time paths (world-lines). The blue world-line (x_1) is causal as its angle with respect to the x-axis is larger than that of the light-cone. Where as the red world line (x_2) is acausal as the angle is smaller than that of the light-cone.

2.2.2 Causal Wave Packets

Causality plays an important role in the calculation of Klein-Gordon wave-packets[2]. To illustrate this, a 'frequency representation' of equations (2.4) and (2.5) is used. We create this by rearranging (2.3) for k and substituting this into (2.4) and (2.5).

$$k(\omega) = \frac{1}{c}\sqrt{\omega^2 - \frac{m^2c^4}{\hbar^2}} \tag{2.6}$$

$$\Psi(x,t) = \int_C \sigma(\omega) \exp\left[i\left(\frac{x}{c}\sqrt{\omega^2 - \frac{m^2c^4}{\hbar^2}} - \omega t\right)\right] d\omega \tag{2.7}$$

$$\sigma(\omega) = \frac{1}{2\pi}\int_0^\infty \Psi(0,t)e^{i\omega t}dt \tag{2.8}$$

The limits of the integral in (2.8) are taken as 0 to ∞ because we are only interested in the effects caused by the event at $t = 0$, $x = 0$ and nothing that precedes it. We

[2]We will show later in the chapter that, in specific cases, causality isn't always conserved in Klein-Gordon wave packets

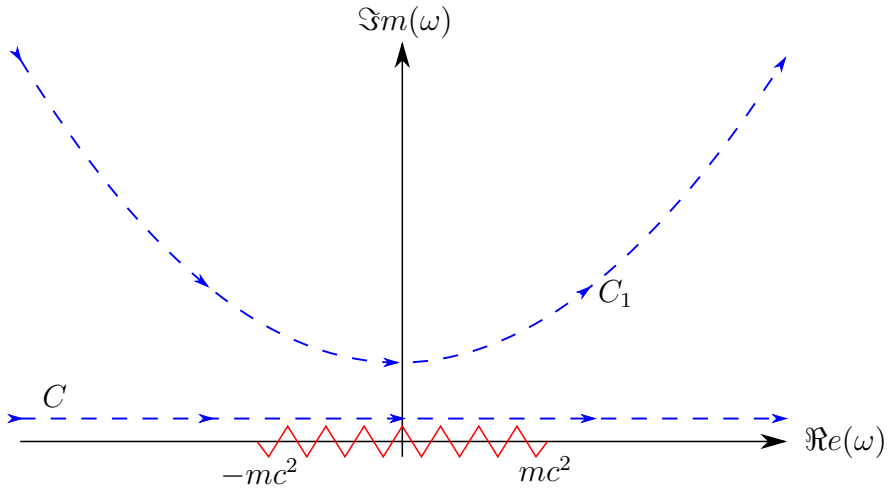

FIGURE 2.3: Complex plane of the frequency, ω, in (2.7). Indicating the branch cut (red) and contours (blue).

have also omitted the range of integration in (2.7) and replaced it with a contour, C, which will now be explained.

Figure 2.3 shows the complex plane through which we integrate in (2.7). Along the real axis, we have a branch cut running from $-mc^2 \leq \omega \leq mc^2$ which emanates from the branch points of the square root. (2.8) shows that $\sigma(\omega)$ is analytic for $\Im m(\omega) > 0$, which implies that the contour, C, must run from $-\infty$ to ∞ above the branch cut.

This is not the only possible configuration of the complex frequency plane. It could be set up with a branch structure in which there are two cuts: one running from $mc^2 \leq \omega < \infty$ and the other from $-\infty < \omega \leq -mc^2$. The branch structure shown in figure 2.3 is chosen as, for positive real ω, the resultant momentum is positive and hence the waves are travelling forward. Similarly, for negative real ω, the momentum is positive.

We now look at the argument of the exponential in (2.7) in the limit $\omega \to \infty$ and find:

$$\frac{x}{c}\sqrt{\omega^2 - \frac{m^2c^4}{\hbar^2}} - \omega t \to \omega(x/c - t) \tag{2.9}$$

Therefore, for $x > ct$ we can deform our contour C in the upper half of the plane to infinity via C_1 in figure 2.3. As it doesn't come into contact with the branch cut along

the real axis and, providing $\sigma(\omega)$ doesn't include any singularities in this region of the plane, the result of the integral along C_1 is zero:

$$\Psi(x,t) = 0 \quad (x > ct) \tag{2.10}$$

Through inspection of the analyticity of our Klein-Gordon wave packet, we have estabilished causality [26], [106], [99], [34]; if an analytic signal enters the half-space at $t = 0$ and $x = x_0$, we can extrapolate (2.10) in the following way:

$$\Psi(x + x_0, t) = 0 \quad (x + x_0 > ct). \tag{2.11}$$

This states that the time taken for the signal to travel from x_0 to $x + x_0$ cannot be less than $t = \frac{(x+x_0)}{c}$ as it is a requirement of such signals to be zero for any times less than this. This boundary is the light-cone meaning that any analytic signal cannot cross the light-cone and is causal, therefore.

2.2.3 Negative Energy States

To further our understanding of (2.7), we now discuss the negative frequency (energy) states. As, for convergence, we take the Contour C in figure 2.3 from $-\infty$ to ∞ along the real axis, these frequencies are intrinsic to the calculation of our causal wave-packet[3]. The energies $-\frac{mc^2}{\hbar} \leq \omega \leq 0$ (which, due to the how we treated the branch cut in figure 2.3, are not included in previous discussion of equation (2.7)) correspond to evanescent waves; waves that decrease exponentially with x in the half-space. Therefore, the negative energies which will be present for all time are those in the range $-\infty \leq \omega \leq -\frac{mc^2}{\hbar}$.

Therefore, causal wave-packets are created through superposition of frequencies in the spectrum:

$$|\omega| \geq \frac{mc^2}{\hbar} \tag{2.12}$$

[3]Note that in our original wave-packet integral (2.4), we do not include both positive and negative energies and can hence use this method to create entirely positive or negative energy wave-packets

We have so far only touched upon the fact that we can create acausal wave-packets. This will be considered in the next section in which we create an integral representation of the free Klein-Gordon by using our integral over the momentum k (2.4).

2.3 The Free Particle Klein-Gordon Propagator

2.3.1 Building A Propagator

Consider an initial wave-packet, $\psi(x, 0)$. We have shown the time-evolution of the wave-packet can be analysed by taking the Fourier transform of $\psi(x, 0)$. Although a very useful tool, this is not always feasible as we may not be able to evaluate the Fourier transform of our initial wave-packet. We therefore look for another way to allow us to calculate the evolution of our wave-packet.

We begin by considering how our initial wave-packet will evolve from one point in space-time, $(x', 0)$. To do this we define the dimensionless function $S(x - x', t)$:

$$\Psi(x - x', t) = S(x - x'; t)\psi(x', 0) \tag{2.13}$$

Which propagates the initial wavefunction, $\psi(x', 0)$ through space-time, returning the result: $\Psi(x - x', t)$. In order to find the wavefunction as a function of x (as opposed to $x - x'$) and t, the result of (2.13) is integrated over all x'. To demonstrate why this is necessary, we show an example in which our initial wavefunction evolves in a discrete space:

Consider the one dimensional space, x', as made of $2n + 1$ points, each separated by a distance δ. To propagate our initial wave-packet we use $\Delta(x - x_i, t)$ at each point in the discrete space, x_i, where x_i plays the role of x' in (2.13). This creates $2n + 1$ wavefunctions, the superposition of which will give the time-dependent

wavefunction $\Psi(x,t)$:

$$\Psi(x,t) = \sum_{i=-n}^{n} \Psi(x_i,0)S(x-x_i,t) \tag{2.14}$$

In order to get a complete wavefunction from (2.14), an infinite number of waves emanating from an infinite number of points must be summed. To achieve this, the limit $\delta \to 0$ is taken :

$$\Psi(x,t) = \int_{-\infty}^{\infty} \Psi(x',0)\Delta(x-x',t)dx', \tag{2.15}$$

where $\Delta(x-x';t)$ plays the same role of $S(x-x';t)$ but has units of m^{-1}. Equation (2.15) is the well known 'integral over a propagator' formalism of a time-dependent wavefunction, in which the propagator is denoted as $\Delta(x-x',t)$.

To begin our understanding of $\Delta(x-x',t)$, we consider its general case for $t=0$. As can be discerned from the previous discussion, the product:

$$P = \Psi(\alpha)S(x-\alpha;t), \tag{2.16}$$

in which we have replaced x' with the arbitrary spatial constant, α. To begin the derivation, we consider the evolution from $\alpha = 0$ therefore, at $t=0$, the propagator must take the form [26]:

$$\Delta(x,0) = \delta(x) \tag{2.17}$$

For $t > 0$, we begin with the general description of a time-dependent, free particle wave-packet as an integral over momentum, k :

$$\Delta(x,t) = \int_{-\infty}^{\infty} \phi(k)\psi(x,k)\exp\left[i\frac{W(k)}{\hbar}t\right]dk \tag{2.18}$$

In which, $\psi(x,k)$ are the free particle eigenfunctions and its eigenvalues, $W(k)$, are given by (2.3). Using (2.5) and (2.17) we get:

$$\phi(k) = \frac{1}{2\pi}\int_{-\infty}^{\infty}\delta(x)e^{ikx}dx = \frac{1}{2\pi} \tag{2.19}$$

$$\Rightarrow \Delta(x,t) = \frac{1}{2\pi}\int_{-\infty}^{\infty}\exp\left[i\left(kx - \frac{W(k)}{\hbar}t\right)\right]dk \tag{2.20}$$

(2.20) gives a closed-form representation of a propagator for a free-particle wave-function with energy eigenvalues $W(k)$. We now use this integral to produce the free-particle Klein-Gordon propagators.

2.3.2 Positive/Negative Energy Free Particle Klein-Gordon Propagator

When discussing Klein-Gordon propagators (or any relativistic propagator), the energy of the wave-packet we wish to propagate, whether it is positive or negative, must be considered. Positive and negative energy eigenfunctions evolve differently and it would therefore be expected that their respective propagators accommodate this. We know the eigenvalues for the free Klein-Gordon Hamiltonian:

$$W(k) = \pm\sqrt{\hbar^2c^2k^2 + m^2c^4} \tag{2.21}$$

and the eigenfunctions:

$$\psi(x,k) = \frac{1}{\sqrt{V}}e^{ikx} \tag{2.22}$$

Substituting these into (2.20) gives:

$$\Delta_{\pm}(x,t) = \frac{1}{2\pi}\int_{-\infty}^{\infty}e^{i\left(kx\mp\frac{\sqrt{\hbar^2c^2k^2+m^2c^4}}{\hbar}t\right)}dk \tag{2.23}$$

We already see that the result of the integral over k is going to depend on the sign of $W(k)$. In its present form, (2.23) cannot be solved. Multiplying the integrand by $\frac{W(k)}{W(k)}$ gives:

$$\Delta_{\pm}(x,t) = \frac{1}{2\pi}\int_{-\infty}^{\infty} \frac{W(k)}{W(k)} e^{i\left(kx \mp \frac{\sqrt{\hbar^2c^2k^2+m^2c^4}}{\hbar}\right)} dk. \tag{2.24}$$

This may at first seem a fairly arbitrary step but we notice that:

$$\frac{\partial}{\partial t}\left[e^{i\left(kx \mp \frac{\sqrt{\hbar^2c^2k^2+m^2c^4}}{\hbar}t\right)}\right] = \mp i\frac{\sqrt{\hbar^2c^2k^2+m^2c^4}}{\hbar} e^{i\left(kx \mp \frac{\sqrt{\hbar^2c^2k^2+m^2c^4}}{\hbar}t_{\pm}\right)}. \tag{2.25}$$

Using this relation in (2.24):

$$\Delta_{\pm}(x,t) = \frac{\pm i\hbar}{2\pi}\frac{\partial}{\partial t}\left[\int_{-\infty}^{\infty} \frac{1}{W} e^{i\left(kz \mp \frac{\sqrt{\hbar^2c^2k^2+m^2c^4}}{\hbar}t\right)} dk\right] \tag{2.26}$$

(2.26) is still not in an integrable form. Separating e^{ikx} into its real and imaginary parts,

$$\Delta_{\pm}(x,t) = \frac{\pm i\hbar}{2\pi}\frac{\partial}{\partial t}\left[\int_{-\infty}^{\infty} \frac{\exp\left[-i\frac{\sqrt{\hbar^2c^2k^2+m^2c^4}}{\hbar}t\right]}{\sqrt{\hbar^2c^2k^2+m^2c^4}}\Big(\cos(kx) + i\sin(kx)\Big)dk\right] \tag{2.27}$$

gives an integral that can be split in to two parts, one including the term $\cos(kx)$ and the other, $i\sin(kx)$. The integrand in the second integral is odd and hence, when integrated from $-\infty$ to ∞, the result is zero, leaving:

$$\Delta_{\pm}(x,t) = \frac{\pm i\hbar}{2\pi}\frac{\partial}{\partial t}\left[\int_{-\infty}^{\infty} \frac{\exp\left[\mp i\frac{\sqrt{\hbar^2c^2k^2+m^2c^4}}{\hbar}t\right]}{\sqrt{\hbar^2c^2k^2+m^2c^4}}\cos(kx)dk\right] \tag{2.28}$$

Using 3.961.2 in [54]:

$$\int_{-\infty}^{\infty} \frac{\exp\left[-\beta\sqrt{\gamma^2+x^2}\right]}{\sqrt{\gamma^2+x^2}}\cos(ax)dx = 2K_0\Big(\gamma\sqrt{a^2+\beta^2}\Big) \tag{2.29}$$

(where $K_0(x)$ is the modified Bessel function of the second kind) with the following substitutions:

$$\beta = \pm ict_{\pm},\ \gamma = \frac{mc}{\hbar},\ a = x,\ x = k \tag{2.30}$$

gives:

$$\int_{-\infty}^{\infty} \frac{\exp\left[\mp i\frac{\sqrt{\hbar^2c^2k^2+m^2c^4}}{\hbar}t_{\pm}\right]}{\sqrt{\hbar^2c^2k^2+m^2c^4}}\cos(kx)dk = K_0\left(\frac{mc}{\hbar}\sqrt{x^2-c^2t_{\pm}^2}\right). \tag{2.31}$$

(2.29) is only convergent for $\Re e(\beta) > 0$ and $\Re e(\gamma) > 0$. Clearly from (2.30), γ is always real and positive. In order to ensure the real part of β is greater than zero, we add a small imaginary term to t such that $t \to t_{\pm} = t \mp i\epsilon$. Substitution of (2.31) into (2.28) gives:

$$\Delta_{\pm}(x, t_{\pm}) = \frac{\pm i}{\pi c}\frac{\partial}{\partial t}\left[K_0\left(\frac{mc}{\hbar}\sqrt{x^2-c^2t_{\pm}^2}\right)\right] \tag{2.32}$$

Lastly, we differentiate the Bessel function with respect to time to give our propagator, this is done using the recurrence relation from 10.29.4 in [1].

$$\frac{d}{dx}\left[\frac{K_{\nu}(x)}{x^{\nu}}\right] = -\frac{K_{\nu+1}(x)}{x^{\nu}} \tag{2.33}$$

$$\therefore \Delta_{\pm}(x, t_{\pm}) = \mp\frac{im}{\pi\hbar}c^2t_{\pm}\frac{K_1\left(\frac{mc}{\hbar}\sqrt{x^2-c^2t_{\pm}^2}\right)}{\sqrt{x^2-c^2t_{\pm}^2}} \tag{2.34}$$

Taking the limit $\epsilon \to 0$ and off-setting x by x' gives:

$$\Delta_{\pm}(x-x', t) = \mp\frac{im}{\pi\hbar}c^2t\frac{K_1\left(\frac{mc}{\hbar}\sqrt{((x-x')^2-c^2t^2}\right)}{\sqrt{(x-x')^2-c^2t^2}} \tag{2.35}$$

(2.35) is the closed form of our free Klein-Gordon propagator for positive/negative energy states. Making the substitution $t \to -t$, in the case of the positive energy propagator, gives its negative energy counterpart. This further affirms the statement

made earlier that negative energy wavefunctions are positive energy wavefunctions moving backwards in time.

2.3.2.1 Causal and Acausal Regions of the Positive/Negative Energy Propagator

Moving from the causal region ($x' < x + ct$) to the acausal region ($x' > x + ct$) in (2.35) the square root goes from being imaginary to real, with the sign determined by the sign of the energy. This allows us to write (2.35) in the following way:

$$\Delta_{\pm}(x-x',t) = \mp\frac{im}{\pi\hbar}c^2t\frac{K_1\big(\pm\frac{im}{\hbar}c^2t\sqrt{1-\frac{(x-x')^2}{c^2t^2}}\big)}{ict\sqrt{1-\frac{(x-x')^2}{c^2t^2}}} \quad (c^2t^2 > (x-x')^2) \tag{2.36}$$

(2.36) gives a form of the positive/negative energy Klein-Gordon propagator inside the light-cone. As mentioned previously, the square root is real outside the light-cone so the form of the propagator doesn't change from that shown in (2.35), in this instance. To see how the propagator behaves inside the light-cone we use the following relations given by 10.27.8 in [1]:

$$K_\nu\left(e^{\frac{1}{2}i\pi}z\right) = -\frac{1}{2}\pi i e^{-\frac{1}{2}\nu\pi i}H_\nu^{(2)}(z) \quad \left(-\frac{1}{2}\pi \leq \text{ph}z \leq \pi\right) \tag{2.37}$$

$$K_\nu\left(e^{-\frac{1}{2}i\pi}z\right) = \frac{1}{2}\pi i e^{\frac{1}{2}\nu\pi i}H_\nu^{(1)}(z) \quad \left(-\pi \leq \text{ph}z \leq \frac{1}{2}\pi\right), \tag{2.38}$$

where $H_\nu^{(1,2)}(z)$ are the Hankel functions of the first and the second kind and ph z represents the phase of z. For a positive energy propagator, the pre-factor in (2.36) is positive if $x' < x + ct$ and negative if $x' > x - ct$. Using (2.37) and (2.38) for these situations in (2.36):

$$\Delta_+(x-x',t) = \frac{m}{2\hbar}c^2t\begin{cases} -\frac{H_1^{(2)}\left(\frac{mc}{\hbar}\sqrt{c^2t^2-(x-x')^2}\right)}{\sqrt{c^2t^2-(x-x')^2}} & (x+ct > x') \\ \frac{2i}{\pi}\frac{K_1(\frac{mc}{\hbar}\sqrt{((x-x')^2-c^2t^2)})}{\sqrt{(x-x')^2-c^2t^2}} & (|x|+ct < |x'|) \\ \frac{H_1^{(1)}\left(\frac{mc}{\hbar}\sqrt{c^2t^2-(x-x')^2}\right)}{\sqrt{c^2t^2-(x-x')^2}} & (x-ct < x') \end{cases} \tag{2.39}$$

Outside the lightcone ($|x| + ct < |x'|$), the propagator is non-zero. Therefore, the propagator for a positive/negative energy Klein-Gordon free particle propagator does allow for acausal contributions to the wavefunction. These will be discussed later on in the chapter. We now do the same for a negative energy propagator:

$$\Delta_-(x-x',t) = -\frac{im}{\pi\hbar}c^2t\frac{K_1\big(-\frac{im}{\hbar}c^2t\sqrt{1-\frac{(x-x')^2}{c^2t^2}}\big)}{ict\sqrt{1-\frac{(x-x')^2}{c^2t^2}}} \quad (c^2t^2 > (x-x')^2) \tag{2.40}$$

Note that whereas we factored out $\pm ict$ from the square root for the positive energies, we now factor out $\mp ict$ for negative energies. Applying (2.37) and (2.38) to (2.40) gives :

$$\Delta_-(x-x',t) = -\frac{m}{2\hbar}c^2t\begin{cases}\frac{H_1^{(1)}\left(\frac{mc}{\hbar}\sqrt{c^2t^2-(x-x')^2}\right)}{\sqrt{c^2t^2-(x-x')^2}} & (x+ct>x')\\ \frac{2i}{\pi}\frac{K_1(\frac{mc}{\hbar}\sqrt{((x-x')^2-c^2t^2)}}{\sqrt{(x-x')^2-c^2t^2}} & (|x|+ct<|x'|)\\ \frac{-H_1^{(2)}\left(\frac{mc}{\hbar}\sqrt{c^2t^2-(x-x')^2}\right)}{\sqrt{c^2t^2-(x-x')^2}} & (x-ct<x')\end{cases} \tag{2.41}$$

2.3.2.2 Approaching the Light-Cone

For (2.39) to be valid, all the cases must be equal as $x' \to x \pm ct$. As x' reaches this limit, the arguments of the Bessel and Hankel functions become very small and tend to zero. Using this, we now take limiting forms of the three cases in (2.39) and show that they are all equal as $x' \to x \pm ct$. This is shown only for the positive energy propagator; proofs for the negative energy propagator follow trivially [87].

We begin with the case where $0 \leq x' < x + ct$; the first case in (2.39). From 10.7.7 in [1], the limiting form for a Hankel function of the second kind is:

$$H_\nu^{(2)}(z) \sim \frac{i}{\pi}\Gamma(\nu)\left(\frac{1}{2}z\right)^{-\nu} \quad (z \to 0) \tag{2.42}$$

Substituting z for the argument of the Hankel function of the second kind in (2.41):

$$\therefore H_1^{(2)}\left(\frac{mc}{\hbar}\sqrt{c^2t^2-z^2}\right) \sim \frac{2i}{\pi}\left(\frac{mc}{\hbar}\sqrt{c^2t^2-z^2}\right)^{-1} \quad (ct \to z) \tag{2.43}$$

We can now replace the Hankel function of the second kind in (2.41) with the approximation (2.43).

$$\Rightarrow \Delta(z,t) \sim -\frac{i}{\pi}ct(c^2t^2-z^2)^{-1} \quad (ct \to z) \tag{2.44}$$

Next, we look at the region outside of the lightcone; the second case in (2.39). We have from 10.30.2 in [1]:

$$K_\nu(z) \sim \frac{1}{2}\Gamma(\nu)\left(\frac{1}{2}z\right)^{-\nu} \quad (z \to 0) \tag{2.45}$$

(2.46) is identical to (2.42) apart from the pre-factors in front of the gamma functions. (2.42) is multiplied by $\frac{i}{\pi}$ and (2.46) has the pre-factor $\frac{1}{2}$. We now replace z in (2.46) with the argument of the modified Bessel function in (2.41):

$$K_1\left(\frac{mc}{\hbar}\sqrt{z^2-c^2t^2}\right) \sim \frac{\hbar}{mc\sqrt{z^2-c^2t^2}} \quad (z \to ct) \tag{2.46}$$

Substituting this approximation into (2.41):

$$\therefore \Delta_+(z,t) \sim \frac{i}{\pi}ct(z^2-c^2t^2)^{-1} \quad (z \to ct) \tag{2.47}$$

$$\Delta_+(z,t) \sim -\frac{i}{\pi}ct(c^2t^2-z^2)^{-1} \quad (z \to ct) \tag{2.48}$$

Lastly, we have the region $x - ct > x' \leq 0$. We have from 10.7.7 in [1]:

$$H_\nu^{(1)}(z) \sim -\frac{i}{\pi}\Gamma(\nu)\left(\frac{1}{2}z\right)^{-\nu} \quad (z \to 0) \tag{2.49}$$

In which this approximation to the Hankel function of the first kind differs from the corresponding approximation to the Hankel function of the second kind given in (2.42) only by sign. The proceeding steps follow in the same way as the previous approximations:

$$H_1^{(1)}\left(\frac{mc}{\hbar}\sqrt{c^2t^2-z^2}\right) \sim -\frac{2i}{\pi}\left(\frac{mc}{\hbar}\sqrt{c^2t^2-z^2}\right)^{-1} \quad (ct \to z) \tag{2.50}$$

$$\Rightarrow \Delta_-(z,t) \sim \frac{i}{\pi}ct(c^2t^2-z^2)^{-1} \quad (-ct \to z) \tag{2.51}$$

As x′ approaches the light-cone, the three cases in (2.39) are all equal. Furthermore, the propagator behaves as a simple pole at the light-cone. Lastly, as $t \to 0$ and $x - x' \to 0$ the initial condition for a propagator (2.17) (that the propagator is a delta function for $t = 0$) is recovered.

2.3.2.3 The WKB Limit of the Positive/Negative Energy Klein-Gordon Propagator

The WKB (Wentzel-Kramers-Brillouin) limit in quantum mechanics, provides a useful approximation in the limit $\hbar \to 0$. Mathematically, WKB solutions are approximations to differential equations of the form [56]:

$$\frac{\partial^2 w}{\partial w^2} + \gamma^2 q(z,h)w = 0 \tag{2.52}$$

in which the WKB limit is found by taking the parameter, γ, to be very large [4]. We can compare (2.52) to the Klein-Gordon equation (2.1) and see that the two are of the same form.

The Klein-Gordon equation is solvable by WKB methods:

$$\left(\frac{\partial^2}{\partial x^2} - \frac{1}{c^2}\frac{\partial^2}{\partial t^2} - \frac{m^2c^2}{\hbar^2}\right)\Psi(x,t) = 0 \tag{2.53}$$

[4]Further information about the WKB method can be found in appendix A.

In the limit, $\hbar \to 0$, the term $\frac{m^2c^2}{\hbar^2}$ tends to infinity and hence, plays the role of γ in (2.52) [5]. This causes the argument of the propagator (2.35) to become very large. Therefore, an approximation to the modified Bessel function in which the argument becomes very large is required. This is given by 10.25.3 in [1]. Applying this to the Bessel function in (2.35) gives:

$$K_1\left(\frac{mc}{\hbar}\sqrt{(x-x')^2-c^2t^2}\right) \sim \sqrt{\frac{\pi}{\frac{2mc}{\hbar}\sqrt{(x-x')^2-c^2t^2}}}\exp\left[-\frac{mc}{\hbar}\sqrt{(x-x')^2-c^2t^2}\right] \tag{2.54}$$

Giving the propagator[87]:

$$\Delta_{WKB,\pm}(x-x',t) = \pm ict\sqrt{\frac{mc}{2\pi\hbar\sqrt{(x-x')^2-c^2t^2}}}\frac{\exp\left[-\frac{mc}{\hbar}\sqrt{(x-x')^2-c^2t^2}\right]}{\sqrt{(x-x')^2-c^2t^2}} \tag{2.55}$$

Unlike the light-cone approximation, the WKB limit does not become $\delta(x')$ in the limit $(x-x',t) \to 0$. The Klein-Gordon propagator shares this disagreement between the light-cone (small argument) limit and the WKB limit with some curved space propagators [96].

If neither m, c or $\hbar$ are particularly large (or small for the case of $\hbar$) this is still a valid approximation for $x - x \gg ct$. Therefore, the WKB approximation can provide insight into the acausal contributions of the Klein-Gordon propagator. Figure 2.6 shows how effective the different approximations (light-cone and WKB) to our propagator are in different regions of space and different times. For large t, the WKB approximation becomes very accurate in the causal region of x despite stating that the WKB approximation was valid well in the acausal region of x. Similar accuracies are also found in the large c limit of the propagator.

[5] $c, m \to \infty$ can also be taken. $m \to \infty$ follows trivially from what follows. $c \to \infty$ is discussed later in the chapter.

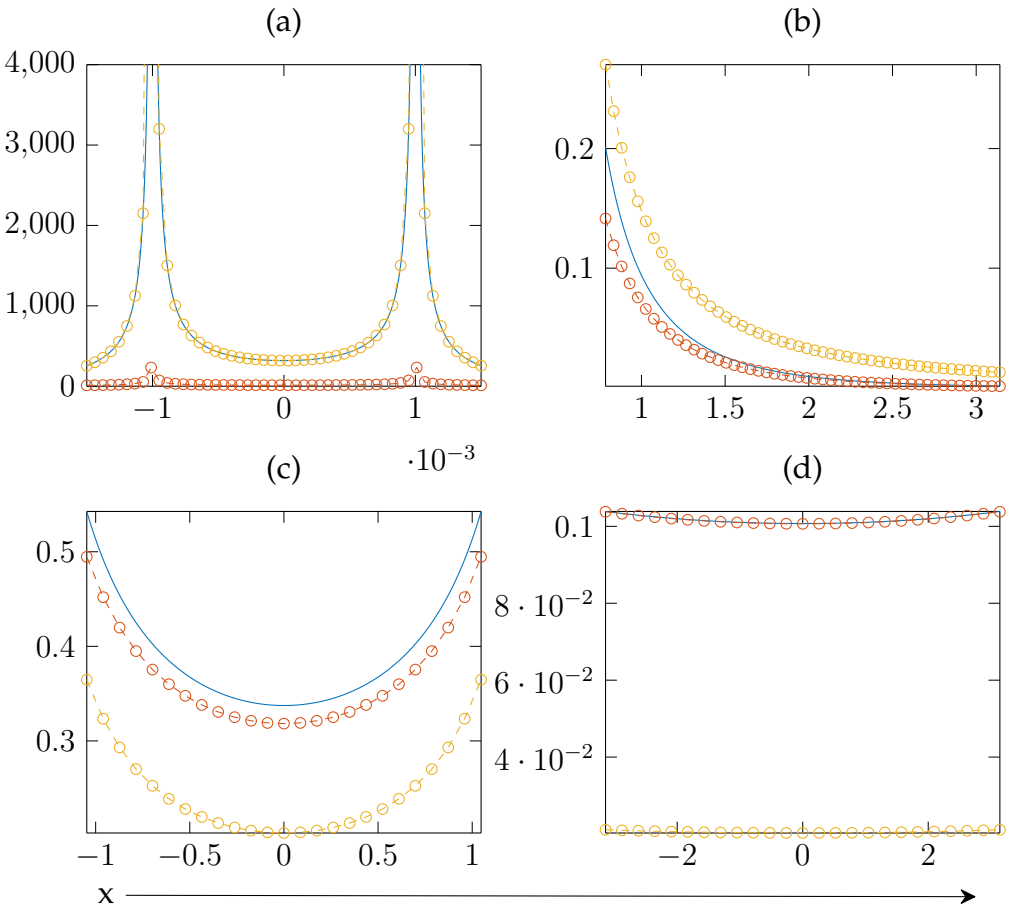

FIGURE 2.4: Exact positive energy Klein-Gordon propagator (2.35) (blue line), light-cone approximation (2.48) (yellow circles) and WKB approximation (2.55) (orange circles). For (a) $t = 0.001$ and $-0.0015 \leq x \leq 0.0015$, (b) $t = \pi/8$ and $\pi/4 \leq x \leq \pi$, (c) $t = \pi/2$ and $-\pi/3 \leq x \leq \pi/3$ and (d) $t = 5\pi$ and $-\pi \leq x \leq \pi$. $\hbar = c = m = 1$ is used throughout.

2.3.2.4 The Intermediate Case

Contributions from the light-cone approximation arise from the residues of the poles in (2.47) and contributions from the WKB approximation (2.55) often come from saddles of the phase of the exponential. Situations can occur in which these two contributions approach one another and start to coalesce [43], [30], [115].

This is problematic as the approximations are not equal at the pole; the WKB approximation has a singularity at this point whereas the light-cone approximation has a simple pole. Figure 2.6 shows that the light-cone approximation gives the best fit to the exact propagator at the pole. Whereas, moving away from the pole, the

WKB approximation is the most accurate. Therefore a propagator that, as $x' \to x \pm ct$. behaves as a simple pole and, as $x' \gg x \pm ct$, decays exponentially is needed. To do this, the following Mellin-Barnes type representation of the modified Bessel function 10.32.14[1] is used:

$$K_\nu(z) = \frac{1}{2\pi^2 i}\left(\frac{\pi}{2z}\right)^{\frac{1}{2}} e^{-z}\cos(\nu\pi)\int_{-i\infty}^{i\infty}\Gamma(\tau)\Gamma\left(\frac{1}{2}-\tau-\nu\right)\Gamma\left(\frac{1}{2}-\tau+\nu\right)(2z)^\tau d\tau \quad (2.56)$$

$$\Rightarrow K_1\left(\frac{mc}{\hbar}\sqrt{(x-x')^2-c^2t^2}\right) = \frac{-1}{2\pi^2 i}\left(\frac{\pi\hbar}{2mc\sqrt{(x-x')^2-c^2t^2}}\right)^{\frac{1}{2}} e^{-\frac{mc}{\hbar}\sqrt{(x-x')^2-c^2t^2}}\times\dots$$

$$\cdots\times\int_{-i\infty}^{i\infty}\Gamma(\tau)\Gamma\left(\frac{1}{2}-\tau-\nu\right)\Gamma\left(\frac{1}{2}-\tau+\nu\right)\left(2\frac{mc}{\hbar}\sqrt{(x-x')^2-c^2t^2}\right)^\tau d\tau \quad (2.57)$$

Substituting into (2.36):

$$\Delta_\pm(x-x';t) = \frac{\mp m}{2\pi^3\hbar}c^2 t\left(\frac{\pi\hbar}{2mc\sqrt{(x-x')^2-c^2t^2}}\right)^{\frac{1}{2}}\frac{e^{-\frac{mc}{\hbar}\sqrt{(x-x')^2-c^2t^2}}}{\sqrt{(x-x')^2-c^2t^2}}\times\dots$$

$$\cdots\times\int_{-i\infty}^{i\infty}\Gamma(\tau)\Gamma\left(\frac{1}{2}-\tau-\nu\right)\Gamma\left(\frac{1}{2}-\tau+\nu\right)\left(2\frac{mc}{\hbar}\sqrt{(x-x')^2-c^2t^2}\right)^\tau d\tau \quad (2.58)$$

We see that the pre-factor in front of the integral in (2.58) looks very similar to the WKB approximation. Therefore, in order to have this as an approximation in which the light-cone and WKB approximations coalesce, we solve the integral in the light-cone approximation. Rearranging (2.57) gives:

$$\int_{-i\infty}^{i\infty}\Gamma(\tau)\Gamma\left(\frac{1}{2}-\tau-\nu\right)\Gamma\left(\frac{1}{2}-\tau+\nu\right)\left(2\frac{mc}{\hbar}\sqrt{(x-x')^2-c^2t^2}\right)^\tau d\tau =$$

$$-2\pi^2 i K_1\Big(\frac{mc}{\hbar}\sqrt{(x-x')^2-c^2t^2}\Big)\left(\frac{\pi\hbar}{2mc\sqrt{(x-x')^2-c^2t^2}}\right)^{-\frac{1}{2}} e^{\frac{mc}{\hbar}\sqrt{(x-x')^2-c^2t^2}} \tag{2.59}$$

Using (2.46) to get the approximation for the modified Bessel function in (2.59) gives the same result as in the case of approaching the light-cone. In this limit, the argument of the exponential tends to zero and we can therefore approximate it to unity.

$$\int_{-i\infty}^{i\infty}\Gamma(\tau)\Gamma\left(\frac{1}{2}-\tau-\nu\right)\Gamma\left(\frac{1}{2}-\tau+\nu\right)\left(2\frac{mc}{\hbar}\sqrt{(x-x')^2-c^2t^2}\right)^{\tau}d\tau \approx$$

$$-2\pi^2 i\left(\frac{\pi\hbar}{2mc\sqrt{(x-x')^2-c^2t^2}}\right)^{-\frac{1}{2}}\frac{\hbar}{mc\sqrt{(x-x')^2-c^2t^2}} \tag{2.60}$$

Substituting (2.60) into (2.58):

$$\Delta(x-x';t)=\frac{\mp i}{\pi}ct\frac{1}{(x-x')^2-c^2t^2}e^{-\frac{mc}{\hbar}\sqrt{(x-x')^2-c^2t^2}} \tag{2.61}$$

This is the propagator for when the light-cone approximation and the WKB approximation coalesce. As we take the light-cone limit, (2.61) behaves as a simple pole whereas, moving away from this into the WKB regime, the exponential takes over. It also gives a delta function as $x-x', t\to 0$.

2.3.2.5 The Non-Relativisitic Limit of the Klein-Gordon Propagator

Taking the non-relativistic limit of our Klein-Gordon propagator provides us with a useful way to check the validity of our calculations. We wish to show that as $c\to\infty$, the free-particle Klein-Gordon propagator takes the form of the free particle Schrödinger propagator given by:

$$\Delta(x-x';t)=\left(\frac{m}{2i\pi\hbar t}\right)^{\frac{1}{2}}e^{-\frac{m(x-x')^2}{2i\hbar t}} \tag{2.62}$$

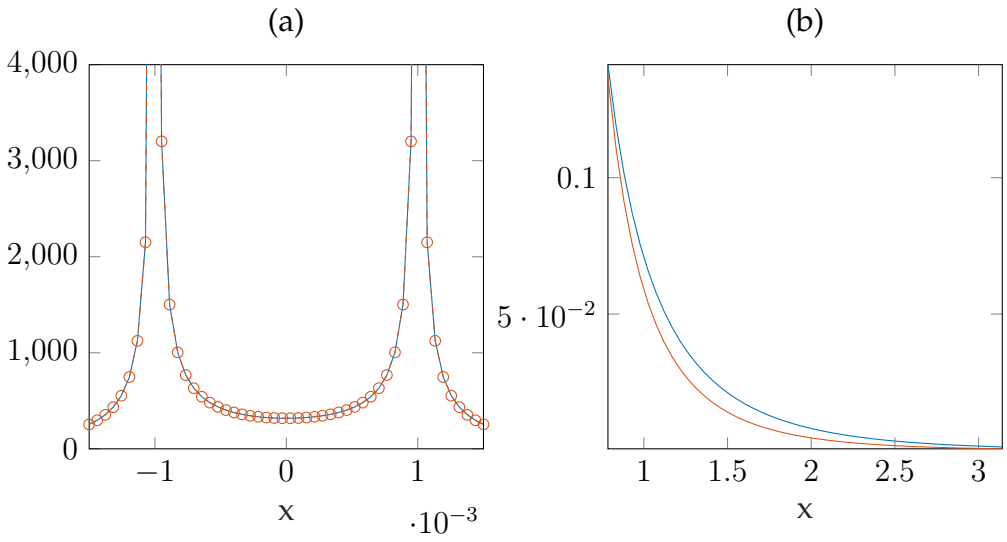

FIGURE 2.5: (a) Showing the light-cone approximation (2.47) (blue line) and our pole-WKB propagator (2.61) (orange circles) for $t = 0.001$ and $-0.0015 \leq x \leq 0.0015$. (b) The WKB approximation (2.55) (blue line) and the pole-WKB propagator (orange line) for $t = \pi/8$ and $\pi/4 \leq x \leq \pi$.

The derivation of the Schrödinger propagator employing the methods used previously in the chapter is found in Appendix C. As negative energy states do not exist in non-relativistic quantum mechanics, we only consider the positive energy propagator in this derivation. As c gets large, we can use the large argument approximation to our Bessel function again. The starting point is the WKB approximation (2.55). With c large, we make a further approximation to the square root:

$$\sqrt{(x-x')^2 - c^2t^2} \approx ict\left(1 - \frac{(x-x')^2}{2c^2t^2}\right) \tag{2.63}$$

such that the WKB approximation now becomes:

$$K_1\left(\frac{mc}{\hbar}\sqrt{(x-x')^2 - c^2t^2}\right) \approx \sqrt{\frac{\pi\hbar}{2imc^2t\left(1 - \frac{(x-x')^2}{2c^2t^2}\right)}}\exp\left[-\frac{imc^2t}{\hbar}\left(1 - \frac{(x-x')^2}{2c^2t^2}\right)\right] \tag{2.64}$$

Multiplying out the denominator of the square root gives two terms: $2imc^2t$ and $\frac{m(x-x')^2}{it}$. The first term is of $\mathcal{O}(c^2)$ whereas the second term is of $\mathcal{O}(1)$. Hence, as c

gets large, the first term dominates and the second becomes negligible. This gives:

$$\Delta_+(x-x',t) \approx \left(\frac{m}{2i\pi\hbar t}\right)^{\frac{1}{2}} e^{\frac{-m(x-x')^2}{2i\hbar t}} e^{\frac{-imc^2 t}{\hbar}} \tag{2.65}$$

Which is the same the Schrödinger propagator (2.62) with a rest-mass term in the phase of the second exponential. We can now use our Klein-Gordon propagator confidently knowing that it reproduces the non-relativistic limit as $c \to \infty$.

2.3.3 Mixed-State Klein-Gordon Propagator

By a 'mixed state propagator', we mean a propagator composed, of both positive and negative energy contributions. From the previous discussion of causal wave packets, in which the wavepackets were composed of both positive and negative energies (frequencies), it might be expected that such a propagator would be causal[67]. We now present two derivations of such propagators. The first which follows on directly from the positive and negative energy propagators derived previously and the second that is constructed in a similar way to the causal wave-packet (2.7).

2.3.3.1 Mixed-State Propagator: Position Representation

We compose the mixed-state propagator using equal amounts of positive and negative energy:

$$\Delta(x-x';t) = \frac{1}{2}\big(\Delta_+(x-x';t) + \Delta_-(x-x';t)\big) \tag{2.66}$$

Using the representations (2.39) and (2.41) allows us to see how the propagator behaves in the causal and acausal regions. For the case $ct > x - x'$;

$$\Delta(x-x';t) = \frac{m}{4\hbar}c^2 t\left(\frac{H_1^{(2)}\big(\frac{mc}{\hbar}\sqrt{c^2t^2-(x-x')^2}\big)}{\sqrt{c^2t^2-(x-x')^2}} + \frac{H_1^{(1)}\big(\frac{mc}{\hbar}\sqrt{c^2t^2-(x-x')^2}\big)}{\sqrt{c^2t^2-(x-x')^2}}\right) \tag{2.67}$$

Using the following relation from 10.4.4 in [1]

$$J_\nu(z) = \frac{1}{2}\big(H_\nu^{(1)}(z) + H_\nu^{(2)}(z)\big), \tag{2.68}$$

where $J_\nu(z)$ are Bessel functions of the first type. We get:

$$\Delta(x-x';t) = \frac{m}{2\hbar}c^2 t \frac{J_1\big(\frac{mc}{\hbar}\sqrt{c^2t^2-(x-x')^2}\big)}{\sqrt{c^2t^2-(x-x')^2}} \quad (ct > x-x'). \tag{2.69}$$

Moving onto $ct < x'-x$:

$$\Delta(x-x';t) = -\frac{m}{4\hbar}c^2 t\left(\frac{H_1^{(2)}\big(\frac{mc}{\hbar}\sqrt{c^2t^2-(x-x')^2}\big)}{\sqrt{c^2t^2-(x-x')^2}} + \frac{H_1^{(1)}\big(\frac{mc}{\hbar}\sqrt{c^2t^2-(x-x')^2}\big)}{\sqrt{c^2t^2-(x-x')^2}}\right) \tag{2.70}$$

$$= -\frac{m}{2\hbar}c^2 t \frac{J_1\big(\frac{mc}{\hbar}\sqrt{c^2t^2-(x-x')^2}\big)}{\sqrt{c^2t^2-(x-x')^2}} \quad (ct < x'-x), \tag{2.71}$$

lastly for $ct < |x-x'|$:

$$\Delta(x-x';t) = \frac{im}{\pi\hbar}c^2 t\left(\frac{K_1\big(\frac{mc}{\hbar}\sqrt{(x-x')^2-c^2t^2}\big)}{\sqrt{(x-x')^2-c^2t^2}} - \frac{K_1\big(\frac{mc}{\hbar}\sqrt{(x-x')^2-c^2t^2}\big)}{\sqrt{(x-x')^2-c^2t^2}}\right) = 0 \tag{2.72}$$

Which gives our full mixed-state propagator:

$$\Delta(x-x';t) = \frac{m}{2\hbar}c^2 t \begin{cases} \frac{J_1\left(\frac{mc}{\hbar}\sqrt{c^2t^2-(x-x')^2}\right)}{\sqrt{c^2t^2-(x-x')^2}} & (c|t| > |x-x'|) \\ 0 & (c|t| < |x-x'|) \end{cases} \tag{2.73}$$

As predicted, our mixed state propagator is causal as it is zero for $c|t| > |x-x'|$; outside the light-cone. As with the positive/negative energy propagators, the next step is to derive expressions for the limiting forms of (2.73).

2.3.3.2 Light-Cone Approximation of the Mixed-State Propagator

As the propagator approaches the light-cone, the argument of the Bessel function gets very small. We can therefore use the following approximation:

$$J_\nu(z) \sim \frac{z^\nu}{2^\nu \Gamma(\nu+1)} \tag{2.74}$$

giving the Bessel function in (2.73) as:

$$J_1\left(\frac{mc}{\hbar}\sqrt{(c^2t^2 - x - x')^2}\right) \sim \frac{mc}{2\hbar}\sqrt{c^2t^2 - (x-x')^2}. \tag{2.75}$$

Substituting this approximation back into (2.73), we get the propagator:

$$\Delta(x-x';t) \sim \frac{m^2c^3t}{4\hbar^2}\theta(|ct| - |x-x'|) \quad (x' \to x \pm ct) \tag{2.76}$$

where θ is the Heaviside step function. Clearly, unlike the positive/negative energy light-cone limit, the condition $\Delta(x-x';0) = \delta(x-x')$ is not met in (2.76). However, by using (2.66) with the light-cone approximations for the positive and negative energy propagators, we can retrieve the delta function at $t = 0$.

$$\Delta(x-x';t) \sim \frac{i}{\pi}\left(\frac{ct}{(x-x')^2 - c^2t^2} - \frac{ct}{(x-x')^2 - c^2t^2}\right) = \delta(x-x' \pm ct) \tag{2.77}$$

Therefore our full light-cone approximation to the mixed-state propagator is:

$$\Delta(x-x';t) \sim \delta(x-x' \pm ct) + \frac{m^2c^3t}{4\hbar^2}\theta(|ct| - |x-x'|) \quad (x' \to x \pm ct) \tag{2.78}$$

Clearly, for $t = 0$, we get the initial propagator requirement (2.17).

2.3.3.3 The WKB Approximation of the Mixed State Propagator

In the WKB limit, the positive and negative energy propagators take the form of 2.55. It is quite clear that when using (2.55) in (2.66) to get a WKB approximation to

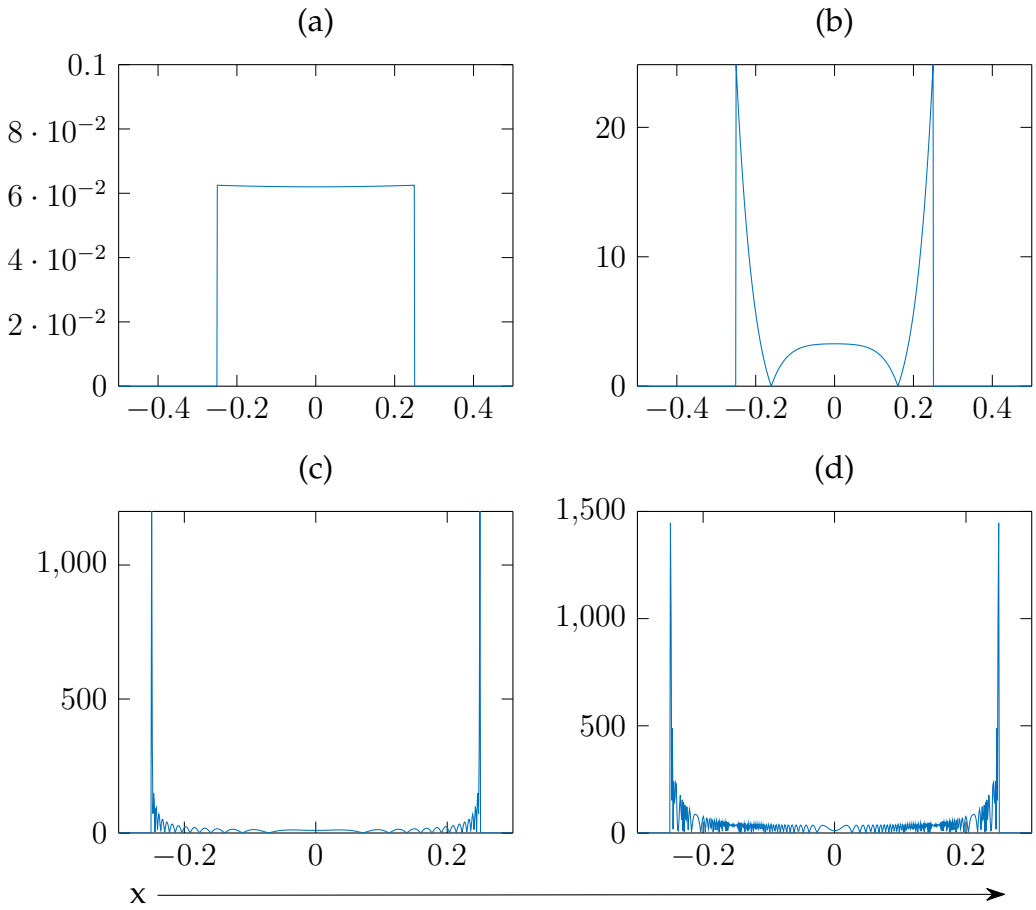

FIGURE 2.6: Showing $|\Delta(x - x'; t)|$; the WKB approximation (2.79) for the mixed-state propagator (2.73) for $t = 0.25$ and (a) $\hbar = 1$), (b) $\hbar = 1/20$, (c) $\hbar = 1/200$ and (d) $\hbar = 1/2000$.

the mixed-state propagator, the result is zero. However, this does not mean that the resulting wavefunction in the WKB limit for a mixed-state is zero. We mentioned earlier that approximation (2.55) fails at the light-cone because it doesn't produce a delta function for $t = 0$. Therefore, as $\hbar \to 0$, the only non-zero approximation to the mixed state propagator is the light-cone approximation:

$$\Delta_{WKB}(x - x'; t) \sim \delta(x - x' \pm ct) + \frac{m^2 c^3 t}{4\hbar^2}\theta(|ct| - |x - x'|) \quad (\hbar \to 0) \tag{2.79}$$

We see in figure 2.6, how as we take smaller values of $\hbar$, the mixed-state propagator (2.73) starts to resemble the delta function: $\delta((x - x')^2 - c^2 t^2)$.

2.3.3.4 Mixed-State Propagator: Time Representation

We now derive the mixed-state (causal) propagator by beginning with the causal wave-packets discussed earlier. Unlike the previous mixed-state propagator (2.73), this will be given in terms of a time variable t' as opposed to the position variable, x'. Recalling (2.7) and (2.8):

$$\Psi(x,t) = \int_C \sigma(\omega) \exp\left[i\left(\frac{x}{c}\sqrt{\omega^2 - \frac{m^2c^4}{\hbar^2}} - \omega t\right)\right] d\omega \tag{2.80}$$

$$\sigma(\omega) = \frac{1}{2\pi}\int_0^\infty \Psi(0,t)e^{i\omega t}dt \tag{2.81}$$

Taking $\Psi(0,t) = \delta(t-t')$ gives:

$$\sigma(\omega) = \frac{1}{2\pi} \tag{2.82}$$

Which gives the propagator as:

$$\Delta(t-t';x) = \frac{1}{2\pi}\int_C \exp\left[i\left(\frac{x}{c}\sqrt{\omega^2 - \frac{m^2c^4}{\hbar^2}} - \omega(t-t')\right)\right] d\omega, \tag{2.83}$$

note that as this propagates in time, the units of $\Delta(t-t';x)$ are s^{-1}. We now wish to separate out the large ω behaviour in (2.83). From our discussion in section 2.2.2 we know that as $\omega \to \infty$ the argument of the square root becomes:

$$\frac{x}{c}\sqrt{\omega^2 - \frac{m^2c^4}{\hbar^2}} - \omega t \to \omega(x/c - t) \tag{2.84}$$

Separating this out from the exponential in (2.83):

$$\Delta(t-t';x) = \frac{1}{2\pi}\int_C \left(e^{i\frac{x}{c}\sqrt{\omega^2 - \frac{m^2c^4}{\hbar^2}}} + e^{i\frac{\omega x}{c}} - e^{i\frac{\omega x}{c}}\right) e^{-i\frac{\omega(t-t')}{\hbar}} d\omega \tag{2.85}$$

Which can then be split into two separate integrals:

$$\Delta(t-t';x) = \frac{1}{2\pi}\int_C e^{-i\omega(t-t')}\left(e^{i\frac{x}{c}\sqrt{\omega^2-\frac{m^2c^4}{\hbar^2}}} - e^{i\frac{\omega x}{c}}\right)d\omega + \frac{1}{2\pi}\int_C e^{i\omega(\frac{x}{c}-(t-t'))}d\omega \quad (2.86)$$

Beginning with the second integral in (2.86), we see that there are no singularities anywhere in the complex plane and can therefore have our contour running from $-\infty$ to ∞ along the real axis:

$$\frac{1}{2\pi}\int_{-\infty}^{\infty} e^{i\omega(\frac{x}{c}-(t-t'))}d\omega = \delta\left(\frac{x}{c}-(t-t')\right) \quad (2.87)$$

Clearly, this part of the integral accounts for the light-cone limit of our mixed-state propagator. Moving onto the integral:

$$I(t-t';x) = \int_C e^{-i\omega(t-t')}\left(e^{i\frac{x}{c}\sqrt{\omega^2-m^2c^4}} - e^{i\frac{\omega x}{c}}\right)d\omega \quad (2.88)$$

From the discussion of the general case for the causal wave-packet, it is known that for $x > c(t-t')$ (which is the case when we deform C into the upper half of the complex plane) the result of the integral is zero. Therefore, we deform C into the lower half of the complex plane. Doing this allows the integral to converge for the (causal) case, $x < c(t-t')$. The fact that the upper-half of the plane doesn't contribute means we multiply the result of the integral in the lower half of the plane by the Heaviside step function $\theta(\frac{x}{c}-t)$. In contrast to when we deformed C into the upper half of the plane (which was entirely regular), we encounter two singularities at $\omega = \pm mc^2$; the result of (2.88) will be non-zero. Writing the integrand of (2.88) as:

$$f(\omega) = e^{i\omega(\frac{x}{c}-(t-t'))}\left(\exp\left[i\frac{x}{c}\left(\sqrt{\omega^2-\frac{m^2c^4}{\hbar^2}}-\omega\right)\right]-1\right)d\omega \quad (2.89)$$

(2.89) shows that as $\omega \to -i\infty$ and $\frac{x}{c} > t-t'$, the integrand tends to zero. As there are no other singularities in the complex plane aside from the branch cut, we can deform

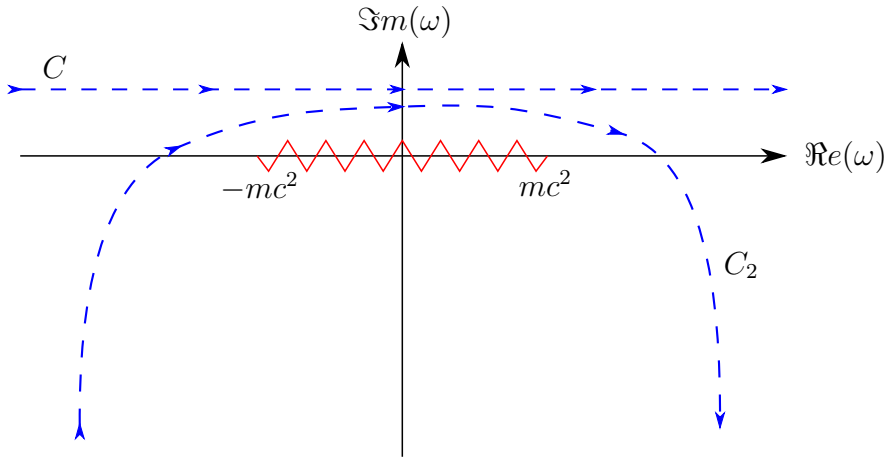

FIGURE 2.7: Complex plane of frequency, ω, for the integral (2.88). We can deform the contour C into C_2 only if $x < c(t - t')$. The branch cut running from $-mc^2$ to mc^2 is marked by the red line.

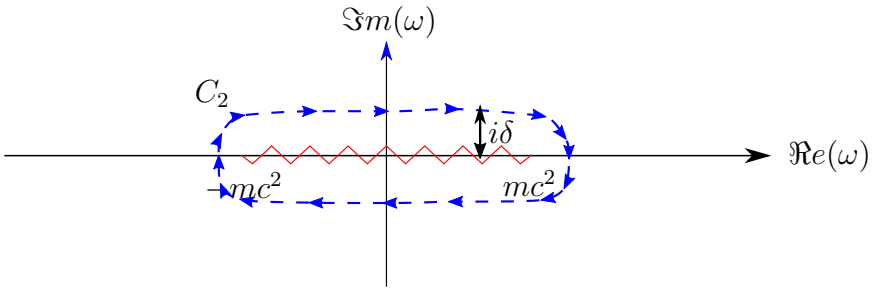

FIGURE 2.8: Complex plane of frequency, ω, for the integral over (2.89). We can further deform the contour C_2 shown in figure 2.7 so that it fully surrounds the branch cut shown by the red line.

C_2 in figure 2.7 such that it is closed to completely surround the branch-cut. Referring back to equation (2.88), the term $e^{i\frac{\omega x}{\hbar c}}$ contains no singularities, and therefore does not contribute to the integral. Contributions arise from the term $e^{i\frac{x}{c}\sqrt{\omega^2 - m^2c^4}}$.

Figure 2.8 shows how we deform C_2 to surround the branch cut. It runs a value $i\delta$ (where δ is small and has units of energy) above and below the branch cut. As δ becomes smaller, the vertical contributions either side of the branch cut become negligible, allowing us to write (2.88) as:

$$I(t - t'; x) = \int_{-mc^2}^{mc^2} f(p + i\delta)dp - \int_{-mc^2}^{mc^2} f(p - i\delta)dp \tag{2.90}$$

where $p = \Re e(\omega)$. When C_2 runs above the branch cut, it goes from left to right and gives the square root in (2.89) a phase (the angle of the contour with respect to the x-axis of 0). Whereas, when it runs below the branch cut, it goes from the right to left and has as phase of π. Denoting the square root as $\mu(\omega)$

Above the cut:

$$\mu(\omega) = e^{i0}\sqrt{p^2 - \frac{m^2c^4}{\hbar^2}} = i\sqrt{\frac{m^2c^4}{\hbar^2} - p^2} \tag{2.91}$$

Below the cut:

$$\mu(\omega) = e^{i\pi}\sqrt{p^2 - \frac{m^2c^4}{\hbar^2}} = -i\sqrt{\frac{m^2c^4}{\hbar^2} - p^2} \tag{2.92}$$

Writing (2.88) as:

$$I(t-t';x) = \int_{-\frac{mc^2}{\hbar}}^{\frac{mc^2}{\hbar}} e^{-ip(t-t')}\left(e^{-\frac{x}{c}\sqrt{p^2-\frac{m^2c^4}{\hbar^2}}} - e^{\frac{x}{c}\sqrt{p^2-\frac{m^2c^4}{\hbar^2}}}\right)dp \tag{2.93}$$

using the identity:

$$2\sinh(x) = e^x - e^{-x} \tag{2.94}$$

we get:

$$I(t-t';x) = \frac{1}{2\pi}\int_{-\frac{mc^2}{\hbar}}^{\frac{mc^2}{\hbar}} e^{-ip(t-t')}\sinh\left(\frac{x}{c}\sqrt{\frac{m^2c^4}{\hbar^2} - p^2}\right)dp \tag{2.95}$$

To further evaluate (2.95) substitute:

$$p = \frac{mc^2}{\hbar^2}\sin(\theta) \tag{2.96}$$

$$I(t-t';x) = -\frac{mc^2}{\pi\hbar}\int_{-\frac{1}{2}\pi}^{\frac{1}{2}\pi} e^{-i\frac{mc^2\sin(\theta)}{\hbar}(t-t')}\sinh\left(\frac{x}{\hbar c}\sqrt{m^2c^4 - m^2c^4\sin^2(\theta)}\right)\cos(\theta)d\theta \tag{2.97}$$

$$= -\frac{mc^2}{\pi\hbar}\int_{-\frac{1}{2}\pi}^{\frac{1}{2}\pi} e^{-i\frac{mc^2\sin(\theta)}{\hbar}(t-t')}\sinh\left(\frac{mc}{\hbar}x\cos(\theta)\right)\cos(\theta)d\theta \tag{2.98}$$

Next, we separate the integral into it's real and imaginary components:

$$I(t-t',x) = -\frac{mc^2}{\pi\hbar}\int_{-\pi/2}^{\pi/2}\cos\left(\frac{mc^2(t-t')}{\hbar}\sin(\theta)\right)\sinh\left(\frac{mcx}{\hbar}\cos(\theta)\right)\cos(\theta)d\theta + \dots$$

$$i\frac{mc^2}{\pi\hbar}\int_{-\pi/2}^{\pi/2}\sin\left(\frac{mc^2(t-t')}{\hbar}\sin(\theta)\right)\sinh\left(\frac{mcx}{\hbar}\cos(\theta)\right)\cos(\theta)d\theta. \tag{2.99}$$

The second term in (2.99) is an odd function and will integrate to zero in the range $-\frac{1}{2}\pi \leq \theta \leq \frac{1}{2}\pi$, leaving:

$$I(t-t',x) = -\frac{mc^2}{\pi\hbar}\int_{-\pi/2}^{\pi/2}\cos\left(\frac{mc^2(t-t')}{\hbar}\sin(\theta)\right)\sinh\left(\frac{mcx}{\hbar}\cos(\theta)\right)\cos(\theta)d\theta \tag{2.100}$$

As we are integrating over one period of the integrand, we can change the limits to $0 \leq \theta \leq \pi$:

$$I(t-t',x) = -\frac{mc^2}{\pi\hbar}\int_{0}^{\pi}\cos\left(\frac{mc^2(t-t')}{\hbar}\sin(\theta)\right)\sinh\left(\frac{mcx}{\hbar}\cos(\theta)\right)\cos(\theta)d\theta. \tag{2.101}$$

To solve this we use the following integral representation of the Bessel function of the first type from 10.9.13 in [1]

$$\left(\frac{z+\zeta}{z-\zeta}\right)^{\frac{\nu}{2}} J_\nu\left(\left(z^2-\zeta^2\right)^{\frac{1}{2}}\right) = \frac{1}{\pi}\int_0^\pi e^{\zeta\cos(\theta)}\cos(z\sin(\theta)-\nu\theta)d\theta\dots$$

$$\dots - \frac{\sin(\nu\pi)}{\pi}\int_0^\infty e^{-\zeta\cosh(t)-z\sinh(t)-\nu t}dt \tag{2.102}$$

Making the substitutions: $z = \frac{mc^2}{\hbar}(t-t')$, $\zeta = \frac{mc}{\hbar}x$, $\nu = 1$:

$$\left(\frac{\frac{mc^2}{\hbar}(t-t')+\frac{mcx}{\hbar}}{\frac{mc^2}{\hbar}(t-t')-\frac{mcx}{\hbar}}\right)^{\frac{1}{2}} J_1\left(\frac{mc}{\hbar}\sqrt{c^2(t-t')^2-x^2}\right) =$$

$$\frac{1}{\pi}\int_0^\pi e^{\frac{mc}{\hbar}x\cos(\theta)}\cos\left(\frac{mc^2}{\hbar}(t-t')\sin(\theta)-\theta\right)d\theta \tag{2.103}$$

Doing the same but instead substituting $\zeta = -\frac{mc}{\hbar}x$:

$$\left(\frac{c(t-t')-x}{c(t-t')+x}\right)^{\frac{1}{2}} J_1\Big(\frac{mc}{\hbar}\sqrt{c^2(t-t')^2-x^2}\Big) =$$

$$\frac{1}{\pi}\int_0^{\pi} e^{-\frac{mc}{\hbar}x\cos(\theta)}\cos\Big(\frac{mc^2}{\hbar}(t-t')\sin(\theta)-\theta\Big)d\theta \tag{2.104}$$

Subtracting (2.104) from (2.103):

$$\left(\left(\frac{c(t-t')+x}{c(t-t')-x}\right)^{\frac{1}{2}} - \left(\frac{c(t-t')-x}{c(t-t')+x}\right)^{\frac{1}{2}}\right) J_1\Big(\frac{mc}{\hbar}\sqrt{c^2(t-t')^2-x^2}\Big) =$$

$$\frac{2}{\pi}\int_0^{\pi} \cos\Big(\frac{mc^2}{\hbar}(t-t')\sin(\theta)-\theta\Big)\sinh\Big(\frac{mc}{\hbar}x\cos(\theta)\Big)d\theta \tag{2.105}$$

Using the well known trigonometric identity, expand the $\cos$ term in (2.105) to give the following two integrals:

$$\frac{2}{\pi}\int_0^{\pi} \cos\Big(\frac{mc^2}{\hbar}(t-t')\sin(\theta)\Big)\cos(\theta)\sinh\Big(\frac{mc}{\hbar}x\cos(\theta)\Big)d\theta + \ldots$$

$$\frac{2}{\pi}\int_0^{\pi} \sin\Big(\frac{mc^2}{\hbar}(t-t')\sin(\theta)\Big)\sin(\theta)\sinh\Big(\frac{mc}{\hbar}x\cos(\theta)\Big)d\theta \tag{2.106}$$

By symmetry, the second integral is zero:

$$\frac{2}{\pi}\int_0^{\pi} \cos\Big(\frac{mc^2}{\hbar}(t-t')\sin(\theta)\Big)\cos(\theta)\sinh\Big(\frac{mc}{\hbar}x\cos(\theta)\Big)d\theta = 2x\frac{J_1(\frac{mc}{\hbar}\sqrt{c^2(t-t')^2-x^2})}{\sqrt{c^2(t-t')^2-x^2}} \tag{2.107}$$

From (2.95):

$$I(t-t;x) = -\frac{mc^2}{\hbar}x\frac{J_1(\frac{mc}{\hbar}\sqrt{c^2(t-t')^2-x^2})}{\sqrt{c^2(t-t')^2-x^2}} \tag{2.108}$$

And, finally, from (2.85) and (2.86) we have the propagator:

$$\Delta(t-t';x) = \delta\left(\frac{x}{c} - (t-t')\right) - \frac{mc^2}{\hbar}x\frac{J_1(\frac{mc}{\hbar}\sqrt{c^2(t-t')^2 - x^2})}{\sqrt{c^2(t-t')^2 - x^2}} \tag{2.109}$$

2.3.4 Example Calculations

Now we have derived our propagators, we use them in some example calculations. This gives us two insights: A check to see if the results produced are the same as those directly from the Klein-Gordon equation and a method of producing time-dependent relativistic wavefunctions. We will present three calculations: First, reproducing (2.2) using the positive energy propagator. Secondly, using our light-cone, WKB and light-cone/WKB approximations to the positive energy propagator to produce a plane-wave. Lastly, we perform a numerical calculation with the time-representation of our mixed-state propagator to produce a wave-function for a Gaussian signal.

2.3.4.1 Example 1: Plane Wave

We begin with our initial wavefunction (2.14):

$$\psi_+(x,0) = \frac{1}{\sqrt{V}}e^{i\kappa x} \tag{2.110}$$

Using (2.15) and (2.35) - the positive energy propagator, gives the integral:

$$\psi(x,t) = \frac{i}{\pi}\frac{mc^2}{\hbar}t\frac{1}{\sqrt{V}}\int_{-\infty}^{\infty}\frac{K_1(\frac{mc}{\hbar}\sqrt{(x-x')^2 - c^2t^2}}{\sqrt{(x-x')^2 - c^2t^2}}e^{i\kappa x'}dx' \tag{2.111}$$

In its current form, (2.111) cannot be solved. Replacing the closed form of the propagator with the integral representation (2.23) gives:

$$\psi(x,t) = \frac{1}{2\pi}\frac{1}{\sqrt{V}}\int_{-\infty}^{\infty}\int_{-\infty}^{\infty}\exp\left[i\left(k(x-x') - \frac{\sqrt{c^2k^2 + m^2c^4}}{\hbar}t\right)\right]e^{i\kappa x'}dx'dk \tag{2.112}$$

$$= \frac{1}{2\pi}\frac{1}{\sqrt{V}}\int_{-\infty}^{\infty} e^{ikx}e^{-i\frac{\sqrt{c^2k^2-m^2c^4}}{\hbar}t}\int_{-\infty}^{\infty} e^{-i(k-\kappa)x'}dx'dk \tag{2.113}$$

For the second integral we have the solution:

$$\int_{-\infty}^{\infty} e^{-i(k-\kappa)x'}dx' = 2\pi\delta(k-\kappa) \tag{2.114}$$

Giving:

$$\psi(x,t) = \frac{1}{\sqrt{V}}\int_{-\infty}^{\infty} e^{ikx}e^{-i\frac{W(k)}{\hbar}t}\delta(k-\kappa)dk \tag{2.115}$$

$$= \frac{1}{\sqrt{V}}e^{i(\kappa x-\frac{W(\kappa)}{\hbar}t)} \tag{2.116}$$

Which is the same wavefunction as that shown in (2.2); we have shown that the Klein-Gordon propagator reproduces the exact result for a plane wave. However, to do this we didn't use the closed form of our propagator (2.35). This highlights a significant challenge with using these propagators: often the integral that needs to be solved is too complex to be evaluated analytically. However, the approximations previously derived do not possess this problem.

2.3.4.2 Example 2: Plane Wave Approximations

We start with a same initial wavefunction as the previous section:

$$\psi_+(x,0) = \frac{1}{\sqrt{V}}e^{iqx} \tag{2.117}$$

Using the light-cone approximation to the Klein-Gordon propagator, the integral we need to solve is:

$$\psi(x,t) = \frac{i}{\pi\sqrt{V}}ct\int_{-\infty}^{\infty}\frac{e^{i\kappa x'}}{(x-x')^2-c^2t^2}dx' \tag{2.118}$$

(2.118) contains poles at $x' = x \pm ct$. We deform our contour away from the real axis

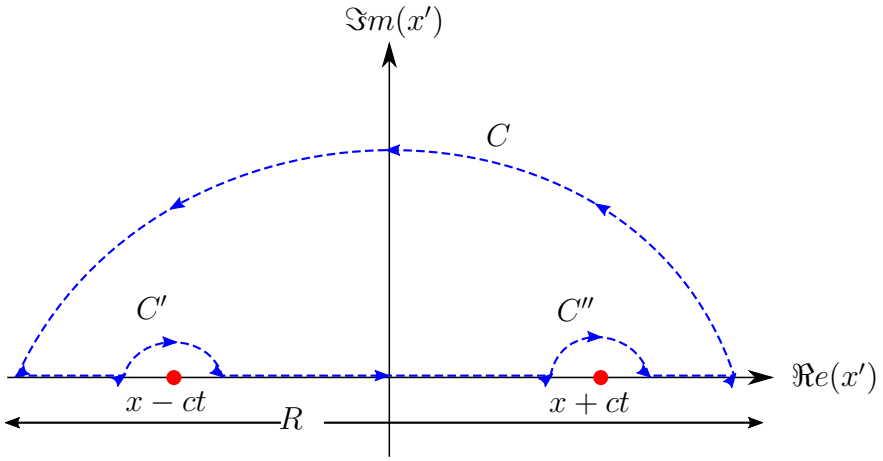

FIGURE 2.9: Showing the deformed contour C for x' plane in (2.118). Poles are shown by red circles.

such that it encloses the two poles. In figure 2.8 the contour is closed in the upper half of the plane. This is done because, as (2.118) shows, it is only in this half of the plane that the integral converges. To solve (2.118), take $R \to \infty$. The integral around C is zero and the integrals around C' and C'' are the sum of their respective residues multiplied by $i\pi$. Simple application of the residue theorem produces:

$$\text{Res}(x + ct) = -\frac{1}{2ct} e^{i\kappa(x+ct)} \tag{2.119}$$

$$\text{Res}(x - ct) = \frac{1}{2ct} e^{i\kappa(x-ct)} \tag{2.120}$$

Which gives the wavefunction as:

$$\psi(x,t) = \frac{e^{i\kappa x}}{2\sqrt{V}} \left(e^{i\kappa ct} - e^{-i\kappa ct} \right) \tag{2.121}$$

$$= i \frac{e^{i\kappa x}}{2\sqrt{V}} \sin(\kappa ct) \tag{2.122}$$

We see from (2.122) that the light-cone approximation produces a sum of two plane waves, one moving forwards in time and the other moving back. This shows that,

despite only using a positive energy propagator, some negative energy states (positive energy states moving backwards in time) are still produced. By comparing the result to the known result (2.116), we see that the light cone approximation is only valid if $W(\kappa) = \frac{\kappa c}{\hbar}$, i.e. for a particle with no mass. Therefore, this approximation is not the most useful for a free-particle of purely positive/negative energy.

For the WKB approximation, the integral we wish to solve is:

$$\psi(x,t) = it\sqrt{\frac{mc^3}{\pi\hbar V}}\int_{-\infty}^{\infty}\left((x-x')^2 - c^2t^2\right)^{-\frac{3}{4}} e^{(ikx' - \frac{mc}{\hbar}\sqrt{(x-x')^2-c^2t^2})}dx' \tag{2.123}$$

In which we have factored out $\frac{1}{\hbar}$ in the phase of the exponential. Initially, (2.123) seems quite tricky to solve. However, we are helped by the fact we have a large parameter $\frac{1}{\hbar}$. This allows us to use the saddle-point method to solve the integral. Full details of the saddle point method are shown in appendix B but in essence, the saddle point method states that for highly oscillatory integrals of the form:

$$\int_C e^{\nu w(z)}\phi(z)dz \quad (\nu \to \infty) \tag{2.124}$$

solutions arise from the saddles of $w(z)$. Allowing our contour, C, to pass through these saddle points gives us the result of the integral. Solutions are of the form:

$$\int_C e^{\nu w(z)}\phi(z)dz = \phi(z_0)\sqrt{\frac{-2\pi}{\nu w''(z_0)}}e^{\nu w(z_0)} \quad (\nu \to \infty) \tag{2.125}$$

Where z_0 are the saddles of $w(z)$. In order to solve (2.123) we need to find the saddles of:

$$w = ikx' - \frac{mc}{\hbar}\sqrt{(x-x')^2 - c^2t^2} \tag{2.126}$$

Saddles occur at points where the differential of (2.126) is equal to zero. Such points are given by the relationship:

$$x_\pm(x,t) = x \mp \sqrt{\frac{1}{1+k^2}}ct, \tag{2.127}$$

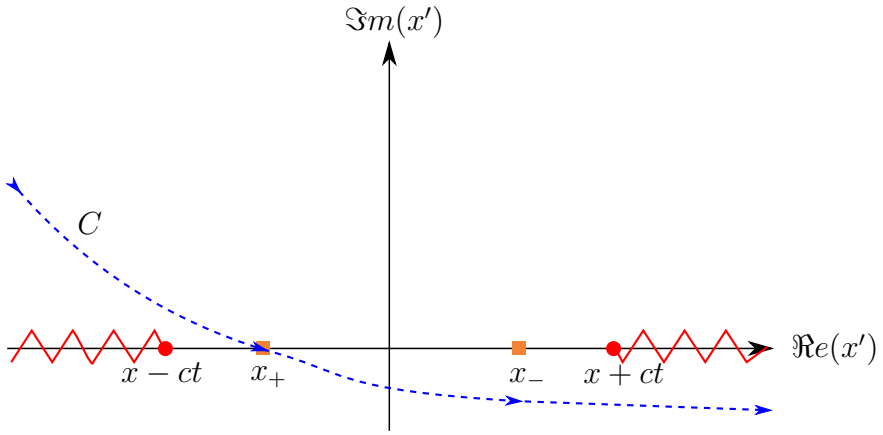

FIGURE 2.10: Showing the deformed contour, C, (blue line) for the integral (2.123). Branch cuts (red lines) occur at the branch points (red circles) $x' = x \pm ct$. Saddles of (2.126) are marked by orange squares.

where $k = \frac{mc}{\hbar\kappa}$. We see that both of these saddles are causal. This is because the term $\sqrt{\frac{1}{1+k^2}}$ cannot be greater than one and only reaches unity when $m = 0$ in which our light-cone approximation is valid. It would seem that again, we still have contributions from positive energy states moving backwards in time ($x_-(x,t)$ in 2.127). Therefore in order to get a purely positive energy wavefunction we allow our contour to only pass through the saddle x_+.

In the complex plane, we have two branch points at $x \pm ct$ both arising from the term $\left((x-x')^2 - c^2t^2\right)^{-\frac{3}{4}}$. In order to ensure that the contour does not cross the resulting cuts we have the cuts extending out to $\pm\infty$ respectively. Figure 2.10 shows how we deform our contour so that it doesn't pass through any branch cuts and that the only contributing saddle is one moving forwards in time. Using (2.125) we can solve (2.123). Denoting (2.126) as $w(x_+(x,t),x,t)$we have the solution:

$$\psi(x,t) = -ct\sqrt{\frac{mc}{2Vw''(x_+,x,t)}}\left((x-x_+)^2 - c^2t^2\right)^{-\frac{3}{4}}e^{w(x_+(x,t),x,t)} \tag{2.128}$$

where

$$w''(x',x,t) = \frac{\partial^2 w(x,t)}{\partial x'^2} = \frac{mc(x-x')^2}{\hbar((x-x')^2 - c^2t^2)^{\frac{3}{2}}} - \frac{mc}{\hbar\sqrt{(x-x')^2 - c^2t^2}} \tag{2.129}$$

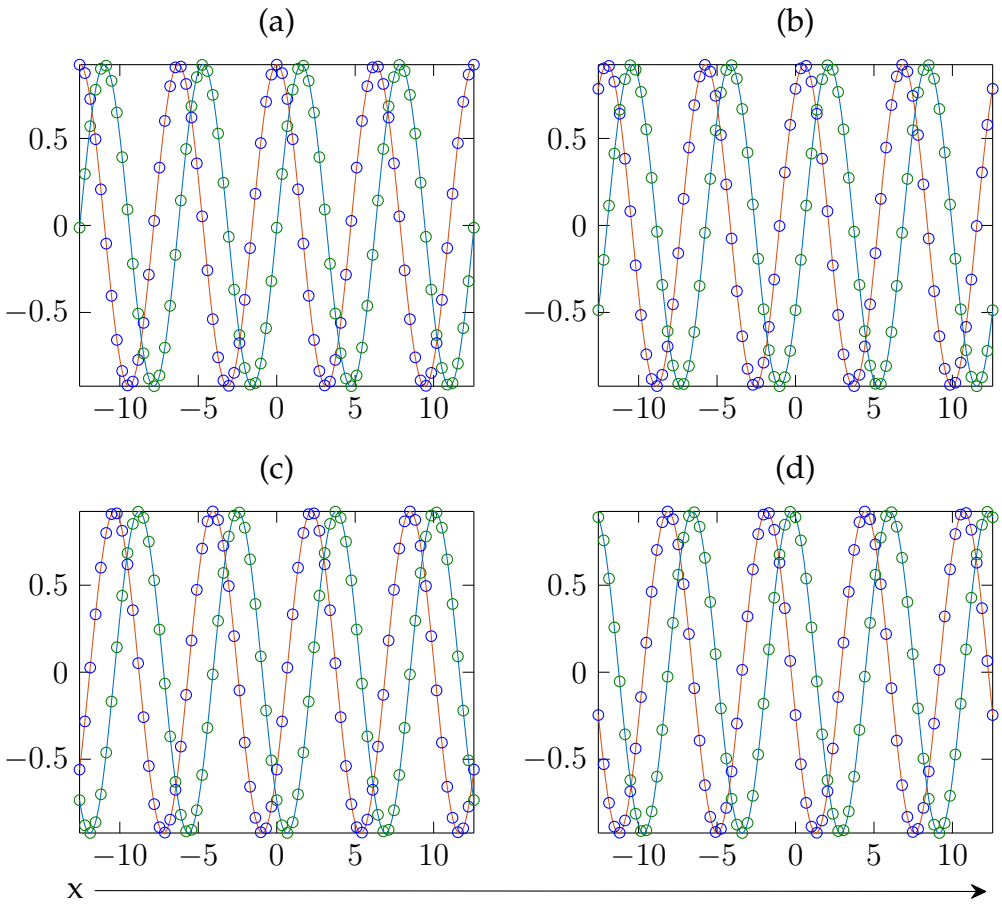

FIGURE 2.11: Full lines: real (orange) and imaginary (blue) WKB approximation to the initial plane-wave (2.128). Circles: real (blue) and imaginary (green) parts to the direct solution for the free-particle Klein-Gordon equation (2.23). (a) $t = 0.001$, (b) $t = \pi/8$, (c) $t = \pi/2$ and (d) $t = 5\pi$. $m = c = k = \hbar$ used throughout.

We now take these results and compare them to the known solution (2.23).

Figure 2.11 shows that there is excellent agreement between the WKB approximation to a plane wave (2.128) and the eigenfunction solution to the free particle Klein-Gordon equation (2.23). Furthermore, note that in all the graphs, we have taken $\hbar = 1$. This shows that not only is the WKB approximation very accurate for any value of time, it is also very accurate for any value of $\hbar$[6]. This is an initially interesting result as the WKB approximation is only valid for $\hbar \to 0$. However, such accuracy is found in this case due to the fact that the eigenfunction solutions to the free particle Klein-Gordon equation are of the same form as the eigenfunction

[6]Computations have also been done for much larger values of $\hbar$, results of the same accuracy with respect to the eigenvalues were found.

solutions to the free-particle Schrödinger equation; an asymptotic form of the Klein-Gordon equation. Therefore, if the asymptotic results are the same to the standard results, performing an asymptotic approximation there will be very accurate.

It is possible, as $\kappa \to \infty$, that the saddles in (2.127) get very close to the pole at $x' = x - ct$. In this instance, we can use the pole-WKB propagator (2.61)[7]. To get the wavefunction in this case we calculate the integral:

$$\psi(x,t) = -\frac{i}{\pi\sqrt{V}}ct\int_{-\infty}^{\infty}\left((x-x')^2 - c^2t^2\right)^{-1}e^{\kappa\left(ix'-\frac{mc}{\hbar\kappa}\sqrt{(x-x')^2-c^2t^2}\right)}dx' \tag{2.130}$$

We can further simplify this by splitting the pole contribution in (2.130) into partial fractions:

$$\frac{1}{(x-x')^2-c^2t^2} = \frac{1}{2ct}\left(\frac{1}{x-x'-ct} - \frac{1}{x-x'+ct}\right) \tag{2.131}$$

As we are only interested in the region where the saddle coalesces with the pole, we can therefore simplify (2.130) by only taking into account the pole at $x' = x - ct$:

$$\psi(x,t) = -\frac{i}{2\pi\sqrt{V}}\int_{-\infty}^{\infty}\left(x-x'-ct\right)^{-1}e^{\kappa\left(ix'-\frac{mc}{\hbar\kappa}\sqrt{(x-x')^2-c^2t^2}\right)}dx' \tag{2.132}$$

When making asymptotic approximations, the integral is mapped to a comparison integral with a similar structure of saddle points. In the case of the saddle-point method, the integral is mapped to the Gaussian integral which has a saddle at the origin. However, this mapping would not work for (2.130) as it does not take the pole into account. The comparison integral we use is [26] [115] (c.f. 7.7.2 and 7.2.3 of [[1]):

$$\int_{-\infty}^{\infty}\frac{e^{-u^2}}{u-z}du = i\pi e^{-z^2}\text{erfc}(-iz) \tag{2.133}$$

[7]The WKB approximation gives a very accurate result for this case. The saddle-pole approximation is included here to show how wavefunctions can be created using it.

In which erfc$(-iz)$ is the complementary error function. The first step in mapping (2.130) to (2.131) is to ensure that the saddles coincide. This can be done by setting:

$$u^2 = f(x';x,t) - f(x_+;x,t) \tag{2.134}$$

In which $\kappa f(x';x,t)$ is the argument of the exponential in (2.130). This implies that when $x' = x_+$, $u = 0$ and hence the saddles occur at the same place. From this we get the Jacobian:

$$\frac{\partial u}{\partial x'} = \frac{\partial}{\partial x'}\big[\sqrt{f(x';x,t) - f(x_+;x,t)}\big] = \frac{f'(x';x,t)}{2\sqrt{f(x';x,t) - f(x_+;x,t)}} \tag{2.135}$$

Lastly, we now get the position of the pole at $x' = x - ct$ in the u plane:

$$z = \sqrt{f(x-ct;x,t) - f(x_+;x,t)} \tag{2.136}$$

Using these substitutions in (2.132) gives:

$$\psi(x,t) = -\frac{i}{2\pi\sqrt{V}} e^{\kappa f(x_+;x,t)} \int_{-\infty}^{\infty} g(u) e^{-\kappa u^2} du \tag{2.137}$$

in which,

$$g(u) = \frac{2u}{f'(x';x,t)(x - x' - ct)} \tag{2.138}$$

To proceed further, we need to simplify $g(u)$. This is done using the following representation:

$$g(u) = \frac{A}{u - z} + B + u(u - z)h(u) \tag{2.139}$$

This is chosen so that we can isolate certain features of $g(u)$. The term $\frac{A}{u-z}$ incorporates the pole, B gives the value of $g(u)$ as $u \to 0$ (approaches the saddle) and the final term vanishes at both the pole and the saddle with $h(u)$ containing information about the higher order asymptotic properties of $g(u)$, which will not be considered

in this simple treatment. Calculating A is akin to calculating the residue of $g(u)$:

$$A = \lim_{u\to z}(u-z)g(u) = \lim_{x'\to x-ct}\frac{2u}{f'(x';x,t)(x-x'-ct)} \tag{2.140}$$

$$= \text{Res}\left(\frac{1}{x-x'-ct}\Big|_{x'=x-ct}\right) = -\frac{1}{2ct} \tag{2.141}$$

For B we take the limit $u \to 0$ and subtract by $\frac{A}{u-z}$ to eliminate contributions from the pole:

$$B = \lim_{u\to 0} g(u) - \frac{A}{u-z} = \lim_{x'\to x_+}\frac{2u(u-z)}{f'(x';x,t)(x-x'-ct)} + \frac{A}{z} \tag{2.142}$$

To get a more transparent representation of B, we expand $f(x';x,t)$ around the saddle:

$$f(x';x,t)|_{x'\to x_+} \approx f(x_+;x,t) + \frac{1}{2}(x'-x_+)^2 \tag{2.143}$$

This allows us to get an expression for $f'(x';x,t)$ in the neighbourhood of x_+:

$$f'(x';x,t)|_{x'\to x_+} \approx \sqrt{f(x';x,t)-f(x_+;x,t)}\sqrt{-2f''(x_+;x,t)} \tag{2.144}$$

Which gives B as:

$$B = \frac{1}{x-x_+-ct}\sqrt{\frac{2}{f''(x_+;x,t)}} - \frac{1}{2\sqrt{f(x-ct;x,t)-f(x_+;x,t)}} \tag{2.145}$$

As mentioned previously, we ignore the third term in (2.139).

$$g(u) \approx -\frac{1}{2ct(u-z)} + \frac{1}{x-x_+-ct}\sqrt{\frac{2}{f''(x_+;x,t)}} - \frac{1}{2\sqrt{f(x-ct;x,t)-f(x_+;x,t)}} \tag{2.146}$$

This gives the integral in (2.137) as:

$$\int_{-\infty}^{\infty} g(u)e^{-\kappa u^2}du \approx$$

$$\int_{-\infty}^{\infty}\left(-\frac{1}{2ct(u-z)}+\sqrt{\frac{2}{(x-x_+-ct)^2f''(x_+;x,t)}}-\frac{1}{2z}\right)e^{-\kappa u^2}du \tag{2.147}$$

Splitting (2.147) into two integrals:

$$I_1=-\frac{1}{2ct}\int_{-\infty}^{\infty}\frac{1}{u-z}e^{-\kappa u^2}du \tag{2.148}$$

$$I_2=\left(\sqrt{\frac{2}{(x-x_+-ct)^2f''(x_+;x,t)}}-\frac{1}{2z}\right)\int_{-\infty}^{\infty}e^{-\kappa u^2}du \tag{2.149}$$

To solve (2.148) we use the comparison integral (2.133) and to solve (2.149) we use the Gaussian integral. Denoting (2.147) as I we have:

$$I=-\frac{i\pi}{2}e^{-\kappa(f(x-ct;x,t)-f(x_+;x,t))}\text{erfc}(-i\sqrt{\kappa(f(x-ct;x,t)-f(x_+;x,t))}+\dots$$

$$\sqrt{\frac{\pi}{\kappa}}\left(\sqrt{\frac{2}{(x-x_+-ct)^2f''(x_+;x,t)}}-\frac{1}{2\sqrt{(f(x-ct;x,t)-f(x_+;x,t)}}\right) \tag{2.150}$$

Which gives the wavefunction as:

$$\psi(x,t)=-\frac{i}{2\pi\sqrt{V}}e^{\kappa f(x_+;x,t)}\left(\frac{\pi}{2ict}e^{-\kappa z^2}\text{erfc}(-i\sqrt{\kappa}z)+\dots\right.$$

$$\left.\sqrt{\frac{\pi}{\kappa}}\left(\sqrt{\frac{2}{(x-x_+-ct)^2f''(x_+;x,t)}}-\frac{1}{2z}\right)\right) \tag{2.151}$$

Figure 2.12 compares the saddle-pole approximation to the exact solution (2.116). We see that for very small times, the approximation is fairly accurate. However, as t increases, the approximation gets smaller whereas the exact solution retains the same amplitude. This is due to the fact that as t increases the saddle moves further away from the pole. As this happens, the saddle and pole no longer coalesce and this method becomes redundant.

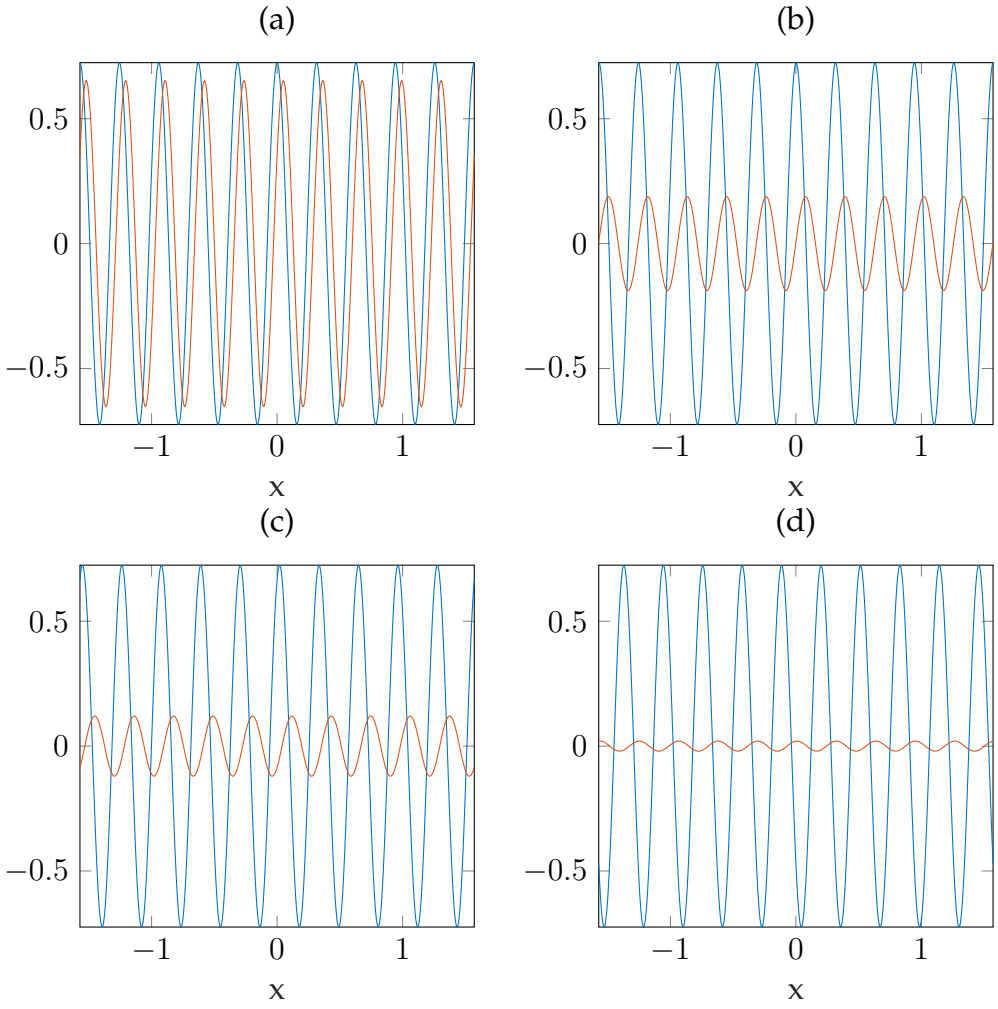

FIGURE 2.12: Showing the real parts of the wavefunction (2.116) (blue lines) and the real parts of the saddle-pole wavefunction (2.151) (orange lines). (a) $t = 0.0002$, (b) $t = 0.002$, (c) $t = 0.02$ and (d) $t = 0.2$. $-\pi/2 \leq x \leq \pi/2$, $m = c = \hbar = 1$ and $\kappa = 20$ is used throughout.

Another reason for the failure is that the uniform approximation is useful for cases in which the contribution from a pole is initially dominant and is then overtaken by the contribution from the saddle or vice-versa. 'Classical' methods for calculating the integral fail at the point where one contribution takes over from the other; the uniform approximation is used here. As we have shown, the WKB approximation is valid throughout the evolution and hence the need to capture the transition from saddle to pole is not necessary.

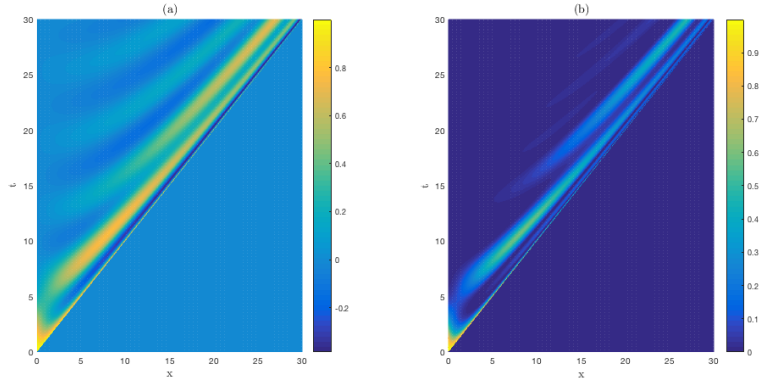

FIGURE 2.13: (a) $\Re e(\psi(x,t))$ and (b) $|\psi(x,t)|^2$ from (2.153). $m = c = \hbar = 1$, $0 \leq x \leq 30$ and $0 \leq t \leq 30$.

2.3.4.3 Example 3: Numerical Calculation of a Causal Gaussian Signal

Propagators need not only be solved analytically. Numerical evaluation of the integral over the propagator can provide good insight into the evolution of a quantum system. This can often be followed up by approximated analysis of the wavefunction using (2.4). This is done in [26] for a plane-wave with complex frequency. Here we will numerically evaluate a Gaussian signal injected in to the half-space ($x \geq 0$) at $x = 0$ using our causal propagator (2.109). The initial wavefunction is:

$$\psi(0,t) = Ae^{-\omega^2 t^2} \tag{2.152}$$

which gives our wavefunction as:

$$\psi(x,t) = Ae^{-\omega^2(t-x/c)^2} - \frac{A}{\pi}\int_0^{x+ct} \frac{J_1(\frac{mc}{\hbar}\sqrt{c^2(t-t')^2 - x^2}}{\sqrt{c^2(t-t')^2 - x^2}} e^{-k^2 t'^2} dt' \tag{2.153}$$

Figure 2.13 shows the numerically calculated time evolution of the wavefunction (2.153) and its probability density. We see that some of the interference patterns in figure 2.13 exceed an angle of 45^o with respect to the t axis. This means that these parts of the wavefunction are super-luminal. They are not however, acausal. This simply reflects that the phase velocity for these parts of the wavefunction is larger than c. This is caused by features of the waveform trying to catch up with the causal part of the wavefunction; near the light-cone. We also see that as these parts of the

wavefunction approach the light cone, they fade out and propagate causally.

Along with discussion of the initially surprising features of relativistic quantum dynamics, in this chapter we have provided a thorough derivation of the Klein-Gordon free particle propagators in 1+1 dimension. Due to the complicated mathematical nature of these propagators, it was crucial to also derive their limiting forms. We looked at the $\hbar \to 0$ (WKB) limit which provides a form of the propagator that lends itself to be solved by the saddle point method. We also derived the light-cone limit $(x - x' \to ct)$. This is best solved through contour integration. It was found that the WKB approximation provided the most accurate for any particle of $m > 0$.

It is also possible that these two limits could occur in the same region of space, it is necessary to consider the approximation to the propagator in this case. This method did not provide an accurate representation in the example calculations. However, this approximation is there for the case when the WKB limit exchanges dominance with the light-cone limit which, in our example, did not happen.

We have omitted higher dimensions, there are good accounts of their derivation in the literature [106], [109], [119]. These are written in terms of the Dirac equation but all begin with the formula (2.20).

In relativistic quantum theory, propagators are mostly used in a second-quantised language; the propagators derived here are built within a first-quantised framework. Using a first-quantised relativistic system is problematic for high-energy relativistic calculations in which particle creation/annihilation is intrinsic [92], [84]. However, the first quantised propagators, as shown, still highlight interesting features of the relativistic dynamics of a quantum free particle.

Chapter 3

Non-Relativistic Free Particle Superoscillations

We now begin the study of free-particle quantum superoscillations in $1+1$ dimensions. Our starting point is the non-relativistic case; observing how an initially superoscillatory wavefunction evolves according to the Schrödinger equation.

Up to this point (as mentioned in the introduction), there has been a reasonable amount of work in the field of quantum superoscillations. Beginning with the link between superoscillations and weak values [3]. Superoscillations have been investigated in many non-relativistic quantum systems including, the harmonic oscillator [37], and with an applied electric or magnetic field [5], [41]. In this chapter we focus on the paper *Evolution of Quantum Superoscillations and Optical Superresolution Without Evanescent Waves*, which describes a quantum free-particle wavefunction, initially exhibiting superoscillations evolves according to the Scr ödinger equation.

We begin with an analysis of the superoscillatory function presented in the introductory chapter:

$$f(x) = (\cos(\kappa x) + ia\sin(\kappa x))^{N\rho} \quad (a > 1,\ N \gg 1). \tag{3.1}$$

This involves looking at key features such as its Fourier series representation (plane-wave expansion), local momentum and the region in which it superoscillates.

Having an understanding of the initial superoscillatory function, we take the

plane-wave expansion and demonstrate how it evolves in a non-relativistic quantum mechanical system. This representation presents us with the features of its evolution we wish to understand. However, an expansion of plane waves is too opaque a representation to analyse the evolution of the exponentially small superoscillations. We therefore use propagator methods, as discussed in the previous chapter, to uncover the features of the superoscillatory wavefunction's evolution before uncovering the underlying physics.

3.1 Superoscillatory Initial State

We begin with the superoscillatory function (3.1), where κ is a wavenumber of order unity. In the case of quantum mechanics N is equivalent to the ratio $\frac{m}{\hbar}$ and hence, has dimensions $\mathrm{m}^{-2}\mathrm{s}$. In order to achieve a dimensionless power in (3.1), ρ has dimensions $\mathrm{m}^{2}\mathrm{s}^{-1}$, its physical interpretation will become apparent in chapter 4.

It is important that the asymptotic parameter, $N\rho$, is dimensionless as this allows us to compare the relative influence of each term in the power of (3.1). In this case, we are considering a system in which the energy scale is comparable to N however, with the requirement $N \gg 1$, the energy scale therefore large in comparison to $\hbar$.

Figure 3.1 shows the superoscillatory function, (3.1). Superoscillations are concentrated around $x = 0$ and they are a number of orders of magnitude smaller than the conventional oscillations. The fact that in (a) the wavefunction appears flat where $f(x)$ is superoscillating demonstrates this. We now look at some of the properties of (3.1).

By setting $a = 1$, (3.1) becomes a plane wave travelling from the left to right. However, if $a > 1$, the oscillation around $x = 0$ becomes faster. Using small-x approximations to the $\sin$ and $\cos$ in (3.1), we can further understand the behaviour of the function in the region where it appears to be superoscillating:

$$f(x) \approx (1 + ia\kappa x)^{N\rho} = \exp[\ln(1 + ia\kappa x)^{N\rho}] = \exp[N\rho \ln(1 + ia\kappa x)] \qquad (3.2)$$

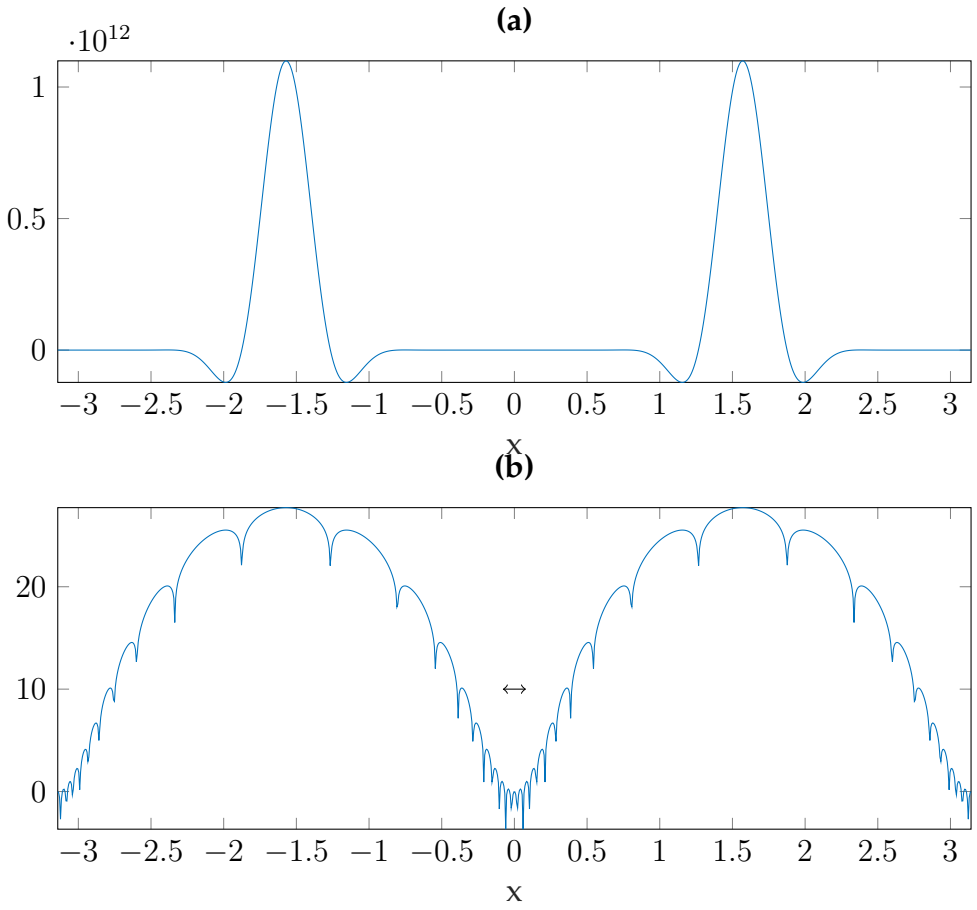

FIGURE 3.1: (a) $f(x)$ and (b) $\Re e(\log(\Re e(f(x)))$ from (3.1) for $N = 20$, $a = 4$, $\kappa = \rho = 1$, $-\pi \leq x \leq \pi$. In (b), vertical lines represent points at which the function passes through the origin. The double arrow represents the shortest period in the Fourier series (corresponding to π/N).

From this we can approximate the logarithm:

$$\ln(1 + ia\kappa x) \approx (ia\kappa x) \tag{3.3}$$

$$\Rightarrow f(x) \approx \exp[iaN\rho\kappa x] \tag{3.4}$$

(3.4) shows that the frequency of (3.1) increases exponentially with a around $x = 0$.

In order to confirm (3.1) as a superoscillatory function, a Fourier series representation must be determined. We begin with representing the $\sin$ and $\cos$ in their

exponential configurations:

$$f(x) = (\cos(\kappa x) + ia\sin(\kappa x))^{N\rho} = \frac{1}{2^{N\rho}}(e^{i\kappa x}(1+a) + e^{-i\kappa x}(1-a))^{N\rho} \tag{3.5}$$

Using a binomial expansion to expand (3.5) gives:

$$(e^{i\kappa x}(1+a) + e^{-i\kappa x}(1-a))^{N\rho} =$$

$$\sum_{m=0}^{N\rho} \frac{(N\rho)!}{m!(N\rho-m)!}(1-a)^{N\rho-m}(1+a)^m e^{im\kappa x}e^{-i(N\rho-m)\kappa x}. \tag{3.6}$$

Using the substitution

$$k_m = 1 - \frac{2m}{N\rho}, \tag{3.7}$$

(3.5) becomes:

$$\Rightarrow f(x) = \frac{1}{2^{N\rho}}\sum_{m=0}^{N\rho} \frac{(N\rho)!}{m!(N\rho-m)!}(1-a)^{N\rho-m}(1+a)^m \exp[iN\rho k_m \kappa x], \tag{3.8}$$

and can be written as the sum:

$$f(x) = \sum_{m=0}^{N\rho} c_m \exp[iN\rho k_m \kappa x], \tag{3.9}$$

in which the coefficients, c_m, are given as:

$$c_m = \frac{(N\rho)!}{2^{N\rho}}(-1)^m \frac{(a^2-1)^{\frac{1}{2}N\rho}[(a-1)/(a+1)]^{\frac{1}{2}N\rho k_m}}{[\frac{1}{2}N\rho(1+k_m)]![\frac{1}{2}N\rho(1-k_m)]!}. \tag{3.10}$$

(3.7) gives the Fourier components for the superoscillatory function; it is clear that they are band-limited: $|k_m| \leq 1$. From the small-x approximation (3.4), around $x = 0$ the frequency is governed by the superoscillatory parameter, a; it is a requirement that $a > 1$.

The superoscillatory nature of (3.1) can also be observed through representation in terms of it's local momentum :

$$k(x) = \frac{1}{N\rho}\Im m\left(\frac{d}{dx}[\ln(f(x))]\right) \tag{3.11}$$

We begin with a conversion to polar coordinates:

$$r = |x + y| = \sqrt{rr^*} = \sqrt{f(x)f^*(x)} \tag{3.12}$$

$$\theta = \arctan\left[\frac{\Im m(f(x))}{\Re e(f(x))}\right] \tag{3.13}$$

Substituting (3.1) into (3.12)

$$r = \sqrt{f(x)f^*(x)} = (\cos^2(\kappa x) + a^2\sin^2(\kappa x))^{\frac{1}{2}N\rho} \tag{3.14}$$

and hence:

$$\cos(\kappa x) + ia\sin(\kappa x) = f_1(x) = \sqrt{f(x)f^*(x)}e^{i\theta} = re^{i\theta} \tag{3.15}$$

$$\Rightarrow f(x) = f_1^N(x) = r^{N\rho}e^{iN\rho\theta}. \tag{3.16}$$

We can then define θ in terms of the superoscillatory parameter, a.

$$\theta = \arctan(a\tan(\kappa x)) \tag{3.17}$$

To get the local wavenumber (3.11) the logarithm of $f(x)$ is taken and differentiated with respect to x.

$$\frac{d}{dx}[\ln(f(x)] = \frac{N\rho\kappa((a^2-1)\sin(\kappa x)\cos(\kappa x) + ia)}{\cos^2(\kappa x) + a^2\sin^2(\kappa x)} \tag{3.18}$$

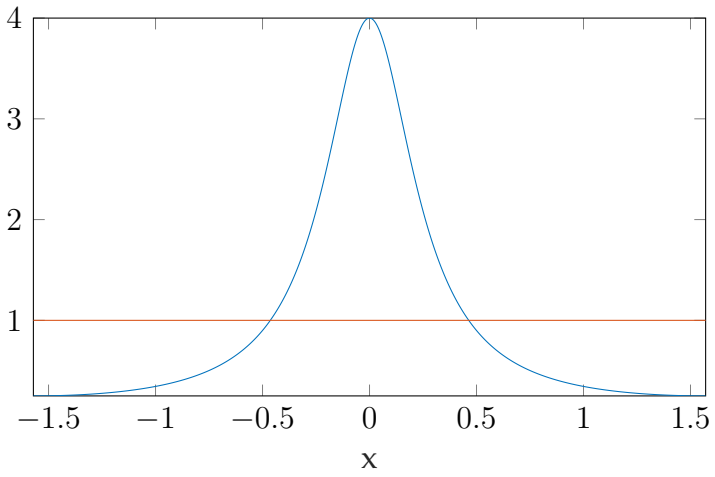

FIGURE 3.2: Local momentum (3.20) of the superoscillatory function (3.1), blue line and the fastest Fourier component, $k_m = 1$, orange line. $\kappa = 1$ and $a = 4$, $-\pi/2 \leq x \leq \pi/2$.

splitting this into it's real and imaginary parts,

$$\frac{d}{dx}[\ln(f(x))] = \frac{N\rho\kappa((a^2-1)\sin(\kappa x)\cos(\kappa x))}{\cos^2(\kappa x) + a^2\sin^2(\kappa x)} + i\frac{N\rho\kappa a}{\cos^2(\kappa x) + a^2\sin^2(\kappa x)}. \tag{3.19}$$

Which gives the local momentum:

$$k(x) = \frac{1}{N\rho}\Im m\left(\frac{d}{dx}[\ln(f(x))]\right) = \frac{\kappa a}{\cos^2(\kappa x) + a^2\sin^2(\kappa x)} \tag{3.20}$$

Figure 3.2 shows the local momentum of the superoscillatory function, (3.20) and the fastest Fourier component. Around $x = 0$, the local momentum is greater in magnitude than the fastest Fourier component and therefore, in this region (which shall later be quantified) the function is superoscillatory.

The local momentum has been determined. We now look to use it in order to create a new representation of $f(x)$:

$$r = (\cos^2(\kappa x) + a^2\sin^2(\kappa x))^{\frac{1}{2}N\rho} = \left(\frac{a\kappa}{k(x)}\right)^{\frac{1}{2}N\rho} \tag{3.21}$$

Consider the integral:

$$I = \int_0^x k(x')dx = \int_0^x \frac{a\kappa}{\cos^2(\kappa x') + a^2\sin^2(\kappa x')}dx' \tag{3.22}$$

To solve (3.22) we use 2.562.1 in [54]:

$$\text{For } \frac{b}{a} > -1,\ \int \frac{1}{a + b\sin^2(x)}dx = \frac{1}{\sqrt{a(a+b)}}\arctan\left(\sqrt{\frac{a+b}{a}}\tan(x)\right) \tag{3.23}$$

$$\Rightarrow I = \arctan(a\tan(\kappa x)) \tag{3.24}$$

From (3.16), (3.17), (3.21) & (3.24), we get a representation of $f(x)$ in terms of the local momentum:

$$f(x) = \left(\frac{a\kappa}{k(x)}\right)^{\frac{1}{2}N\rho}\exp\left[iN\rho\int_0^x k(x')dx'\right] \tag{3.25}$$

Before looking at how $f(x)$ evolves according to the Schrödinger equation, we wish to evaluate the region in which $f(x)$ is superoscillatory. As superoscillations are found where $|k(x)| > 1$, we can use this property to determine the superoscillatory region:

$$\frac{a\kappa}{\cos^2(\kappa x) + a^2\sin^2(\kappa x)} = \frac{a\kappa}{1 - (a^2 - a)\sin^2(\kappa x)} > 1. \tag{3.26}$$

Which gives the following two conditions:

$$\frac{1}{a+1} > \sin^2(\kappa x), \quad \cos^2(\kappa x) > \frac{a}{a+1} \tag{3.27}$$

$$\Rightarrow \frac{1}{\sqrt{a+1}} > \sin(\kappa x),\ \sqrt{\frac{a}{a+1}} > \cos(\kappa x) \tag{3.28}$$

$$\therefore \frac{\cos(\kappa x)}{\sin(\kappa x)} > \frac{\sqrt{\frac{a}{a+1}}}{\sqrt{\frac{1}{a+1}}} \tag{3.29}$$

(3.29) can then be solved to give the superoscillatory region:

$$|x| < x_s = \text{arccot}(\sqrt{a}) \tag{3.30}$$

where x_s represents the superoscillatory boundary. (3.30) shows that $|x_s|$ increases with a and therefore a not only determines the degree to which $f(x)$ superoscillates but also the size of the superoscillatory region.

We can now determine the number of superoscillations through:

$$n_{osc} = \frac{N\rho}{2\pi} \int_{-\operatorname{arccot}(\sqrt{a})}^{\operatorname{arccot}(\sqrt{a})} k(x)dx. \tag{3.31}$$

Substituting the local momentum (3.20) into (3.31) gives:

$$\int_{-\text{arccot}(\sqrt{a})}^{\text{arccot}(\sqrt{a})} k(x)dx = \Big[\arctan(a\tan(\kappa x)) \Big]_{-\operatorname{arccot}(\sqrt{a})}^{\operatorname{arccot}(\sqrt{a})} \tag{3.32}$$

$$= \arctan(a\tan(\operatorname{arccot}(\sqrt{a}))) - \arctan(a\tan(-\operatorname{arccot}(\sqrt{a}))) \tag{3.33}$$

Using the fact that $\tan$ is an odd function:

$$\int_{-\operatorname{arccot}(\sqrt{a})}^{\operatorname{arccot}(\sqrt{a})} k(x)dx = 2\arctan(a\tan(\operatorname{arccot}(\sqrt{a}))) \tag{3.34}$$

$$\therefore n_{osc} = \frac{N\rho}{\pi} \arctan(a\tan(\operatorname{arccot}(\sqrt{a}))) \tag{3.35}$$

$$= \frac{N\rho}{\pi} \arctan(\sqrt{a}) \tag{3.36}$$

The number of superoscillations in the window is directly proportional to N. This is not a surprising result as N represents the number of plane waves present in the function's Fourier series.

This concludes the analysis of the superoscillatory function, $f(x)$. The most important features are the way in which the parameters a and N affect the superoscillations.

We began by stipulating that a must be greater than 1 however; a more precise statement would be to say that it must be larger than the fastest Fourier component. If this is not the case, a plane wave is produced.

Not only does N determine the number of plane waves, it is also directly proportional to the number of oscillations in the superoscillatory region. Therefore, in order to get an interesting form of $f(x)$, N must be considerably greater than 1. As it is found in the exponential of the local momentum, it is referred to as an asymptotic parameter.

3.2 Eigenfunction Expansion

As the eigenfunction expansion of the superoscillatory function (3.9) is a series of plane waves, it is a solution to the time-dependent Schrödinger equation:

$$\Psi(x,0) = \frac{A}{\sqrt{L}} \sum_{m=0}^{N\rho} c_m \exp[iN\rho k_m \kappa x], \tag{3.37}$$

where A is a dimensionless normalisation constant and L, a normalisation length. The time-dependent wavefunction can then be determined through multiplication by the Schrödinger time-evolution operator:

$$\Psi(x,t) = \sum_{m=0}^{N\rho} \Psi(x,0) e^{-\frac{1}{2}iN\rho k_m^2 \omega t}. \tag{3.38}$$

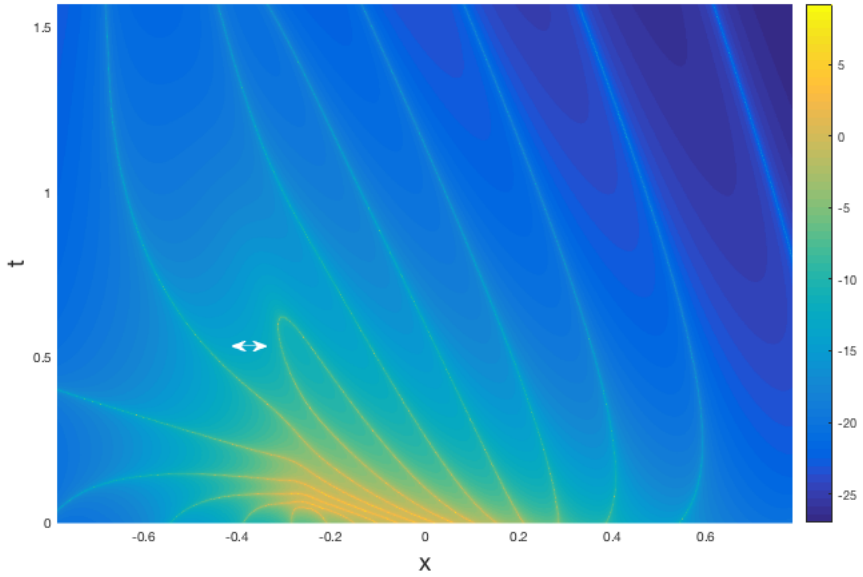

FIGURE 3.3: $-\Re e(\log(\Re e(\Psi(x,t))))$ from (3.39). $N = 20$, $a = 4$, $\rho = \kappa = 1$ and $-\pi/2 \leq x \leq \pi/2$, $0 \leq t \leq \pi/2$ Yellow lines correspond to points where $\Re(\Psi(x,t))$ is equal to zero. The white double arrow represents the minimum possible spacing for a conventional oscillation.

Therefore the time-dependent superoscillatory wavefunction, in it's eigenfunction expansion is:

$$\Psi(x,t) = \frac{A}{\sqrt{L}} \sum_{m=0}^{N\rho} c_m \exp\left[iN\rho\left(k_m \kappa x - \frac{1}{2}k_m^2 \omega t\right)\right], \tag{3.39}$$

where c_m is given by (3.10).

Figures 3.3 and 3.4 show how equation (3.39) evolves. There are two key features: the asymmetrical evolution (with respect to a line located $x = 0$) and the disappearance of superoscillations.

The asymmetrical evolution can be seen at small t where there is a higher concentration of yellow lines (which correspond to vertical lines in figure 3.4) on the left side compared to the right of figure 3.3. This phenomenon is given the term 'the wall effect'[30] as the function evolves differently either side of a line, or 'wall', at $x > 0$.

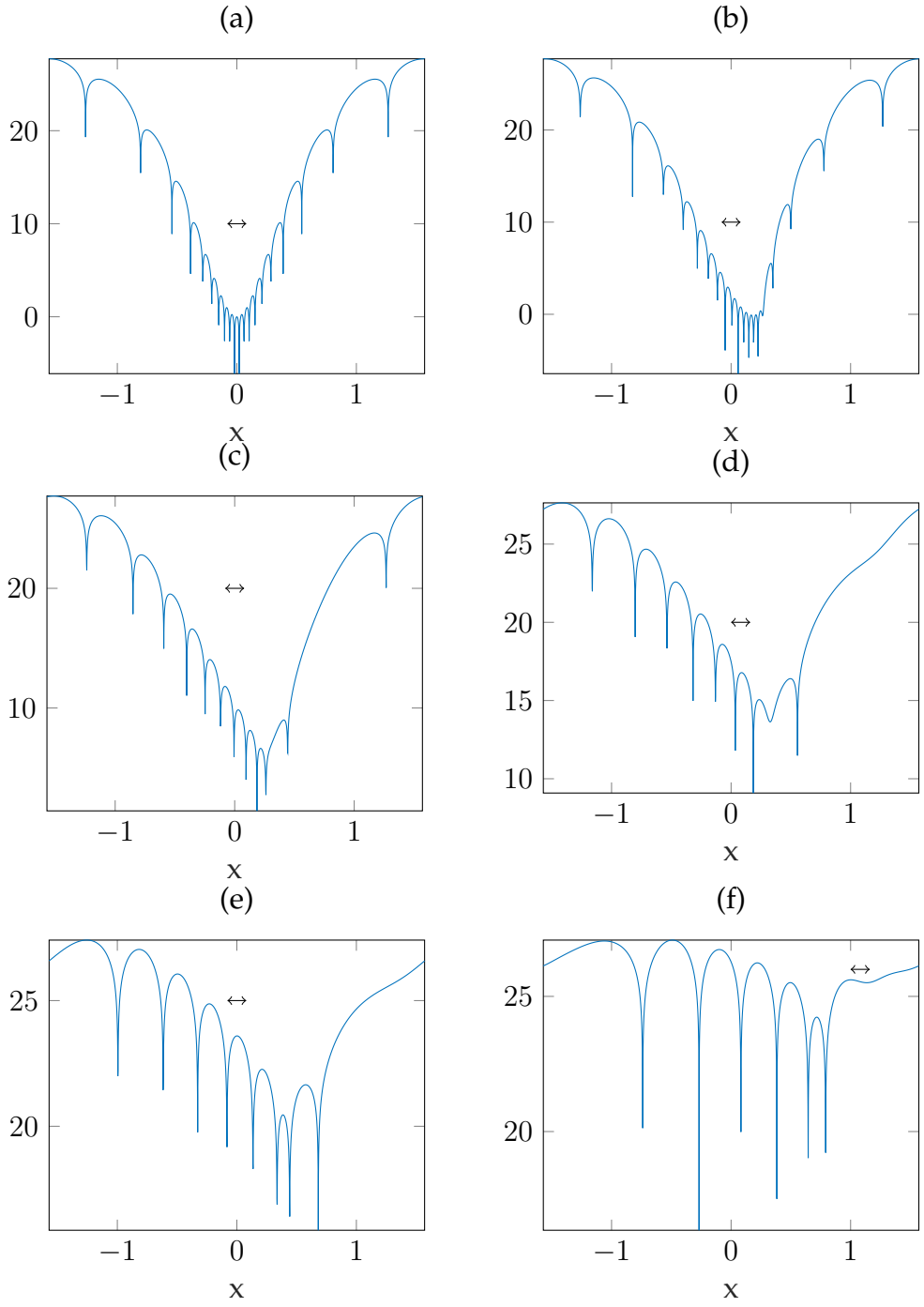

FIGURE 3.4: $-\Re e(\log(\Re e(\Psi(x,t))))$ from (3.39). $N = 20$, $a = 4$, $\rho = \kappa = 1$ and $-\pi/2 \leq x \leq \pi/2$ for times: (a) $t = 0$; (b) $t = 0.015\pi$; (c) $t = 0.08\pi$; (d) $t = (3+\sqrt{7})/8$; (e) $t = 0.5\pi$; (f) $t = \pi$. The logarithm has been taken because every time the wavefunction crosses 0 (i.e. it oscillates) the logarithm gives negative infinity. Oscillations can then be easily seen as vertical lines. Double arrows represent the shortest period of the Fourier series.

The disappearance of the superoscillations corresponds to the fact that as t increases, the distance between the vertical lines in figure 3.4 become larger and more

regular and hence any superoscillations, observed as high concentrations of lines, have disappeared.

Despite providing useful insight into the features of the initial superoscillatory function's evolution, the eigenfunction expansion is not a suitable representation with which to gain understanding. As the superoscillations are created by almost perfect destructive interference, finding the cause of the wall effect and disappearance using the component plane waves will not be a profitable exercise.

3.3 Evaluation of the Propagator

To understand the wall effect and disappearance of superoscillations, we represent the time-dependent wavefunction as an integral over a propagator.

$$\Psi(x,t) = \int_{-\infty}^{\infty} \Delta(x-x';t)\psi(x')dx', \tag{3.40}$$

where $\psi(x) = \Psi(x,0)$. Such representations were seen, in a relativistic context, in chapter 2. The non-relativistic propagator was derived as the limit of the Klein-Gordon propagator and was found to be (ignoring the rest mass term):

$$\Delta(x-x';t) = \sqrt{\frac{N}{2\pi it}} e^{-\frac{N(x-x')^2}{2it}}, \tag{3.41}$$

such that the integral to be solved to get the time-dependent superoscillatory wavefunction is:

$$\Psi(x,t) = \sqrt{\frac{NA^2}{2\pi Lit}} \int_{-\infty}^{\infty} \Big(\cos(\kappa x') + ia\sin(\kappa x') \Big)^{N\rho} e^{-\frac{N(x-x')^2}{2it}} dx'. \tag{3.42}$$

3.3.1 Representation in Terms of the Complex Momentum

In order to solve the integral in (3.42), a different representation of the initial wavefunction is required. We choose one similar to that of (3.25) but instead of using the

local momentum, we use the complex (local) momentum, this is given as:

$$q(x) = -\frac{i}{N\rho}\frac{\partial}{\partial x}\left[\log(\frac{\sqrt{L}}{A}\psi(x))\right], \tag{3.43}$$

where the local momentum is defined as $k(x) = \Re e(q(x))$. Substituting $\psi(x)$ into (3.43) gives:

$$q(x) = \kappa\frac{a\cos(\kappa x) + i\sin(\kappa x)}{\cos(\kappa x) + ia\sin(\kappa x)}. \tag{3.44}$$

From this, the initial wavefunction can be represented as:

$$\psi(x) = \frac{A}{\sqrt{L}}\exp\left[iN\rho\int_0^x q(x')dx'\right]. \tag{3.45}$$

Substituting this representation into the integral over the propagator:

$$\Psi(x,t) = \sqrt{\frac{NA^2}{2i\pi Lt}}\int_{-\infty}^{\infty}\exp\left[iN\left(\rho\int_0^{x'} q(x'')dx'' + \frac{(x-x')^2}{2t}\right)\right]dx' \tag{3.46}$$

This now gives the propagator representation of $\Psi(x,t)$ in a form which can be solved by the saddle point method, which produces solutions to integrals of the form:

$$I = \int_{-\infty}^{\infty} g(z)e^{\nu w(z)}dz \tag{3.47}$$

in which $\nu \gg 1$, general solutions are found to be:

$$I = \sum_j \sqrt{\frac{-2\pi}{\nu w''(z_j)}}g(z_j)e^{\nu w(z_j)} \tag{3.48}$$

where z_j are the saddle points of the phase of the exponential $w(z_j)$, a general derivation of (3.48) is given in appendix **??**.

Therefore, in order to solve (3.46), the saddle points of the phase of the exponential must be found.

$$\phi(x';x,t) = i\left(\rho\int_0^{x'} q(x'')dx'' + \frac{(x-x')^2}{2t}\right), \tag{3.49}$$

is the phase of the exponential. Saddle points occur when:

$$\frac{\partial}{\partial x'}\Big[\phi(x';x,t)\Big] = i\frac{\partial}{\partial x'}\left[\rho\int_0^{x'} q(x'')dx'' + \frac{(x-x')^2}{2t}\right] = 0 \tag{3.50}$$

giving the saddle point condition:

$$q(x_j) = \frac{x - x_j}{\rho t}, \tag{3.51}$$

where x_j are the saddles of (3.49). Now we have an equation for the contributing saddles of the integral (3.46), by comparing this and the general saddle point solution (3.48) we get:

$$\nu = N,\ w = \phi(x';x,t),\ g = \sqrt{\frac{N}{2\pi i t}} \tag{3.52}$$

$$w'' = \frac{\partial^2}{\partial x'^2}\left[\rho\int_0^{x'} q(x'')dx'' + \frac{(x-x')^2}{2t}\right] = i\frac{\partial}{\partial x'}\left[\rho q(x') - \frac{x-x'}{t}\right] \tag{3.53}$$

$$= i\left(\rho q'(x') + \frac{1}{t}\right). \tag{3.54}$$

We then have the saddle point solution to the integral over the propagator:

$$\Psi(x,t) \approx \sum_j \sqrt{\frac{-A^2}{2\pi L(\rho q'(x_j)t+1)}}\exp\left[iN\left(\rho\int_0^{x_j} q(x'')dx'' + \frac{(x-x_j)^2}{2t}\right)\right]. \tag{3.55}$$

3.3.2 Analytic Solutions

To obtain an analytic solution to the saddle point condition (3.51), small x and t approximations to the initial superoscillatory function and hence, it's complex momentum, are required. Before doing this however, we check to see whether these approximations retain the features of interest in the evolution of the superoscillatory wave.

We begin with approximations to $\cos$ and $\sin$ in the initial superoscillatory function:

$$\cos(\kappa x) \approx 1,\ \sin(\kappa x) \approx \kappa x \tag{3.56}$$

which gives:

$$\psi(x) = \frac{A}{\sqrt{L}}\big(\cos(\kappa x) + ia\sin(\kappa x)\big)^{N\rho} \approx \frac{A}{\sqrt{L}}(1 + ia\kappa x)^{N\rho} \tag{3.57}$$

and therefore the complex momentum:

$$q(x) = -\frac{i}{N\rho}\frac{\partial}{\partial x}[\ln(\psi(x))] = \frac{a\kappa}{1 + ia\kappa x}. \tag{3.58}$$

To simplify further calculations, we introduce the superoscillatory variables:

$$\xi = ax,\ \tau = a^2 t \tag{3.59}$$

giving:

$$\Psi(\xi,\tau) = \sqrt{\frac{NA^2}{2\pi L i\tau}}\int_{-\infty}^{\infty}\exp\left[iN\left(\frac{(\xi-\xi')^2}{2\tau} + \rho\int_0^{\xi} q(\xi'')d\xi''\right)\right]d\xi'. \tag{3.60}$$

We know the exponential of the integral over the complex momentum:

$$iN\rho\int_0^{\xi'} q_(\xi'')d\xi'' = iN\rho\int_0^{\xi'}\frac{\kappa}{1 + i\kappa\xi'}d\xi' = N\rho\ln(1 + i\kappa\xi). \tag{3.61}$$

Substituting (3.61) into (3.60) gives:

$$\Psi(\xi,\tau) = \sqrt{\frac{NA^2}{2\pi L i\tau}}\int_{-\infty}^{\infty}(1 + i\kappa\xi')^{N\rho}\exp\left[iN\frac{(\xi-\xi')^2}{2\tau}\right]d\xi'. \tag{3.62}$$

By making the substitution:

$$y = \sqrt{\frac{iN}{2\tau}}(\xi - \xi'), \tag{3.63}$$

transforms (3.62):

$$\Psi(\xi,\tau)=\frac{A}{\pi\sqrt{L}}\int_{-\infty}^{\infty}\left(1+i\kappa\xi-i\kappa\sqrt{\frac{2\tau i}{N}}y\right)^{N\rho}e^{-y^2}dy \tag{3.64}$$

The subsequent substitution:

$$z=\frac{\kappa}{1+i\kappa\xi}\sqrt{\frac{2\tau i}{N}}, \tag{3.65}$$

gives:

$$\Psi(\xi,\tau)=\frac{A}{\sqrt{\pi L}}(1+i\kappa\xi)^{N\rho}\int_{-\infty}^{\infty}(1-zy)^{N\rho}e^{-y^2}dy \tag{3.66}$$

By using a binomial expansion on $(1-zy)^{N\rho}$, we get:

$$(1-zy)^{N\rho}=\sum_{m=0}^{N\rho}\frac{(N\rho)!}{m!(N\rho-m)!}(-1)^m z^m y^m. \tag{3.67}$$

$$\Rightarrow\Psi(\xi,\tau)=\frac{A(N\rho)!}{\sqrt{\pi L}}(1+i\kappa\xi)^{N\rho}\sum_{m=0}^{N\rho}\frac{(-1)^m}{m!(N\rho-m)!}z^m\int_{-\infty}^{\infty}y^m e^{y^2}dy \tag{3.68}$$

Note that, due to the power of y^m in (3.68), for odd values of m, $\Psi(\xi,\tau)$ is equal to zero. For even powers values of m, we replace m with $2m$ and sum to values of $\frac{1}{2}N$ to get a standard integral:

$$\Psi(\xi,\tau)=\frac{A(N\rho)!}{\sqrt{\pi L}}(1+i\kappa\xi)^{N\rho}\sum_{m=0}^{\text{int}(\frac{1}{2}N\rho)}\frac{(-1)^{2m}}{(2m)!(N\rho-2m)!}z^{2m}\int_{-\infty}^{\infty}y^{2m}e^{y^2}dy, \tag{3.69}$$

$$\int_{-\infty}^{\infty}y^{2m}e^{-y^2}dy=\frac{(2m)!}{2^{2m}m!}\sqrt{\pi}, \tag{3.70}$$

$$\therefore\Psi(\xi,\tau)=\frac{A}{\sqrt{L}}(N\rho)!(1+i\kappa\xi)^{N\rho}\sum_{m=0}^{\text{int}(\frac{1}{2}N\rho)}\frac{1}{m!(N\rho-2m)!}\left(\frac{1}{2}z\right)^{2m}, \tag{3.71}$$

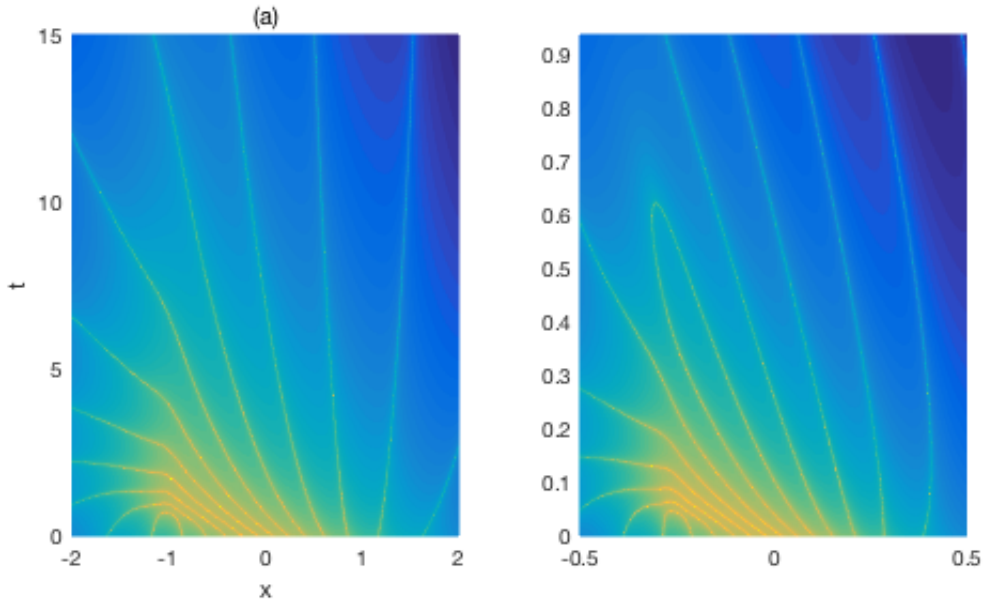

FIGURE 3.5: (a) The small ξ and τ approximation to the time-dependent superoscillatory wavefunction, $\Re e(\log(\Re e(\Psi(\xi,\tau))))$ from (3.72) for $-2 \leq \xi \leq 2$ and $0 \leq \tau \leq 15$. (b) the eigenfunction expansion $\Re e(\log(\Re e(\Psi(x,t))))$ (3.39) for $-0.5 \leq x \leq 0.5$ and $0 \leq t \leq \frac{15}{16}$. $N = 20, a = 4$ and $\kappa = \rho = 1$ in both.

and finally, re-substitution for z gives the small ξ and τ approximation to the superoscillatory wavefunction:

$$\Psi(\xi,\tau) = \frac{A}{\sqrt{L}}(N\rho)!(1+i\kappa\xi)^{N\rho} \sum_{m=0}^{\text{int}(\frac{1}{2}N\rho)} \frac{1}{m!(N\rho-2m)} \left(\frac{-2i\kappa^2\tau}{N(1+i\kappa\xi)^2}\right)^m \tag{3.72}$$

In figure 3.5, the small ξ and τ approximation is compared to the Fourier series representation, in regions where the approximation is valid, there is very strong agreement between the two.

This therefore allows us to pursue a saddle-point method solution using these approximations in the hope that it might provide a clear enough description of the wavefunction to allow us to understand the wall effect and the disappearance of superoscillations.

We begin by deriving the saddle-point condition (3.51) in terms of the superoscillatory variables ξ and τ:

The phase of the exponential is:

$$\Phi(\xi';\xi,\tau) = i\left(\frac{(\xi-\xi')^2}{2\tau} + \rho\int_0^{\xi} q(\xi'')d\xi''\right), \tag{3.73}$$

saddles are found by differentiating with respect to ξ', setting the result to zero and solving for ξ'.

$$\frac{\partial}{\partial\xi'}[\Phi(\xi';\xi,\tau)] = 0. \tag{3.74}$$

Recalling (3.61):

$$\int_0^{\xi'} \frac{\kappa}{1+i\kappa\xi'}d\xi' = -i\ln(1+i\kappa\xi), \tag{3.75}$$

(3.76) becomes:

$$\Phi(\xi';\xi,\tau) = i\left(\frac{(\xi-\xi')^2}{2\tau} - i\rho\ln(1+i\kappa\xi)\right). \tag{3.76}$$

Through differentiation, this becomes:

$$\frac{\partial}{\partial\xi'}[\Phi(\xi';\xi,\tau)] = \frac{\xi-\xi'}{\tau} - \frac{\rho\kappa}{1+i\kappa\xi'}. \tag{3.77}$$

At points $\xi' = \xi_j,\ \frac{\partial\Phi(\xi';\xi,\tau)}{\partial\xi'} = 0$:

$$\Rightarrow \frac{\xi-\xi_j}{\tau} - \frac{\rho\kappa}{1+i\kappa\xi_j} = 0 \tag{3.78}$$

$$\therefore (\xi-\xi_j)(1+i\kappa\xi_j) = \kappa\tau\rho, \tag{3.79}$$

which gives the quadratic equation:

$$i\kappa\xi_j^2 + (1-i\kappa\xi)\xi_j + \kappa\tau\rho - \xi = 0 \tag{3.80}$$

which gives the saddle points in the small ξ, τ limit as:

$$\xi_j = \xi_\pm = \frac{1}{2\kappa}\Big((i+\kappa\xi) \pm i\sqrt{1-\kappa^2\xi^2+2\kappa i(2\rho\kappa\tau-\xi)}\Big) \tag{3.81}$$

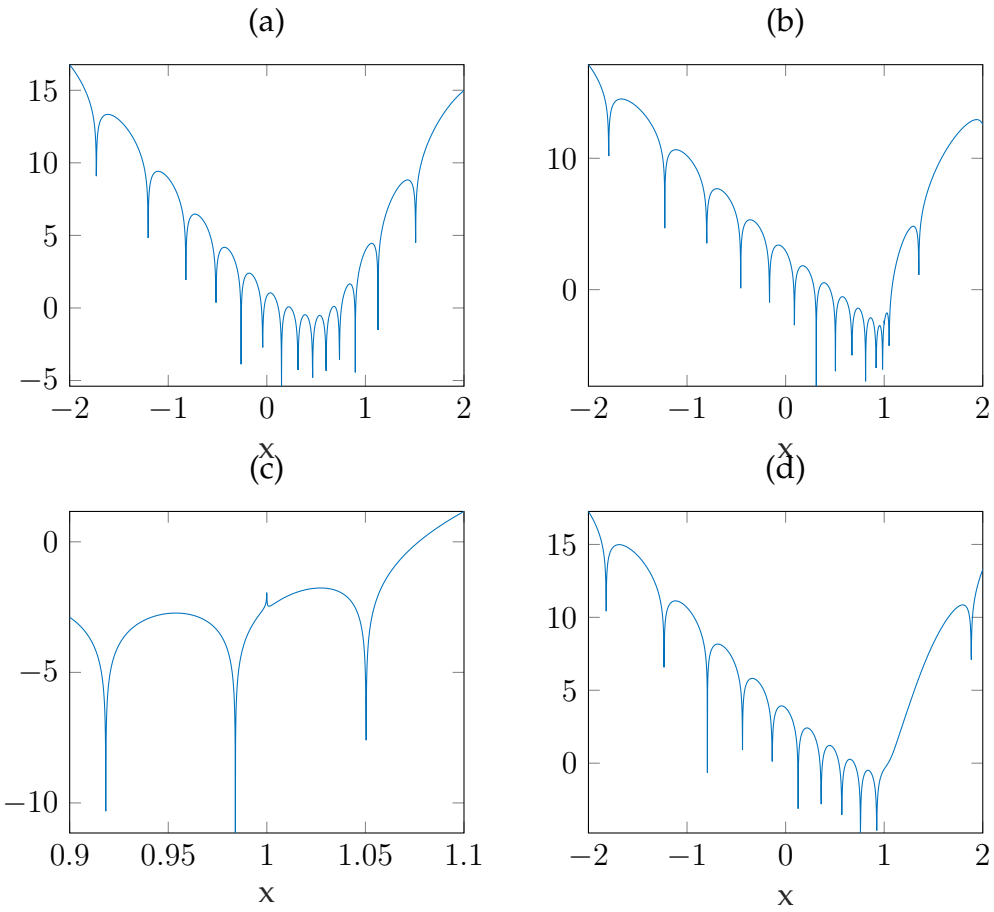

FIGURE 3.6: $\Re e(\log(\Re e(\Psi(\xi,\tau))))$ from (3.83). (a) $-2 \leq \xi \leq 2$, $\tau = 0.25$; (b) $-2 \leq \xi \leq 2$, $\tau = 0.5$; (c) $-0.9 \leq \xi \leq 1.1$, $\tau = 0.5$; (d) $-2 \leq \xi \leq 2$, $\tau = 0.75$. $N = 20$ for all graphs.

Therefore, two saddles contribute to the integral:

$$\Psi(\xi,\tau) = \sqrt{\frac{NA^2}{2\pi L i\tau}} \int_{-\infty}^{\infty} \exp\left[iN\left(\frac{(\xi-\xi')^2}{2\tau} + \rho\int_0^{\xi} q(\xi'')d\xi''\right)\right] d\xi'. \tag{3.82}$$

We can use (3.55) to get the saddle-point approximation to (3.82):

$$\Psi(\xi,\tau) \approx \sum_{\pm} \sqrt{\frac{-A^2}{2\pi L(\rho\tau q'(\xi_{\pm})+1)}} \exp\left[iN\left(\rho\int_0^{\xi_{\pm}} q(\xi'')dx'' + \frac{(\xi-\xi_{\pm})^2}{2\tau}\right)\right]. \tag{3.83}$$

Figure 3.6 shows the evolution of (3.83). It is clear that the wall effect is captured by this representation, it also shows that for a certain point (ξ,τ), there is a discontinuity, seen in (c), at which the method fails.

3.4 Analysis

By evaluating the integral over the propagator using small ξ and τ approximations and then applying the saddle-point method, we have created a representation of the superoscillatory wavefunction through which we can explain the wall effect and the disappearance of superoscillations.

In this method, contributions to the integral over the propagator arise from saddles, which can be viewed as complex momenta. We now consider how they affect the evolution of the superoscillatory wavefunction by observing how the two saddles exchange dominance in the (ξ, τ) plane.

To observe how the saddles exchange dominance we calculate their Stokes and anti-Stokes lines[28] [101]. In order to do this, recall the phase of the exponential in (3.82):

$$\Phi_{\pm}(\xi_{\pm}; \xi, \tau) = \frac{(\xi - \xi_{\pm})^2}{2\tau} + \rho \int_0^{\xi_{\pm}} q(\xi'')d\xi''. \tag{3.84}$$

The two saddles result in two contributing phases which, due to N being an asymptotic parameter, are the primary cause of the evolution of the wavefunction. It is from these phases that the Stokes and anti-Stokes lines are calculated:

$$\text{anti-Stokes line: } \Im m(\Phi_+(\xi_{\pm}; \xi, \tau) - \Phi_-(\xi_{\pm}; \xi, \tau)) = 0 \tag{3.85}$$

$$\text{Stokes line: } \Re e(\Phi_+(\xi_{\pm}; \xi, \tau) - \Phi_-(\xi_{\pm}; \xi, \tau)) = 0 \tag{3.86}$$

Stokes lines are created at the points in which absolute values of the two phases, Φ_+ and Φ_-, are maximally different. At these points, a sub-dominant saddle (the one of smallest amplitude) can either disappear behind or, emerge from, a dominant saddle (the saddle of largest amplitude).

Anti-Stokes lines occur at points in which the absolute values of the two phases are equal. Across these lines, the respective dominance of any contributing saddles changes; a dominant saddle becomes sub-dominant and vice-versa.

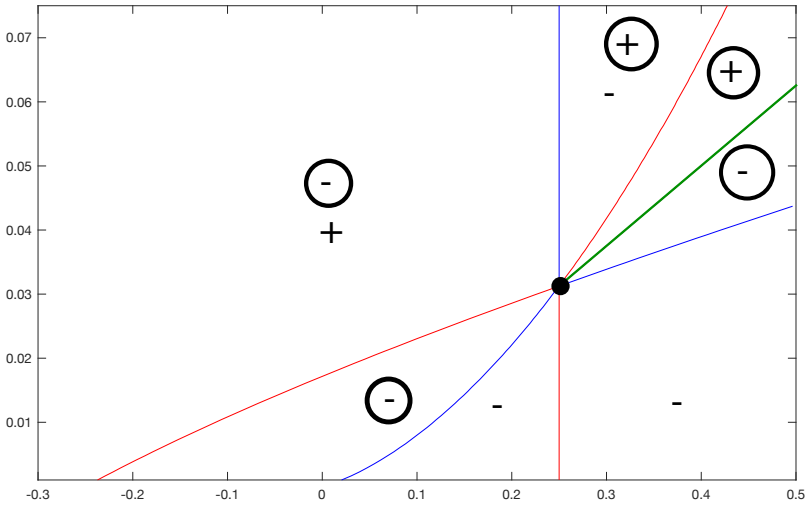

FIGURE 3.7: The (x, t) plane as calculated from the saddle point equation. Red curves: Stokes lines; blue curves: anti-Stokes lines; green line: branch cut; black dot: saddle coalescence. The two saddles are represented by $+$ and $-$, the dominant saddle is encircled. These lines were calculated numerically.

Alongside Stokes and anti-Stokes lines, branch cuts also affect the relative dominance of the saddles. If a branch cut is crossed, the two saddles swap. This is not to be confused with the exchange of dominance that occurs when crossing and anti-Stokes line; if only one (dominant) saddle were contributing and it crossed an anti-Stokes line, it would become sub-dominant with no dominant partner. However, if it were to cross a branch cut, the saddle would turn into its previously non-contributory partner, which would now be dominant.

3.4.1 The Wall Effect

The Stokes and anti-Stokes lines are shown in figure 3.7. The most striking feature of their construction occurs at $\tau = 0.5$ and $\xi = 1$ where the saddles coalesce and the absolute value of the phase is zero. Such points are vital to the composition of Stokes and anti-Stokes lines as it from these that they emerge. It is at this point where the discontinuity is observed in figure 3.6

To understand how the saddles exchange dominance we describe figure 3.7 starting from the bottom right corner and moving clockwise. We are therefore first confronted with the $-$ saddle, which is currently sub-dominant but has no dominant companion. In fact, $-$ is contributing exclusively along the bottom of the figure.

It is not until $-$ has crossed an anti-Stokes line, making it dominant but still companion-less, that it encounters another Stokes line. Upon crossing the $+$ saddle emerges; sub-dominant.

This situation continues as we move up along the left-hand side of figure 3.7. We then cross the anti-Stokes line that occurs for $\xi = 1, \tau > 0.5$. It is at this point that the $-$ and the $+$ saddles swap dominance. This event is crucial to the wall effect as the majority of the superoscillatory information is contained within the $-$ saddle. Upon crossing this anti-Stokes line the conventionally oscillatory saddle, $+$ is dominant on one side where the superoscillatory $-$ is dominant on the other. Therefore, the superoscillations persist for longer on the left-side of the anti-Stokes line as opposed to the right.

A Stokes line is then crossed, causing $-$ to disappear, $-$ then re-emerges once the branch cut (where the argument of the square root in (3.81) is real and negative) is navigated and the two saddles swap. Finally, another Stokes line is crossed and $-$ is unaccompanied and sub-dominant.

3.4.2 Disappearance Time

The anti-Stokes line at $\xi = 1, \tau > 0.5$ does not only explain the wall effect. By looking at how the local momentum changes either side of it we can uncover how the superoscillations disappear. We begin by deriving the local momentum in the small ξ, τ approximation:

$$k_{\pm} = \Re e(q_{\pm}(\xi_{\pm}(1,\tau),1,\tau)) = \Re e\left(\frac{\kappa}{1+i\kappa\xi_{\pm}(1,\tau)}\right), \tag{3.87}$$

$$= \kappa \Re e \left(\frac{1 - i\kappa\xi_{\pm}^{*}(1,\tau)}{(1 + i\kappa\xi_{\pm}(1,\tau))(1 - i\kappa\xi_{\pm}^{*}(1,\tau))} \right), \tag{3.88}$$

in which we have also set $\kappa = \rho = 1$. Evaluating the saddles (3.81) at $\xi = 1$ gives:

$$\xi_{\pm} = \frac{1}{2}(1+i)(1 \pm^{2} \sqrt{2\tau - 1}) \tag{3.89}$$

$$\therefore \xi_{\pm}^{*} = \frac{1}{2}(1-i)(1 \pm^{2} \sqrt{2\tau - 1})^{*} \tag{3.90}$$

For $\tau > 0.5$, the argument of the square root in (3.89) and (3.90) is real and positive, giving the local momentum:

$$k_{\pm} = \frac{1 \mp \sqrt{2\tau - 1}}{2\tau} \tag{3.91}$$

We first notice that, at $\tau = 0.5$, $k_{+} = k_{-} = 1$ which, from taking into account the scaling in (3.59) corresponds to the superoscillatory value of k. As τ increases, both local momenta decrease in value, with k_{+} decreasing faster and hence retaining any superoscillatory information for a shorter amount of time. It is for this reason that $+$ was previously referred to as 'the conventionally oscillatory saddle'; it is from $+$'s contributions that conventional oscillations are first seen in the superoscillatory region. For $\tau > 1$, k_{+} becomes negative which implies it is travelling from left to right.

Therefore, superoscillations persist longest for $\tau > \frac{1}{2}$ and $-$ dominates. Therefore, when $k_{-} < \frac{1}{a}$, which is the value of the fastest Fourier component in the scaled units (3.59), along the line $\xi = 1$, the superoscillations disappear.

$$k_{-}(1,\tau_d) = \frac{1 \mp \sqrt{2\tau_d - 1}}{2\tau_d} = \frac{1}{a} \tag{3.92}$$

$$\Rightarrow \tau_d = \frac{a^2}{4}\left(1 + \frac{2}{a} + \sqrt{1 + \frac{4}{a} - \frac{4}{a^2}}\right) \underset{a \gg 1}{\rightarrow} \frac{a^2}{2} \tag{3.93}$$

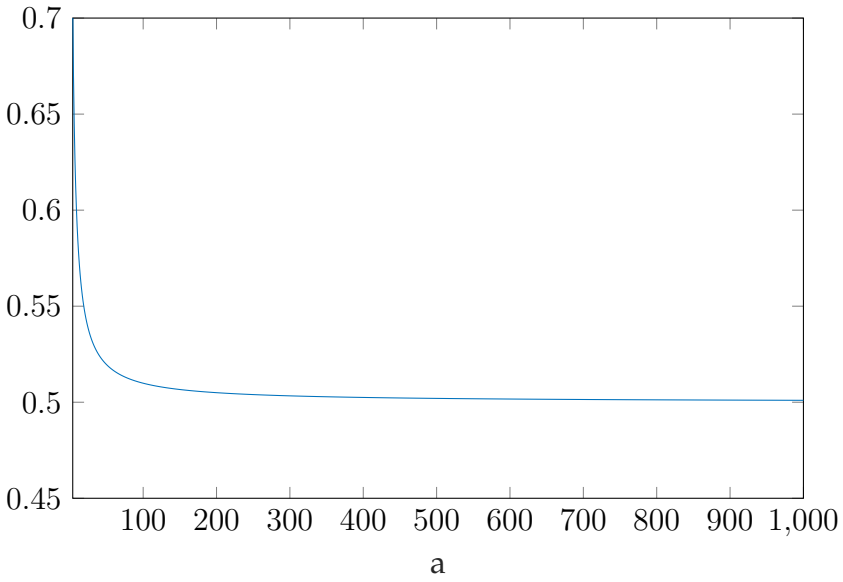

FIGURE 3.8: t_d (3.94) as a function of a for $4 \leq a \leq 1000$.

(3.93) gives the disappearance time in the superoscillatory units, in the original variables used in this chapter, it is:

$$t_d = \frac{1}{4}\left(1 + \frac{2}{a} + \sqrt{1 + \frac{4}{a} - \frac{4}{a^2}}\right) \underset{a \gg 1}{\rightarrow} \frac{1}{2} \tag{3.94}$$

(3.94) shows that, of the initial superoscillatory parameters a and N, the disappearance time is only dependent on a and the dependence is weak, as $a \rightarrow \infty$, it limits to $t_d = \frac{1}{2}$. Figure 3.8 shows how t_d changes as a function of a.

3.5 Conclusion

The evolution of an initial superoscillatory wavefunction in the free-particle one-dimensional Schrödinger equation has a very interesting structure. Expressing the initial wavefunction as a sum of its eigenfunctions first illustrated the structure. This showed two important features: an asymmetry in the way the wavefunction evolved (the wall effect) and, the disappearance of the superoscillations. However, the presentation of the superoscillatory wavefunction as a series of eigenfunctions

provided a description too impenetrable to describe a phenomenon as subtle as superoscillation.

To provide a more accessible description of the wavefunction, its representation as an integral over the propagator was employed. It was demonstrated that this was solvable using the saddle point method and that, using approximations for small x and t, an analytic solution was possible; contributions to the integral arose from two saddles which could be viewed as complex momenta. From this the wall effect and disappearance of the superoscillations could be explained.

Crucial to both phenomena is an anti-Stokes line at $\xi = 1$ and $\tau > \frac{1}{2}$. It is across this line that the two contributory saddles exchange dominance. As the superoscillatory information disappears quicker on the right-hand side of the line as opposed to the left, an asymmetrical evolution is observed. The superoscillations then disappear as the local wavenumber of the left hand saddle decreases to a value lower than the fastest Fourier component. The resultant disappearance time was found to be weakly dependent on a but independent of N. However, recent research into non-relativistic quantum superoscillations has shown that, by using a more general Hamiltonian, the disappearance time becomes directly proportional to N, becoming infinite as $N \to \infty$ [5] [41].

This chapter also provides a base as we move forward into investigating free-particle relativistic quantum superoscillations. All relativistic calculations should recover their non-relativistic analogues as $c \to \infty$. Therefore, in the following chapters, where necessary, non-relativistic limits shall be taken and compared to the results of this chapter. As the same initial wavefunction will be used, direct comparisons between relativistic and non-relativistic quantum superoscillations will also be made.

Chapter 4

Relativistic Free Particle Superoscillations for a Spin-Zero Wavefunction

Discussion of quantum free-particle superoscillations in which the Schrödinger equation is used does not paint the entire picture of their nature. In this representation, space and time are treated as separate from one another when it is known that, as a body approaches the speed of light space and time must be treated on an equal footing. To do this, the wave equations of relativistic quantum mechanics are employed in the treatment of the initial superoscillatory function. Unlike in the previous chapter, where there had been a lot of work done in the area of non-relativistic quantum superoscillations, very little has been done in a relativistic regime.

This chapter concerns descriptions of relativistic, free particle, quantum superoscillations using the Klein-Gordon equation which describes a spin-zero wavefunction. The general dynamics of such superoscillations have been described in chapter 3, in which it was shown that their evolution is affected by whether the energy of the wavefunction is positive or negative.

This chapter employs a similar format to chapter 3. Beginning with the eigenfunction expansion of the positive energy wavefunction, the way in which the initial superoscillatory function evolves will be shown and compared to the non-relativistic

evolution. Again, we are presented with interesting results but further work is required to gain understanding.

The integral over the positive energy Klein-Gordon propagator for the initial superoscillatory function will be solved and the results analysed. Further problems are posed in the relativistic regime namely, which of the limits of the Klein-Gordon propagator discussed in chapter 2 is most applicable this case. Finally, the case of mixed energy superoscillations will be discussed with results and analysis presented in much the same way.

4.1 Lorenz Boosted Superoscillations

Before considering superoscillations in the Klein-Gordon equation, we first consider a simpler case; a Lorenz boost of the initial superoscillatory function:

$$f(x) = \Big(\cos(x) + ia\sin(x)\Big)^N \tag{4.1}$$

Two key phenomena are observed under a Lorenz boost; time dilation and length contraction. To see how this effects (4.2) we make the transformation:

$$x' = \gamma(x - vt), \tag{4.2}$$

where:

$$\gamma = \left(1 - \frac{v^2}{c^2}\right)^{-\frac{1}{2}}. \tag{4.3}$$

In this transformation, the primed reference frame is observed as moving at a velocity v from the un-primed reference frame along the x axis. The Lorenz boosted wave is then:

$$f(x') = \Big(\cos(\gamma(x - vt)) + ia\sin(\gamma(x - vt))\Big)^N \tag{4.4}$$

Figure 4.1 shows the effect of Lorentz boosting on the initial superoscillatory function for different values of v relative to c. The two notable features are the effect of

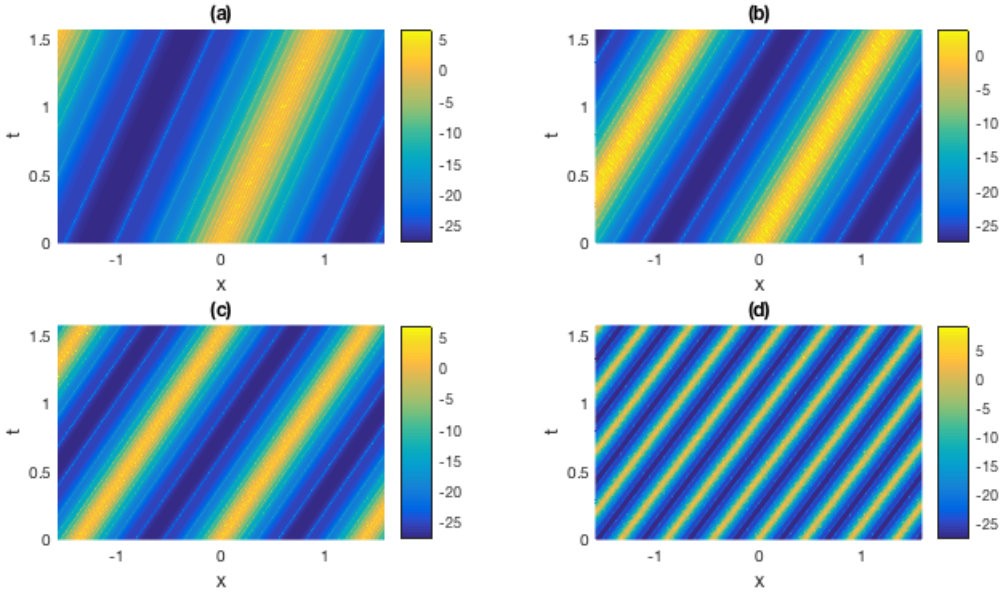

FIGURE 4.1: Density plot for (4.4) for $a = 4$, $N = 20$, $-\pi/2 \leq x \leq \pi/2$, $0 \leq t \leq \pi/2$, (a) $v = 0.6c$, (b) $v = 0.8c$, (c) $v = 0.9c$ and (d) $v = 0.99c$.

length contraction, this is seen as the period of the function decrease as v increases. As v increases, the function evolves closer to light-cone; it is travelling closer to the speed of light. This is hardly a surprising result as this is exactly what we are doing as we increase v.

4.2 Positive Energy Spin-Zero Superoscillations

As negative energy states do not occur in non-relativistic quantum mechanics, positive energy, relativistic wavefunctions are the most comparable to those discussed in the previous chapter. It is from a positive energy, relativistic wavefunction the non-relativistic limit is found as $c \to \infty$. This is demonstrated for the case of the positive energy propagator in chapter 2.

To get a full comparison between relativistic and non-relativistic free particle, quantum superoscillations, the same initial wavefunction is used:

$$\Psi(x,0) = \frac{A}{\sqrt{L}}\Big(\cos(\kappa x) + ia\sin(\kappa x)\Big)^{Ncs} \tag{4.5}$$

The difference between (4.15) and (3.1) is in the power; ρ, which has units $\mathrm{m}^2\mathrm{s}^{-1}$, is now composed of two constants: c, the speed of light and s, a spatial constant of magnitude $1/c$. Despite, as mentioned in the previous chapter, it is crucial for the power of (4.5) to be dimensionless, ascribing physical quantities to the individual terms is necessary for correct dimensional analysis further on in the chapter.

4.2.1 Eigenfunction Expansion

As in the previous chapter, (4.5) can be represented as a series of plane waves, in this case, corresponding to eigenfunctions of the free-particle Klein-Gordon equation:

$$\Psi(x,0) = \frac{A}{\sqrt{L}} \sum_{m=0}^{Ncs} c_m e^{iNcs\kappa k_m x} \tag{4.6}$$

where c_m and k_m are given by (3.10) and (3.7). The time-dependence of (4.6) can be found by multiplying by $e^{-iW(\kappa)t}$ where, in terms of N and s:

$$W(\kappa) = Nc^2\sqrt{1 + s^2\kappa^2 k_m^2}, \tag{4.7}$$

giving the time-dependent wavefunction:

$$\Psi(x,t) = \frac{A}{\sqrt{L}} \sum_{m=0}^{Ncs} c_m e^{i(Ncs\kappa k_m x - W(\kappa)t)} \tag{4.8}$$

Figure 4.2 shows the evolution of the wavefunction (4.8) according to the free-particle Klein-Gordon equation. Initially, the evolution of (4.5) looks very different to that of (3.39); the solution to the Schrödinger equation. The wall effect and the disappearance of the superoscillations are still apparent; the wall has seemed to have shifted.

To ensure that the results of the previous chapter are recovered in the non-relativistic limit, $c \to \infty$ is taken. Through (visual) comparison to figure 3.3, figure

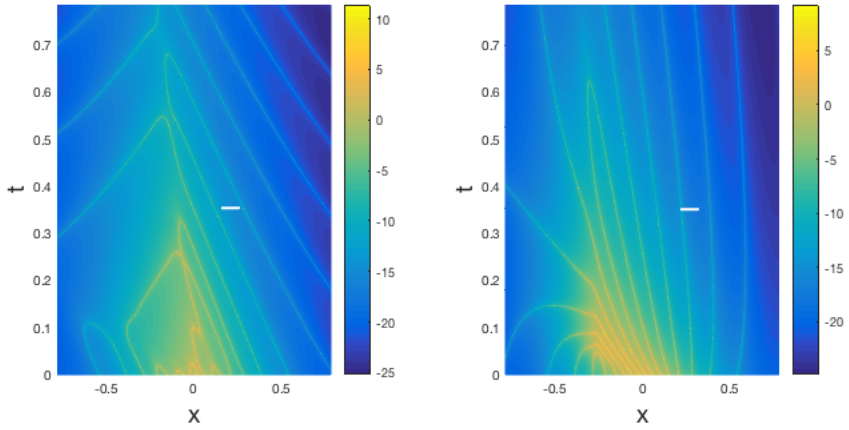

FIGURE 4.2: Density plot for $\Re e(\log(\Re e(\Psi(x,t))))$ in equation (4.8). Left: for $a = 4$, $N = 20$, $c = s = \kappa = A = L = 1$ and $-\pi/4 \leq x \leq \pi/4$, $0 \leq t \leq \pi/4$. Right: $c = 100$, $s = 1/100$ otherwise the same as before. The wavefunction is also multiplied by e^{-iNc^2t} to eliminate the rest-mass term that arises from taking the non-relativistic limit. White horizontal lines represent the spacing of the fastest conventional oscillations.

4.2 shows this. Figure 4.3 shows the wavefunction as a whole. As expected the differences in magnitude between the superoscillatory and conventional regions are very large. Although not providing much insight into the evolution of superoscillations, diagrams of the wave-function as opposed to its natural logarithm are very important for assessing the entire applicability of any further approximations to (4.8).

It is vital to understand the relative length and time scales of the relativistic and non-relativistic superoscillations. To do this, we can look at the Compton wavelength and time:

$$\lambda_C = \frac{1}{Nc}, \tag{4.9}$$

$$\tau_C = \frac{1}{Nc^2}. \tag{4.10}$$

From (4.9)) and (4.10) we see that for constant N (which is set to $\frac{m}{\hbar}$),the length is equal to $1/Nc$ and time to $1/Nc^2$; we would expect the relative length and time scales to be significantly smaller for relativistic superoscillations than non-relativistic.

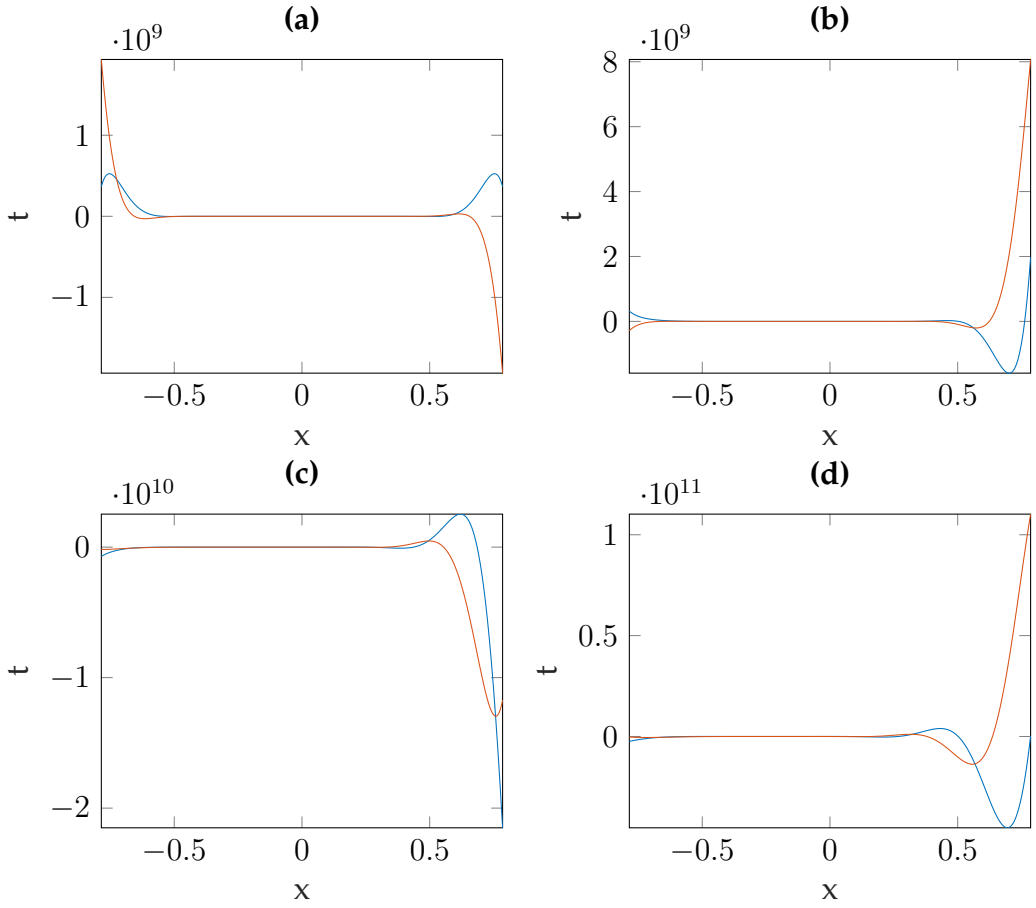

FIGURE 4.3: Showing the wave function $\Psi(x,t)$ in equation (4.8), the real parts of $\Psi(x,t)$ are shown in blue and the imaginary in orange. With parameters: $a = 4$, $N = 20$, $c = s = \kappa = A = L = 1$, $-\pi/4 \leq x \leq \pi/4$ with times: (a) $t = 0$, (b) $t = \pi/16$, (c) $t = \pi/8$ and (d) $t = \pi/4$.

To understand the difference between the two regimes, we look at how $\hbar$ and c are related. This is through the fine-structure constant:

$$\alpha = \frac{e^2}{4\pi\epsilon_0\hbar c} \equiv \frac{1}{137}. \tag{4.11}$$

As α must always be equal to $\frac{1}{137}$, to change $\hbar$ and c, would require a change in the charge, e. Although it is clear that the length and time scales in a relativistic super-oscillatory system will be considerably smaller, it is not possible to define generally by how much as the charge of the wave will have to change with N and/or c.

4.2.2 Evaluation of the Propagator

Due to the subtlety of the interference between each contributing wave, evaluation of the eigenfunction expansion provides little insight into the workings of the wavefunction's evolution. To gain further understanding, the propagator representation is used.

$$\Psi(x,t) = \int_{-\infty}^{\infty} \Psi(x',0)\Delta_+(x-x';t)dx' \tag{4.12}$$

in which $\Delta_+(x-x';t)$, the free particle, Klein-Gordon, positive energy propagator, is given by (2.35):

$$\Delta_+(x-x',t) = \frac{i}{\pi}Nc^2t\frac{K_1\Big(Nc\sqrt{((x-x')^2-c^2t^2}\Big)}{\sqrt{(x-x')^2-c^2t^2}}. \tag{4.13}$$

Therefore, (4.8) can be written as:

$$\Psi(x,t) = \frac{iA}{\pi\sqrt{L}}Nc^2t\int_{-\infty}^{\infty}\frac{K_1\Big(Nc\sqrt{((x-x')^2-c^2t^2}\Big)}{\sqrt{(x-x')^2-c^2t^2}}\Big(\cos(\kappa x')+ia\sin(\kappa x')\Big)^{Ncs}dx'. \tag{4.14}$$

This is not an integral that can be solved directly; the limiting forms, discussed in chapter 2, of the propagator must be used. These approximations arise from two limits: the light-cone (poles) and the WKB (saddles).

4.2.2.1 Pole Contributions

To begin with, the light-cone approximation to the propagator is taken (2.47) giving the wavefunction at the light-cone:

$$\Psi(x,t) \approx \frac{iA}{\pi\sqrt{L}}ct\int_{-\infty}^{\infty}\frac{\Big(\cos(\kappa x')+ia\sin(\kappa x')\Big)^{Ncs}}{\big((x-x')^2-c^2t^2\big)}dx'. \tag{4.15}$$

As discussed when evaluating a plane wave in this limit the resultant integral contains two poles: one moving forwards in time, the other backwards. In order to get an entirely positive energy wavefunction, only the poles moving forwards in time

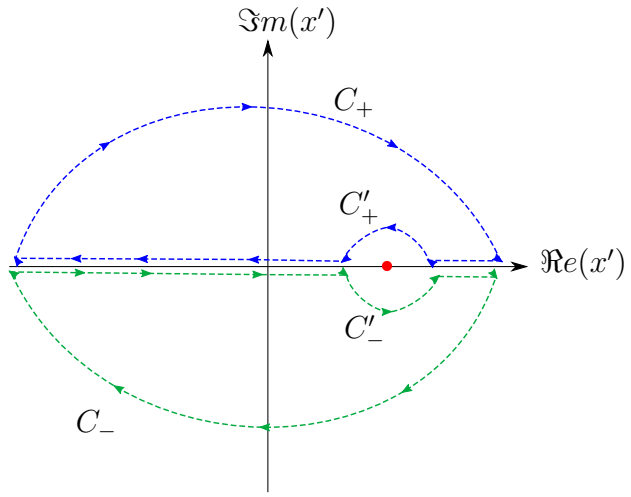

FIGURE 4.4: Showing how the sign of k_m in (4.18) affects how the contour is deformed around the pole (red circle) at $x' = x + ct$ in the x' plane. If $k_m > 0$, the contour is deformed into C_+, if $k_m < 0$, the contour is deformed into C_-.

must be considered. A partial fractions representation of (4.15) allows this:

$$\Psi(x,t) \approx \frac{iA}{2\pi\sqrt{L}} \int_{-\infty}^{\infty} \Big(\cos(\kappa x') + ia\sin(\kappa x')\Big)^{Ncs} \left(\frac{1}{x - x' - ct} - \frac{1}{x - x' + ct}\right) dx', \tag{4.16}$$

taking only positive t into account:

$$\Psi(x,t) \approx -\frac{iA}{2\pi\sqrt{L}} \int_{-\infty}^{\infty} \frac{\Big(\cos(\kappa x') + ia\sin(\kappa x')\Big)^{Ncs}}{\big(x - x' + ct\big)} dx'. \tag{4.17}$$

(4.17) can be solved using the residue theorem. However, care must be taken when deforming the contour. Representing the initial wavefunction as a sum of it's eigenfunctions(4.6) and substituting into (4.17) gives:

$$\Psi(x,t) \approx -\frac{iA}{2\pi\sqrt{L}} \sum_{m=0}^{Ncs} c_m \int_{-\infty}^{\infty} \frac{e^{iNcs\kappa k_m x'}}{\big(x - x' + ct\big)} dx'. \tag{4.18}$$

For positive k_m, the integrand diverges as $x' \to -i\infty$ and, for negative k_m, the integrand diverges as $x' \to i\infty$. When $k_m = 0$, the integrand is entirely convergent so the choice of contour is not important. Figure 4.4 shows how the contour is deformed

with respect to the sign of k_m, giving the integrals:

$$\Psi(x,t) \approx -\frac{iA}{2\pi\sqrt{L}}\left(\sum_{m=0}^{\frac{1}{2}Ncs-1} c_m \int_{C_-} \frac{e^{iNcsk_mx'}}{\big(x-x'+ct\big)}dx' + \sum_{m=\frac{1}{2}Ncs}^{Ncs} c_m \int_{C_+} \frac{e^{iNcsk_mx'}}{\big(x-x'+ct\big)}dx'\right). \tag{4.19}$$

The residue theorem can now be applied. A trivial calculation of the residue at $x' = x + ct$ gives $\text{Res}(x+ct) = \exp[iNcsk_m(x+ct)]$ resulting in the wavefunction:

$$\Psi(x,t) \approx \frac{A}{\sqrt{L}}\sum_{m=0}^{Ncs} c_m e^{iNcsk_m(x+ct)} \tag{4.20}$$

$$= \frac{A}{\sqrt{L}}\Big(\cos(\kappa(x+ct)) + ia\sin(\kappa(x+ct))\Big)^{Ncs} \tag{4.21}$$

Figure 4.5 shows the evolution of the wavefunction at the light-cone compared to the eigenvalue-function expansion. The differences are quite similar to that of the plane wave discussed in chapter 2. That is, the results are only accurate for $t = 0$. This is because the light-cone approximation propagates the initial wavefunction along the line $x - ct$ whereas, the eigenfunction evolution is an interference of N number of plane waves all travelling at different speeds.

Figure 4.6 shows the full wavefunction according to the light-cone approximation. Comparing this to figure 4.3, it is clear that for small t (when the superoscillations are in existence) the pole contributions do not give an accurate approximation to the conventional oscillations. However, as t increases, this approximation becomes quite accurate for the region of conventional oscillation.

The result for the light-cone approximation bear a significant resemblance to the Lorenz-boosted superoscillations previously discussed. Figure 4.1 (d) shows a Lorenz-boosted wavefunction at $v = 0.99c$. The evolution is almost identical to that of our light-cone approximation aside from the effect of length contraction shown in the Lorenz boost.

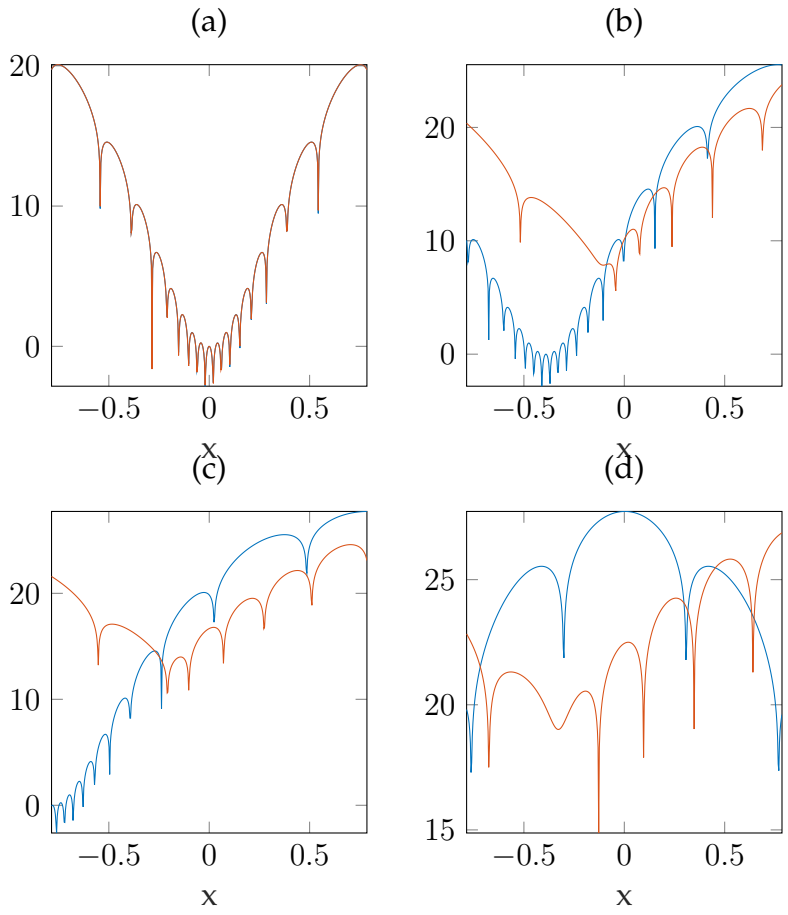

FIGURE 4.5: $\Re e(\log(\Re e(\Psi(x,t))))$ for the complete wavefunction (4.8) (orange lines) and for the pole approximation (4.20) (blue line), for (a) $t = 0.000001$, (b) $t = \pi/8$, (c) $t = \pi/4$ and (d) $t = \pi/2$ for all graphs, $-\pi/4 \leq x \leq \pi/4$ and $a = 4$, $N = 20$, $c = s = A = L = 1$.

4.2.2.2 Saddle Contributions

The WKB approximation to the positive energy free-particle Klein-Gordon propagator (2.55) often results in an integral which can be solved by the saddle point method. This provides very accurate approximations for both plane-wave and non-relativistic superoscillations.

The WKB approximation to the positive energy free-particle Klein-Gordon propagator is given by (2.55). In order to get a wavefunction that is solvable through the saddle point method, the following representation of (4.5) is used:

$$\Psi(x,0) = \frac{A}{\sqrt{L}} \exp\left[iNcs \int_0^{x'} q(x'')dx''\right], \tag{4.22}$$

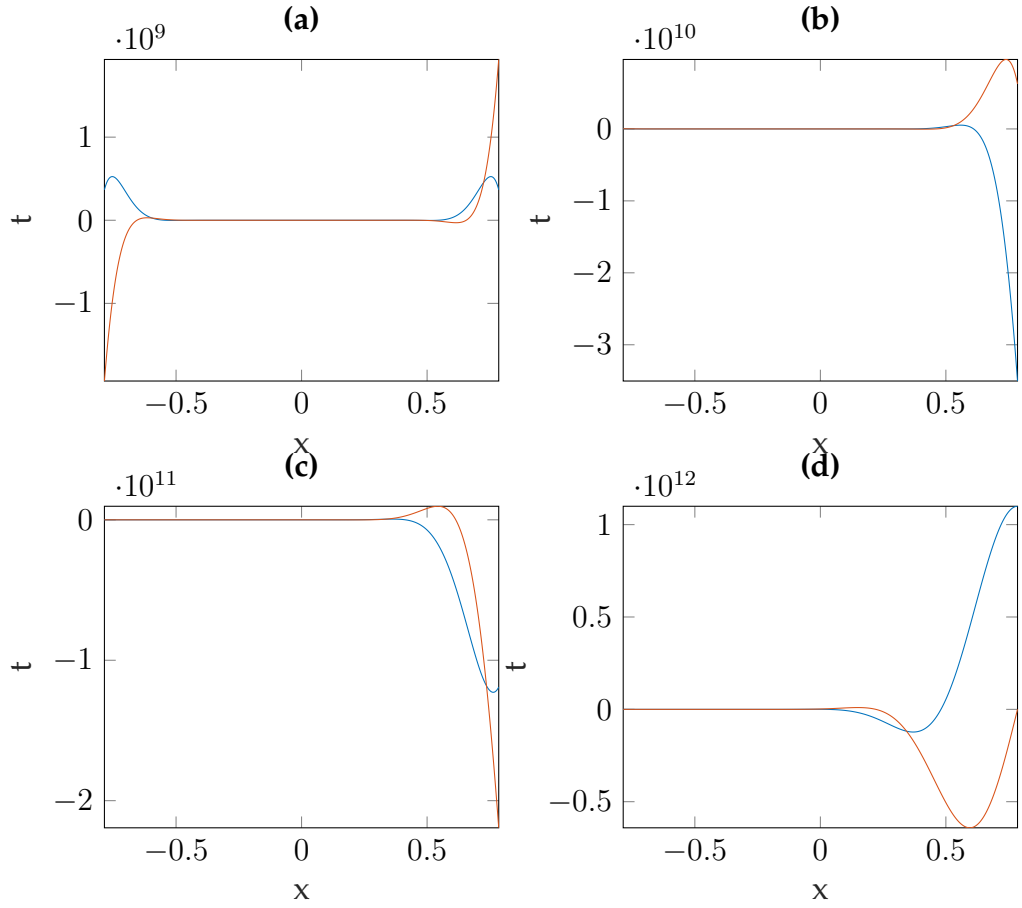

FIGURE 4.6: Showing the wave function $\Psi(x,t)$ in equation (4.21) the real parts of $\Psi(x,t)$ are shown in blue and the imaginary in orange. With parameters: $a = 4$, $N = 20$, $c = s = \kappa = A = L = 1$, $-\pi/4 \leq x \leq \pi/4$ with times: (a) $t = 0$, (b) $t = \pi/16$, (c) $t = \pi/8$ and (d) $t = \pi/4$.

in which $q(x)$ is given in (3.58). The wavefunction, in the WKB approximation, is therefore:

$$\Psi(x,t) \approx ct\sqrt{\frac{Nc}{2\pi}}\int_{-\infty}^{\infty}\frac{\exp\left[Nc(is\int_0^{x'}q(x'')dx'' - \sqrt{(x-x')^2-c^2t^2})\right]}{((x-x')^2-c^2t^2)^{\frac{3}{4}}}dx' \tag{4.23}$$

A requirement of the saddle point method is that there is an asymptotic parameter multiplying the phase of the exponential. This is achieved as, in order for (4.5) to be superoscillatory, N must be large. Saddles are located using the derivative of the phase of the exponential which shall be denoted $\phi(x';x,t)$:

$$\phi(x';x,t) = is\int_0^{x'}q(x'')dx'' - \sqrt{(x-x')^2-c^2t^2} \tag{4.24}$$

Differentiating (4.24) with respect to x' and setting it to zero gives the saddle point condition:

$$q(x_j) = \frac{i(x - x_j)}{s\sqrt{(x - x_j)^2 - c^2t^2}}, \tag{4.25}$$

where $x' = x_j$ at points in which (4.25) is valid. Saddle points occur at values of x' in which the complex momenta is equal to the derivative of the space-time interval, multiplied by $\frac{i}{s}$ [1].

As with the non-relativistic case, to solve (4.23), small x approximations must be made to the initial wavefunction:

$$\Psi(x, 0) \approx \frac{A}{\sqrt{L}}(1 + ia\kappa x)^{Ncs} \tag{4.26}$$

$$\Rightarrow q(x) \approx \frac{ia\kappa}{1 + ia\kappa x} \tag{4.27}$$

Substituting (4.27) into (4.25) and rearranging gives the quartic equation:

$$a^2\kappa^2x_j^4 + 2ia\kappa(ia\kappa x - 1)x_j^3 + (4ia\kappa x + a^2k^2x^2 - s^2a^2\kappa^2 - 1)x_j^2 +$$

$$(2x - 2ia\kappa x^2 + 2s^2a^2\kappa^2 x)x_j + s^2a^2\kappa^2c^2t^2 - (1 + s^2a^2\kappa^2)x^2 = 0 \tag{4.28}$$

Although an analytical solution to (4.28) may well exist, the result would be unwieldy. Instead, it is solved using the `roots` routine in MATLAB and then sorted by the magnitude of the real parts of the roots [2]. Figure 4.7 shows the real parts of the four solutions to the quartic saddle point equation.

Figure 4.7 also shows that the solutions to the quartic equation are symmetric; there are two sets of solutions, one moving forwards in time the second moving

[1] This is not specific to a superoscillatory wavefunction but is true for all free-particle Klein-Gordon wavefunctions in the WKB limit.

[2] Although as figure 4.7 shows, ordering through magnitude gives the correct sorting, it is only valid for restricted values of x: up to a value of $t = \pi/2$ the sorting works in the range $-\pi/4 \leq x \leq \pi/4$.

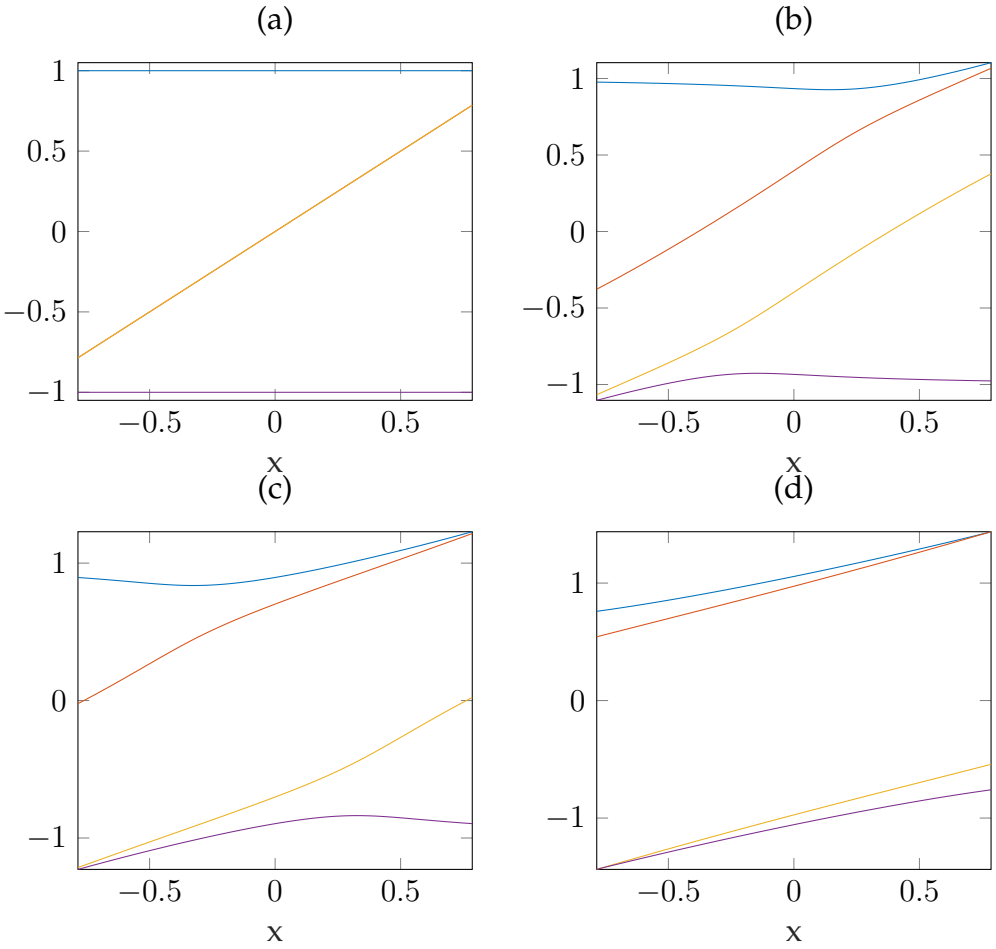

FIGURE 4.7: Real parts of the four solutions to (4.28) for (a) $t = 0.000001$, (b) $t = \pi/8$, (c) $t = \pi/4$ and (d) $t = \pi/2$ for all graphs, $-\pi/4 \leq x \leq \pi/4$ and $a = 4$, $c = s = 1$. When referred to, these solutions will be denoted: x_1 (blue line), x_2 (orange line), x_3 (yellow line) and x_4 (purple line).

backwards. Similar behaviour was observed when analysing the evolution of a plane-wave using the Kein-Gordon propagator. We are able to understand this up to an order of $\frac{1}{c^2}$:

Begin by looking at the square root in the phase, $\phi(x'; x, t)$ (4.24):

$$\sigma = \sqrt{(x - x')^2 - c^2t^2} \tag{4.29}$$

Provided $c^2t^2 \geq (x - x')^2$, it is equal to the following:

$$\sqrt{(x - x')^2 - c^2t^2} = \pm ict\sqrt{1 - \frac{(x - x')^2}{2c^2t^2}}. \tag{4.30}$$

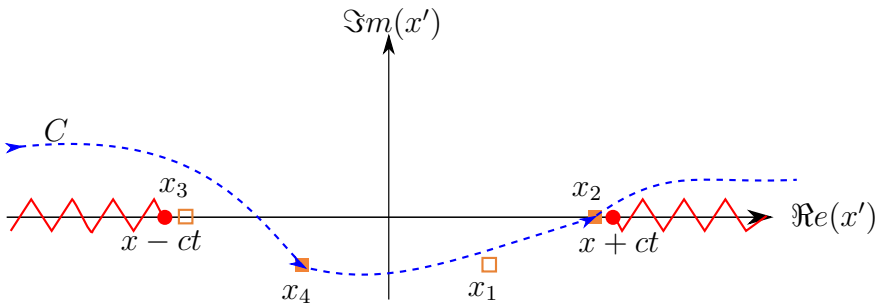

FIGURE 4.8: The complex plane in which the integration contour, C, is deformed through the saddles x_2 and x_4. The branch cut, emanating from the branch points at $x \pm ct$ is shown in red.

In the semi-relativistic limit, the approximation can be made to the square root:

$$\pm ct\sqrt{1-\frac{(x-x')^2}{c^2t^2}} \approx \pm ict\left(1-\frac{(x-x')^2}{2c^2t^2}\right) \tag{4.31}$$

Using the approximation (4.31) as a substitution for the square root in (4.24) will give two quadratic saddle point conditions: one moving forwards in time; the other moving backwards in time.

For the case of the superoscillatory wavefunction the two sets of solutions are $[x_1, x_3]$ and $[x_2, x_4]$. Although not shown here, the same symmetry is found in the imaginary parts of the saddles shown in figure 4.7.

In order to get a wavefunction of purely positive energy, only the solutions which correspond to t moving forwards are considered. Therefore, only two of the four saddles contribute to the wavefunction. Figure 4.8 shows how the contour is deformed so that it passes through the two contributing saddles. It is found numerically that the set $[x_2, x_4]$ contributes; propagating the wavefunction forwards in time.

Now that the saddles and the contour which passes through them have been determined, the saddle point method can be employed to get an approximation to (4.23). The form solutions derived from the saddle point method take is shown in chapter 2. Taking the asymptotic parameter as Nc, the solution to (4.23) as $N \to \infty$

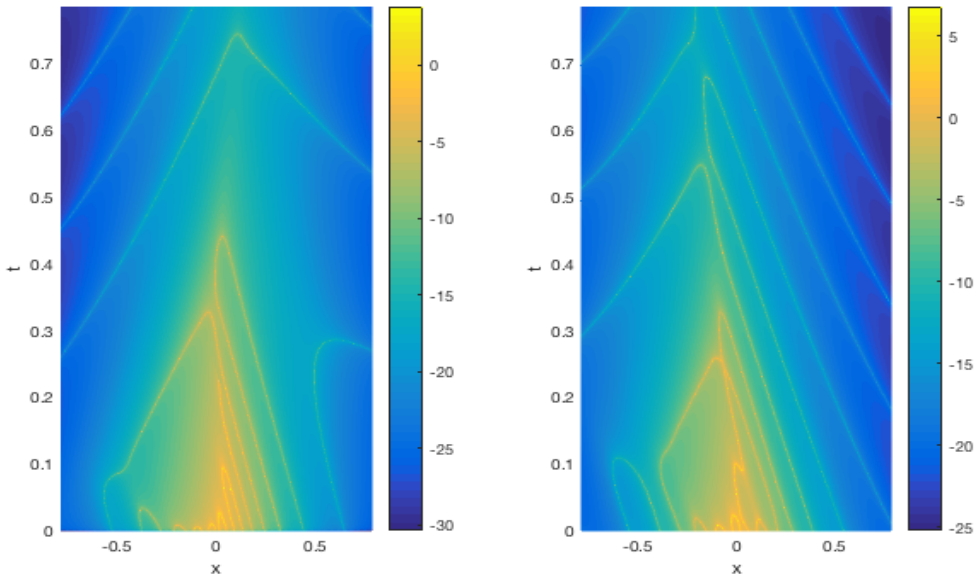

FIGURE 4.9: $\log(\Re e(\Psi(x,t)))$ for left: the WKB approximation (4.32) and right: the eigenfunction expansion (4.75). For $a = 4$, $N = 20$, $-\pi/4 \leq x \leq \pi/4$ and $0.00001 \leq t \leq \pi/4$. Yellow lines correspond to zeros of the wavefunction.

is:

$$\Psi(x,t) \approx ict \sum_j \sqrt{\frac{-A^2}{L\phi''(x_j;x,t)}} \frac{\exp[Nc\phi(x_j;x,t)]}{((x-x_j)^2 - c^2t^2)^{\frac{3}{4}}} \tag{4.32}$$

where x_j are the contributing saddle points $[x_2, x_4]$ and $\phi(x_j;x,y)$ is given by (4.24) with its second derivative:

$$\frac{\partial^2\phi(x';x,y)}{\partial x'^2} = -\frac{ia^2\kappa^2 s}{(1+ia\kappa x')^2} + \frac{(x-x')^2}{((x-x')^2 - c^2t^2)^{\frac{3}{2}}} - \frac{1}{\sqrt{(x-x')^2 - c^2t^2}} \tag{4.33}$$

Figure 4.9 compares the saddle-point approximation (4.32) to the eigenfunction expansion (4.8). The WKB approximation to the superoscillatory initial wavefunction clearly gives a better representation of the superoscillatory wavefunction than the light-cone approximation. Despite not being completely accurate, the essential features of the evolution of the positive energy free-particle superoscillatory Klein-Gordon wavefunction are apparent: the wall effect and the disappearance of the superoscillations, are all present.

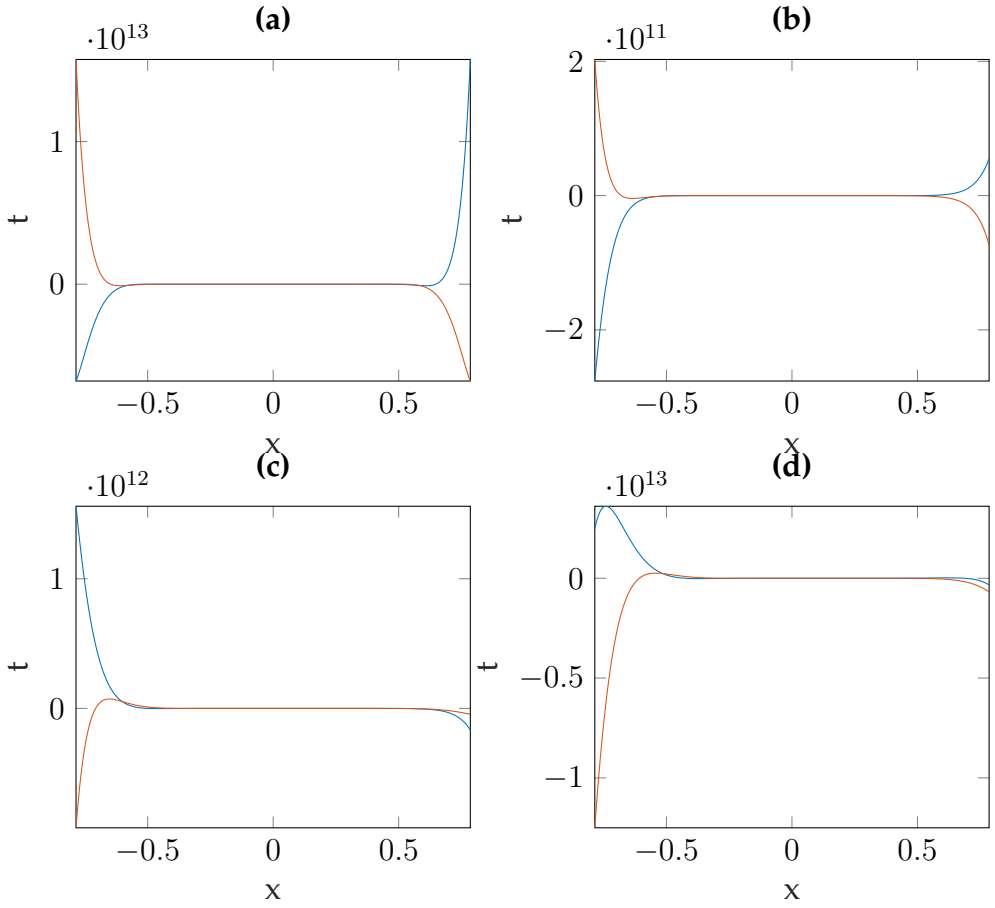

FIGURE 4.10: Showing the wave function $\Psi(x,t)$ in equation (4.32) the real parts of $\Psi(x,t)$ are shown in blue and the imaginary in orange. With parameters: $a = 4$, $N = 20$, $c = s = \kappa = A = L = 1$, $-\pi/4 \leq x \leq \pi/4$ with times: (a) $t = 0$, (b) $t = \pi/16$, (c) $t = \pi/8$ and (d) $t = \pi/4$.

Figure 4.10 shows that, despite providing a good representation of the wavefunction in the superoscillatory region, as far as conventional oscillations are concerned, the saddle-point representation is a poor one. Numerical investigation shows that, at $t = 0$, the points at which the wavefunctions in 4.10 start to diverge are $x = -0.383$ and $x = 0.354$. Therefore, the range in which the approximation is valid is: $-0.382 \leq x \leq 0.345$ which corresponds to the range in which $\Psi(x,t)$ is superoscillatory. This is hardly surprising given the constraints on x and t being small and the conventional oscillations appearing at larger values of x than the superoscillations.

4.2.2.3 Saddle-Pole Contributions

The saddle-point method applied to the WKB approximation of the propagator gives a better representation of the evolution of the superoscillatory method than that of the residue theorem. It now must be checked to see if the pole and saddle coalescing affects the evolution in anyway. To do this, the approximation to the propagator in which the saddle and pole coalesce (2.61) is used.

$$\Delta(x-x';t) = \frac{\mp i}{\pi} ct \frac{1}{(x-x')^2 - c^2t^2} e^{-\frac{mc}{\hbar}\sqrt{(x-x')^2-c^2t^2}}, \tag{4.34}$$

giving the wavefunction:

$$\Psi(x,t) = -\frac{iA}{\pi\sqrt{L}} ct \int_{-\infty}^{\infty} \frac{\exp[Nc\phi(x';x,t)]}{(x-x')^2 - c^2t^2} dx' \tag{4.35}$$

It is shown in figure 4.8 that the saddle, x_2, is in the neighbourhood of the pole at $x' = x + ct$. Therefore, by splitting the denominator in (4.35) into partial fractions and selecting the pole at $x' = x + ct$, the wavefunction becomes:

$$\Psi(x,t) = -\frac{iA}{\pi\sqrt{L}} \int_{-\infty}^{\infty} \frac{\exp[Nc\phi(x';x,t)]}{x - x' + ct} dx' \tag{4.36}$$

To solve this the integrand is mapped to the comparison integral:

$$\int_{-\infty}^{\infty} \frac{e^{-u^2}}{u-z} du = i\pi e^{-z^2} \text{erfc}(-iz) \tag{4.37}$$

Making the substitution,

$$u^2 = \phi(x';x,t) - \phi(x_2;x,t), \tag{4.38}$$

with the Jacobian:

$$\frac{\partial u}{\partial x'} = \frac{\partial}{\partial x'}\left[\sqrt{\phi(x';x,t) - \phi(x_2;x,t)}\right] = \frac{\phi'(x';x,t)}{2\sqrt{\phi(x';x,t) - \phi(x_2;x,t)}}. \tag{4.39}$$

Substituting (4.38) and (4.39) into (4.36) gives:

$$\Psi(x,t) = -\frac{iA}{\pi\sqrt{L}} e^{Nc\phi(x_2;x,t)} \int_{-\infty}^{\infty} g(u) e^{-Ncu^2} du \tag{4.40}$$

where

$$g(u) = \frac{2u}{\phi'(x';x,t)(x-x'+ct)}. \tag{4.41}$$

In the u-plane, the pole is located at:

$$z^2 = \phi(x+ct;x,t) - \phi(x_2;x,t). \tag{4.42}$$

To further progress with solving the integral (4.36), it is necessary to split $g(u)$ into three parts; separating the pole, saddles and higher-order asymptotic contributions:

$$g(u) = \frac{A}{u-z} + B + u(u-z)h(u) \tag{4.43}$$

in which A incorporates the pole at $u = z$ ($x' = x + ct$), B gives the value of $g(u)$ as it approaches the saddle at $u = 0$ ($x' = x_2$) and $h(u)$ accounts for the higher-order asymptotics. The term involving $h(u)$ disappears at the saddle and the pole and is therefore not of interest in this first-order approximation.

$$A = \lim_{u\to z}(u-z)g(u) = \lim_{x'\to x+ct} \frac{2u(u-z)}{\phi'(x';x,t)(x-x'+ct)} \tag{4.44}$$

$$= \text{Res}\left(\frac{1}{x-x'+ct}\Big|_{x'=x+ct}\right) = \frac{1}{2ct} \tag{4.45}$$

In calculating B, the limit $u \to 0$ is taken and $\frac{A}{u-z}$ is subtracted from the result so as to eliminate the effects of the pole.

$$B = \lim_{u\to 0}\left(g(u) - \frac{A}{u-z}\right) = \lim_{x'\to x_2} \frac{2u}{\phi'(x';x,t)(x-x'+ct)} + \frac{A}{z} \tag{4.46}$$

To further understand B, a Taylor expansion of $\phi(x';x,t)$ is taken:

$$\phi(x';x,t)|_{x'\to x_2} \approx \phi(x_2;x,t) + \frac{1}{2}(x'-x_2)^2\frac{\partial^2\phi(x';x,t)}{\partial x'^2}, \tag{4.47}$$

giving the approximation to the first derivative of $\phi(x';x,t)$ as $x' \to x_2$:

$$\phi'(x';x,t)|_{x'\to x_2} \approx \sqrt{\phi(x';x,t)-\phi(x_2;x,t)}\sqrt{-2\phi''(x_2;x,t)}, \tag{4.48}$$

which, in turn, gives B as:

$$B = \frac{1}{x-x_2+ct}\sqrt{\frac{2}{\phi''(x_2;x,t)}} - \frac{1}{2\sqrt{\phi(x+ct;x,t)-\phi(x_2;x,t)}} \tag{4.49}$$

and, hence the approximation to $g(u)$:

$$g(u) \approx \frac{1}{2(u-z)} + \frac{1}{x-x_2+ct}\sqrt{\frac{2}{\phi''(x_2;x,t)}} + \frac{1}{2\sqrt{\phi(x+ct;x,t)-\phi(x_2;x,t)}}. \tag{4.50}$$

This can now be substituted into (4.40) to give the wavefunction:

$$\Psi(x,t) = -\frac{iA}{\pi\sqrt{L}}e^{Nc\phi(x_2;x,t)}\int_{-\infty}^{\infty}\left(\frac{1}{2(u-z)} + \frac{1}{x-x_2+ct}\sqrt{\frac{2}{\phi''(x_2;x,t)}} + \dots\right.$$

$$\left.\frac{1}{2\sqrt{\phi(x+ct;x,t)-\phi(x_2;x,t)}}\right)e^{-Ncu^2}du \tag{4.51}$$

(4.51) can now be solved, this is done by separating the integral in two:

$$I_1 = \frac{1}{2}\int_{-\infty}^{\infty}\frac{1}{u-z}e^{-Ncu^2}du \tag{4.52}$$

$$I_2 = \left(\frac{1}{x-x_2+ct}\sqrt{\frac{2}{\phi''(x_2;x,t)}} + \frac{1}{2\sqrt{\phi(x+ct;x,t)-\phi(x_2;x,t)}}\right)\int_{-\infty}^{\infty}e^{-Ncu^2}du, \tag{4.53}$$

such that the integral in (4.51), which can be denoted as I, is the sum of the integrals I_1 and I_2. I_1 can be solved using the comparison integral (4.37) and I_2 is solved by the Gaussian integral, giving the saddle-pole contribution to the wavefunction as:

$$\Psi(x,t) = -\frac{iA}{\pi\sqrt{L}} e^{Nc\phi(x_2;x,t)} \left(i\pi e^{Ncz^2} \text{erfc}(-i\sqrt{Nc}z) + \ldots \right.$$

$$\left. \sqrt{\frac{\pi}{Nc}} \left(\sqrt{\frac{2}{(x-x_2+ct)^2\phi''(x_2;x,t)}} + \frac{1}{2z} \right) \right) \tag{4.54}$$

To get the full wavefunction (4.54) must be added to saddle point integral involving x_4 which still contributes but doesn't interact with the pole.

Figure 4.11 compares the saddle-pole approximation to that of the WKB approximation solved by the saddle-point method. For small t, the the results are very similar. However, this ceases further on as the saddle and pole become separate and the approximation breaks down. The WKB approximation clearly provides the most accurate solution when analysing the evolution of the Klein-Gordon free particle superoscillations.

In a similar manor to the saddle-point approximation figure 4.12 shows that the saddle-pole approximation fails in the conventional region. In fact, it is even worse than the saddle-point approximation due as can be seen by the orders of magnitude of the conventional oscillations. Where the eigenfunction expansion reaches a magnitude of $\times 10^{12}$, the saddle-pole reaches $\times 10^{18}$.

4.2.2.4 The Non-Relativistic Limit

The last check to make before moving onto analysing the superoscillations is to make sure that, in the limit $c \to \infty$ the integral over the propagator gives the same results as those in the previous chapter. Using the Melin-Barnes representation of

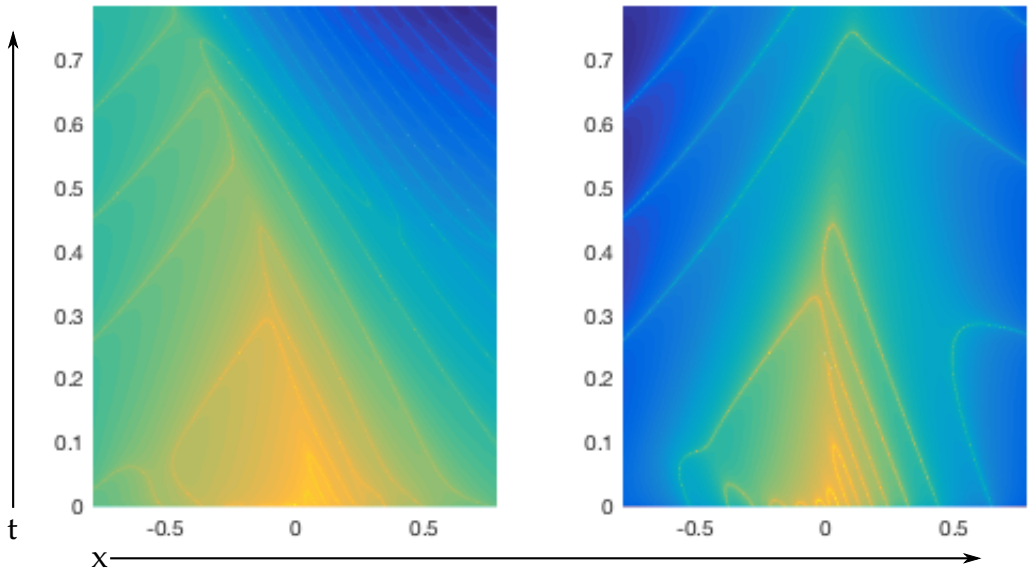

FIGURE 4.11: $\log(\Re e(\Psi(x,t)))$ for left: the saddle-pole approximation (4.54) and right: the eigenfunction expansion (4.32). For $a = 4$, $N = 20$, $-\pi/4 \leq x \leq \pi/4$ and $0.00001 \leq t \leq \pi/4$. Yellow lines correspond to zeros of the wavefunction.

the positive energy propagator (2.58), the integral over the propagator is:

$$\Delta_+(x-x';t) = \frac{Nc^2t}{2\pi^3}\left(\frac{\pi}{Nc\sqrt{(x-x')^2-c^2t^2}}\right)^{\frac{1}{2}} \frac{e^{-Nc\sqrt{(x-x')^2-c^2t^2}}}{\sqrt{(x-x')^2-c^2t^2}} \times \dots$$

$$\int_{-i\infty}^{i\infty} \Gamma(\tau)\Gamma\left(-\frac{1}{2}-\tau\right)\Gamma\left(\frac{3}{2}-\tau\right)\left(2Nc\sqrt{(x-x')^2-c^2t^2}\right)^{\tau} d\tau \tag{4.55}$$

$$\Rightarrow \Psi(x,t) = \frac{ANc^2t}{2\pi^3\sqrt{L}} \int_{-i\infty}^{i\infty} \Gamma(\tau)\Gamma\left(-\frac{1}{2}-\tau\right)\Gamma\left(\frac{3}{2}-\tau\right)\cdots \times$$

$$\int_{-\infty}^{\infty} \left(\frac{\pi}{Nc\sqrt{(x-x')^2-c^2t^2}}\right)^{\frac{1}{2}} \frac{(2Nc\sqrt{(x-x')^2-c^2t^2})^{\tau}}{\sqrt{(x-x')^2-c^2t^2}} \times \dots$$

$$\exp\left[iNc\left(is\int_0^{x'} q(x'')dx'' - \sqrt{(x-x')^2-c^2t^2}\right)\right] dx'd\tau \tag{4.56}$$

Denoting the integral over x' in (4.56) as $I_{x'}$:

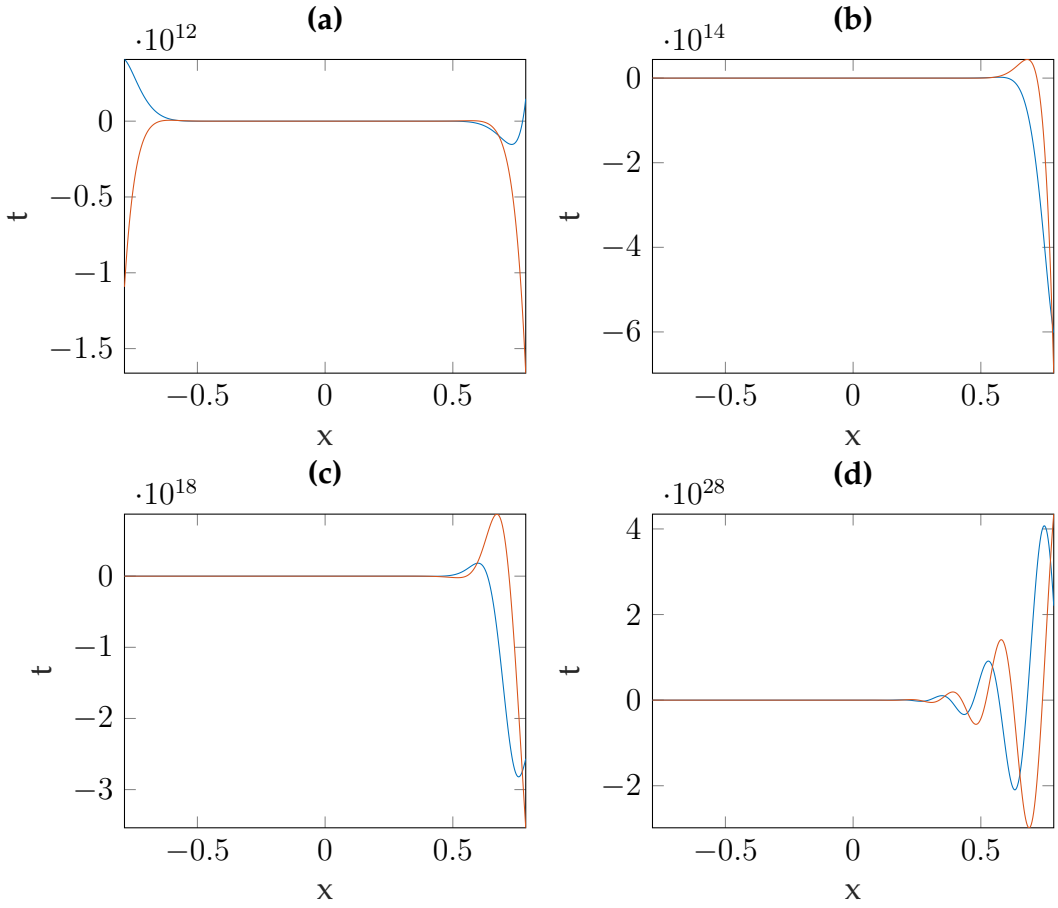

FIGURE 4.12: Showing the wave function $\Psi(x,t)$ in equation (4.54) the real parts of $\Psi(x,t)$ are shown in blue and the imaginary in orange. With parameters: $a = 4$, $N = 20$, $c = s = \kappa = A = L = 1$, $-\pi/4 \leq x \leq \pi/4$ with times: (a) $t = 0$, (b) $t = \pi/16$, (c) $t = \pi/8$ and (d) $t = \pi/4$.

$$I_{x'} = \int_{-\infty}^{\infty} \left(\frac{\pi}{Nc\sqrt{(x-x')^2 - c^2t^2}} \right)^{\frac{1}{2}} \frac{(2Nc\sqrt{(x-x')^2 - c^2t^2})^{\tau}}{\sqrt{(x-x')^2 - c^2t^2}} \times \dots$$

$$\exp\left[iNc\left(is\int_0^{x'} q(x'')dx'' - \sqrt{(x-x')^2 - c^2t^2} \right) \right] dx'. \tag{4.57}$$

To get the non-relativistic limit, the square root is manipulated such that it is in the form $\sqrt{1+\delta} \approx 1 + \frac{1}{2}\delta$, in which δ is small.

$$\sqrt{(x-x')^2 - c^2t^2} = ict\sqrt{1 - \frac{(x-x')^2}{c^2t^2}} \approx ict\left(1 + \frac{(x-x')^2}{2c^2t^2}\right) \tag{4.58}$$

giving $I_{x'}$ as, also reverting back to using ρ instead of cs:

$$I_{x'} = \int_{-\infty}^{\infty} \left(\frac{\pi}{iNc^2t(1-\frac{(x-x')^2}{2c^2t^2})} \right)^{\frac{1}{2}} \frac{(2iNc^2t(1-\frac{(x-x')^2}{2c^2t^2}))^{\tau}}{ict(1-\frac{(x-x')^2}{2c^2t^2})} \times \dots$$

$$\exp\left[iN\left(\rho \int_0^{x'} q(x'')dx'' - ic^2t\left(1 - \frac{(x-x')^2}{2c^2t^2}\right)\right)\right] dx' \tag{4.59}$$

$I_{x'}$ is now in a form in which it can be solved by the saddle point method, saddles arise from the zeros of the derivative of the phase ($\phi(x';x,t)$):

$$\phi(x';x,t) = i\rho \int_0^{x'} q(x'')dx'' - ic^2t\left(1 - \frac{(x-x')^2}{2c^2t^2}\right) \tag{4.60}$$

Differentiating (4.60) and setting the result to zero gives the following saddle point condition:

$$q(x_j) = \frac{x - x_j}{\rho t} \tag{4.61}$$

This is the same saddle-point condition as for the Schrödinger superoscillations in the previous chapter. Therefore, in the limit $c \to \infty$, the saddles are the identical to those obtained by using the Schrödinger propagator.

Now that it has been shown that the contributions to the integral over the propagator in the non-relativistic limit are the same as those in the previous chapter, the final step is to show that the wavefunction takes the same form. Solving (4.59) using the saddle-point method gives:

$$I_{x'} = \sqrt{\frac{-2\pi}{N\phi''(x_j;x,t)}} \left(\frac{\pi}{iNc^2t(1-\frac{(x-x_j)^2)}{2c^2t^2})} \right)^{\frac{1}{2}} \frac{(2iNc^2t(1-\frac{(x-x_j)^2}{2c^2t^2}))^{\tau}}{ict(1-\frac{(x-x_j)^2}{2c^2t^2})} e^{iN\phi(x_j;x,t)} \tag{4.62}$$

Where $\phi(x';x,t)$ is given by (4.60) and its second derivative is:

$$\phi''(x';x,t) = \frac{\partial^2\phi(x';x,t)}{\partial x'^2} = \rho\frac{\partial q(x')}{\partial x'} + \frac{1}{t} \tag{4.63}$$

Substituting (4.63) into (4.56) gives an integral over τ:

$$I_\tau = \int_{-i\infty}^{i\infty} \Gamma(\tau)\Gamma\left(-\frac{1}{2}-\tau\right)\Gamma\left(\frac{3}{2}-\tau\right)\left(2iNc^2t\left(1-\frac{(x-x_j)^2}{2c^2t^2}\right)\right)^{\tau} d\tau \tag{4.64}$$

This can be solved using 10.32.14 in [1] (2.56) to give:

$$I_\tau = 2\pi^2 i\left(\frac{\pi}{iNc^2t(1-\frac{(x-x_j)^2}{2c^2t^2})}\right)^{-\frac{1}{2}} e^{-iNc^2t\left(1-\frac{(x-x_j)}{2c^2t^2}\right)} K_1\left(iNc^2t\left(1-\frac{(x-x_j)^2}{2c^2t^2}\right)\right), \tag{4.65}$$

giving $\Psi(x,t)$ as:

$$\Psi(x,t) = \frac{iA}{\pi\sqrt{L}} Nc^2t\sqrt{\frac{-2\pi}{N\phi''(x_j;x,t)}}\exp\left[iN\rho\int_0^{x_j} q(x'')dx''\right]\frac{K_1(iNc^2t(1-\frac{(x-x_j)^2}{2c^2t^2}))}{ict(1-\frac{(x-x_j)^2}{2c^2t^2})} \tag{4.66}$$

Using the approximation to the modified Bessel function for large arguments; 10.25.3 in [1] gives:

$$K_1\left(iNc^2t(1-\frac{(x-x_j)^2}{2c^2t^2})\right) \approx \sqrt{\frac{\pi}{2iNc^2t(1-\frac{(x-x_j)^2}{2c^2t^2})}}\exp\left[-iNc^2t\left(1-\frac{(x-x_j)^2}{2c^2t^2}\right)\right] \tag{4.67}$$

In both denominators of (4.66) and (4.67), the approximation $(1-\frac{(x-x_j)^2}{2c^2t^2}) \approx 1$ can be made:

$$\Psi(x,t) = \frac{A}{\pi\sqrt{L}} Nc\sqrt{\frac{-2\pi}{N\phi''(x_j;x,t)}}\exp\left[iN\left(\rho\int_0^{x'} q(x'')dx'' + \frac{(x-x_j)^2}{2c^2t^2}\right)\right]e^{-iNc^2t} \tag{4.68}$$

$$= \sqrt{\frac{NA^2}{2iL\pi t}}\sqrt{\frac{-2\pi}{N\phi''(x_j;x,t)}}\exp\left[iN\left(\rho\int_0^{x'} q(x'')dx'' + \frac{(x-x_j)^2}{2c^2t^2}\right)\right]e^{-iNc^2t} \tag{4.69}$$

This has the same from as the Schrödinger solution with the addition of a rest mass term in the second exponential; a feature of all non-relativistic limit calculations.

4.2.3 Analysis

In deriving an asymptotic approximation to the evolution of a Klein-Gordon free-particle superoscillatory function, it is found that the dominant contributions arise from saddles in the WKB regime ($N \to \infty$) of the propagator. This isn't a surprising result as a requirement of the initial superoscillatory function is that N is very large. The contributions from the poles (the propagator approaching the light-cone) are relevant but only when one of the saddles is in the same neighbourhood. As the saddle moves away from the pole, the contribution becomes negligible.

As with the Schrödinger superoscillations, the analysis concerns itself with two features of evolution: the wall effect (asymmetrical time evolution in which the wavefunction evolves differently either side of a line on the x axis) and the disappearance of superoscillations. Both phenomena are principally explained through the change in dominance of saddles.

4.2.3.1 The Wall Effect

To understand how the two contributing saddles, $[x_2, x_4]$, exchange dominance; Stokes and anti-Stokes lines are computed:

$$\begin{aligned} \text{Stokes Line:} \quad & \Re e(\phi(x_2; x.t) - \phi(x_4; x, t)) = 0 \\ \text{anti-Stokes Line:} \quad & \Im m(\phi(x_2; x.t) - \phi(x_4; x, t)) = 0 \end{aligned} \tag{4.70}$$

where $\phi(x_j; x, t)$ is given by (4.24). Along a Stokes line, the phase is purely imaginary. Such lines represent points in the (x, t) plane in which the contribution from one saddle over another is maximal. On crossing a Stokes line, the sub-dominant saddle either disappears behind the dominant saddle or, if it is not contributing, reappears. Along an anti-Stokes line, the difference between the two phases is purely real, crossing an anti-Stokes line causes the dominant saddle to become sub dominant and the sub dominant saddle to become dominant, provided they are both contributing.

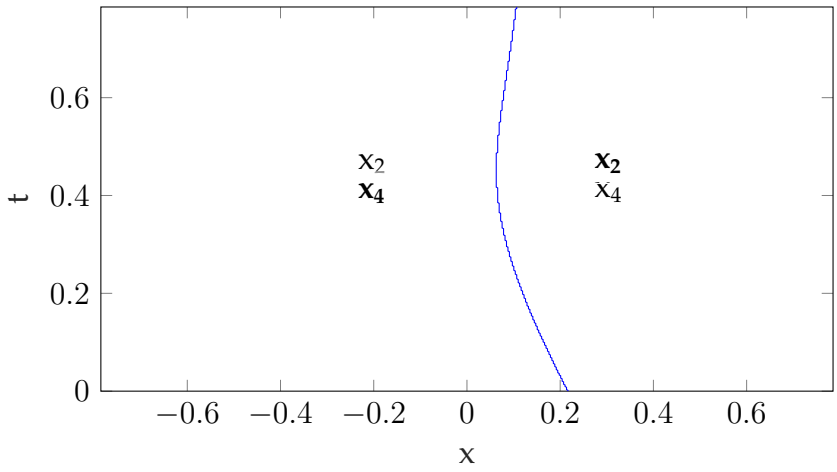

FIGURE 4.13: Anti-Stokes line (blue) for the x, t plane to the WKB approximation for $c = 1$, $s = 1$, $\kappa = 1$ and $a = 4$. Dominant saddles are in bold.

With respect to the wall effect, most important are the anti-Stokes lines; a change in dominance of saddles will have a much greater effect on the overall evolution of the wavefunction than the disappearance or re-emergence of a sub dominant saddle.

Figure 4.13 shows the anti-Stokes line for the phases in the WKB superoscillatory wavefunction (4.32), giving a clear indication of how the wall effect is caused. On crossing the anti-Stokes line, going from right to left, the dominance changes from x_2 being dominant (with x_4 sub dominant) to x_4 being dominant (with x_2 sub dominant). Superimposing the anti-Stokes line over the WKB approximation to the wavefunction gives a better picture of how this happens:

Figure 4.14 shows that most of the superoscillation occurs when x_4 is the dominant saddle. It would therefore not be surprising to suggest that it is the saddle responsible for the superoscillations. This, however, is not the case. Figure 4.15 shows how either saddle contributes to the overall wavefunction for specific times.

Clearly, x_2 is responsible for the superoscillations; it's wavefunction evolves in a very similar manor to that of the light-cone approximation. Despite crossing the anti-Stokes line and x_4 being dominant, the superoscillatory saddle's contribution

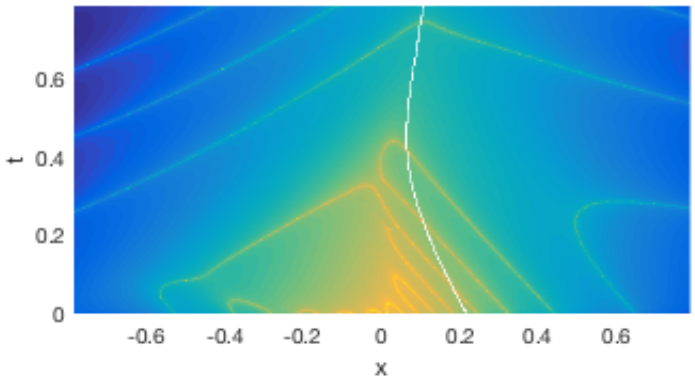

FIGURE 4.14: $\log(\Re e(\Psi(x,t)))$ for the WKB approximation (4.32). For $a = 4$, $N = 20$, $-\pi/4 \leq x \leq \pi/4$ and $0.00001 \leq t \leq \pi/4$. Yellow lines correspond to zeros of the wavefunction. The anti-Stokes line in figure 4.13 is superimposed as the white line.

is far from negligible for early times. This causes the superoscillations to persist despite x_2 being sub dominant. As t gets larger, x_2's contribution reduces severely after crossing the anti-Stokes line. This causes the superoscillations to decay far quicker when x_4 is dominant as opposed to when x_2 is dominant, giving the wall effect. Similar behaviour is found when looking at effect the saddle has on the phase. (4.24).

For small t, the values of $\Re e(\phi(x_2; x, t))$ and $\Re e(\phi(x_4; x, t))$ are very similar despite x_4 being dominant. However, this is not the case for large t. In fact, as t is increased, one would expect Stokes lines to appear either side of the the anti-Stokes line. This is illustrated in figure 4.16.

An interesting feature of figure 4.13 is the lack of Stokes lines and hence, the lack of a singularity (a point at which the Stokes and ant-Stokes lines coalesce). It is the missing singularity which is of most interest as this was a key feature of the Stokes/anti-Stokes plane for the non-relativistic superoscillations.

As all Stokes and anti-Stokes lines emerge from singularities, one will certainly exist somewhere in the (x, t) plane but it does not affect the disappearance of the superoscillations or the wall effect. A singularity, as shown in chapter 3, can be found as $c \to \infty$. However, the units used in this chapter cause the singularity to be out of reach of the approximations required to solve the wavefunction.

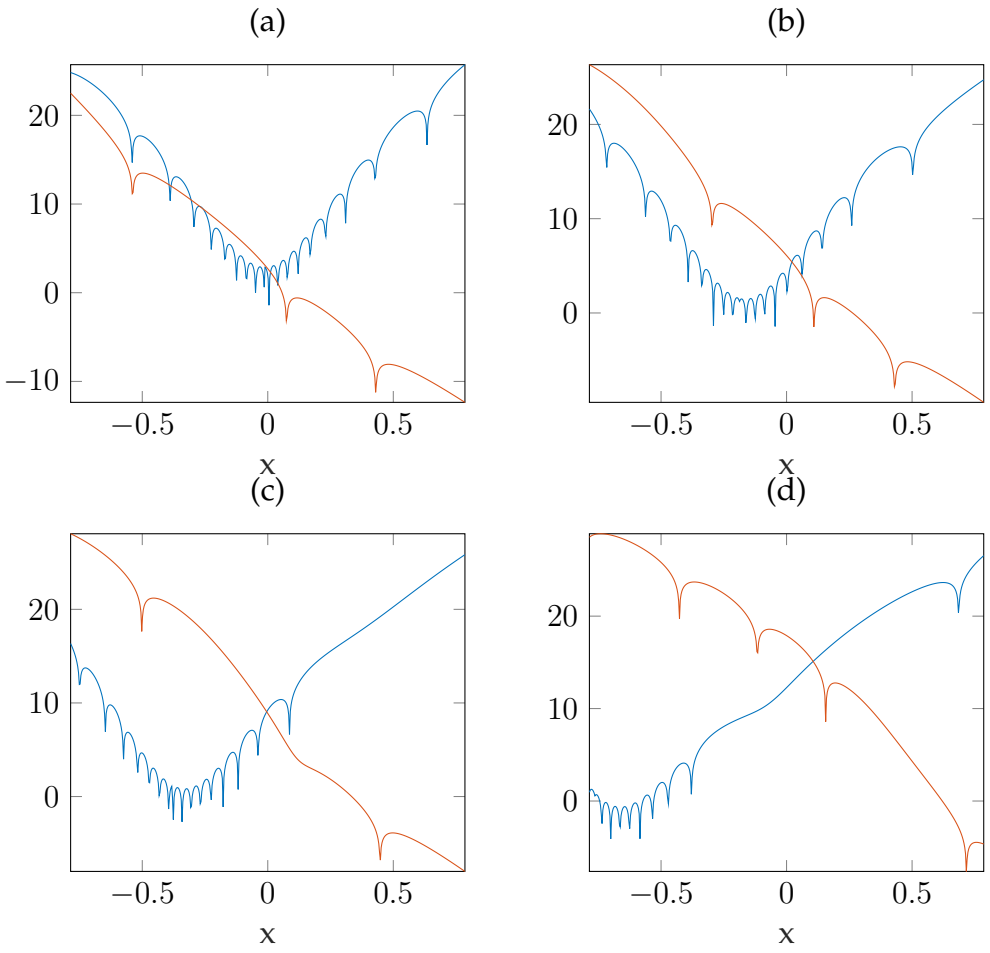

FIGURE 4.15: Cross-sections of figure 4.15 $\log(\Re e(\psi_{2,4}(x,t)))$ saddle point contributions; blue line: (ψ_2) contribution from x_2; orange line: contribution from x_4. For $a = 4$, $N = 20$, $-\pi/4 \leq x \leq \pi/4$ and $0.00001 \leq t \leq \pi/4$.(a): $t = 0.000001$; (b): $t = \pi/16$; (c): $t = \pi/8$; (d): $t = \pi/4$.

4.2.3.2 Disappearance Time

Now that the wall effect has been understood, the original question of this section, concerning the disappearance of the superoscillations, can be answered. The disappearance corresponds to the time t in which the local wave number of the superoscillatory saddle, x_2, along the anti-Stokes line decreases to the value corresponding to the fastest Fourier component. As the anti-Stokes line was computed numerically, a fit must be made. The function:

$$x_{a-s} = \left(\frac{0.2168 - t}{0.31}\right)^{\frac{4}{3}}, \tag{4.71}$$

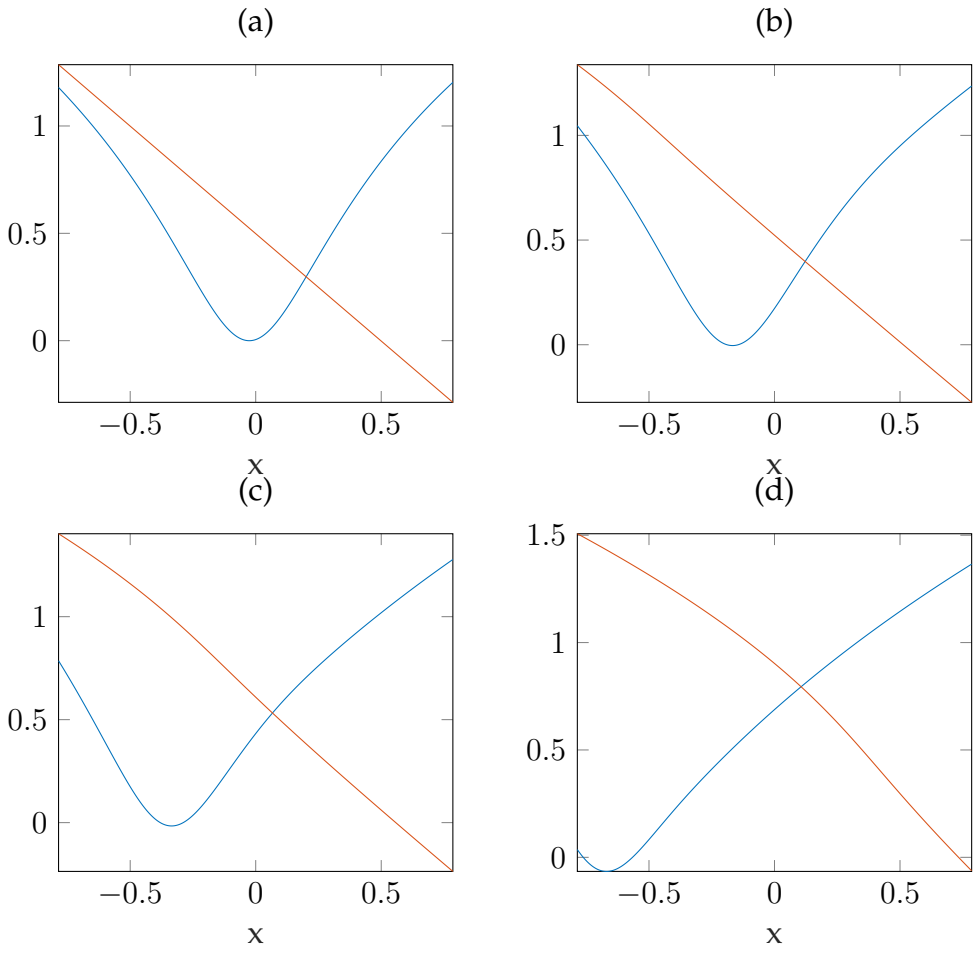

FIGURE 4.16: blue line $\Re e(\phi(x_2; x, t))$; orange line: $\Re e(\phi(x_4; x, t))$ for $a = 4$ $-\pi/4 \leq x \leq \pi/4$. (a): $t = 0.000001$; (b): $t = \pi/16$; (c): $t = \pi/8$; (d): $t = \pi/4$.

is found to be a satisfactory approximation to the anti-Stokes line. Due to the fact that the saddle-points have been numerically computed, an analytical expression for the disappearance time, t_d, cannot be obtained. However, it can be evaluated numerically.

Using the approximation to the anti-Stokes line (4.71), the disappearance time is determined by looking at the times at which the local momentum of the saddle x_2 decreases to a value of 1 (the fastest Fourier component) along the line (4.71). Figure 4.17 shows how the disappearance time, t_d changes as the superoscillatory parameter, a, is increased. It shows that, in the relativistic case (blue line), for large a, the disappearance time converges to $t_d = 0.3715$. This is different to the non-relativistic

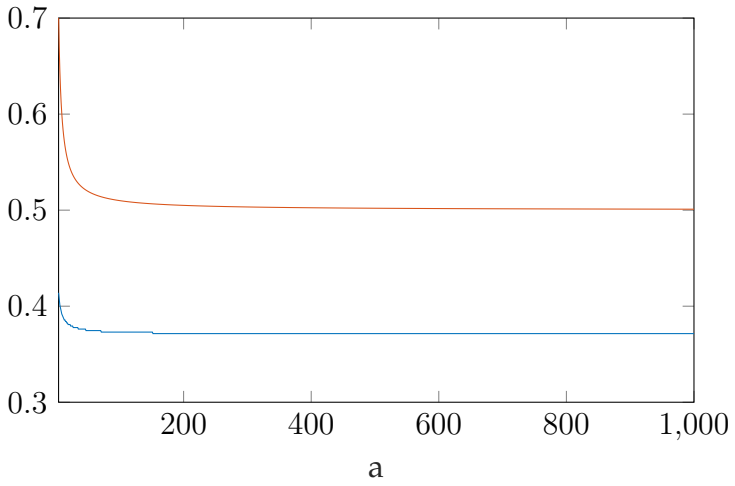

FIGURE 4.17: Disappearance times as a function of a. Blue line: Klein Gordon superoscillations; orange line: Schrödinger superoscillations in the range $4 \leq a \leq 1000$.

case which approaches a disappearance time of $t_d = 0.5$ as a becomes large. However, both the non-relativistic and relativistic disappearance times decay in a similar manner. One possible explanation for this disparity between relativistic and non-relativistic disappearance times is the that, for small t, only one saddle contributes in the non-relativistic evolution. However, the time for which this is the case is $t = 1/32$ which does not account for a difference in disappearance times of ~ 1.3. The main reason is to do with the side of the wall that the superoscillations persist for the longest. In the non-relativistic case, the superoscillations persist longest on the left-hand side of the wall, as the wall is located at $x = 0.25$, there is more space for the superoscillatory contribution to be dominant than if it were located on the right-hand side of the wall. However, the relativistic superoscillations are located on the right hand side of the wall. Again, the anti-Stokes line is found in the half-space $x > 0$ and therefore, the superoscillations will disappear more quickly.

4.3 Mixed State Spin-Zero Superoscillations

The presence of negative energies in relativistic quantum mechanics gives rise to another type of relativistic wavefunction: the mixed state wavefunction, composed

of both positive and negative energies. In this section, the mixed state solution to the initial superoscillatory state (4.5) is derived and, in much the same way as before, the integral over the propagator is solved (approximately) and the results are analysed.

4.3.1 Eigenfunction Expansion

For simplicity, the mixed state solution discussed will be composed of equal amounts of positive and negative energy:

$$\Psi(x,t) = \Psi_+(x,t) + \Psi_-(x,t). \tag{4.72}$$

Using the same initial wavefunction as previously:

$$\Psi(x,0) = \frac{A}{\sqrt{L}}\Big(\cos(\kappa x) + ia\sin(\kappa x)\Big)^{Ncs} \tag{4.73}$$

and using the representation of a sum over its eigenfunctions:

$$\Psi(x,0) = \frac{A}{\sqrt{L}}\sum_{m=0}^{Ncs} c_m e^{iNcs\kappa k_m x}, \tag{4.74}$$

the energy can be either positive or negative:

$$W_\pm(\kappa) = \pm Nc^2\sqrt{1+s^2\kappa^2 k_m^2}. \tag{4.75}$$

The positive/negative energy wavefunction is then given by:

$$\Psi_\mp(x,t) = \frac{A}{\sqrt{L}}\sum_{m=0}^{Ncs} c_m e^{i(Ncs\kappa k_m x \mp W(\kappa)t)}. \tag{4.76}$$

Using (4.77) and (4.72), the mixed state eigenfunction expansion is:

$$\Psi(x,t) = \frac{A}{2\sqrt{L}}\sum_{m=0}^{Ncs} c_m e^{iNcs\kappa k_m x}\cos(W(\kappa)t) \tag{4.77}$$

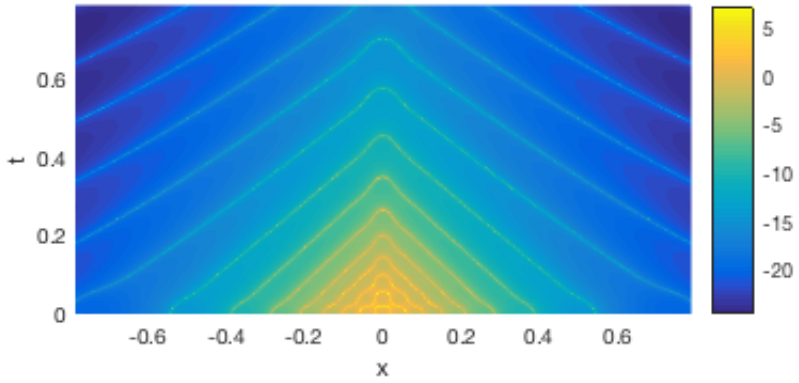

FIGURE 4.18: $\log(\Re e(\Psi(x,t)))$ for the mixed state eigenfunction expansion (4.77). For $a = 4$, $N = 20$, $-\pi/4 \leq x \leq \pi/4$ and $0.00001 \leq t \leq \pi/4$. Yellow lines correspond to zeros of the wavefunction.

The mixed state wavefunction is shown in figure 4.18. This is considerably different from the positive energy case, most notably; the evolution is no longer asymmetric. However, the superoscillations still disappear.

The eigenfunction representation does not provide a useful way of explaining why the wall effect disappears and how the superoscillations disappear. Once again, the integral over the propagator is used.

4.3.2 Evaluation of the Propagator

Recalling the mixed-state propagator from chapter 2:

$$\Delta(x-x';t) = \frac{1}{2}Nc^2t\,\mathrm{sgn}(t)\begin{cases} \frac{J_1\left(Nc\sqrt{c^2t^2-(x-x')^2}\right)}{\sqrt{c^2t^2-(x-x')^2}} & (c|t| > |x-x'|) \\ 0 & (c|t| < |x-x'|) \end{cases} \tag{4.78}$$

the integral over a propagator representation of a mixed state free particle superoscillatory function is therefore given by:

$$\Psi(x,t) = \frac{A}{2\sqrt{L}}Nc^2t\int_{x-ct}^{x+ct}\frac{J_1\left(Nc\sqrt{c^2t^2-(x-x')^2}\right)}{\sqrt{c^2t^2-(x-x')^2}}\left(\cos(\kappa x')+ia\sin(\kappa x')\right)^{Ncs}dx'. \tag{4.79}$$

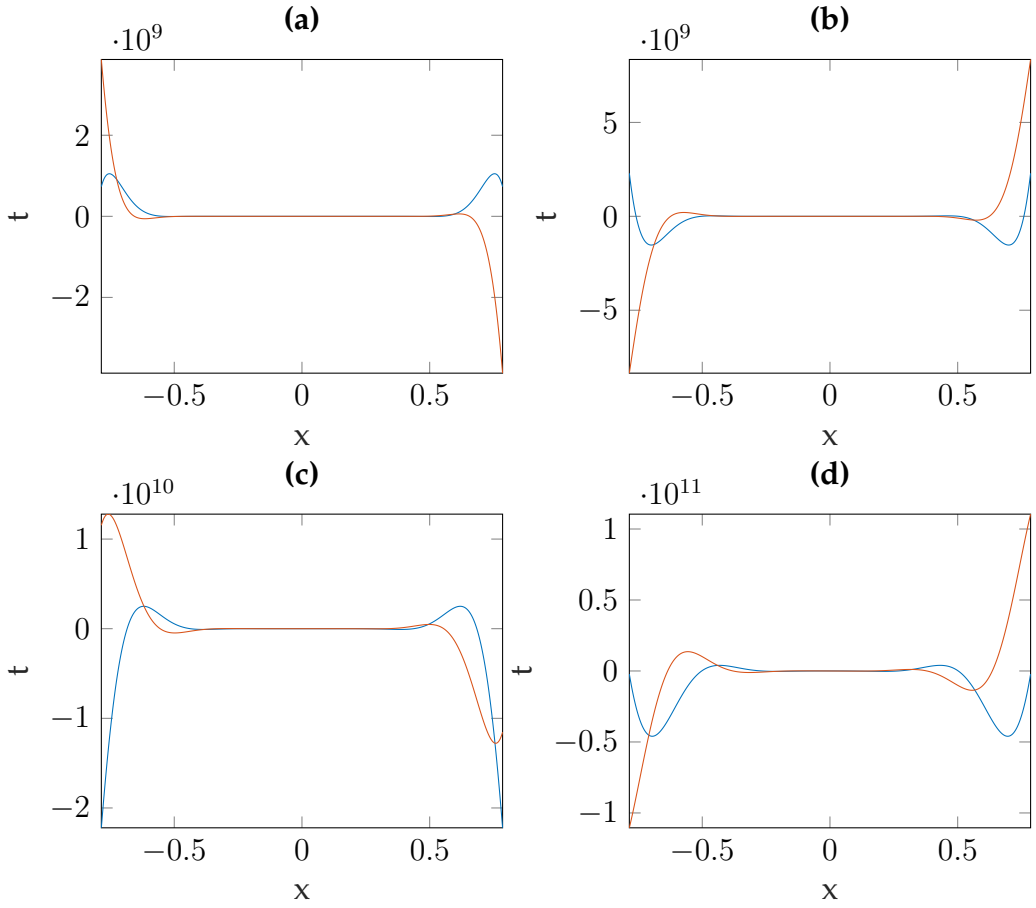

FIGURE 4.19: Showing the wave function $\Psi(x,t)$ in equation (4.77) the real parts of $\Psi(x,t)$ are shown in blue and the imaginary in orange. With parameters: $a = 4$, $N = 20$, $c = s = \kappa = A = L = 1$, $-\pi/4 \leq x \leq \pi/4$ with times: (a) $t = 0$, (b) $t = \pi/16$, (c) $t = \pi/8$ and (d) $t = \pi/4$.

As with the positive energy wavefunction, this is not an integral that can be solved directly.

4.3.2.1 Light-Cone/WKB Approximation

In chapter 2, it was shown that the light-cone and the WKB approximations to the mixed-state propagator were identical; the exponential contributions from the WKB approximations cancel out, which leaves the light-cone as the only limit in which an approximation is found:

$$\Delta(x - x'; t) \sim \delta((x - x')^2 - c^2 t^2), \tag{4.80}$$

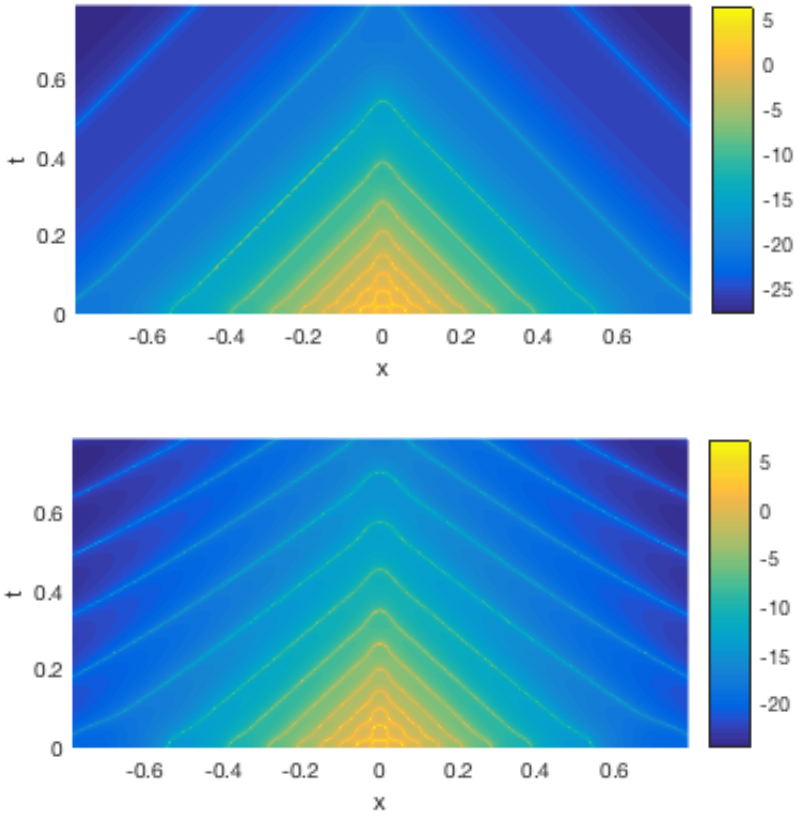

FIGURE 4.20: Above: $\log(\Re e(\Psi(x,t)))$ for the mixed state propagator, light-cone approximation(4.82). For $a = 4$, $N = 20$, $-\pi/4 \leq x \leq \pi/4$ and $0.00001 \leq t \leq \pi/4$. Yellow lines correspond to zeros of the wavefunction. Below: Figure 4.19 (eigenfunction expansion) for comparison with the light-cone approximation.

Only the first term of the light-cone approximation will be considered. The integral (4.79) therefore becomes:

$$\Psi(x,t) = \frac{A}{2\sqrt{L}} \int_{x-ct}^{x+ct} \delta((x-x')^2 - c^2t^2)\big(\cos(\kappa x') + ia\sin(\kappa x')\big)^{Ncs} dx', \tag{4.81}$$

giving the wavefunction:

$$\Psi(x,t) \sim \frac{A}{2\sqrt{L}}\Big(\big(\cos(\kappa(x+ct))+ia\sin(\kappa(x+ct))\big)^{Ncs}+\big(\cos(\kappa(x-ct))+ia\sin(\kappa(x-ct))\big)^{Ncs}\Big) \tag{4.82}$$

Comparing figures 4.18 and 4.20, the light-cone/WKB approximation clearly gives a very accurate result and captures the essential features of the evolution of a mixed state free-particle, relativistic Klein-Gordon wavefunction. Figure 4.21 show the full

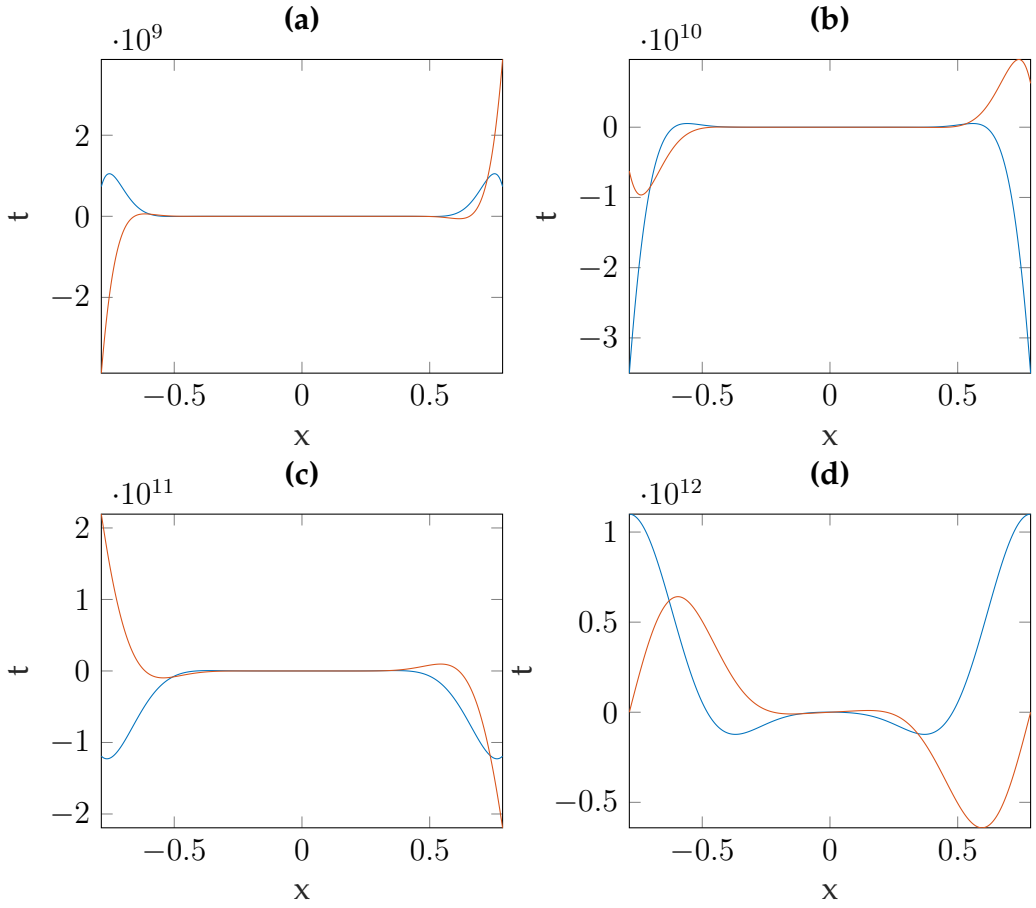

FIGURE 4.21: Showing the wave function $\Psi(x,t)$ in equation (4.82) the real parts of $\Psi(x,t)$ are shown in blue and the imaginary in orange. With parameters: $a = 4$, $N = 20$, $c = s = \kappa = A = L = 1$, $-\pi/4 \leq x \leq \pi/4$ with times: (a) $t = 0$, (b) $t = \pi/16$, (c) $t = \pi/8$ and (d) $t = \pi/4$.

wavefunction (4.82) for various times. Comparing this to figure 4.19, there are similarities in the evolution of the conventional oscillations in the eigenvalue solution and the pole approximation however, the orders of magnitude in the pole approximation are far larger than the eigenvalue solution.

4.3.3 Analysis

The mixed-state wavefunction can be approximated as the sum of the initial wavefunction being propagated along either side of the light-cone. This accounts for the lack of a wall effect in this energy set up; the two waves exchange dominance along the line $x = 0$ but, as the two waves are identical except for the fact that they are propagating in different directions along the x axis, there is no asymmetry in the

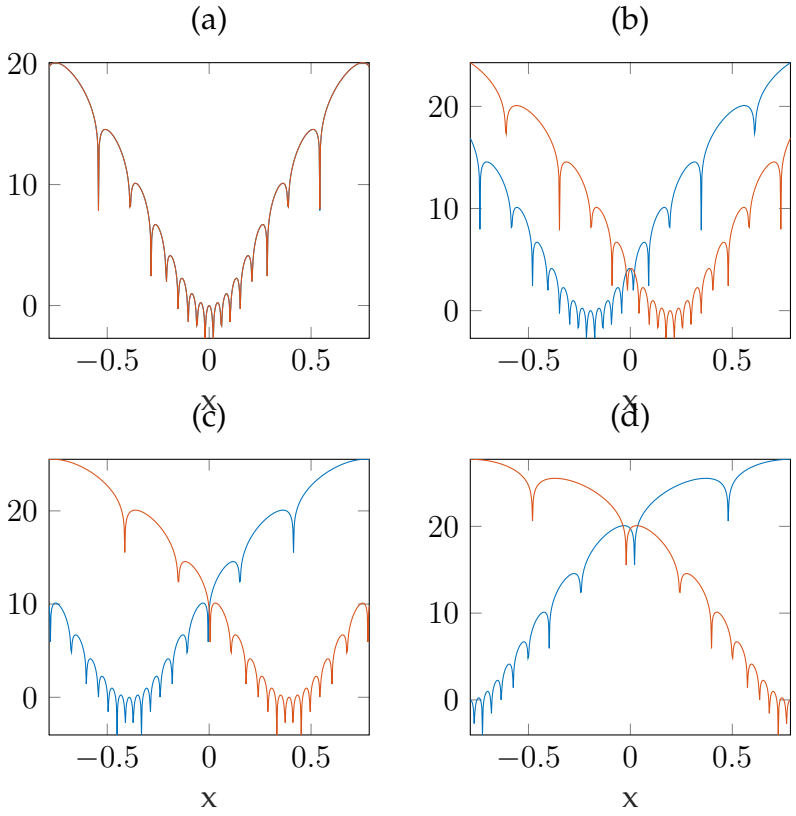

FIGURE 4.22: Blue line: $\log(\Re e(\Psi_+(x,t)))$; orange line: $\log(\Re e(\Psi_-(x,t)))$. For $a = 4$, $N = 20$, $-\pi/4 \leq x \leq \pi/4$ (a): $t = 0.000001$; (b): $t = \pi/16$; (c): $t = \pi/8$; (d): $t = \pi/4$.

evolution. This is shown in figure 4.22 in which the transition point and symmetry are clearly shown.

4.3.3.1 Disappearance Time

In the case of the mixed state, the disappearance time corresponds to the time in which the local momentum of either contribution is equal to the fastest Fourier component along the line $x = 0$. The choice of contribution is not important as they are equal along $x = 0$. Figure 4.22 shows how the disappearance time changes with the superoscillatory parameter, a: it shows that as a increases, the disappearance time decays to 0. This can be understood by looking at (4.82). As a tends to ∞, the $\cos$ term becomes negligible. As superoscillations in the function (4.5) are caused by the almost perfect destructive interference between the $\cos$ and $\sin$ term. If one term

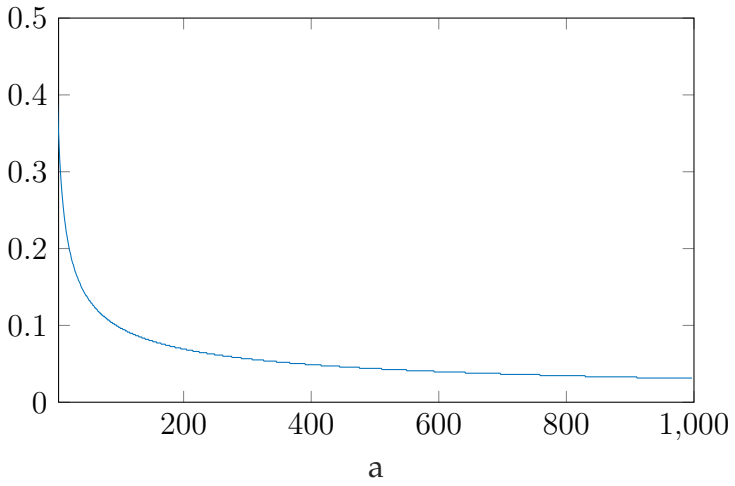

FIGURE 4.23: Disappearance times as a function of $a$for the mixed state wavefunction in the range $4 \leq a \leq 1000$.

were to drop out due to the other becoming significantly dominant, the superoscillations would cease.

4.4 Conclusion

The relativistic and non-relativistic positive energy free particle superoscillations initially seem to evolve in very different fashions. However, by closely examining the factors responsible for the evolution, similarities are found. This is principally due to the fact that non-relativistic superoscillations are an asymptotic limit of the relativistic superoscillations.

Studying the limiting forms of the positive energy, free particle Klein-Gordon propagator; it was found that the WKB approximation, giving contributions in the form of saddles, gave the best representation of the evolution of the initial superoscillatory function. The contribution from the light cone, appearing as the residue of a simple pole, gave a poor representation. Coalescence between the saddles and the poles was also investigated; it was found that, although a the saddle and pole do coalesce, this effect was not substantial enough to provide a better representation than the WKB method.

Both the evolution of relativistic and non-relativistic superoscillations can be explained through the exchanging of dominance between the two contributing saddles. Where the phase of the non-relativistic superoscillations has a complex structure, in the relativistic case there exists only one anti-Stokes line in the superoscillatory region. The result initially seems incorrect as no singularity through which Stokes and anti-Stokes lines emerge is present. However, the singularity is found as $t \to \infty$.

Two features of the evolution of the relativistic, free-particle, superoscillatory wavefunction are of interest: the wall effect and the disappearance of the superoscillations. The anti-Stokes line, found in the relativistic phase, is responsible for the wall effect, a phenomena that both relativistic and non-relativistic superoscillations share, although not at the same location. This is mirrored in the phase structure of the two wavefunctions in which the anti-Stokes line in which dominance is exchanged between saddles [3] occurs in different places.

The anti-Stokes line responsible for the wall effect in both the relativistic and non-relativistic case is also responsible for the disappearance of the superoscillations. The disappearance occurs at the point on the anti-Stokes line at which the local momentum of the superoscillatory saddle decreases to the value corresponding to the fastest Fourier component. As the units used in the relativistic calculations are much smaller than those used in the non-relativistic calculations, it is not surprising that the superoscillations decay far quicker in the relativistic framework: for $a = 4$ the relativistic superoscillations decay after a time of $t_d = 0.414$ whereas the non-relativistic superoscillations decay after a time of $t_d = 0.7057$. This is due to the fact that, the anti-Stokes line responsible for the change in dominance of saddles is not present for the initial part of the evolution of the non-relativistic wavefunction; the saddle responsible for the decay of superoscillations either doesn't appear or is

[3] For both the non-relativistic and relativistic case, there exists only one anti-Stokes line in which both saddle are present.

sub dominant. Lastly, both disappearance times depend on the superoscillatory parameter, a. As a is increased, both decay to a finite value. This is found analytically to be $t_d = 0.5$ for the non-relativistic superoscillations however, due to the numerical nature of the saddle points an analytic value was not achievable. Numerically, it was found that the relativistic superoscillations decay to a disappearance time of $t_d = 0.3715$ as $a \to \infty$.

The final superoscillatory wavefunction discussed in this chapter was that of mixed energy. Unlike the positive energy wavefunction, the mixed state has no non-relativistic counterpart. This is due to the presence of negative energy states. Such states are also responsible for the disappearance of the wall effect with primary contributions coming from either side of the light cone. This is shown by using the light-cone approximation to the propagator; the results found were very accurate.

Like the positive energy wavefunction, the mixed state superoscillations also disappear after a certain time and decay as a is increased. However, they do not reach a finite value but instead converge to $t_d = 0$. This is because as $a \to \infty$, the $\cos$ term in the superoscillatory function drops out and the interference between the $\cos$ and $\sin$ terms responsible for superoscillations ceases.

In [30], a comparison to optical superoscillations was made by remarking on the similarities between the Schrödinger equation and the paraxial wave equation. Although here we do not work the problem through as done by Berry and Popescu however, we do note the resemblance between the Klein-Gordon equation and the wave equation:

$$\frac{\partial^2}{\partial x^2}\left[\Psi(x,t)\right] - N^2 c^2 \Psi(x,t) = \frac{1}{c^2}\frac{\partial^2}{\partial t^2}\Psi(x,t) \tag{4.83}$$

$$\frac{\partial^2}{\partial x^2}\left[\Psi(x,t)\right] = \frac{1}{c^2}\frac{\partial^2}{\partial t^2}\Psi(x,t) \tag{4.84}$$

Where the Klein-Gordon euqation (4.83) and the wave equation (4.84) differ only by the extra term and parameter, N, in the Klein-Gordon equation. Therefore, an

interesting next step in this research would be to consider the $m \to 0$ limit of the results presented here.

Chapter 5

Relativistic Free Particle Superoscillations for a Spin-Half Wavefunction

Up to this point, a superoscillatory wavefunction has only been described, in a relativistic context, for a spin-zero free particle. In this chapter, the case of a superoscillatory spin-half relativistic free particle wavefunction will be studied. To account for the change in spin, a different equation is used to calculate the wavefunction: the Dirac equation.

The aim of this chapter is therefore to compare the spin-half wavefunction to its spin-zero counterpart. To do this, a way creating a spin-half wavefunction is used that takes an initial spin-zero wavefunction and manipulates to produce a four component wavefunction that is a solution to the Dirac equation. The method which achieves this is called the $KG \rightarrow D$ procedure.

In chapter 4, it was shown that the key features of the evolution of a superoscillatory quantum free particle; the wall effect and the disappearance of the superoscillations, are found in both the non-relativistic and relativistic (positive/negative energy) frameworks. However, when studied using spin-zero relativistic quantum mechanics, other types of wavefunctions arise; negative energy and mixed-states. The negative energy case is analogous to that of the postive energy but a mixed-state (which defined here means a state of equal parts positive and negative energy)

possesses different properties to those seen in other superoscillatory wavefunctions.

Therefore, in this chapter, positive energy and mixed-state free-particle superoscillatory wavefunctions are created by taking the wavefunctions derived in chapter 4 and applying the $KG \rightarrow D$ procedure. When this is achieved the differences and similarities between them and their spin-zero counterparts seen in the previous chapter will be discussed.

5.1 The $KG \rightarrow D$ Procedure

In chapter 2, we derived propagators exclusively for a relativistic, free particle of spin zero. However, these are not valid for spin-half particles which obey the Dirac equation:

$$(i\gamma^{(\mu)}\partial_\mu - Nc)\mathbf{\Psi}(\mathbf{r}, t) = 0, \tag{5.1}$$

there are standard expressions for the $\gamma^{(\mu)}$ matrices but these are not the ones to be used here. Instead, we use the Weyl (chiral) [32] representation. Such a format of the Dirac equation is usually used in the case of particle accelerators; the results apply for particles in which the energy is much larger than the mass. However, this representation also provides an interesting link between a spin-zero and a spin-half relativistic wavefunction.

$$\gamma^{(0)} = \begin{bmatrix} 0 & I \\ I & 0 \end{bmatrix}, \quad \gamma^{(i)} = \begin{bmatrix} 0 & -\sigma_i \\ \sigma_i & 0 \end{bmatrix}, \tag{5.2}$$

Although propagators which obey (5.1) have been derived [106], [109], the process of constructing a spin-half wavefunction is greatly simplified by starting with a solution to the Klein-Gordon equation [33], [26]; a spin-zero wavefunciton. This can be achieved through the $KG \rightarrow D$ procedure, described in [33].

To demonstrate how this is possible, we begin by substituting the matrices in

(5.2) into (5.1):

$$\left(\gamma^{(0)}\frac{1}{c}\frac{\partial}{\partial t}-\gamma^{(1)}\frac{\partial}{\partial x}-\gamma^{(2)}\frac{\partial}{\partial y}-\gamma^{(3)}\frac{\partial}{\partial z}-iNc\right)\mathbf{\Psi}(\mathbf{r},t)=0, \tag{5.3}$$

and expand it giving the following equations:

$$\frac{1}{c}\frac{\partial}{\partial t}\big[\Psi_3(\mathbf{r},t)\big]+\frac{\partial}{\partial x}\big[\Psi_4(\mathbf{r},t)\big]-i\frac{\partial}{\partial y}\big[\Psi_4(\mathbf{r},t)\big]+\frac{\partial}{\partial z}\big[\Psi_3(\mathbf{r},t)\big]-iNc\Psi_1(\mathbf{r},t)=0, \tag{5.4}$$

$$\frac{1}{c}\frac{\partial}{\partial t}\big[\Psi_4(\mathbf{r},t)\big]+\frac{\partial}{\partial x}\big[\Psi_3(\mathbf{r},t)\big]+i\frac{\partial}{\partial y}\big[\Psi_3(\mathbf{r},t)\big]-\frac{\partial}{\partial z}\big[\Psi_4(\mathbf{r},t)\big]-iNc\Psi_2(\mathbf{r},t)=0, \tag{5.5}$$

$$\frac{1}{c}\frac{\partial}{\partial t}\big[\Psi_1(\mathbf{r},t)\big]-\frac{\partial}{\partial x}\big[\Psi_2(\mathbf{r},t)\big]+i\frac{\partial}{\partial y}\big[\Psi_2(\mathbf{r},t)\big]-\frac{\partial}{\partial z}\big[\Psi_1(\mathbf{r},t)\big]-iNc\Psi_3(\mathbf{r},t)=0, \tag{5.6}$$

$$\frac{1}{c}\frac{\partial}{\partial t}\big[\Psi_2(\mathbf{r},t)\big]-\frac{\partial}{\partial x}\big[\Psi_1(\mathbf{r},t)\big]-i\frac{\partial}{\partial y}\big[\Psi_1(\mathbf{r},t)\big]+\frac{\partial}{\partial z}\big[\Psi_2(\mathbf{r},t)\big]-iNc\Psi_4(\mathbf{r},t)=0. \tag{5.7}$$

These can be rearranged in the following way:

$$\Psi_1(\mathbf{r},t)=-\frac{i}{Nc}\left(\left(\frac{1}{c}\frac{\partial}{\partial t}+\frac{\partial}{\partial z}\right)\Psi_3(\mathbf{r},t)+\left(\frac{\partial}{\partial x}-i\frac{\partial}{\partial y}\right)\Psi_4(\mathbf{r},t)\right), \tag{5.8}$$

$$\Psi_2(\mathbf{r},t)=-\frac{i}{Nc}\left(\left(\frac{1}{c}\frac{\partial}{\partial t}-\frac{\partial}{\partial z}\right)\Psi_4(\mathbf{r},t)+\left(\frac{\partial}{\partial x}+i\frac{\partial}{\partial y}\right)\Psi_3(\mathbf{r},t)\right), \tag{5.9}$$

$$\Psi_3(\mathbf{r},t)=-\frac{i}{Nc}\left(\left(\frac{1}{c}\frac{\partial}{\partial t}-\frac{\partial}{\partial z}\right)\Psi_1(\mathbf{r},t)-\left(\frac{\partial}{\partial x}-i\frac{\partial}{\partial y}\right)\Psi_2(\mathbf{r},t)\right), \tag{5.10}$$

$$\Psi_4(\mathbf{r},t) = -\frac{i}{Nc}\left(\left(\frac{1}{c}\frac{\partial}{\partial t}+\frac{\partial}{\partial z}\right)\Psi_2(\mathbf{r},t) - \left(\frac{\partial}{\partial x}+i\frac{\partial}{\partial y}\right)\Psi_1(\mathbf{r},t)\right). \tag{5.11}$$

Equations (5.8)-(5.11), can then be expressed through the matrix equations (it is for this reason that the less common matrices were used in (5.2)):

$$\begin{bmatrix}\Psi_1(\mathbf{r},t)\\ \Psi_2(\mathbf{r},t)\end{bmatrix} = -\frac{i}{Nc}\begin{bmatrix}\frac{1}{c}\frac{\partial}{\partial t}+\frac{\partial}{\partial z} & \frac{\partial}{\partial x}-i\frac{\partial}{\partial y}\\ \frac{\partial}{\partial x}+i\frac{\partial}{\partial y} & \frac{1}{c}\frac{\partial}{\partial t}-\frac{\partial}{\partial z}\end{bmatrix}\begin{bmatrix}\Psi_3(\mathbf{r},t)\\ \Psi_4(\mathbf{r},t)\end{bmatrix}, \tag{5.12}$$

$$\begin{bmatrix}\Psi_3(\mathbf{r},t)\\ \Psi_4(\mathbf{r},t)\end{bmatrix} = -\frac{i}{Nc}\begin{bmatrix}\frac{1}{c}\frac{\partial}{\partial t}-\frac{\partial}{\partial z} & -\frac{\partial}{\partial x}+i\frac{\partial}{\partial y}\\ -\frac{\partial}{\partial x}-i\frac{\partial}{\partial y} & \frac{1}{c}\frac{\partial}{\partial t}+\frac{\partial}{\partial z}\end{bmatrix}\begin{bmatrix}\Psi_1(\mathbf{r},t)\\ \Psi_2(\mathbf{r},t)\end{bmatrix}. \tag{5.13}$$

Our aim is to have $\Psi_1(\mathbf{r},t)$ as a solution to the Klein-Gordon equation. To achieve this, we set $\Psi_2(\mathbf{r},t)$, this means that the results will not be the most general. Substituting $\Psi_2(\mathbf{r},t)=0$ into (5.8)-(5.11) gives:

$$\Psi_1(\mathbf{r},t) = -\frac{i}{Nc}\left(\left(\frac{1}{c}\frac{\partial}{\partial t}+\frac{\partial}{\partial z}\right)\Psi_3(\mathbf{r},t) + \left(\frac{\partial}{\partial x}-i\frac{\partial}{\partial y}\right)\Psi_4(\mathbf{r},t)\right), \tag{5.14}$$

$$\Psi_3(\mathbf{r},t) = -\frac{i}{Nc}\left(\frac{1}{c}\frac{\partial}{\partial t}-\frac{\partial}{\partial z}\right)\Psi_1(\mathbf{r},t), \tag{5.15}$$

$$\Psi_4(\mathbf{r},t) = \frac{i}{Nc}\left(\frac{\partial}{\partial x}+i\frac{\partial}{\partial y}\right)\Psi_1(\mathbf{r},t). \tag{5.16}$$

Substituting (5.15) and (5.16) into (5.14):

$$\left(\frac{1}{c}\frac{\partial^2}{\partial t^2}-\frac{\partial^2}{\partial x^2}-\frac{\partial^2}{\partial y^2}-\frac{\partial}{\partial z^2}\right)\Psi_1(\mathbf{r},t)+N^2c^2\Psi_1(\mathbf{r},t)=0. \tag{5.17}$$

This is the three dimensional Klein-Gordon equation and hence, if $\Psi_1(\mathbf{r},t)$ is a solution to the Klein-Gordon equation then,

$$\mathbf{\Psi}(\mathbf{r},t) = \begin{bmatrix} \Psi_1(\mathbf{r},t) \\ 0 \\ \Psi_3(\mathbf{r},t) \\ \Psi_4(\mathbf{r},t) \end{bmatrix} = \begin{bmatrix} \phi(\mathbf{r},t) \\ \chi(\mathbf{r},t) \end{bmatrix} \tag{5.18}$$

is a solution to the Dirac equation (5.1). $\phi(\mathbf{r},t)$ and $\chi(\mathbf{r},t)$ are the two-component spinors:

$$\phi(\mathbf{r},t) = \begin{bmatrix} \Psi_1(\mathbf{r},t) \\ 0 \end{bmatrix}, \quad \chi(\mathbf{r},t) = \begin{bmatrix} \Psi_3(\mathbf{r},t) \\ \Psi_4(\mathbf{r},t) \end{bmatrix} \tag{5.19}$$

In order to differentiate between the two, we shall refer to $\phi(\mathbf{r},t)$ as the 'Klein-Gordon' spinor and $\chi(\mathbf{r},t)$ as the 'Dirac' spinor from now on.

With one component being set to 0, (5.18) is a very specific wavefunction. However, this step is crucial to the KG→D procedure. This does not mean that that $\Psi_2(\mathbf{r},t) = 0$ is not a pre-requisite to observe superoscillations in a relativistic, spin-half wavefunction. Superoscillations can be created from the 'standard' Dirac equation but, doing so doesn't provide as direct a comparison between Klein-Gordon and Dirac superoscillations as wavefunctions created from the KG→D procedure do.

5.2 Positive Energy Spin-Half Superoscillations

We have derived a method which allows us to get from a spin-zero wavefunction to a spin-half wavefunction. Now we are in a position where we can create spin-half wavefunctions using the results of the previous chapter. We begin by examining superoscillations in a positive energy wavefunction.

5.2.1 Eigenfunction Expansion

We start with the two-component spinor, $\phi(x,t)$, created by using a solution to the Klein-Gordon equation. For this we use the eigenfunction expansion for a super-oscillating free-particle, positive energy Klein-Gordon wavefunction given as:

$$\psi(x,t) = \frac{A}{\sqrt{L}} \sum_{m=0}^{Ncs} c_m e^{i(Ncs\kappa k_m x - W(\kappa)t)}, \tag{5.20}$$

with

$$W(\kappa) = Nc^2\sqrt{1 + s^2\kappa^2 k_m^2}. \tag{5.21}$$

From this the Klein - Gordon spinor is trivial. To get the final two components of the spin-half wavefunction, we use the matrix operator given in (5.12) which results in:

$$\chi(x,t) = -\frac{i}{Nc}\begin{bmatrix} \frac{1}{c}\partial_t\psi(x,t) \\ -\partial_x\psi(x,t) \end{bmatrix} = \begin{bmatrix} \chi_1(x,t) \\ \chi_2(x,t) \end{bmatrix} \tag{5.22}$$

The first component of (5.22) is:

$$\chi_1(x,t) = -\frac{i}{Nc^2}\frac{A}{\sqrt{L}} \sum_{m=0}^{Ncs} c_m \frac{\partial}{\partial t}\left[e^{i(Ncs\kappa k_m x - W(\kappa)t)}\right] \tag{5.23}$$

$$= -\frac{1}{Nc^2}\frac{A}{\sqrt{L}} \sum_{m=0}^{Ncs} W(\kappa) c_m e^{i(Ncs\kappa k_m x - W(\kappa)t)}. \tag{5.24}$$

The second component is then:

$$\chi_2(x,t) = \frac{i}{Nc}\frac{A}{\sqrt{L}} \sum_{m=0}^{Ncs} c_m \frac{\partial}{\partial x}\left[e^{i(Ncs\kappa k_m x - W(\kappa)t)}\right] \tag{5.25}$$

$$= -s\kappa\frac{A}{\sqrt{L}} \sum_{m=0}^{Ncs} k_m c_m e^{i(Ncs\kappa k_m x - W(\kappa)t)}, \tag{5.26}$$

giving the two-component spinor:

$$\chi(x,t) = -\frac{A}{\sqrt{L}} \sum_{m=0}^{Ncs} c_m e^{i(Ncs\kappa k_m x - W(\kappa)t)} \begin{bmatrix} \frac{W(\kappa)}{Nc^2} \\ sk_m\kappa \end{bmatrix}, \tag{5.27}$$

and finally:

$$\Psi(x,t) = \begin{bmatrix} \phi(x,t) \\ \chi(x,t) \end{bmatrix} = \frac{A}{\sqrt{L}} \sum_{m=0}^{Ncs} c_m e^{i(Ncs\kappa k_m x - W(\kappa)t)} \begin{bmatrix} 1 \\ 0 \\ -\frac{W(\kappa)}{Nc^2} \\ -sk_m\kappa \end{bmatrix} \tag{5.28}$$

Figure 5.1 shows the non-zero components of the four component wavefunction (5.28), all three of which are initially superoscillating. The differences between them are clear but they all evolve in a similar manner. As with the spin-zero wavefunction, the subtlety of the superoscillations does not allow the eigenfunction expansion to give a clear enough description of their evolution. We now move on to using the $KG \to D$ procedure on propagator representation.

Figures 5.2 and 5.3 show the full wavefunction, giving insight into the conventional oscillations and differences between the two components of $\chi(x,t)$. Both $\chi_1(x,t)$ and $\chi_2(x,t)$ evolve in a very similar manner; $\chi_2(x,t)$ is simply $\chi_1(x,t)$ reflected along the x-axis. However, they do differ in magnitude with $\chi_2(x,t)$ being a factor of 10 larger than χ_1. This is due to the factor of N in the denominator of the third component in (5.28).

5.2.2 Evaluation of the Propagator

To get a propagator representation of a spin-half wavefunction, explicit Dirac-propagators have been developed [106] [109]. However, the propagator used in this treatment is derived through use of the $KG \to D$ procedure on the propagator representation of

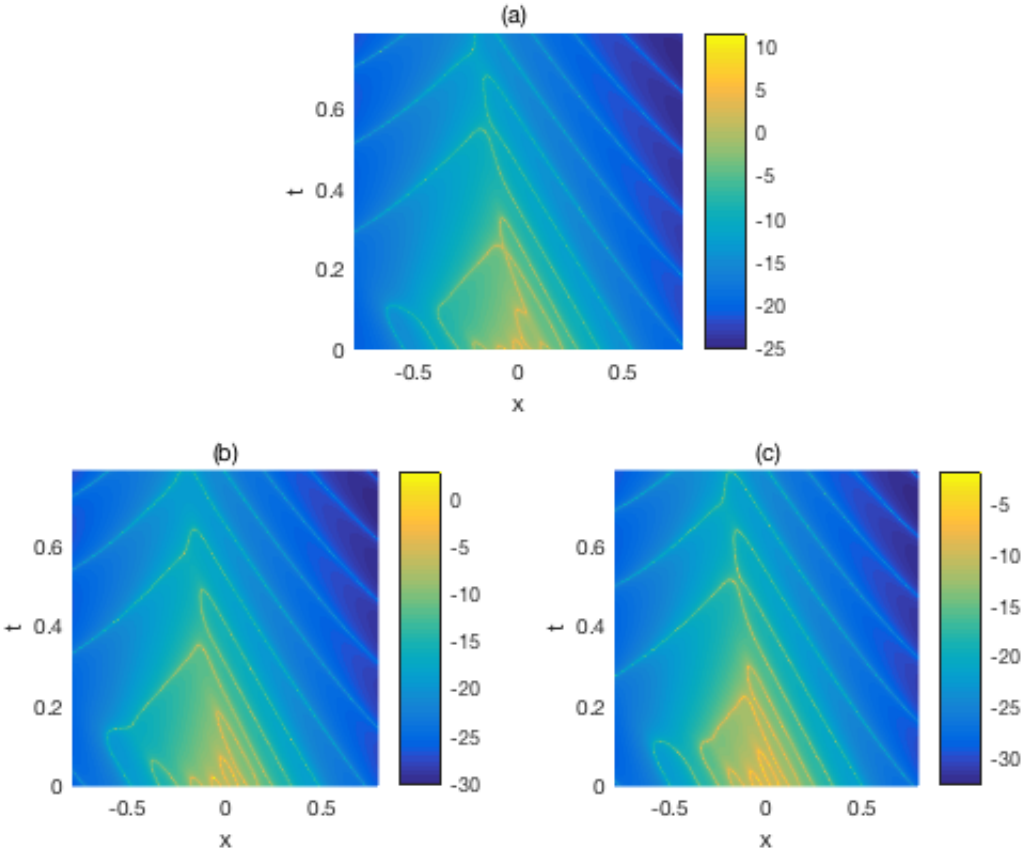

FIGURE 5.1: $\log(\Re e(\Psi(x,t)))$ for the eigenfunction expansion to the superoscillatory spin-half free-particle obtained through use of the $KG \rightarrow D$ procedure. (a): the spin-zero solution $\psi(x,t)$; (b): $\chi_1(x,t)$; (c): $\chi_2(x,t)$. For $a = 4$, $c = 1$, $N = 20$ $k = A = L = s = 1$, $\pi/4 \leq x \leq \pi/4$, $0 \leq t \leq \pi/4$.

a spin-zero wavefunction:

$$\psi(x,t) = \int_{-\infty}^{\infty} \psi(x',0)\Delta(x-x';t)dx'. \tag{5.29}$$

The first spinor used to create the bi-spinor $\Psi(x,t)$ is therefore:

$$\phi(x,t) = \begin{bmatrix} \int_{-\infty}^{\infty} \psi(x',0)\Delta(x-x';t)dx' \\ 0 \end{bmatrix} \tag{5.30}$$

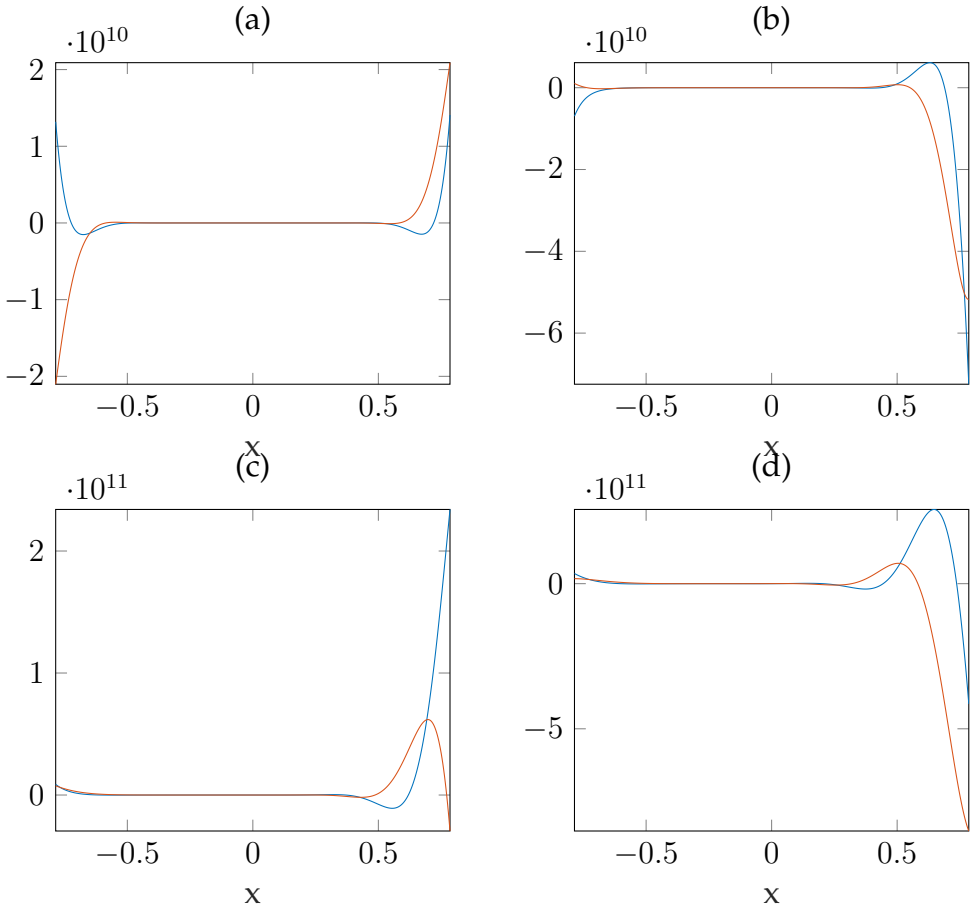

FIGURE 5.2: Showing the wave function $\chi_1(x,t)$ in equation (4.8) the real parts of $\Psi(x,t)$ are shown in blue and the imaginary in orange. With parameters: $a=4$, $N=20$, $c=s=\kappa=A=L=1$, $-\pi/4 \leq x \leq \pi/4$ with times: (a) $t=0$, (b) $t=\pi/16$, (c) $t=\pi/8$ and (d) $t=\pi/4$.

To get the second spinor, (5.30) is operated on by the matrix:

$$\chi(x,t) = -\frac{i}{Nc}\begin{bmatrix} \frac{1}{c}\partial_t - \partial_z & -\partial_x + i\partial_y \\ -\partial_x - i\partial_y & \frac{1}{c}\partial_t + \partial_z \end{bmatrix}\begin{bmatrix} \int_{-\infty}^{\infty}\psi(x',0)\Delta(x-x';t)dx' \\ 0 \end{bmatrix} \tag{5.31}$$

$$= -\frac{i}{Nc}\begin{bmatrix} \frac{1}{c}\int_{-\infty}^{\infty}\psi(x',0)\frac{\partial}{\partial t}\left[\Delta(x-x';t)\right]dx' \\ -\int_{-\infty}^{\infty}\psi(x',0)\frac{\partial}{\partial x}\left[\Delta(x-x';t)\right]dx'. \end{bmatrix} \tag{5.32}$$

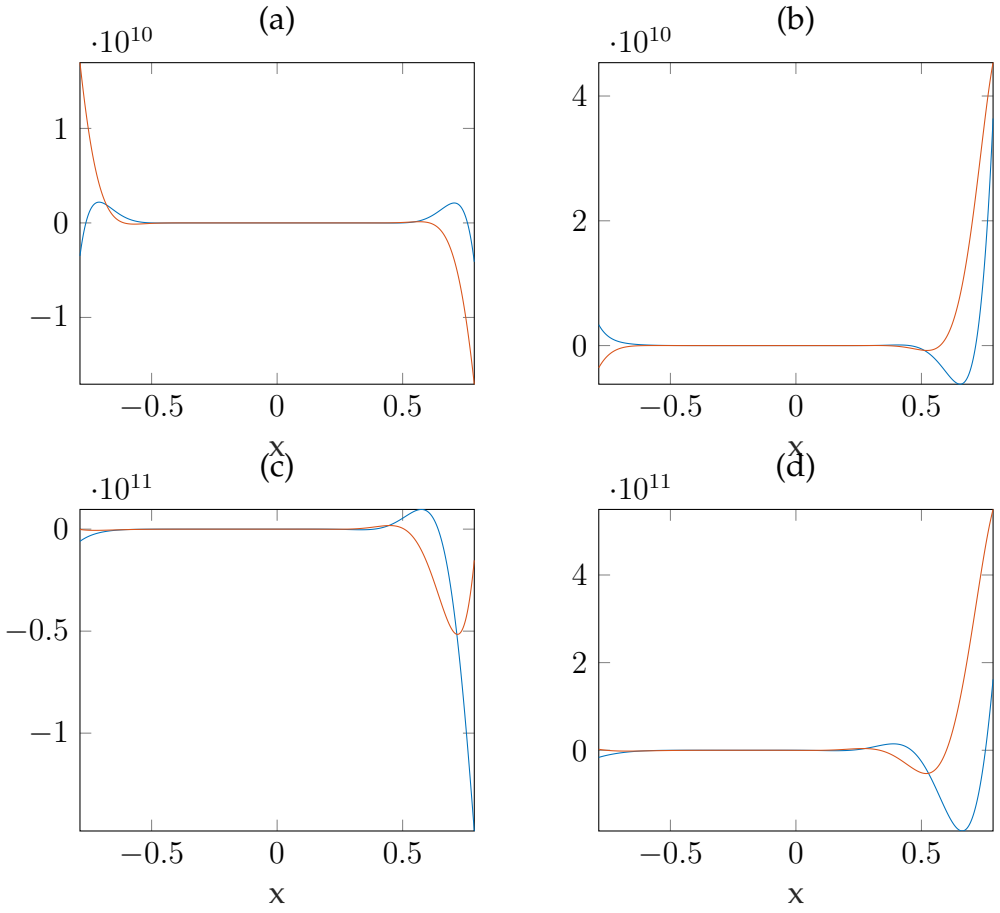

FIGURE 5.3: Showing the wave function $\chi_2(x,t)$ in equation (4.8) the real parts of $\Psi(x,t)$ are shown in blue and the imaginary in orange. With parameters: $a = 4$, $N = 20$, $c = s = \kappa = A = L = 1$, $-\pi/4 \leq x \leq \pi/4$ with times: (a) $t = 0$, (b) $t = \pi/16$, (c) $t = \pi/8$ and (d) $t = \pi/4$.

It follows that the propagator representation of the four-component, spin-half wavefunction is:

$$\Psi(x,t) = -\frac{i}{Nc}\begin{bmatrix} iNc\int_{-\infty}^{\infty}\psi(x',0)\Delta(x-x';t)dx' \\ 0 \\ \frac{1}{c}\int_{-\infty}^{\infty}\psi(x',0)\frac{\partial}{\partial t}\big[\Delta(x-x';t)\big]dx' \\ -\int_{-\infty}^{\infty}\psi(x',0)\frac{\partial}{\partial x}\big[\Delta(x-x';t)\big]dx'. \end{bmatrix} \tag{5.33}$$

Evaluation of the first component in (5.33) has been dealt with in the previous chapter; it is the spin-zero wavefunction. This chapter concerns itself with the third and fourth components in (5.33). Expressions in terms of the explicit Klein-Gordon propagator will be derived for each of these components before moving onto analysis.

Recalling the positive energy, free-particle, Klein-Gordon propagator (2.35):

$$\Delta(x-x';t) = \frac{i}{\pi}Nc^2t\frac{K_1(Nc\sqrt{(x-x')^2-c^2t^2})}{\sqrt{(x-x')^2-c^2t^2}} \tag{5.34}$$

The two components; $\chi_1(x,t)$ and $\chi_2(x,t)$ are:

$$\chi_1(x,t) = \frac{1}{\pi}\int_{-\infty}^{\infty}\psi(x',0)\frac{\partial}{\partial t}\left[t\frac{K_1(Nc\sqrt{(x-x')^2-c^2t^2})}{\sqrt{(x-x')^2-c^2t^2}}\right]dx' \tag{5.35}$$

$$\chi_2(x,t) = \frac{1}{\pi}ct\int_{-\infty}^{\infty}\psi(x',0)\frac{\partial}{\partial x}\left[\frac{K_1(Nc\sqrt{(x-x')^2-c^2t^2})}{\sqrt{(x-x')^2-c^2t^2}}\right]dx' \tag{5.36}$$

Using the relation:

$$\frac{d}{dx}\left[\frac{K_\nu(x)}{x}\right] = -\frac{K_{\nu+1}(x)}{x} \tag{5.37}$$

gives:

$$\chi_1(x,t) = -\frac{1}{\pi}\int_{-\infty}^{\infty}\psi(x',0)\left(Nc^3t^2\frac{K_2(Nc\sqrt{(x-x')^2-c^2t^2})}{(x-x')^2-c^2t^2}\cdots\right.$$

$$\left.-\frac{K_1(Nc\sqrt{(x-x')^2-c^2t^2})}{\sqrt{(x-x')^2-c^2t^2}}\right)dx' \tag{5.38}$$

$$\chi_2(x,t) = \frac{1}{\pi}Nc^2t\int_{-\infty}^{\infty}\psi(x',0)(x-x')\frac{K_2(Nc\sqrt{(x-x')^2-c^2t^2})}{(x-x')^2-c^2t^2}dx' \tag{5.39}$$

The rest of this section is now concerned with solving (5.38) and (5.39) in the positive energy configuration for the various limits of the propagator (5.34).

5.2.2.1 The 'Dirac' Spinor, $\chi(x,t)$, in the light-cone approximation

The light-cone approximation is valid when $x' \approx x \pm ct$; x' is in the neighbourhood of the light-cone. In this limit, the argument of the Bessel function in both (5.38) and (5.39) becomes very small and the approximation for small arguments can be used:

$$K_\nu(z) \approx \frac{1}{2}\Gamma(\nu)\left(\frac{1}{2}z\right)^{-\nu} \qquad (z \to 0) \tag{5.40}$$

Applying this to (5.38) and (5.39) gives:

$$\chi_1(x,t) = -\frac{1}{\pi}\int_{-\infty}^{\infty}\psi(x',0)\left(\frac{2ct^2}{N((x-x')^2-c^2t^2)^2} - \frac{1}{Nc((x-x')^2-c^2t^2)}\right)dx' \quad (5.41)$$

$$\chi_2(x,t) = \frac{2t}{N\pi}\int_{-\infty}^{\infty}\frac{\psi(x',0)(x-x')}{\left((x-x')^2-c^2t^2\right)^2}dx' \quad (5.42)$$

As with the case for the spin-zero wavefunction in this limit, the integrand is dominated by poles at the light cone $x \pm ct$. However, where we previously saw simple poles, the spin-half wavefunction also contains second order poles. Both integrals are of $\mathcal{O}(\frac{1}{N})$, this is different from the spin-zero wavefunction in which, at the light-cone, the integral is of order unity.

It is important, at this point, to check whether the propagator condition, $\Delta_{\chi_1}(x-x';0) = \delta(x-x')$, is maintained. It is crucial that, in the light-cone limit, this condition is met. It was shown, in chapter 2, that this is the approximation to the propagator that preserves this feature. Extracting the propagator from (5.41) gives:

$$\Delta_{\chi_1}(x-x';t) = -\frac{1}{\pi}\left(\frac{2ct^2}{N((x-x')^2-c^2t^2)^2} - \frac{1}{Nc((x-x')^2-c^2t^2)}\right) \quad (5.43)$$

By taking the limit $t = 0$ in (5.43), it is clear that the second term does not produce a delta function as required. This is therefore a 'non-propagator' term and will not be included in further calculations of the light-cone approximation [1]. It can be seen in (5.42) that no such terms will be present in the second component of the Dirac spinor.

As with the spin-zero case, in order to evaluate the evolution the initial superoscillatory function the eigenfunction expansion (5.20) must be used. This is necessary otherwise the integrand is seemingly divergent as $x' \to i\infty$. For $\chi_1(x,t)$ (5.38),

[1] Note that this non-propagator term is also dimensionless and not m^{-1} as required. These terms will be discussed further in the conclusion to this chapter.

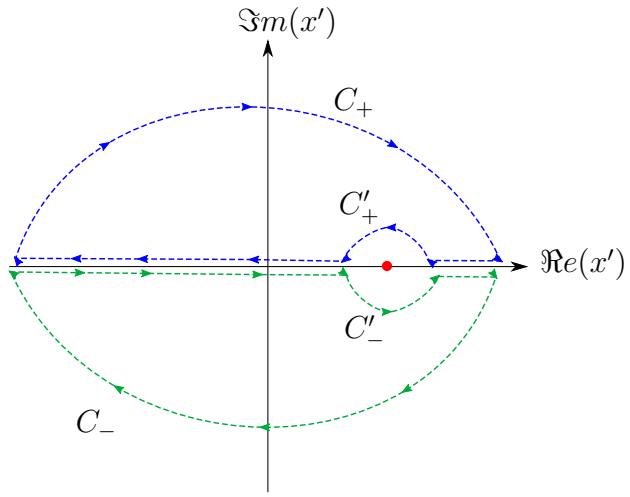

FIGURE 5.4: Showing how the sign of k_m in (5.44) affects how the contour is deformed around the pole (red circle) at $x' = x - ct$ in the x' plane. If $k_m > 0$, the contour is deformed into C_+, if $k_m < 0$, the contour is deformed into C_-.

using (5.20) as the initial wavefunction ($t = 0$) gives:

$$\chi_1(x,t) \approx -\frac{A}{\sqrt{L\pi}} \sum_{m=0}^{Ncs} c_m \int_{-\infty}^{\infty} \frac{2ct^2 e^{iNcs\kappa k_m x}}{N\Big((x-x')^2 - c^2t^2\Big)^2} dx' \tag{5.44}$$

With the integral in this form, we can split the integrand into a part which converges as $x' \to i\infty$ ($k_m > 0$) and a part which converges as $x' \to -i\infty$ ($k_m < 0$). By splitting the integral as described, the result is:

$$\chi_1(x,t) \approx -\frac{A}{\sqrt{L\pi}} \Bigg(\sum_{m=0}^{\frac{1}{2}Ncs-1} c_m \int_{C_-} \frac{2ct^2 e^{iNcs\kappa k_m x}}{N\Big((x-x')^2 - c^2t^2\Big)^2} dx' + \dots$$

$$\sum_{m=\frac{1}{2}Ncs}^{Ncs} c_m \int_{C_+} \frac{2ct^2 e^{iNcs\kappa k_m x}}{N\Big((x-x')^2 - c^2t^2\Big)^2} dx' \Bigg). \tag{5.45}$$

To evaluate the integrals in (5.45) the residue theorem, for a pole of order two, must be applied to the integrand:

$$I_1(x',x,t) = \frac{e^{iNcs\kappa k_m x'}}{\Big((x-x')^2 - c^2t^2\Big)^2} \tag{5.46}$$

As described in the previous chapter, the pole which represents a positive energy wavefunction is the pole at $x' = x - ct$. Calculating the residue at this point gives:

$$\text{Res}(I_1(x', x, t), x - ct) = \frac{1}{2c^2t^2}\Big(iNcs\kappa k_m + \frac{1}{ct}\Big)\exp\big[iNcs\kappa k_m(x - ct)\big], \tag{5.47}$$

giving the result to the integral :

$$\int_{C_+,C_-} \frac{e^{iNcs\kappa k_m x'}}{\Big((x - x')^2 - c^2t^2\Big)^2}dx' = \frac{i\pi}{Nc}\Big(iNcs\kappa k_m + \frac{1}{ct}\Big)\exp\big[iNcs\kappa k_m(x - ct)\big]. \tag{5.48}$$

From this, $\chi_1(x, t)$ in the limit $x' \to x - ct$, is:

$$\chi_1(x, t) \approx -\frac{A}{Nc\pi\sqrt{L}}\Bigg(\sum_{m=0}^{\frac{1}{2}Ncs-1} c_m\Big(iNcs\kappa k_m + \frac{1}{ct}\Big)\exp\big[iNcs\kappa k_m(x - ct)\big] + \dots$$

$$\sum_{m=\frac{1}{2}Ncs}^{Ncs} c_m\Big(iNcs\kappa k_m + \frac{1}{ct}\Big)\exp\big[iNcs\kappa k_m(x - ct)\big]\Bigg) \tag{5.49}$$

$$= -\frac{A}{Nc\pi\sqrt{L}}\sum_{m=0}^{Ncs} c_m\Big(iNs\kappa k_m + \frac{1}{ct}\Big)\exp\big[iNcs\kappa k_m(x - ct)\big] \tag{5.50}$$

Figure 5.5 shows that, aside at $t = 0$, the pole approximation is not an accurate way of describing the evolution of the first component of the spinor $\chi(x, t)$. However, as noted previously, the integral (5.41) is of $\mathcal{O}(\frac{1}{N})$. This is not true for (5.50) which is composed of two terms; one of $\mathcal{O}(\frac{1}{N})$ and the other of order unity.

In the initial superoscillatory wavefunction, N (which is related to the number of superoscillations) is very large. As the term that causes the inaccuracies is the one that is of order $\mathcal{O}(\frac{1}{N})$, the light-cone approximation will become more accurate the higher the number of superoscillations there are in the initial wavefunction. By disregarding the second term in (5.50), we get results similar to those of the spin-zero wavefunction in the light-cone limit:

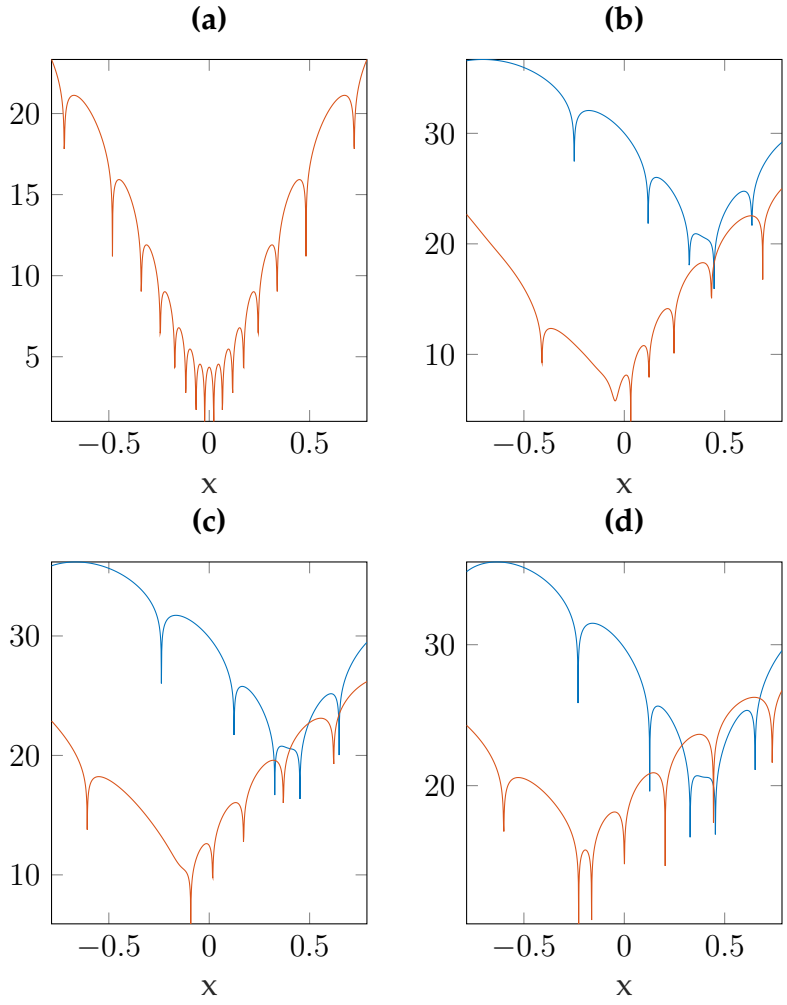

FIGURE 5.5: $\Re e(\log(\Re e(\chi_1(x,t))))$ for the complete wavefunction (5.38) (orange) and for the pole approximation (5.49) (blue) for (a) $t = 0.000001$, (b) $t = \pi/8$, (c) $t = \pi/4$ and (d) $t = \pi/2$ for all graphs, $-\pi/4 \leq x \leq \pi/4$ and $a = 4$, $N = 20$, $c = s = A = L = 1$.

Figure 5.6 shows a similar evolution to the spin-zero case; the initial wavefunction is propagated along the line $x - ct$.

We now evaluate $\chi_2(x,t)$ in the limit $x' \to x - ct$, substituting the Fourier series representation of the initial wavefunction into (5.39) and splitting the sum as per the contours in figure 5.4 gives:

$$\chi_2(x,t) \approx \frac{2At}{\pi N\sqrt{L}}\left(\sum_{m=0}^{\frac{1}{2}Ncs-1} c_m \int_{C_-} \frac{(x-x')e^{iNcs\kappa k_m x'}}{\left((x-x')^2 - c^2t^2\right)^2}dx' + \dots\right.$$

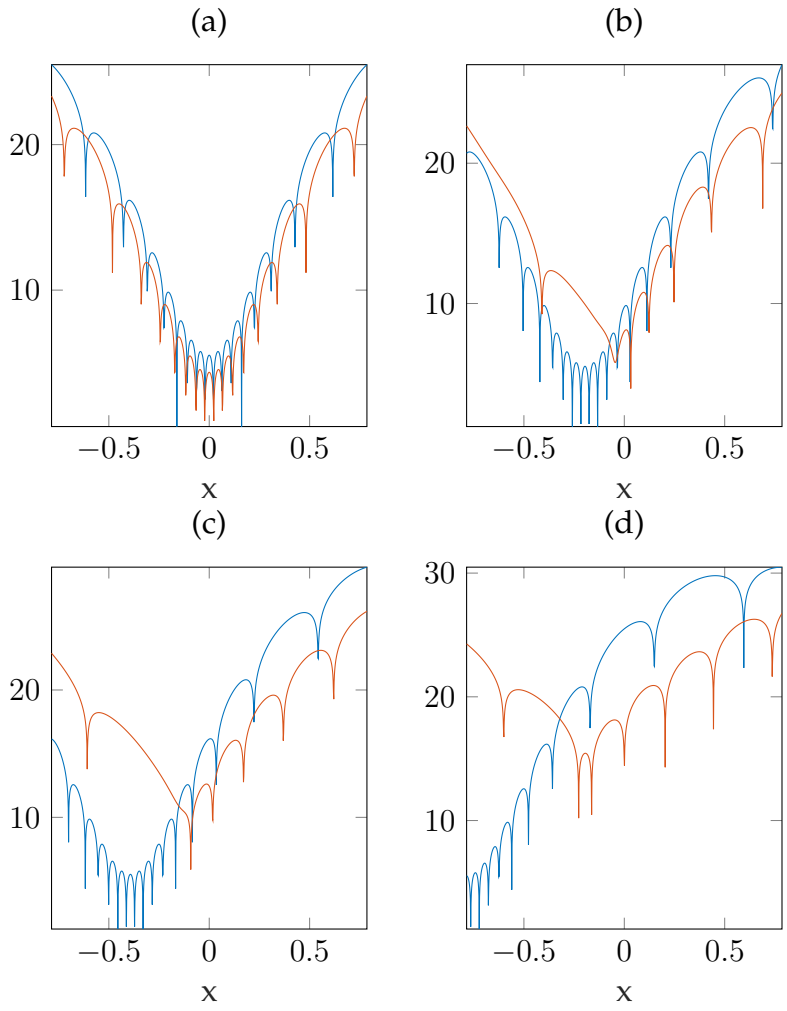

FIGURE 5.6: $\Re e(\log(\Re e(\chi_1(x,t))))$ for the complete wavefunction (5.38) (orange) and for the pole approximation in which the initial wavefunction term dominates over the propagator term (5.50) (blue) for (a) $t = 0.000001$, (b) $t = \pi/8$, (c) $t = \pi/4$ and (d) $t = \pi/2$ for all graphs, $-\pi/4 \leq x \leq \pi/4$ and $a = 4$, $N = 20$, $c = s = A = L = 1$.

$$\sum_{m=\frac{1}{2}Ncs}^{Ncs} c_m \int_{C_+} \frac{(x-x')e^{iNcs\kappa k_m x'}}{\left((x-x')^2 - c^2t^2\right)^2} dx' \Bigg). \tag{5.51}$$

To evaluate the integrals in (5.51), the residue of the integrand must be determined:

$$I_2 = \frac{(x-x')e^{iNcs\kappa k_m x'}}{\left((x-x')^2 - c^2t^2\right)^2} \tag{5.52}$$

The residue is then:

$$\text{Res}(I_2(x,t), x-ct) = \frac{iNs\kappa k_m e^{iNcs\kappa k_m(x-ct)}}{4t}, \tag{5.53}$$

giving the solution to the integral:

$$\int_{C_+,C_-} \frac{(x-x')e^{iNcs\kappa k_m x'}}{\left((x-x')^2 - c^2t^2\right)^2} = -\frac{\pi Ns\kappa k_m e^{iNcsk_m(x-ct)}}{2t}. \tag{5.54}$$

Which gives $\chi_2(x,t)$ as:

$$\chi_2(x,t) \approx -\frac{As\kappa}{\sqrt{L}}\left(\sum_{m=0}^{\frac{1}{2}Ncs-1} c_m k_m \exp\left[iNcs\kappa k_m(x-ct)\right] + \ldots \right.$$

$$\left. \sum_{m=\frac{1}{2}Ncs}^{Ncs} c_m k_m \exp\left[iNcs\kappa k_m(x-ct)\right]\right) \tag{5.55}$$

Figure 5.7 shows the evolution of (5.55). It is very similar to the spin-zero wavefunction and $\chi_1(x,t)$ (large N) both in their light-cone approximations. Unlike the first component of the Dirac spinor, the effect of the matrix operator does not result in terms involving $\frac{1}{t}$. However, once again, it is not completely accurate as there is a difference in magnitude between the two wavefunctions.

In figures 5.8 and 5.9, we show the full versions of the two components. The pole approximations captures the same reflective symmetry about the x-axis as seen in the eigenfunciton expansion. However, the orders of magnitude are larger in both cases.

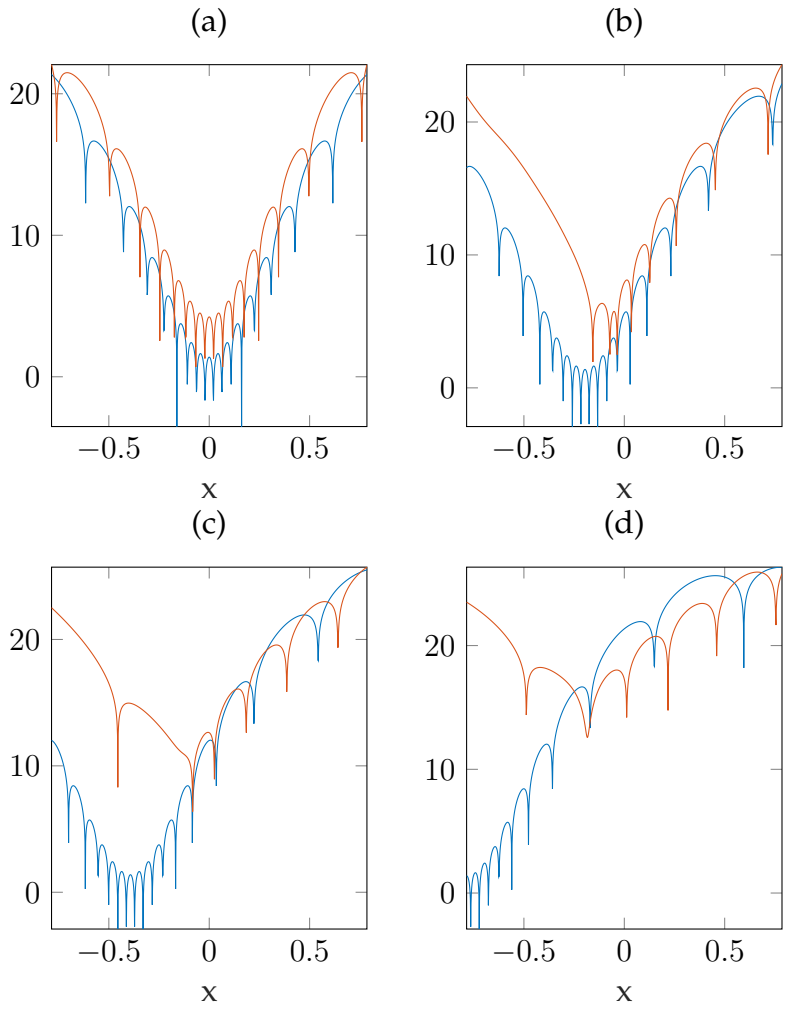

FIGURE 5.7: $\Re e(\log(\Re e(\chi_1(x,t))))$ for the complete wavefunction (5.38) (orange) and for the pole approximation (blue) for (a) $t = 0.000001$, (b) $t = \pi/8$, (c) $t = \pi/4$ and (d) $t = \pi/2$ for all graphs, $-\pi/4 \leq x \leq \pi/4$ and $a = 4$, $N = 20$, $c = s = A = L = 1$.

5.2.2.2 The Dirac Spinor, $\chi(x,t)$, in the WKB approximation

To evaluate $\chi(x,t)$ in the WKB ($N \to \infty$) limit, recall the large argument approximation to the modified Bessel function:

$$K_\nu(z) \approx \sqrt{\frac{\pi}{2z}} e^{-z} \quad (z \to \infty) \tag{5.56}$$

Applying this to (5.38) and (5.39) gives the two components of the Dirac spinor in the WKB limit:

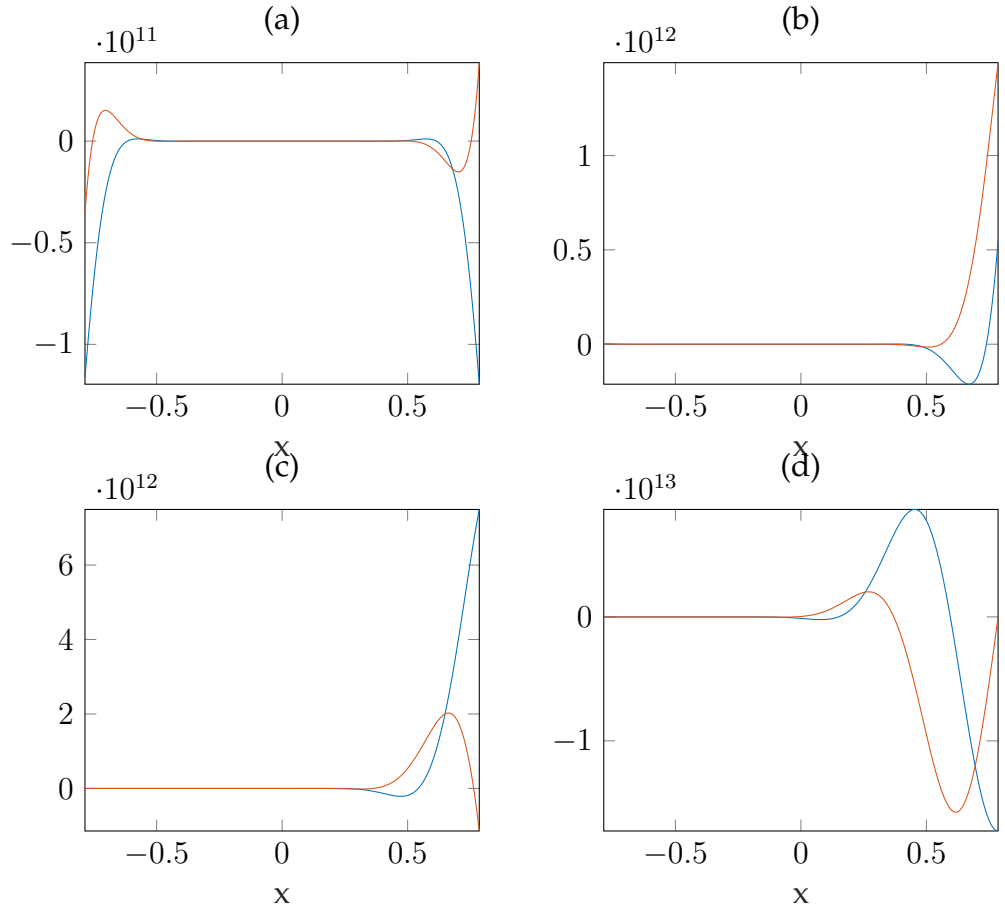

FIGURE 5.8: Showing the wave function $\chi_1(x,t)$ in equation (5.50) the real parts of $\Psi(x,t)$ are shown in blue and the imaginary in orange. With parameters: $a = 4$, $N = 20$, $c = s = \kappa = A = L = 1$, $-\pi/4 \leq x \leq \pi/4$ with times: (a) $t = 0$, (b) $t = \pi/16$, (c) $t = \pi/8$ and (d) $t = \pi/4$.

$$\chi_1(x,t) \approx -\frac{1}{\pi}\int_{-\infty}^{\infty}\psi(x',0)\sqrt{\frac{\pi}{Nc\sqrt{(x-x')^2-c^2t^2}}}\left(\frac{Nc^3t^2}{(x-x')^2-c^2t^2}+\frac{1}{\sqrt{(x-x')^2-c^2t^2}}\right)\cdots$$

$$\exp\left[-Nc\sqrt{(x-x')^2-c^2t^2}\right]dx' \tag{5.57}$$

$$\chi_2(x,t) \approx \frac{1}{\pi}Nc^2t\int_{-\infty}^{\infty}\psi(x',0)\sqrt{\frac{\pi}{Nc\sqrt{(x-x')^2-c^2t^2}}}\frac{(x-x')}{\sqrt{(x-x')^2-c^2t^2}}\cdots$$

$$\exp\left[-Nc\sqrt{(x-x')^2-c^2t^2}\right]dx' \tag{5.58}$$

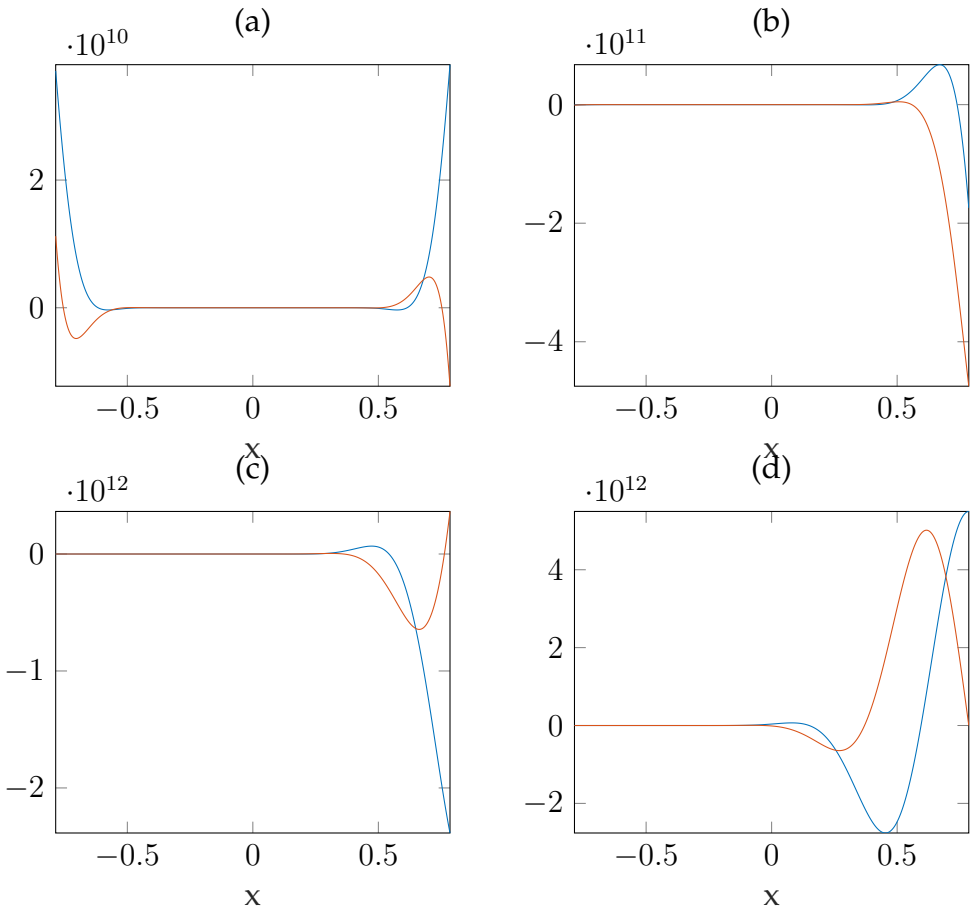

FIGURE 5.9: Showing the wave function $\chi_2(x,t)$ in equation (5.55) the real parts of $\Psi(x,t)$ are shown in blue and the imaginary in orange. With parameters: $a = 4$, $N = 20$, $c = s = \kappa = A = L = 1$, $-\pi/4 \leq x \leq \pi/4$ with times: (a) $t = 0$, (b) $t = \pi/16$, (c) $t = \pi/8$ and (d) $t = \pi/4$.

(5.57) and (5.58) can both be evaluated using the saddle point method. This gives solutions to the integral from contributions due to saddles of the phase of the exponential. In order to use this method, the initial wavefunction is represented in it's complex momenta form:

$$\psi(x,0) = \frac{A}{\sqrt{L}} \exp\left[iNcs \int_0^x q(x'')dx''\right], \tag{5.59}$$

giving:

$$\chi_1(x,t) \approx -\frac{A}{\pi\sqrt{L}} \int_{-\infty}^{\infty} \sqrt{\frac{\pi}{2Nc\sqrt{(x-x')^2 - c^2t^2}}} \left(\frac{Nc^3t^2}{(x-x')^2 - c^2t^2} + \frac{1}{\sqrt{(x-x')^2 - c^2t^2}} \right) \ldots$$

$$\ldots \exp\left[Nc\Big(is\int_0^{x'} q(x'')dx'' - \sqrt{(x-x')^2 - c^2t^2}\Big)\right]dx' \tag{5.60}$$

$$\chi_2(x,t) \approx \frac{1}{\pi}Nc^2t\int_{-\infty}^{\infty}\sqrt{\frac{\pi}{2Nc\sqrt{(x-x')^2-c^2t^2}}}\frac{(x-x')}{\sqrt{(x-x')^2-c^2t^2}}\ldots$$

$$\ldots \exp\left[Nc\Big(is\int_0^{x'} q(x'')dx'' - \sqrt{(x-x')^2 - c^2t^2}\Big)\right]dx' \tag{5.61}$$

Comparing (5.60) and (5.61) to the spin-zero WKB approximation integral (4.23), the phases in the exponentials in all cases are the same. Therefore, the contributing saddles to all three integrals are the same. The derivation of the saddles was considered in chapter 4, they are found through numeric solutions of the quartic equation:

$$a^2\kappa^2x_j^4 + 2ia\kappa(ia\kappa x - 1)x_j^3 + (4ia\kappa x + a^2k^2x^2 - s^2a^2\kappa^2 - 1)x_j^2 + \ldots$$

$$(2x - 2ia\kappa x^2 + 2s^2a^2\kappa^2 x)x_j + s^2a^2\kappa^2c^2t^2 - (1 + s^2a^2\kappa^2)x^2 = 0 \tag{5.62}$$

Solving (5.62) using the `roots` routine in MATLAB, gives four solutions. As described in chapter 4, these can be split into two sets. The first set, $[x_2, x_4]$, are saddles moving forwards in time and hence, relevant to a positive energy wavefunction. The second set, $[x_1, x_3]$, are saddles moving backwards in time and therefore not of interest in a positive energy wavefunction. Deforming the contour of integration through the set $[x_2, x_4]$ the saddle point method can be used which gives integrals in the form:

$$\int_C e^{\nu w(z)}\phi(z)dz \approx \phi(z_0)\sqrt{\frac{-2\pi}{\nu w''(z_0)}}e^{\nu w(z_0)} \quad (\nu \to \infty) \tag{5.63}$$

Denoting the phase of the exponential in (5.60) and (5.61) as:

$$\gamma(x';x,t) = is\int_0^{x'} q(x'')dx'' - \sqrt{(x-x')^2 - c^2t^2}, \tag{5.64}$$

and the terms in brackets in (5.60) as:

$$\mu(x';x,t)=\left(\frac{Nc^3t^2}{(x-x')^2-c^2t^2}+\frac{1}{\sqrt{(x-x')^2-c^2t^2}}\right) \tag{5.65}$$

the WKB approximations to the two components of the Dirac spinor are:

$$\chi_1(x,t)=-\sum_j\sqrt{\frac{-A^2}{NcL\sqrt{(x-x_j)^2-c^2t^2}\gamma''(x_j;x,t)}}\mu(x_j;x,t)\exp\Big[Nc\gamma(x_j;x,t)\Big], \tag{5.66}$$

$$\chi_2(x,t)=Nc^2t\sum_j\sqrt{\frac{-A^2}{NcL\sqrt{(x-x_j)^2-c^2t^2}\gamma''(x_j;x,t)}}\frac{(x-x_j)}{\sqrt{(x-x_j)^2-c^2t^2}}\exp\Big[Nc\gamma(x_j;x,t)\Big]. \tag{5.67}$$

Figure 5.10 compares the WKB (5.66) and (5.67) to the eigenfunction expansion (5.27) of the Dirac spinor. As with the WKB approximation of the spin-zero wavefunction, despite not being a completely accurate representation, the key features (wall effect and) of a superoscillatory wavefunction are captured.

The full wavefunctions are plotted in figures 5.11 and 5.12. For the most part, the relative symmetry between the two components is maintained however for $t=\pi/16$ this is not the case in $\chi_2(x,t)$. The orders of magnitude are also very different from what was previously seen in the eigenfunction expansion. Once again, the WKB approximation is not a good approximation to use when trying to replicate the conventional oscillations. This is largely due to the fact that small x approximations were used in the calculations which will not be valid for the regions of conventional oscillations.

A saddle-pole derivation of the wavefunction is not provided. This is due to the fact that, the poles in the two components of the Dirac spinor are of order two. Therefore in order to evaluate the integral, the integrand must be mapped on to a comparison integral which contains an exponential and a pole of order two. Unfortunately, none exist and hence, such an approximation is not possible.

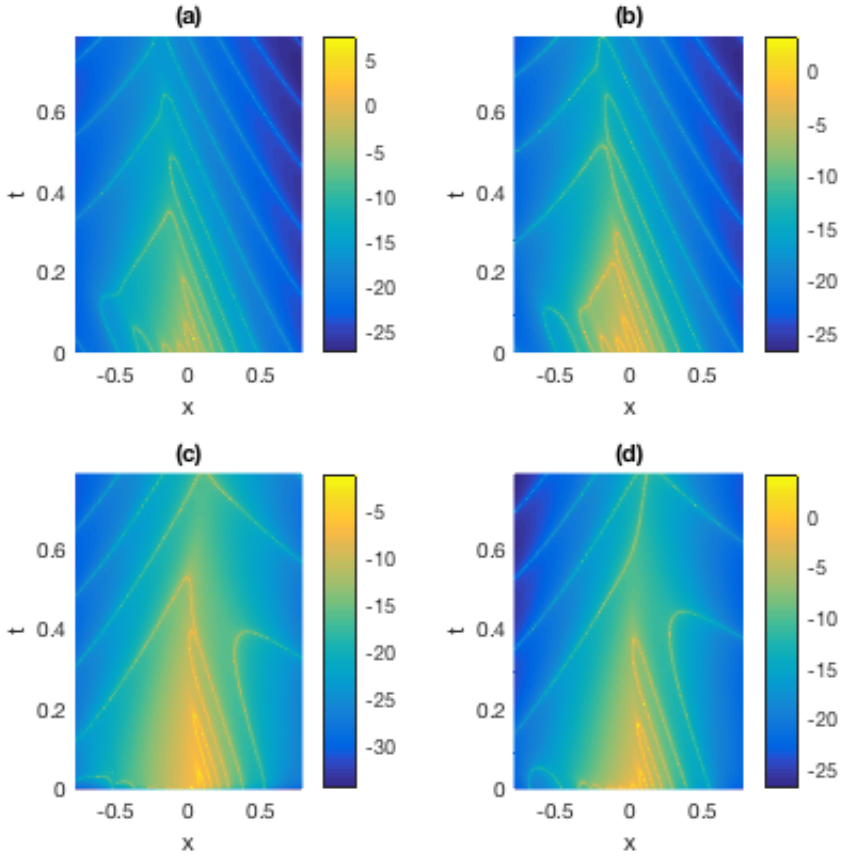

FIGURE 5.10: (a) and (c) $\Re e \log(\Re e(\chi_1(x,t)$ for (a) the eigenfunction expansion (5.24) and (c) the WKB approximation (5.66). (b) and (d) $\Re e \log(\Re e(\chi_2(x,t)$ for (b) the eigenfunction expansion (5.26) and (c) the WKB approximation (5.67). For all graphs $0 \leq t \leq \pi/4$, $-\pi/4 \leq x \leq \pi/4$ and $a = 4$, $N = 20$, $c = s = A = L = 1$.

5.2.3 Analysis

As with the spin-zero superoscillatory wavefunction, the best approximation to the eigenfunction expansion arises from the WKB approximation to the propagator. In fact, as we will discuss, the integrals required to solve the two components of the Dirac spinor rely on the same contributions to those of the Klein-Gordon wavefunction.

A key difference between the spin-zero and spin-half cases is at the light-cone in which the simple pole found in chapter 4 is replaced by a pole of order 2; generally the integral, in this limit, is also of $\mathcal{O}(\frac{1}{N})$. This is where the change in the wavefunction's spin has the most effect on the evolution however, as we have seen in

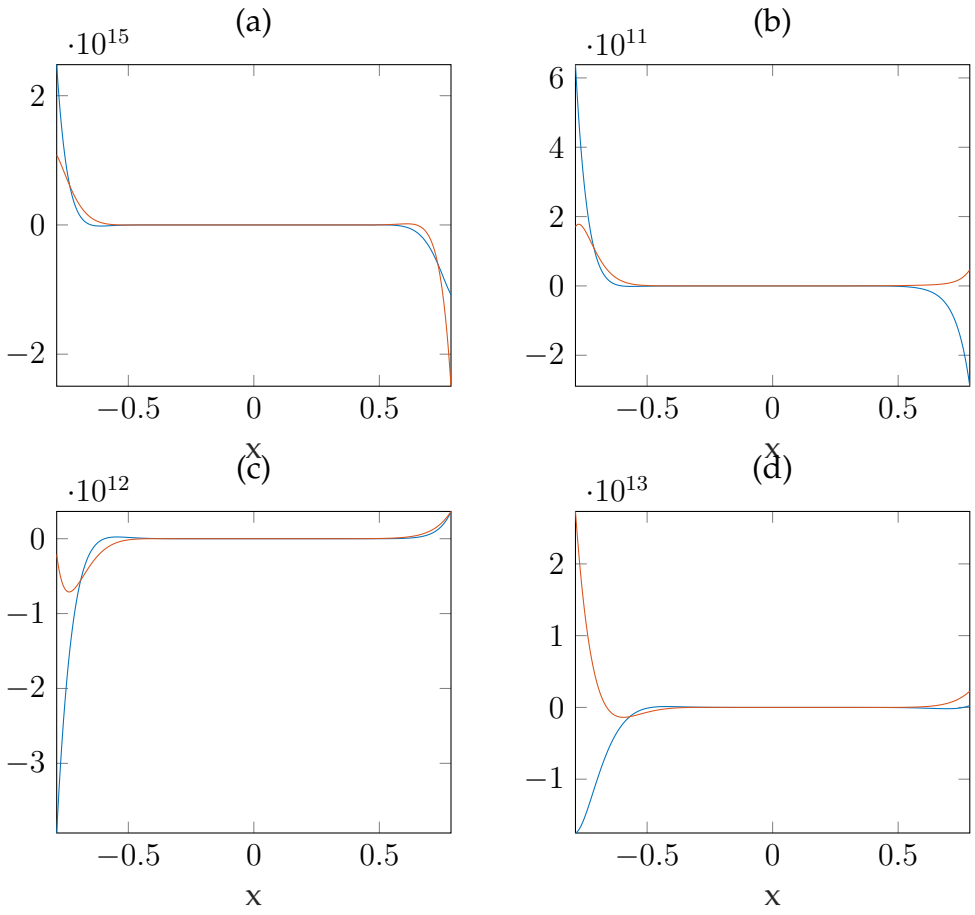

FIGURE 5.11: Showing the wave function $\chi_1(x,t)$ in equation (5.66) the real parts of $\Psi(x,t)$ are shown in blue and the imaginary in orange. With parameters: $a = 4$, $N = 20$, $c = s = \kappa = A = L = 1$, $-\pi/4 \leq x \leq \pi/4$ with times: (a) $t = 0$, (b) $t = \pi/16$, (c) $t = \pi/8$ and (d) $t = \pi/4$.

the spin-zero case and in the spin-half case, this limit does not provide an accurate approximation to the wavefunction.

5.2.3.1 The Wall Effect

In analysing the wall effect, the phase of the exponential in both (5.66) and (5.67) and the way in which the saddles exchange dominance is key to its appearance. The phase of both components of the Dirac spinor is equal to that of the phase of the spin-zero wavefunction. Therefore, the Stokes and anti-Stokes lines created will be the same as those in chapter (4). As they are the same, only a brief description is presented here with the majority of the detail left in chapter 4.

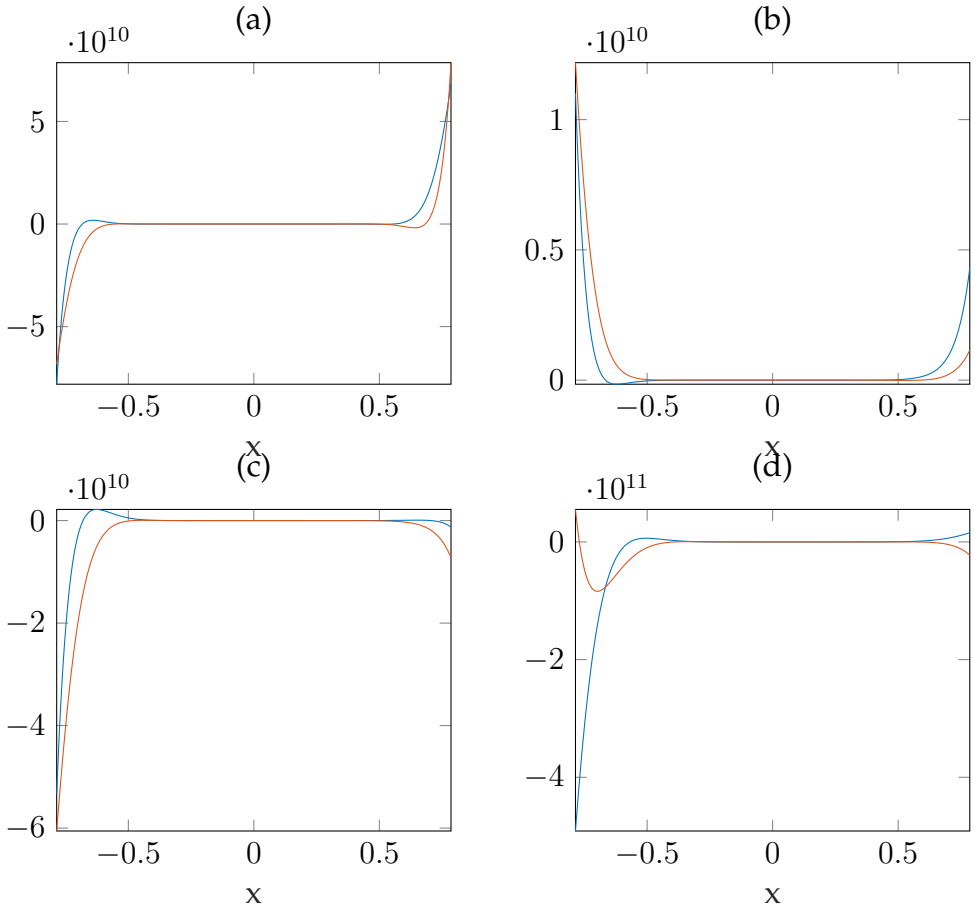

FIGURE 5.12: Showing the wave function $\chi_2(x,t)$ in equation (5.67) the real parts of $\Psi(x,t)$ are shown in blue and the imaginary in orange. With parameters: $a = 4$, $N = 20$, $c = s = \kappa = A = L = 1$, $-\pi/4 \leq x \leq \pi/4$ with times: (a) $t = 0$, (b) $t = \pi/16$, (c) $t = \pi/8$ and (d) $t = \pi/4$.

The Stokes and anti-Stokes lines are found, numerically, by:

$$\begin{aligned} \text{Stokes Line:} \quad & \Re e(\gamma(x_2; x.t) - \gamma(x_4; x, t)) = 0 \\ \text{anti-Stokes Line:} \quad & \Im m(\gamma(x_2; x.t) - \gamma(x_4; x, t)) = 0 \end{aligned} \tag{5.68}$$

With $\gamma(x_j; x, t)$ given by (5.64).

Along a Stokes line, the phase is purely imaginary. These lines represent points in which the the contribution of one saddle over another is maximal; crossing a Stokes line either causes a sub-dominant saddle disappear behind the dominant one or, if no sub-dominant saddle is present, it will emerge once a Stokes line is crossed. An anti-Stokes line is a line in which the phase is purely real. Along these lines, the contribution of one saddle of another is minimal. Hence, once crossed, a dominant

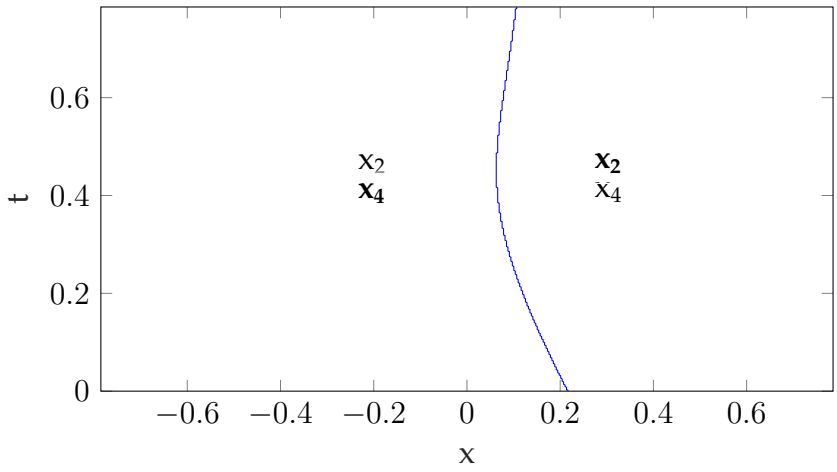

FIGURE 5.13: Anti-Stokes line (blue) for the x, t plane to the WKB approximation. Dominant saddles are in bold.

saddle become sub-dominant and vice-versa.

For the phase of both exponentials, $\gamma(x_j; x, t)$, the Stokes and anti-Stokes lines are given in figure 5.13. This is the same as what was found in the spin-zero superoscillatory wavefunction. We can see more clearly how each component behaves either side of this line by superimposing it onto the WKB approximations in figure 5.10: The saddle responsible for the superoscillations is x_2. This is clear from figure 5.14 in which the superoscillations persist for longer on the right hand side of the anti-Stokes line (the side in which x_2) is dominant). Despite the saddle x_4 producing a wavefunction which is conventionally oscillatory, superoscillations still persist, for a short time, left of the anti-Stokes line. This is due to the fact that there is not a Stokes line in the vicinity of the superoscillations. As an anti-Stokes line represents points in which the contribution of the dominant saddle over the sub-dominant saddle is minimal and the Stokes line represent points in which the relative dominance of the saddles is maximal, not having a Stokes line close to the superoscillations shows that the contributions from either saddle, especially around the anti-Stokes line, are similar in magnitude. This is seen in the spin-zero case and is shown in figure 4.15. As with the spin-zero case, the singularity from which anti-Stokes and Stokes lines emerge is out of reach of the approximations used.

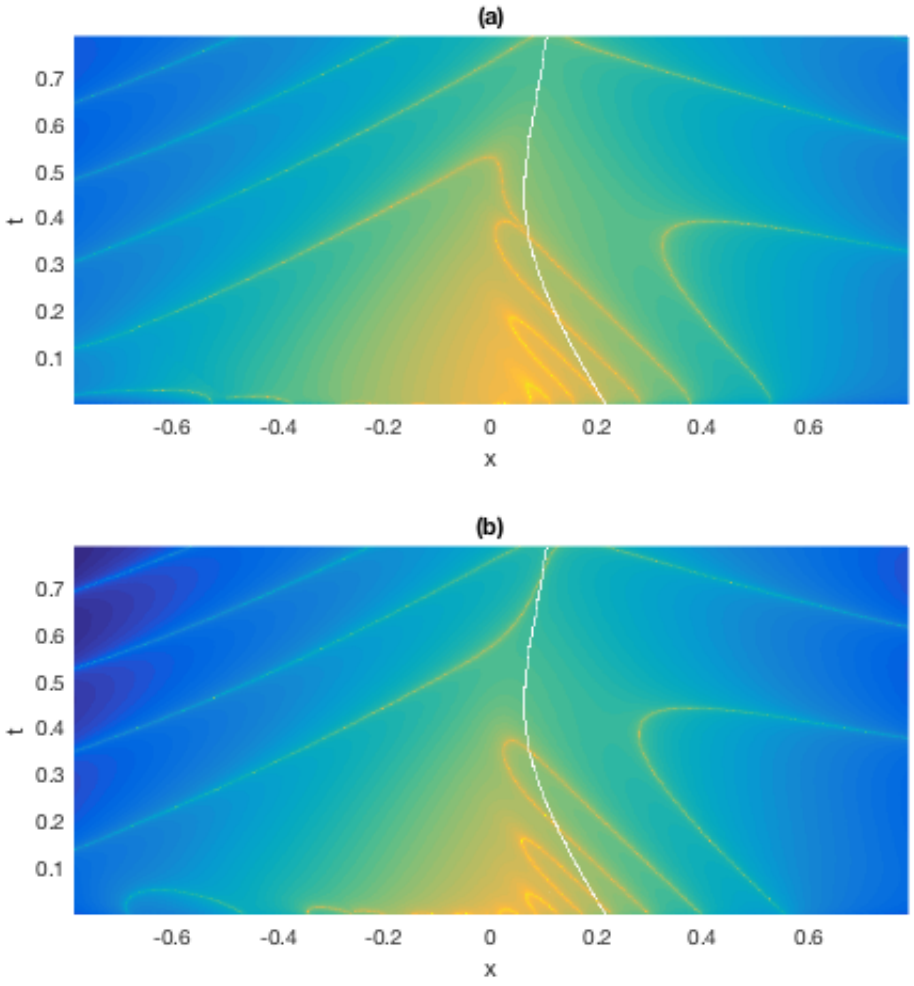

FIGURE 5.14: (a) $\Re e \log(\Re e(\chi_1(x,t)$ in the WKB approximation (5.66) with the anti-Stokes line (white line) superimposed. (b) $\Re e \log(\Re e(\chi_2(x,t)$ in the WKB approximation (5.67) with the anti-Stokes line (white line) superimposed. For all graphs $0 \leq t \leq \pi/4$, $-\pi/4 \leq x \leq \pi/4$ and $a = 4$, $N = 20$, $c = s = A = L = 1$.

5.2.3.2 Disappearance Time

The other important feature of the two components of the Dirac spinor is the disappearance of the superoscillations. Again, as this is governed by the phase of the exponentials in (5.66) and (5.67), it follows in the same way as the spin-zero case.

The disappearance of superoscillations corresponds to a time, t_d in which the local wavenumber of the superoscillatory saddle, x_2, decreases to a value less than or

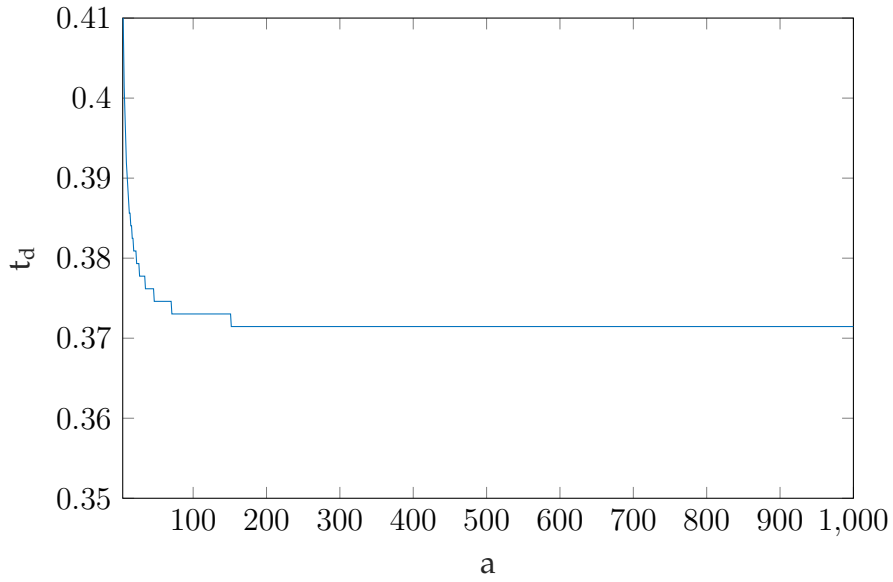

FIGURE 5.15: Disappearance time as a function of a in the range $4 \leq a \leq 1000$, for both components of the Dirac spinor (5.66) and (5.67) in the WKB approximation.

equal to that of the fastest Fourier component. To calculate this a numerical approximation to the anti-Stokes line (the same used in the previous chapter) in figure 5.13 is required:

$$x_{a-s} = \left(\frac{0.2168 - t}{0.31}\right)^{\frac{4}{3}}, \tag{5.69}$$

By substituting this into the local wavenumber and setting the result equal to one, the disappearance time can be determined. As the saddles are computed numerically, an analytical expression for the disappearance time is not possible. However, we can plot the disappearance time as a function of a, the superoscillatory parameter: As figure 5.15 shows, as a increases, the disappearance time decreases to a value of $t_d = 0.3717$. For the case of the wavefunctions in (5.66) and (5.67), the disappearance time is $t_d = 0.4140$ for both.

By looking a figure 5.1, it is quite clear that all three non-zero components of the Dirac wavefunction, $\Psi(x,t)$, have similar properties; they both have the same asymmetrical evolution and the superoscillations seem to disappear at the same time. By evaluating the integral over the propagator, this is found to be a correct prediction. This can also be predicted from the $KG \rightarrow D$ procedure.

The best approximation to the propagator for the initial superoscillatory function is the WKB approximation, which has an exponential form. The $KG \rightarrow D$ procedure derives the two components of the Dirac spinor, in $1+1$ dimensions by differentiating with respect to t and x respectively. Differentiating an exponential does nothing to affect its argument and hence features such as the wall effect and the disappearance of superoscillations are going to be unaffected.

The differences between the two components of the Dirac spinor and the spin-zero wavefunction are therefore superficial and best represented by the eigenfunction expansion:

$$\chi(x,t) = \frac{A}{\sqrt{L}} \sum_{m=0}^{Ncs} c_m e^{i(Ncs\kappa k_m x - W(\kappa)t)} \begin{bmatrix} \frac{W(\kappa)}{Nc^2} \\ -sk_m\kappa \end{bmatrix}, \tag{5.70}$$

The differentiation with respect to t in the first component of (5.70) pulls down the energy of the initial wavefunction whereas, differentiation with respect to x in the second pulls down the momentum. Doing this slightly changes the form of the wavefunction but does nothing to change its key features.

5.3 Spin-Half Superoscillations in a Mixed-State Wavefunction

We now perform the $KG \rightarrow D$ procedure on the mixed state wavefunction. A mixed state is one in which the wavefunction is composed of equal amounts of positive and negative energy. As with the positive energy spin-half wavefunction, we begin by deriving the eigenfunction expansion before moving onto the propagator representation.

5.3.1 Eigenfunction Expansion

Recall the spin-zero mixed state eigenfunction expansion:

$$\psi(x,t) = \frac{A}{2\sqrt{L}} \sum_{m=0}^{Ncs} c_m e^{iNcs\kappa k_m x} \cos(W(\kappa)t) \tag{5.71}$$

To get the two components of the Dirac spinor for (5.71) we use the same matrix operator as derived earlier in the chapter (5.13). This gives the two components of $\chi(x,t)$ as:

$$\chi_1(x,t) = -\frac{iA}{2Nc^2\sqrt{L}} \sum_{m=0}^{Ncs} c_m e^{iNcs\kappa k_m x} \frac{\partial}{\partial t}\big[\cos(W(\kappa)t)\big] \tag{5.72}$$

$$= \frac{iA}{2Nc^2\sqrt{L}} \sum_{m=0}^{Ncs} c_m W(\kappa) e^{iNcs\kappa k_m x} \sin(W(\kappa)t), \tag{5.73}$$

$$\chi_2(x,t) = -\frac{iA}{2Nc\sqrt{L}} \sum_{m=0}^{Ncs} c_m \cos(W(\kappa)t) \frac{\partial}{\partial x}\Big[e^{iNcs\kappa k_m x}\Big] \tag{5.74}$$

$$= \frac{As\kappa}{2\sqrt{L}} \sum_{m=0}^{Ncs} c_m k_m e^{iNcs\kappa k_m x} \cos(W(\kappa)t). \tag{5.75}$$

Figure 5.16 shows how the two mixed-state components of the Dirac spinor evolve. $\chi_2(x,t)$ evolves in a manner very similar to that of the spin-zero mixed state. However, $\chi_1(x,t)$, for small t, is quite different from what was seen in chapter 4. Unlike the positive energy wavefunction in which the results were fairly independent of spin, it would seem that it is in a mixed-state that the effect of spin is most obvious. Again, propagator methods will employed to explain this behaviour.

Figure 5.17 and 5.18 show the full version of the wavefunction for χ_1 and χ_2. As with the case for the spin-zero representation, one part of the wavefunction is symmetric about the line $y = 0$ and the other is not. Which part this is (real or imaginary) changes between each component. This is due to the fact that (5.73) has an i in the prefactor and (5.75) does not.

As χ_1 is not superoscillatory, one might expect to be able to see detail around

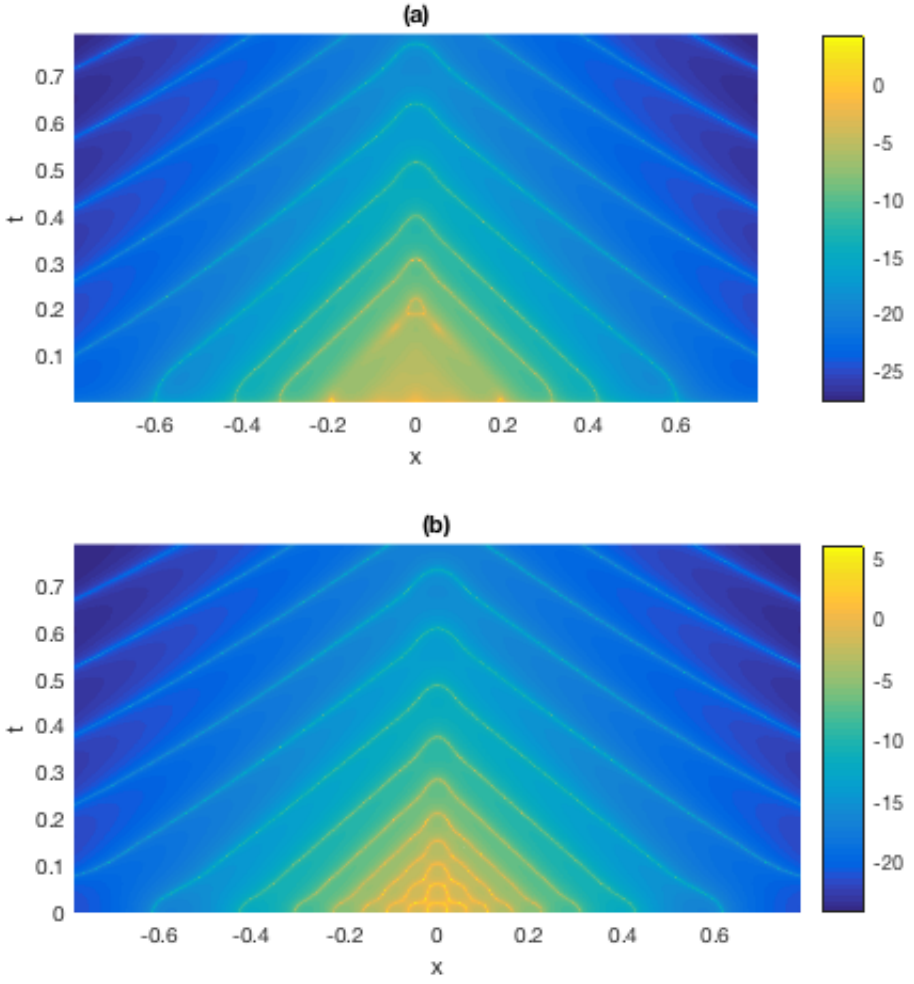

FIGURE 5.16: (a) $\Re e(\log(\Re e(\chi_1(x,t)))$ for the eigenfunction expansion of the mixed state wavefunction (5.73). (b) $\Re e(\log(\Re e(\chi_2(x,t))))$ for the eigenfunction expansion of the mixed state wavefunction (5.75). For all graphs $0 \leq t \leq \pi/4$, $-\pi/4 \leq x \leq \pi/4$ and $a = 4$, $N = 20$, $c = s = A = L = 1$.

$x = 0$ in figure 5.17 however, as seen in figure 5.16, the orders of magnitude in the region are still very small compared to the conventional superoscillations so we would not expect to be able to gain information from this representation.

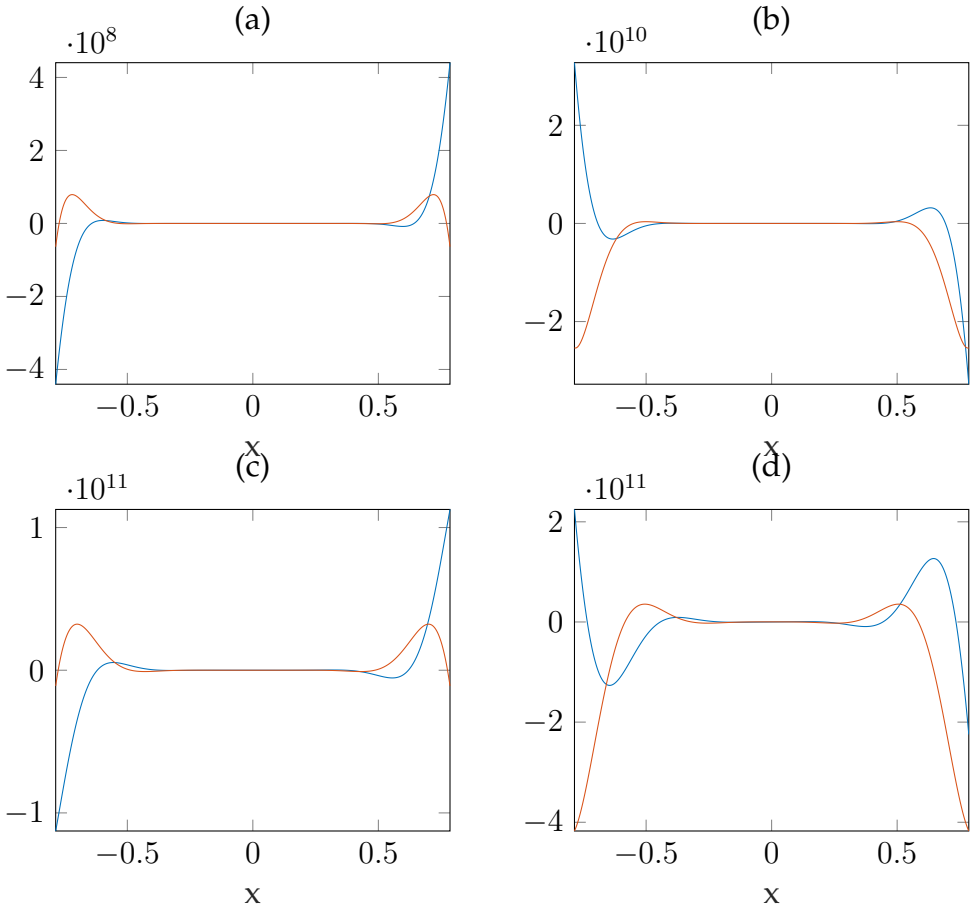

FIGURE 5.17: Showing the wave function $\chi_1(x,t)$ in equation (5.73) the real parts of $\chi_1(x,t)$ are shown in blue and the imaginary in orange. With parameters: $a = 4$, $N = 20$, $c = s = \kappa = A = L = 1$, $-\pi/4 \leq x \leq \pi/4$ with times: (a) $t = 0$, (b) $t = \pi/16$, (c) $t = \pi/8$ and (d) $t = \pi/4$.

5.3.2 Evaluation of The Propagator

To begin the evaluation of the propagator for the mixed state, the $KG \rightarrow D$ procedure is applied to the mixed-state spin-zero propagator:

$$\Delta(x-x';t) = \frac{1}{2}Nc^2t \begin{cases} \frac{J_1\left(Nc\sqrt{c^2t^2-(x-x')^2}\right)}{\sqrt{c^2t^2-(x-x')^2}} & (c|t| > |x-x'|) \\ 0 & (c|t| < |x-x'|) \end{cases} \tag{5.76}$$

This then gives the two components to the Dirac spinor as the derivatives:

$$\Delta_{\chi_1}(x,t) = \frac{1}{2}i\frac{\partial}{\partial t}\left[t\frac{J_1\left(Nc\sqrt{c^2t^2-(x-x')^2}\right)}{\sqrt{c^2t^2-(x-x')^2}}\right] \tag{5.77}$$

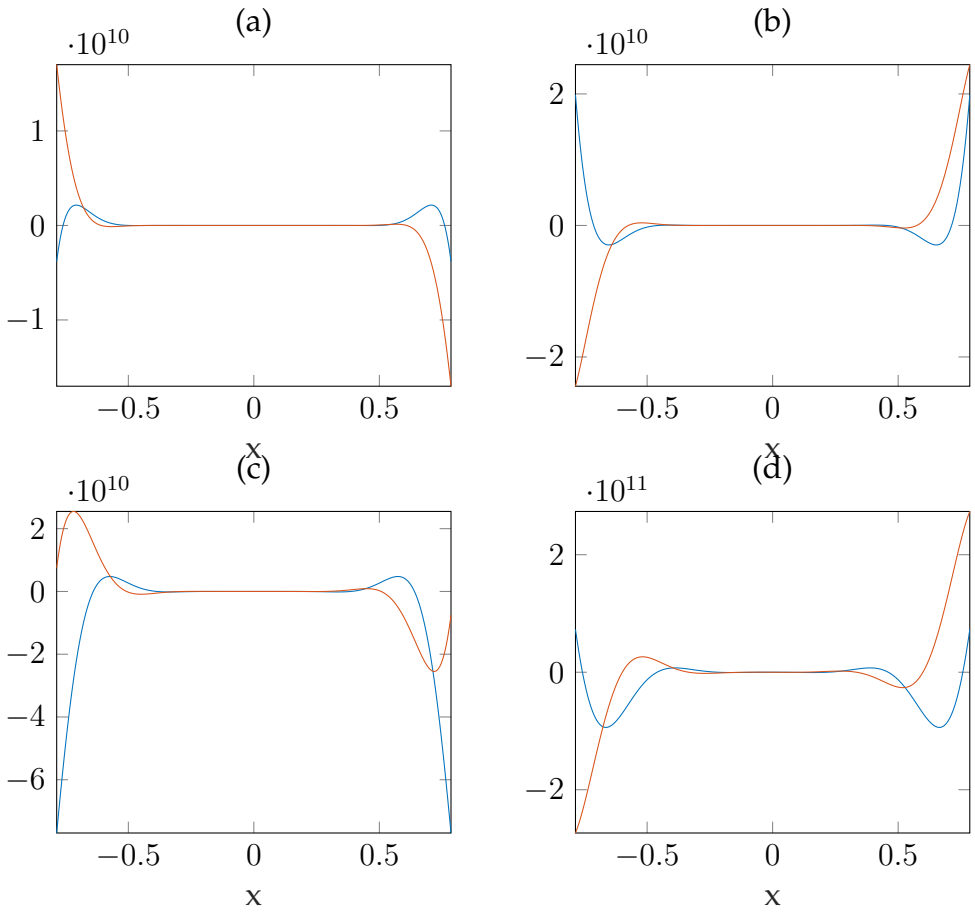

FIGURE 5.18: Showing the wave function $\chi_2(x,t)$ in equation (5.75) the real parts of $\chi_2(x,t)$ are shown in blue and the imaginary in orange. With parameters: $a = 4$, $N = 20$, $c = s = \kappa = A = L = 1$, $-\pi/4 \leq x \leq \pi/4$ with times: (a) $t = 0$, (b) $t = \pi/16$, (c) $t = \pi/8$ and (d) $t = \pi/4$.

$$\Delta_{\chi_2}(x,t) = \frac{1}{2}ict\frac{\partial}{\partial x}\left[\frac{J_1\left(Nc\sqrt{c^2t^2-(x-x')^2}\right)}{\sqrt{c^2t^2-(x-x')^2}}\right] \tag{5.78}$$

As Bessel functions of the first type follow the same differentiation rules as modified Bessel functions of the second type given by (5.37), equations (5.77) and (5.78) can be evaluated:

$$\Delta_{\chi_1}(x,t) = \frac{1}{2}i\Bigg(Nc^3t^2\frac{J_2(Nc\sqrt{c^2t^2-(x-x')^2})}{c^2t^2-(x-x')^2}+\dots$$

$$\dots+\frac{J_1(Nc\sqrt{c^2t^2-(x-x')^2})}{\sqrt{c^2t^2-(x-x')^2}}\Bigg), \tag{5.79}$$

$$\Delta_{\chi_2}(x,t) = -\frac{1}{2}iNc^2t(x-x')\frac{J_2(Nc\sqrt{c^2t^2-(x-x')^2})}{c^2t^2-(x-x')^2}. \tag{5.80}$$

This takes a similar form to the positive energy propagators for the two components of the Dirac spinor (5.38) and (5.39). To understand the two propagators more, we begin by taking the light-cone approximation. This limit occurs when $(x-x') \approx ct$; the argument of the Bessel functions becomes very small. This allows us to use the following approximation to the Bessel function of the first kind:

$$J_\nu(z) \approx \frac{z^\nu}{2^\nu\Gamma(\nu+1)} \tag{5.81}$$

Applying this approximation to (5.79) and (5.80) gives:

$$\Delta_{\chi_1}(x,t) \approx \frac{1}{2}i\Big(\frac{1}{8}N^3c^5t^2+\frac{1}{4}Nc\Big)\theta(|ct|-|x-x'|) \tag{5.82}$$

$$\Delta_{\chi_2}(x,t) \approx -\frac{1}{8}iN^3c^4t(x-x')\theta(|ct|-|x-x'|) \tag{5.83}$$

Where $\theta(|ct|-|x-x'|)$ is the Heaviside step function which ensure the contributions lie solely within the light-cone.

Again, we see the emergence of 'non-propagator' terms in the first component on the Dirac spinor. As in the previous chapter, these shall not be included in further calculations.

(5.82) and (5.83) do not give the entire description of the approximation to the propagator at the light-cone. For a spin-zero wavefunction, the first term of the approximation is a delta function found by adding the light-cone approximations of a positive and negative energy particle. The same is also found for both components of the Dirac spinor for spin-half propagator, giving:

$$\Delta_{\chi_1}(x,t) \approx \delta(x-x'\pm ct)+\frac{1}{2}i\Big(\frac{1}{8}N^3c^5t^2+\frac{1}{4}Nc\Big)\theta(|ct|-|x-x'|) \tag{5.84}$$

$$\Delta_{\chi_2}(x,t) \approx \delta(x-x' \pm ct) - \frac{1}{8} i N^3 c^4 t (x-x') \theta(|ct| - |x-x'|) \tag{5.85}$$

In the spin-zero case, the WKB approximation was the same as the light-cone approximation. As the mixed-state propagator is zero in this region, so must the contributions from the WKB approximation. This is the same for the spin-half case.

We can now get a propagator representation for the Dirac spinor of the mixed state wavefunction and its light-cone approximation; for $\chi_1(x,t)$ we have:

$$\chi_1(x,t) = \frac{1}{2} i \int_{x-ct}^{x+ct} \psi(x',0) \Bigg(N c^3 t^2 \frac{J_2(Nc\sqrt{c^2t^2-(x-x')^2})}{c^2t^2-(x-x')^2} + \dots$$

$$\frac{J_1(Nc\sqrt{c^2t^2-(x-x')^2})}{\sqrt{c^2t^2-(x-x')^2}} \Bigg) dx', \tag{5.86}$$

and its light-cone approximation:

$$\chi_1(x,t) \approx \int_{x-ct}^{x+ct} \psi(x',0) \Bigg(\delta(x-x' \pm ct) + \frac{1}{2} i \Big(\frac{1}{8} N^3 c^5 t^2 + \frac{1}{4} Nc \Big) \Bigg) dx'. \tag{5.87}$$

As with the light-cone approximation to the positive energy propagator, (5.91) features terms which, as $t \to 0$, do not form a delta function and hence, do not represent a propagator. Collecting only the propagator terms:

$$\chi_1(x,t) \approx \int_{x-ct}^{x+ct} \psi(x',0) \Bigg(\delta(x-x' \pm ct) + i \frac{1}{16} N^3 c^5 t^2 \Bigg) dx'. \tag{5.88}$$

For $\chi_2(x,t)$; we have:

$$\chi_2(x,t) = -\frac{1}{2} i N c^2 t \int_{x-ct}^{x+ct} \psi(x',0) \frac{J_2(Nc\sqrt{c^2t^2-(x-x')^2})}{c^2t^2-(x-x')^2} dx' \tag{5.89}$$

and its light-cone approximation:

$$\chi_2(x,t) \approx \int_{x-ct}^{x+ct} \psi(x',0)\left(\delta(x-x'\pm ct) - \frac{1}{8}iN^3c^4t(x-x')\right)dx' \tag{5.90}$$

We now evaluate the two light-cone approximations for the initial superoscillatory function:

$$\psi(x,0) = \frac{A}{\sqrt{L}}\Big(\cos(\kappa x) + ia\sin(\kappa x)\Big)^{Ncs}, \tag{5.91}$$

beginning with the first component of the Dirac spinor:

$$\chi_1(x,t) \approx \frac{A}{\sqrt{L}}\int_{x-ct}^{x+ct}\Big(\cos(\kappa x)+ia\sin(\kappa x)\Big)^{Ncs}\left(\delta(x-x'\pm ct)+i\frac{1}{16}N^3c^5t^2\right)dx'. \tag{5.92}$$

For the case of the spin-zero wavefunction, the second term in the integral over the propagator was ignored in the small t limit. This will not be the case for (5.92) as the second term is of $\mathcal{O}(t^2)$, as opposed to $\mathcal{O}(t)$.

The integral over the first term is trivial, for the second term we solve:

$$I(x,t) = \frac{iA}{16\sqrt{L}}N^3c^5t^2\int_{x-ct}^{x+ct}\Big(\cos(\kappa x) + ia\sin(\kappa x)\Big)^{Ncs}dx'. \tag{5.93}$$

To solve (5.93) the small x approximation is used to the intial wavefunction giving:

$$I(x,t) = \frac{iA}{16\sqrt{L}}N^3c^5t^2\int_{x-ct}^{x+ct}(1+ia\kappa x')^{Ncs}dx'. \tag{5.94}$$

This can be solved using standard methods to give:

$$I(x,t) = \frac{AN^3c^5t^2}{16a\kappa\sqrt{L}(1+Ncs)}\Big((1+ia\kappa(x-ct))^{Ncs+1} - (1+ia\kappa(x+ct))^{Ncs+1}\Big) \tag{5.95}$$

Giving the first component for the Dirac spinor of the mixed state wavefunction as:

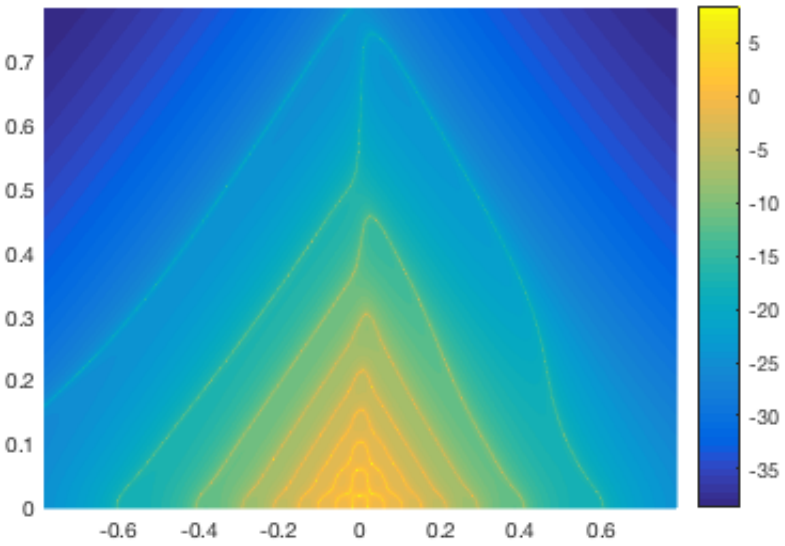

FIGURE 5.19: $\Re e(\log(\Re e(\chi_1(x,t))))$ in the light-cone approximation (5.96) $0 \leq t \leq \pi/4$, $-\pi/4 \leq x \leq \pi/4$ and $a = 4$, $N = 20$, $c = s = A = L = 1$.

$$\chi_1(x,t) = \frac{A}{\sqrt{L}}\left(1 - \frac{N^3c^5t^2}{16a\kappa(1+Ncs)}(1+ia\kappa(x+ct))\right)(1+ia\kappa(x+ct))^{Ncs} + \ldots$$

$$\frac{A}{\sqrt{L}}\left(1 + \frac{N^3c^5t^2}{16a\kappa(1+Ncs)}(1+ia\kappa(x-ct))\right)(1+ia\kappa(x-ct))^{Ncs} \tag{5.96}$$

The most noticeable feature of figure 5.19 is that the symmetry seen in the eigenfunction expansion is not preserved. This is only seen for comparatively large values of x which is where the approximation to the initial wavefunction breaks down. Within the region of interest, around $x \sim 0$ and $t \sim 0$, symmetry is preserved.

Figure 5.20 shows the full representation of the light-cone approximation to the first component $\chi_1(x,t)$. Again, it is a poor approximation to what was seen in the eigenfunction expansion. Where as in figure 5.17, the real part was symmetric about $y = 0$ in this case it is the imaginary part. The orders of magnitude are also considerably different.

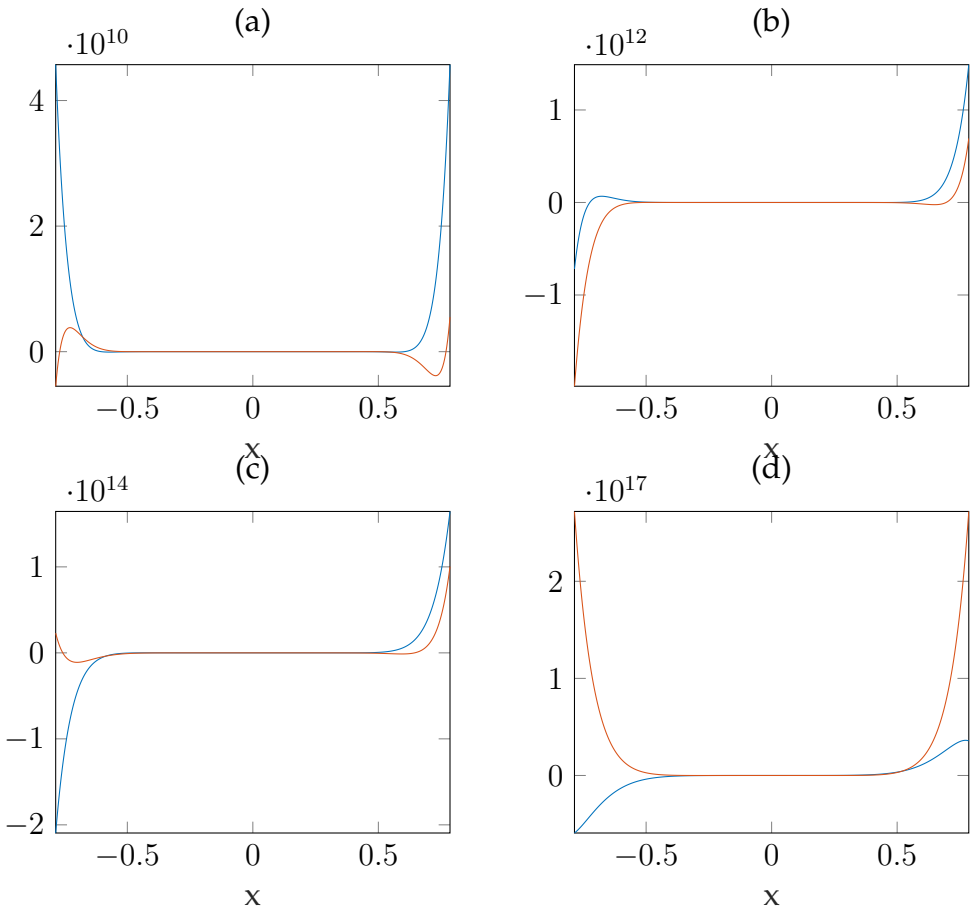

FIGURE 5.20: Showing the wave function $\chi_1(x,t)$ in equation (5.96) the real parts of $\chi_1(x,t)$ are shown in blue and the imaginary in orange. With parameters: $a = 4$, $N = 20$, $c = s = \kappa = A = L = 1$, $-\pi/4 \leq x \leq \pi/4$ with times: (a) $t = 0$, (b) $t = \pi/16$, (c) $t = \pi/8$ and (d) $t = \pi/4$.

As with the spin-zero case, the light-cone approximation to the mixed state wavefunction is composed of waves travelling almost at speed c; half moving forwards in time the other half moving backwards. Up to the first term approximation, the spin-zero and spin-half wavefunctions are identical. However, this ends in the second term of the propagator in which the spin-half case is of $\mathcal{O}(t^2)$ where as the spin-zero case is of $\mathcal{O}(t)$. This means that the effects of the second term in the spin-half propagator are felt more immediately than the second term in the spin-zero propagator. This difference results from the differentiation with respect to t from the $KG \to D$ procedure. Therefore, these differences are all a result of the change in the particle's spin.

The eigenfunction expansion of the first component of the Dirac spinor for a

mixed state wave function depicted in 5.16 shows that, in what would be the superoscillatory region, there are no oscillations. This effect is not picked up when using a light-cone approximation. However, in this limit, it is shown that higher-order terms play a greater role for the first component of the Dirac spinor as it is of $\mathcal{O}(t^2)$ as opposed to $\mathcal{O}(t)$. Due to the effect of N being large, the transition between light-cone terms and WKB terms is very quick. Therefore, the effect of higher-order terms is likely to be seen in the WKB approximation to the wavefunction. To create this, we take the WKB approximations to both the positive and negative energy wavefunctions and sum them:

$$\chi_{1,mix,WKB}(x,t) = \frac{1}{2}(\chi_{1,+,WKB}(x,t) + \chi_{1,-,WKB}(x,t)) \tag{5.97}$$

To this point, we haven't explicitly derived any negative energy wavefunction. However, the derivation of the negative energy state for the first component of the Dirac equation follows almost identically to that of the positive energy state. The only differences are that there is a factor of -1 in front of the negative energy wave function and the contributing saddles. In the positive energy wave function, the two contributing saddles are x_2 and x_4 which, out of the four saddles which emerge from the quartic equation that determines the saddles (5.62) both move forwards in time. The negative energy wave function however, gets contributions from the saddles x_1 and x_3 which move backwards in time. As seen in figure 5.21, the WKB approximation to the mixed state shows similar results to the eigenfunction expansion as there are no superoscillations in the region where they are usually seen. Despite some symmetry being lost, this is predominantly for large t or x.

This is the key difference between the spin-zero and spin-half superoscillatory wavefunctions: for one of the components of the mixed state spin-half wavefunction, the WKB approximation provides the most accurate result. Reasons for this will be discussed later.

The full wavefunction for the WKB approximation to the first component. Clearly,

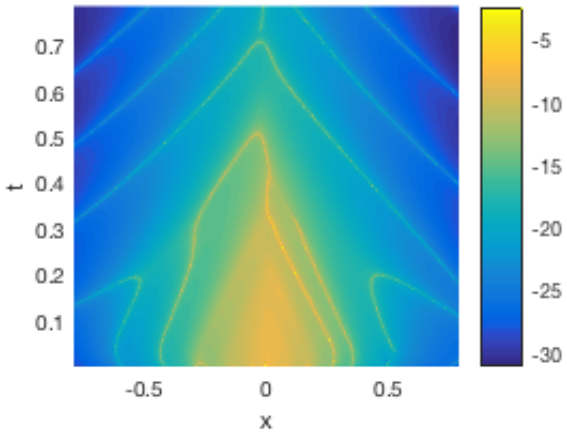

FIGURE 5.21: $\Re e(\log(\Re e(\chi_1(x,t))))$ in the light-cone approximation (5.97) $0 \leq t \leq \pi/4$, $-\pi/4 \leq x \leq \pi/4$ and $a = 4$, $N = 20$, $c = s = A = L = 1$.

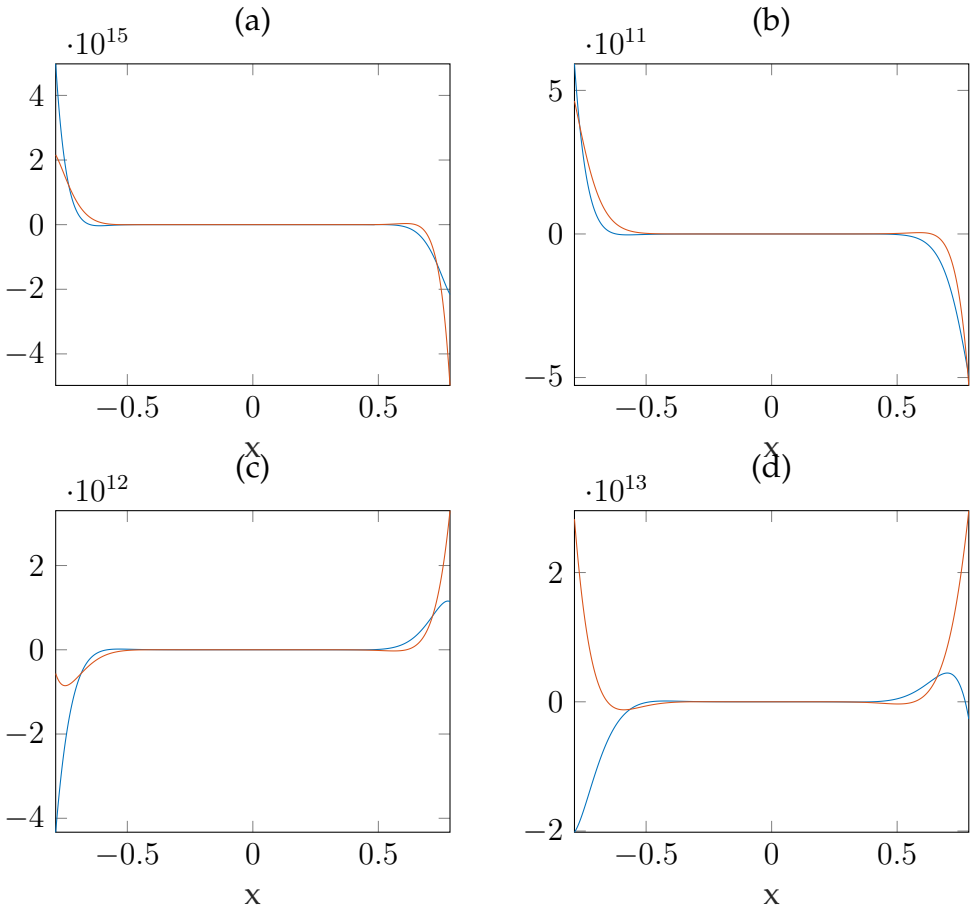

FIGURE 5.22: Showing the wave function $\chi_1(x,t)$ in equation (5.97) the real parts of $\chi_1(x,t)$ are shown in blue and the imaginary in orange. With parameters: $a = 4$, $N = 20$, $c = s = \kappa = A = L = 1$, $-\pi/4 \leq x \leq \pi/4$ with times: (a) $t = 0$, (b) $t = \pi/16$, (c) $t = \pi/8$ and (d) $t = \pi/4$.

as far as conventional oscillations are concerned, this is a poor representation. The symmetry around $y = 0$ is not seen here and the orders of magnitude are also incorrect. This is to be expected however as a further $x \sim 0$ approximation is required to obtain an analytical result.

We now move onto the second component of the Dirac spinor, in which the propagator, in its light-cone approximation, takes the form:

$$\Delta_{\chi_2}(x,t) \approx \delta(x - x' \pm ct) - \frac{1}{8} iN^3 c^4 t(x - x')\theta(|ct| - |x - x'|) \tag{5.98}$$

This takes a very similar form to the spin-zero mixed state and has the dependencies on N and t in the second term. These can, once again be disregarded giving the integral:

$$\chi_2(x,t) = \frac{A}{\sqrt{L}} \int_{-\infty}^{\infty} \delta(x - x' \pm ct) \Big(\cos(\kappa x') + ia \sin(\kappa x') \Big)^{Ncs} dx' \tag{5.99}$$

This integral can be solved to give the result:

$$\chi_2(x,t) = \frac{A}{2\sqrt{L}} \Big(\big(\cos(\kappa(x+ct)) + ia \sin(\kappa(x+ct)) \big)^{Ncs} + \big(\cos(\kappa(x-ct)) + ia \sin(\kappa(x-ct)) \big)^{Ncs} \Big). \tag{5.100}$$

Figure 5.23 is in very good agreement with the eigenfunciton expansion, figure 5.16, especially for small t. As with the spin-zero case, it is created by the super-position of two waves: one, the initial wavefunction, moving at speed c forwards in time and the other, the initial wavefunction, moving at speed c backwards in time.

5.3.3 Analysis

It was found, when using approximations to the mixed-state propagator for the first component of the Dirac spinor, that the resulting wave function was best approximated by the WKB limit as opposed to the light-cone limit. This is an interesting result because all other mixed-state approximations (the spin-zero wave function

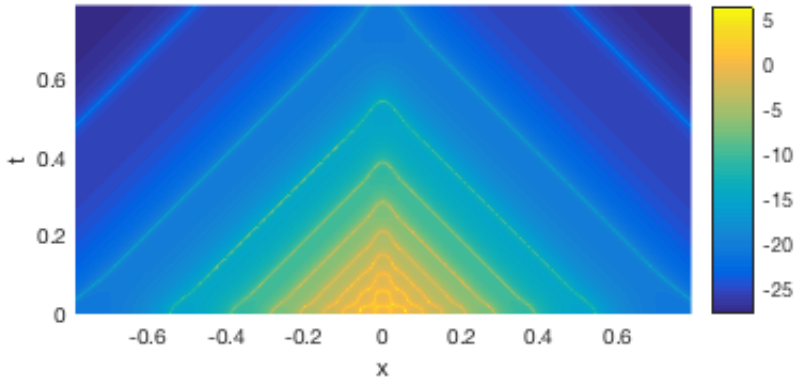

FIGURE 5.23: $\log(\Re e(\chi_2(x,t)))$ for the mixed state propagator, light-cone approximation(4.82). For $a = 4$, $N = 20$, $-\pi/4 \leq x \leq \pi/4$ and $0.00001 \leq t \leq \pi/4$. Yellow lines correspond to zeros of the wavefunction.

and the second component of the Dirac spinor) are at the light-cone. The reason for this can be seen in the difference between the second terms of each propagator in the light cone limit:

$$\Delta_{\chi_1}(x,t) \approx \delta(x - x' \pm ct) + \frac{1}{2}i\Big(\frac{1}{8}N^3c^5t^2 + \frac{1}{4}Nc\Big)\theta(|ct| - |x - x'|) \tag{5.101}$$

$$\Delta_{\chi_2}(x,t) \approx \delta(x - x' \pm ct) - \frac{1}{8}iN^3c^4t(x - x')\theta(|ct| - |x - x'|) \tag{5.102}$$

$$\Delta_{\phi_1}(x,t) \approx \delta(x - x' \pm ct) + \frac{1}{4}N^2c^3t\theta(|ct| - |x - x'|) \tag{5.103}$$

Looking at the two propagators which produce an accurate result using the light-cone approximation (5.102) and (5.103), their second terms are both of $\mathcal{O}(t)$ whereas, (5.101) has a second term of $\mathcal{O}(t^2)$. Therefore, the higher order terms of the mixed state propagator of the first component of the Dirac spinor contribute at earlier times than the higher order terms of the other two propagators. These higher order terms can be approximated by the WKB approximation to the propagator.

The WKB approximation to the mixed state was performed by initially calculating the positive energy wave function and the negative energy wavefunction separately; adding these two wave functions, the mixed state is created. This involves all four saddles calculated from the quartic (5.62). However, although all saddles were used, only two contribute: x_1 and x_4. These are the two non-superoscillatory saddles and hence, the resultant wavefunction does not super-oscillate. As there are no superoscillations in this component, there is therefore no disappearance time, there is however, a wall effect.

5.3.3.1 The Wall Effect

As with all mixed-state superoscillatory wavefunctions studied here, it is symmetric about $x = 0$. However, previously we saw this was due to the two contributing wavefunctions begin of equal magnitude but moving in opposite directions, in the case of the first component of the Dirac spinor, the wall effect is due to the exchange of dominance between the two contributing saddles. This is the reason why we call this a wall effect here but not in the spin zero case.

To look at where the saddles x_1 and x_4 exchange dominance, Stokes and anti-Stokes lines are constructed:

$$\begin{aligned} \text{Stokes Line:} \quad & \Re e(\gamma(x_1; x.t) - \gamma(x_4; x, t)) = 0 \\ \text{anti-Stokes Line:} \quad & \Im m(\gamma(x_1; x.t) - \gamma(x_4; x, t)) = 0 \end{aligned} \tag{5.104}$$

with $\gamma(x_j; x, t)$ being given by:

$$\gamma(x_j; x, t) = is \int_0^{x_j} q(x'')dx'' - \sqrt{(x - x_j)^2 - c^2t^2}. \tag{5.105}$$

As is shown in figure 5.24, the structure of the (x, t) plane in the super-oscillatory region for the mixed state wave function consists of a single anti-Stokes line. It is clear how, in the WKB limit, the symmetry of the mixed state wavefunction is maintained; the anti-Stokes line is a straight line through the origin. This is further confirmed in

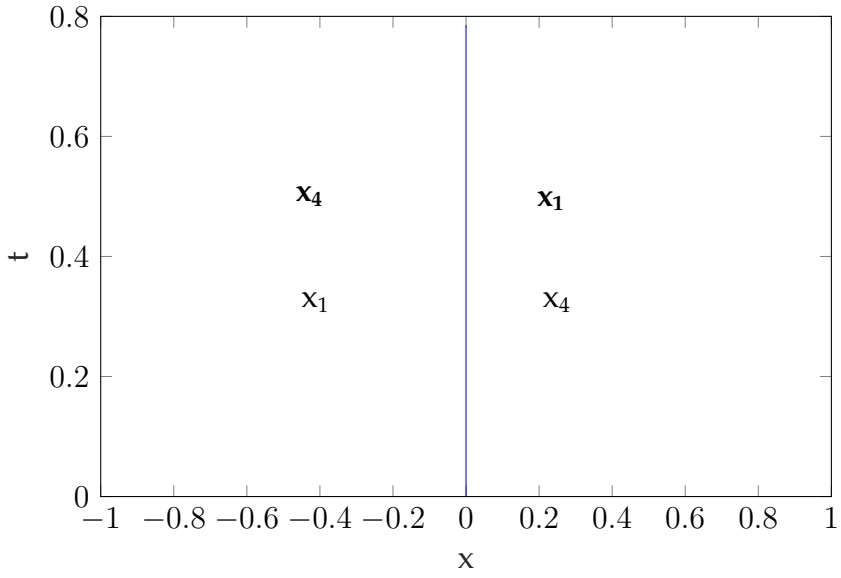

FIGURE 5.24: Anti-Stokes line (blue) for the (x, t) plane to the WKB approximation of the mixed-state superoscillatory wavefunction (5.97). Dominant saddles are in bold.

figure 5.25 in which the wavefunctions from each contributing saddle are shown. It is clear that again, the overall dominance of one contribution over another changes along the line $x = 0$.

As for the second component of the Dirac spinor for the mixed state wavefunction, the analysis is exactly the same as that of the spin-zero mixed-state wavefunction. It is composed of two waves: the initial wave function propagated at a speed c moving forwards in time and the initial wavefunction, propagated at a speed c, backwards in time. Figure 5.26 shows how these two wavefunctions create the symmetric (about $x = 0$) wavefunction seen in figure 5.23; the exchange of dominance occurs on the line $x = 0$.

5.3.3.2 Disappearance Time

Unlike the first component of the Dirac spinor, the second component is, initially, superoscillatory and these superoscillations disappear. This occurs when the local momentum of the mixed state wavefunction decreases to a value lower than the

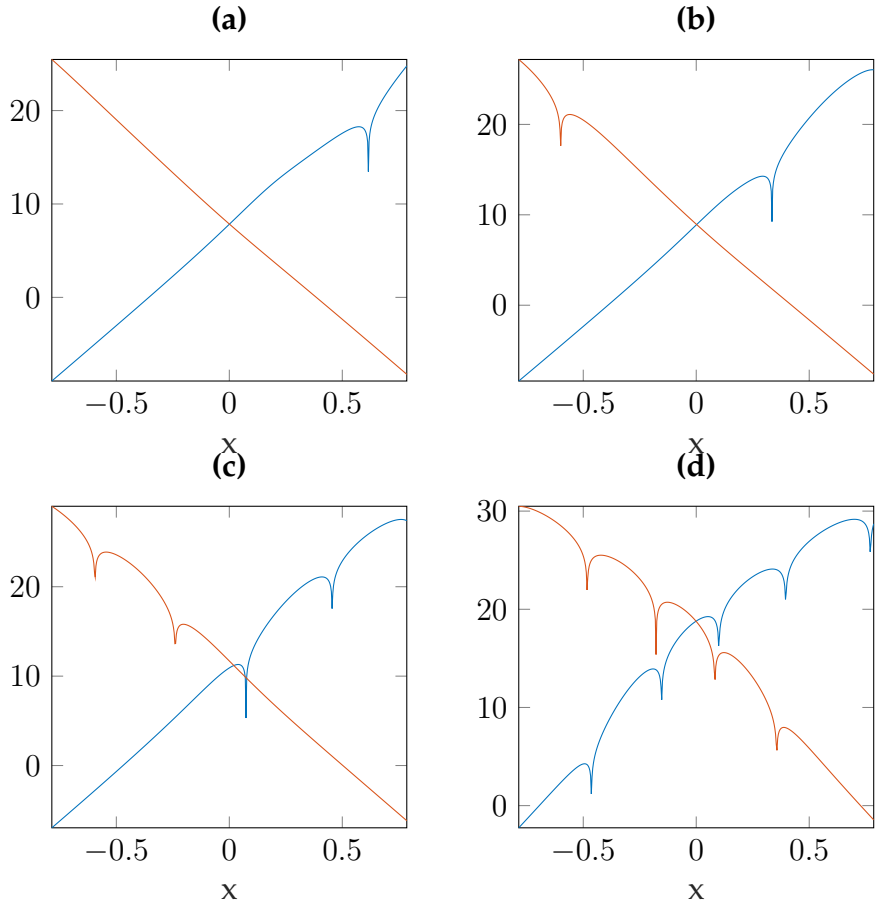

FIGURE 5.25: $\Re e(\log(\Re e(\chi_1(x,t))))$ for blue: the contribution from the saddle x_1 and orange: the contribution from the saddle x_2. (a) t=0.0000001, (b) $t = \pi/8$, (c) $t = \pi/4$, (d) $t = \pi/2$. For all graphs: $-\pi/4 \leq x \leq \pi/4$ and $a = 4$, $N = 20$, $c = s = A = L = 1$.

fastest Fourier component along the line $x = 0$. The disappearance time can the be plotted as a function of the superoscillatory parameter a.

As figure 5.27 shows, as a increases, the disappearance decreases and converges to 0. This is different to the positive energy wavefunction in which the disappearance time decreased to a finite value however, the same behaviour is seen for a spin zero mixed wavefunction. From (5.100), the reason for the disappearance time converging to zero can be understood: As a tends to ∞, the $\cos$ term becomes negligible. As superoscillations are caused by the almost perfect destructive interference between the $\cos$ and $\sin$ term, if one term were to drop out due to the other becoming significantly dominant, the superoscillations would cease.

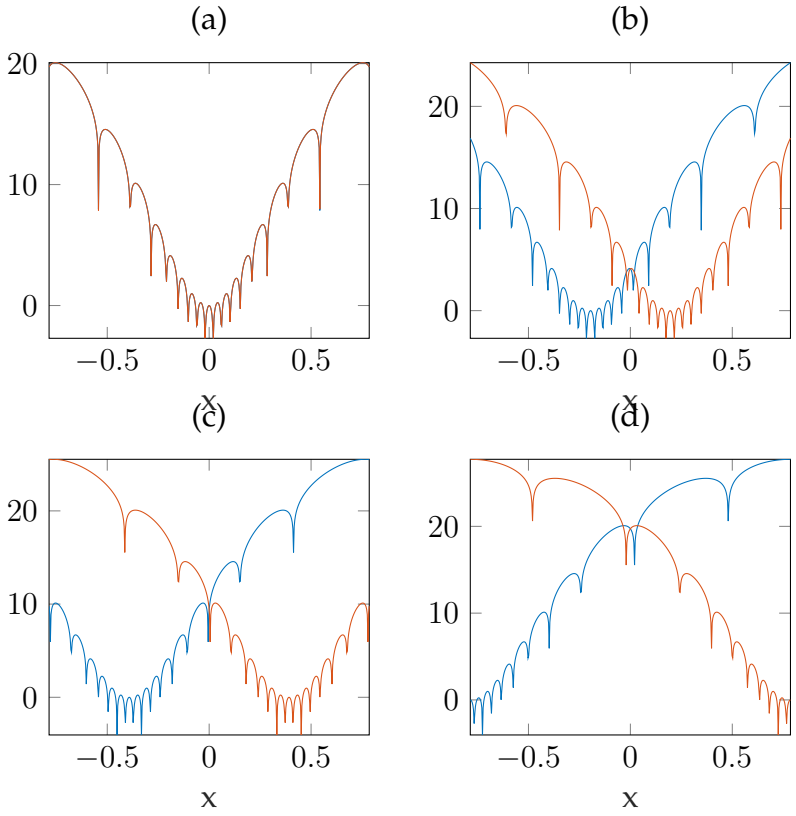

FIGURE 5.26: Blue line: $\log(\Re e(\chi_2(x,t)))$ for the contribution moving forwards in time; orange line: $\log(\Re e(\chi_2(x,t)))$ for the contribution moving backwards in time. For $a = 4$, $N = 20$, $-\pi/4 \leq x \leq \pi/4$ (a): $t = 0.000001$; (b): $t = \pi/16$; (c): $t = \pi/8$; (d): $t = \pi/4$.

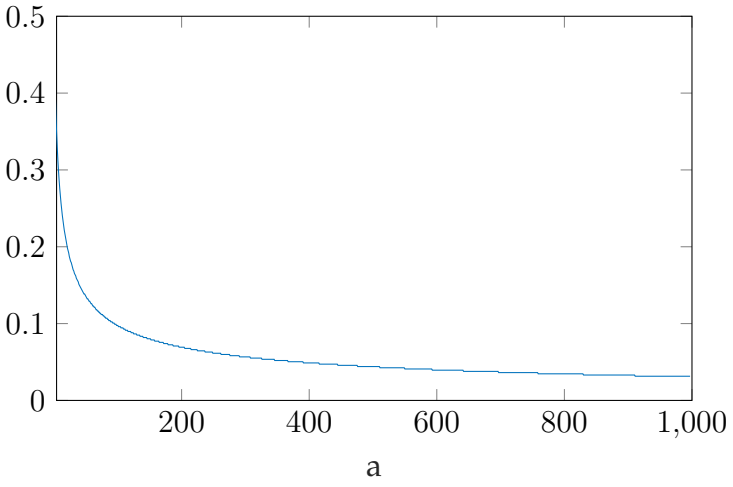

FIGURE 5.27: Disappearance times as a function of a for the second component of the mixed state Dirac spinor in the range $4 \leq a \leq 1000$.

5.4 Conclusion

The spin-half and spin-zero relativistic superoscillating free particle wavefunctions share many similarities but also have some key differences. In general, eigenfunction expansions show that although there are differences between the two types of wave, these are mostly superficial; features of evolution such as the wall effect and disappearance of superoscillations are independent of spin. This is true of the positive energy wavefunctions but when the wavefunction is composed of equal parts positive and negative energy, fundamental differences occur.

By evaluating the integral over the propagator for the positive energy wavefunction, it was again found that the WKB approximation to the propagator gave the most accurate results. In fact, as the WKB approximation produces a propagator that decreases exponentially with distance from the light cone and the conversion from a spin-zero to a spin-half wavefunction is achieved through differentiation; it is hardly surprising that the key features of the evolution are preserved under the $KG \rightarrow D$ procedure. However, it is in the light-cone limit where differences between the spin-half and spin-zero wavefunctions are found. Under differentiation, the first component of the Dirac spinor for the positive energy propagator produces terms which do not go to a delta function as t tends to zero. This is not allowed to happen in the light-cone limit because, as shown in chapter 2, it is in this limit that this property is upheld for the full propagator. In calculating the contribution from the light-cone, these non-propagator terms were disregarded.

When evaluating the integral over the propagator for the mixed-state wavefunction, similar inaccuracies were found in the light-cone approximation for the first component of the Dirac spinor. In fact, it was this component which highlighted the biggest difference between a spin-zero and spin-half superoscillatory wavefunction: for the first component of the Dirac spinor, the best approximation is found in the WKB limit. For all other mixed state superoscillatory wave functions studied in this thesis, the best approximation is found at the light-cone. The reason for this

was found to be that, under differentiation with respect to time, the higher-order components of the light-cone approximation which are usually of order $\mathcal{O}(t)$, were found to be of order $\mathcal{O}(t^2)$. This means that they now feature more strongly at early times which is where superoscillations exist. However, by representing these higher order terms using the WKB approximation, it was found these do not superoscillate, this is in agreement with the eigenfunction expansion.

The light-cone approximation to the propagator, this time for a mixed state wavefunction featured 'non-propagator' terms which were disregarded in further calculations. However, the fact that these terms arise, and the fact that they do so at the light-cone, suggests a fundamental problem with evaluating the propagator at the light-cone. In order for a massive particle to exist at the light-cone, it must have an energy much greater that its rest mass. It is a fundamental principle of particle physics that massive particles with high energies convert their energy to mass via pair production. Therefore, the light-cone approximation should account for extra particles. However, as a first quantised approach was used, this is not possible, as the number of particles is declared at the beginning of the calculations and cannot change from thereon. This is especially significant for a superoscillatory particle in which the energy of its fastest Fourier component is equal to twice its rest mass. Therefore in the superoscillatory region, the energy will be larger than twice the rest mass and particle creation is highly likely. The next logical step in this subject would be to evaluate relativistic free particle quantum superoscillations using a second-quantised approach.

Another interesting direction to take this work would be to study the $m \to 0$ limit. For the Weyl representation of the Dirac equation, this would have an analogue of superoscillations in the electromagnetic field. This phenomena has recently been investigated by Michael Berry and Pragya Shukla [31].

For a Dirac wavefunction, application of an external magnetic reveals a gyromagnetic ration of $g = 2$ for the electron. Application of a superoscillatory magnetic field would cause the electron to respond with the magnetic moment it has

got. An interesting question then arises: Are there solutions to the Dirac equation in which the particle's wavefunction is superoscillatory and the applied field is steady? Although unlikely, the consequences of a positive result are profound; this would deserve additional study.

Chapter 6

Conclusion

When considering the evolution of an initial superoscillatory quantum wavefunction in a relativistic framework, two separate energy states must be considered: pure and mixed[1]. It was shown that, for a particle of spin zero, positive/negative energy superoscillations evolve due to contributions in the WKB limit whereas the mixed energy state superoscillations arise at the light-cone. However, when considering a spin-half wavefunction, both the positve/negative energy and mixed state superoscillations are best explained at in the WKB limit.

We were able to study how different approximations of the wavefunction affect the evolution of the initial superoscillatory wavefunction through the work done in chapter 2. In this we built up a mathematical framework that describes relativistic quantum dynamics in a first-quantised configuration.

Where possible, time-dependent problems in relativistic quantum mechanics are solved through eigenfunction representations [103]. However, as superoscillations have shown themselves to be too subtle a phenomenon to be explained through such methods, an integral over the propagator representation is often employed [30] [37]. In non-relativistic, first-quantised, quantum mechanics the propagator is well known and its derivation taught in many undergraduate courses. However, propagators in a relativistic context are often only considered in the second-quantised representation. As this thesis is written exclusively within a first quantised framework, explicit derivations of the positive, negative and mixed energy propagators

[1] A pure state is one that consists only of positive or negative energy.

for the Klein-Gordon (spin zero) equation, were given as well as their behaviours at the light-cone and in the WKB limit. Example calculations were also given in order to demonstrate how one might apply each approximation. The non-relativistic limit of the positive energy propagator was taken and the result was found to be equal to that of the non-relativistic propagator.

In order to study the evolution of the initial superoscillatory wavefunction according to the Klein-Gordon and Dirac equations, its evolution according to the Schrödinger equation was reviewed first. This was first done in 2006 by Michael Berry and Sandu Popescu [30] and it was this paper that formed the basis of chapter 3. When solved using the eigenfunction representation, it was found that after a certain time, t_d, the superoscillations disappeared. As well as this, an asymmetrical evolution was also observed and entitled the *wall effect*. Both these phenomena were explained using the integral over the propagator and solving it using approximations for small x and t and application of the saddle point method. The resultant integral was therefore given as a sum of contributions arising from saddles in the exponential phase, which can be viewed as complex momenta.

In integrals such as the one solved here, their structure can be explained using Stokes and anti-Stokes lines which give the points in which one saddle's contribution is maximally dominant over the other (Stokes) and points where they are equally dominant (anti-Stokes). For the superoscillatory wavefunction studied, an anti-Stokes line occurring at $x = a$ for $t > \frac{1}{2a^2}$ explains both the disappearance of the superoscillations and the wall effect. It is across this line that an exchange of dominance between the two contributing saddles takes place. The dominant saddle on the left hand side of the anti-Stokes line retains its superoscillatory properties for a longer time than the dominant saddle on the right, this is what causes the wall effect.

As the saddle (termed '$-$') dominant on the left hand side of the 'wall' retains its superoscillatory properties for the longest amount of time, the overall disappearance time is therefore dependent on this. The time at which the local momenta of

the saddle's contribution falls to a value lower than that of the fastest Fourier component therefore gives the disappearance time. It was found that the disappearance time was weakly dependent on the superoscillatory parameter, a and independent of the asymptotic parameter, N.

As in chapter 2, we found that the positive energy Klein-Gordon propagator reduced to the Schrödinger propagator in the non-relativistic limit. We would hence expect that any superoscillatory wavefunctions solved using the positive energy Klein-Gordon propagator will transform to those discussed in chapter 3. Therefore, not only does the content discussed in chapter 3 provide an in-depth review of the features of quantum superoscillatory evolution but also provides a reference for any calculations performed using the Klein-Gordon equation.

When the eigenfunction representation of the initial superoscillatory wavefunction is solved using the positive energy Klein-Gordon equation, the wall effect is observed and the superoscillations disappear after a certain time. However, the wall has seemingly shifted from that produced in the Schrödinger equation and the superoscillations disappear after a shorter amount of time. In fact, in the relativistic case, superoscillations exist over a far smaller space and over a far shorter period of time. This is due to the respective Compton wavelength and Compton time for each case changes with the different values of the speed of light, c. Nonetheless, with respect to their relative 'Compton scaling' relativistic superoscillations seem to disappear more quickly.

To understand how the wall effect and the disappearance of the superoscillations present themselves in a relativistic context, we again employ the integral over a propagator representation of the wavefunction, using the positive energy free particle Klein-Gordon propagator derived in chapter 2. Due to the complexity of the function, obtaining an analytic result requires further approximations beyond the small x and t ones used previously. The light-cone and WKB approximations to the propagator formulated in chapter 2 provide expressions which can be evaluated using complex analysis. Within the light-cone approximation, contributions come

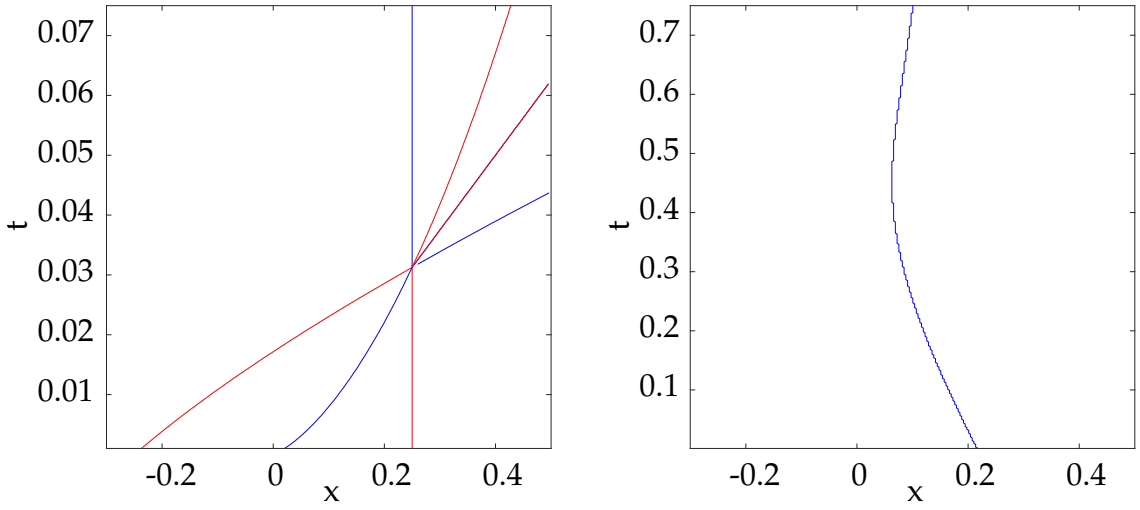

FIGURE 6.1: Stokes lines (red), anti-Stokes lines (blue) and branch cuts (purple) for left: non-relativistic, free-particle superoscillations and right: relativistic, free particle superoscillations.

from residues of poles located on the light-cone whereas, the WKB approximation provides an integrand which lends itself to being solved by the saddle point method.

Even in the WKB approximation, however, solving the saddle point condition requires application of numerical methods. In contrast to the Schrödinger propagator, which produces a quadratic saddle point condition and hence two contributing saddles, the Klein-Gordon propagator produces a quartic saddle point condition which results in four saddles. However, these four saddles can be split into two sets of two saddles: one moving forwards in time; one moving back. Therefore, solving the integral over the propagator for a positive energy, spin-zero, relativistic particle in the WKB limit produces two wavefunctions, one moving forwards in time and one moving backwards in time. By selecting only the saddles moving forwards in time (which, in the limit $c \to \infty$ produce the same saddles as the Schrödinger equation) gives a reasonable approximation of the positive energy wavefunction.

Figure 6.1 shows the difference between the structure of the (x, t) plane for the Schrödiner superoscillations and Klein-Gordon superoscillations. In the relativistic case, in the superoscillatory region, there is one anti-Stokes line across which saddles exchange dominance. The 'wall' is therefore in a different location within the

Klein-Gordon plane and also takes a different shape. Also, it is present for all t whereas in the Schrödinger plane it is only seen for $t > \frac{1}{2a^2}$.

It was shown that all superoscillatory information is contained within one of the contributions from the two saddles. This is in contrast to the non-relativistic case where, although one saddle takes more responsibility for superoscillation than the other, both cause, at certain points, their respective contribution to oscillate faster that its fastest Fourier component. Relativistically, the superoscillatory saddle is dominant on the right hand side of the anti-Stokes line and the saddle of conventional oscillation is dominant on the left. This is another difference between the relativistic and non-relativistic superoscillations; the saddles chiefly responsible for superoscillations are located at different sides of the wall.

Not only does the shape of the wall differ, the transition of dominance is less abrupt in the relativistic case. This by the absence of neighbouring Stokes lines around the relativistic wall. Therefore, superoscillations are still seen where the non-superoscillatory saddle is dominant. However, as they are dependent on a sub-dominant saddle, they disappear very quickly.

It is seen that the relativistic superoscillations disappear over a shorter period of time[2] than their non-relativistic counterparts. At first, it may seem that the fact that the wall is ever-present in the Klein-Gordon plane and hence,a non-superoscillatory contribution is present for all t. However, this only accounts for an extra $t = 1/32$ (for $a = 4$) of superoscillation. This is caused by the superoscillatory contribution existing on the right hand side of the wall as opposed to the left, which is not the case for non-relativistic superoscillations. As the wall is located in the half-space $x > 0$, the superoscillations have less time to develop before the exchange of dominance between the two saddles occur.

Positive energy superoscillations were also investigated for a spin-half particle by using the Dirac equation. To allow for direct comparison between spin-zero

[2]Relative to their respective Compton time's.

and spin-half wavefunctions a method in which the spin-half wavefunction is determined through information of the spin-zero wavefunction is used [33]. As the method is based upon differentiation with respect to space and time of the spin-zero wavefunction, the phase of the exponential in the WKB approximation of the remains unchanged. Therefore, the saddles, Stokes/anti-Stokes lines, wall effect and disappearance time are the same for both spin-zero and spin-half superoscillatory wavefunctions. However, as is usual with spin-half wavefunctions, there are four components. It is intrinsic to the method used to derive the spin-half wavefunctions that the second component is zero. However, the other three are all superoscillatory and evolve in a similar manner.

At the light-cone, contributions arise from residues of the simple poles in the light-cone approximation to the Klein-Gordon propagator. In terms of positive energy superoscillations, this provides a poor approximation as the initial wavefunction is propagated at a speed c along the light-cone. However, it does show the difference between the spin-zero and spin-half wavefunctions. The differentiation required to convert a spin-zero wavefunction into its spin-half analogue does have an effect on the propagator. Where in the spin-zero case the dominant feature was a simple pole at the light cone, this is now a pole of order two.

Similarly to the spin-zero case, the light-cone approximation does not produce a good representation of the positive energy wavefunction. However, it is also seen to fail for the third component of the wavefunction. This is caused by a term which contains a simple pole at $t = 0$.

For a mixed state, which in this case is a state of equal amounts of positive and negative energy, the evolution of the superoscillations is considerably different from the positive energy wavefunction. The superoscillations do disappear but there is no asymmetrical evolution as seen previously. Naturally, the mixed state does not have a non-relativistic counterpart as negative energies are a purely relativistic phenomenon.

For a spin-zero wavefunction, the best approximation to the propagator for a

mixed state is at the light-cone. For a mixed state, the light-cone approximation is given by a delta function which is zero everywhere except for on the light-cone, where it is infinite. Solving the integral over the propagator using this produces a very accurate approximation, especially in the superoscillatory region. The resultant wavefunction is a superposition of two waves: one; the initial wavefunction propagated at a speed c along the light-cone travelling from left to right and two; the initial wavefunction propagated at a speed c along the light-cone travelling from right to left. It is for this reason that the evolution is symmetric around $x = 0$. In this case the 'wall' is at $x = 0$ but is not entirely comparable to the wall in the positive energy wavefunction as that was caused by exchange in dominance between complex momenta whereas for a mixed-energy wavefunction it is the point at which one wavefunction starts contributing more than the other.

The disappearance time is found where the local momentum of either wavefunction reaches a value less than the fastest Fourier component along the line $x = 0$. The disappearance time was found to be shorter than in the case of the positive energy spin-zero wavefunction. It was found that the disappearance time does not converge to a finite value as seen previously.

For two components (the first and the fourth) of the spin-half mixed energy wavefunction, the evolution was very similar to that of the spin-zero; their contributions were both found at the light cone and the evolution was symmetric about the origin and the disappearance time was identical. However the third term, which was the term that causes the light-cone approximation to fail in the spin-zero wavefunction, produced a markedly different evolution.

The third component of the spin-half mixed-energy wavefunction does not superoscillate. Where superoscillations are observed in both the first and third components (the second component is always zero), the third doesn't oscillate at all. This is because, unlike the other two non-zero components and the spin-zero wavefunction, the third-component is best represented by the WKB approximation not the light-cone approximation. As explained in chapter 5, this is due to a term of $\mathcal{O}(t^2)$

in the light-cone approximation. Its evolution is symmetric about the origin.

Using the WKB approximation, the contributions arise from saddles in the exponential phase, these saddles are the same as seen in the positive energy wavefunctions. However, as we now have both positive and negative energies in superposition, we have four saddles contributing. This is quickly reduced to two as the two saddles responsible for superoscillation are always sub-dominant with respect to either non-superoscillatory saddle. By calculating the Stokes and anti-Stokes lines for the resultant wavefunction, once again, only a single anti-Stokes line is found: it is a straight line at $x = 0$. This anti-Stokes line accounts for the symmetric evolution.

The only problem that remains in the treatment of relativistic superoscillations is that of the failure of the third component of the positive energy spin-half wavefunction at the light cone. The answer is likely to exist in a second-quantised treatment of relativistic quantum mechanics. At the light-cone, the energy of the particle is much greater than its rest-mass and hence it is likely that other particles are produced, a result first quantisation cannot account for. The propagator has a far stronger presence at the light-cone for a spin-half wavefunction than one of spin-zero and its effect is felt over a larger space due the presence of a pole of order two as opposed to the spin-zero wavefunction's simple pole.

Using a first-quantised structure to study one dimensional free-particle relativistic superoscillations provides initially surprising evolutions. However, for a positive energy wavefunction, the results are always comparable to the previously studied non-relativistic case. Uniquely, relativistic quantum wavefunctions have negative energy states. In terms of superoscillation, the negative energy states evolve almost analogously to the positive energy case however, from both come mixed-state wavefunction which are again, purely relativistic. These evolve very differently to Berry and Popescu's quantum superoscillations. The limit of the first quantised approach comes at the light-cone. In this approximation, for the third component of the wavefunction, the method fails entirely. At the light-cone the wavefunction attains very high energies such that the results of a second-quantisation (particle creation) would

most clearly apply.

As well as the quantisation of the method used for both Dirac and Klein Gordon superoscillations there exists the $m \to 0$ limit poses interesting questions for both as well. In the case of Dirac superoscillations (using its Weyl representation), the $m \to 0$ has an analogy of superoscillations in an electric field. As for Klein-Gordon superoscillations, the similarity between the Klein-Gordon equation and the wave equation appears as $m \to 0$. As noted in the introduction, the field of optical superoscillations and their use in optical superresolution is a rapidly growing area of research which could be added to through investigation of the $m \to 0$ limit of Klein-Gordon superoscillations.

Appendix A

The WKB Approximation

In general, a second order non-linear ordinary differential equation (such as the Schrödinger or Klein-Gordon equations for a bound particle) has no solution. To counteract this, approximation methods, such as perturbation theory, have been derived. Here we describe one such method: the WKB approximation.

Derived as an approximation to the Schrödinger equation in 1926[70],[110], it assumes a slowly varying potential term, $V(x)$ and provides an accurate description of the $\hbar \to 0$ limit.

With regards to the material in this thesis which only concerns free particles, an approximation which contains a potential might at first, seem inapplicable. However, as we are often looking at a local momentum, which is dependent on x and superoscillations depend on $\hbar \to 0$ the WKB approximation is valid. In this appendix, we derive the WKB approximation for the Klein-Gordon equation.

The one-dimensional Klein-Gordon equation for a system with potential energy $V(x)$ is:

$$\left(\frac{\partial^2}{\partial x^2} + \frac{((W - V(x))^2 - m^2c^4)}{c^2\hbar^2}\right)\Psi(x) = 0, \tag{A.1}$$

where W is the energy eigenvalue of the system. For a free particle ($V(x) = 0$) this gives the solutions:

$$\Psi(x) = \frac{A}{\sqrt{L}}e^{ikx} \tag{A.2}$$

in which k is the wave number. The WKB method specifies that, to approximate the wavefunction, we use an ansatz solution. This takes a similar form to (A.2) except

now k is no longer constant:

$$\Psi(x) \approx e^{i\frac{S(x)}{\hbar}}, \tag{A.3}$$

in which, $S(x)$ has the expansion:

$$S(x) = S_0(x) + \hbar S_1(x) + \hbar^2 S_2(x) + \ldots, \tag{A.4}$$

and derivatives:

$$\frac{\partial \Psi(x)}{\partial x} = \frac{i}{\hbar} S'(x) e^{i\frac{S(x)}{\hbar}}, \tag{A.5}$$

$$\frac{\partial^2 \Psi(x)}{\partial x^2} = \left(\frac{i}{\hbar} S''(x) - \frac{1}{\hbar^2}(S'(x))^2 \right) e^{i\frac{S(x)}{\hbar}}, \tag{A.6}$$

giving (A.1) as:

$$\frac{i}{\hbar^2}(\hbar S''(x) + i(S'(x))^2) e^{i\frac{S(x)}{\hbar}} + \frac{1}{c^2\hbar^2}((W - V(x))^2 - m^2c^4) e^{i\frac{S(x)}{\hbar}} = 0. \tag{A.7}$$

Dividing (A.7) by $e^{i\frac{S(x)}{\hbar}}$, taking the limit $\hbar \to 0$ and considering the first two terms in (A.4) we get:

$$(S_0'(x))^2 = \frac{1}{c^2}((W - V(x))^2 - m^2c^4) \tag{A.8}$$

$$i\hbar S_0''(x) - (S_0'(x))^2 - \hbar S_0'(x) S_1(x) + \frac{1}{c^2}((W - V(x))^2 - m^2c^4) = 0, \tag{A.9}$$

in which (A.8) arises from the first term in (A.4) and (A.9) from the second term. From this point on, we will write $\sqrt{(W - V(x))^2 - m^2c^4}$ as $k(x)$ as it is the momentum of the wavefunction. We begin by solving (A.8):

$$S_0(x) = \frac{1}{c} \int_0^{x'} k(x) dx'. \tag{A.10}$$

We use (A.10) to solve for $S_1(x)$:

$$(S_0'(x))^2 = \frac{1}{c^2} k(x), \tag{A.11}$$

substituting this into (A.9), the second and fourth terms cancel leaving:

$$i\hbar S_0''(x) = \hbar S_0'(x) S_1'(x), \tag{A.12}$$

in terms of $S_1(x)$:

$$S_1(x) = i \int_0^x \frac{S_0''(x')}{S_0'(x')} dx' = i \log(k(x)) + c. \tag{A.13}$$

From (A.10) and (A.13) we get the WKB wavefunction:

$$\Psi(x) = e^{\frac{i}{\hbar}(S_0(x)+\hbar S_1(x))} = \frac{A}{\sqrt{k(x)}} e^{i\int_0^x k(x')dx'}. \tag{A.14}$$

We now look at where (A.14) is valid, from (A.7) it is clear that the approximation relies on the following condition holding:

$$|(S'(x))^2| \gg \hbar |S''(x)|, \tag{A.15}$$

from which it follows:

$$|k(x)^2| \gg \hbar |k'(x)| \tag{A.16}$$

and finally:

$$\left| \frac{\hbar V'(x)}{2(W - V(x))k(x)} \right| \ll 1. \tag{A.17}$$

In order for (A.17) to hold, $V'(x)$ or $\hbar$ must be very small; the WKB approximation depends on a slowly varying potential and $\hbar \to 0$.

Appendix B

Asymptotic Integration

Asymptotic integration is concerned with finding approximate solutions to integrals of the form:

$$I(\lambda) = \int_C \phi(z) e^{\lambda f(z)} dz, \tag{B.1}$$

which, is asymptotic in the limit $\lambda \to \infty$. The key concept is that as $\lambda \to \infty$ the integral, in the complex plane, becomes highly oscillatory along the imaginary axis and contains narrow sharp peaks along the real axis. This results in only saddle points of the phase function, $f(z)$, contributing to the integral; at all other points, the area under the contour is cancelled. We can therefore deform the contour, C, so that it passes through the saddle points and makes its way down into the valley of the complex plane. To achieve this, the contour takes the path of steepest decent[1] [115] [43]. We define a saddle point as being a point in the complex plane, z_0, which is a maximum in one axis and a minimum in the other, as shown in the diagram:

The two types of asymptotic expansion we look at here show how $\phi(z)$ affects the result of the integral. We first consider $\phi(z)$ as being completely regular in the neighbourhood of z_0. After this we consider $\phi(z)$ as having a simple pole in the neighbourhood of z_0.

[1]To be classed as a 'path of steepest decent' the path must obey to rules: 1) That the path passes through one of the zeros of the derivative of the phase, $f(z)$. 2) The imaginary part of $f(z)$ is constant along the path.

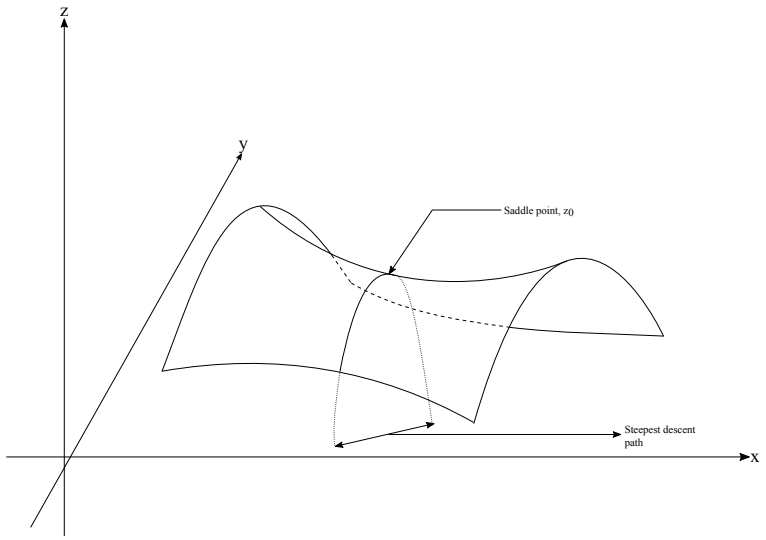

FIGURE B.1: Diagram showing an arbitrary function in the complex plane with a saddle at $z = z_0$ and its steepest descent path

B.0.1 The Saddle Point Method

We begin with our integral (B.1) and consider the case where $f(z)$ has one saddle point at $z = z_0$ and $\phi(z)$ is regular. We now wish to map (B.1) to a comparison integral which has the same structure of saddles as (B.1). For this, we choose the Gaussian integral:

$$I_{gauss}(\lambda) = \int_{-\infty}^{\infty} e^{-\lambda u^2} du = \sqrt{\frac{\pi}{\lambda}} \tag{B.2}$$

(B.2) has a saddle point at $u = 0$. We now want to make the saddles in (B.1) and (B.2) coincide. To do this we make the substitution:

$$-u^2 = f(z) - f(z_0) \tag{B.3}$$

This gives us the Jacobian:

$$\frac{\partial u}{\partial z} = \frac{\partial}{\partial z}\Big[\sqrt{f(z) - f(z_0)}\Big] = \frac{f'(z)}{2\sqrt{f(z) - f(z_0)}} = -\frac{f'(z)}{2u} \tag{B.4}$$

From (B.3) and (B.4) we can write (B.1) as:

$$I(\lambda) = e^{\lambda f(z_0)} \int_C g(u) e^{-\lambda u^2} du \tag{B.5}$$

where:

$$g(u) = -2u\frac{\phi(z)}{f'(z)} \tag{B.6}$$

As we are interested in the neighbourhood of z_0 we now expand $g(u)$ around $u = 0$ which corresponds to z_0 in the z-plane. We begin by Taylor-expanding $f(z)$ around z_0:

$$f(z)|_{z\to z_0} \approx f(z_0) + \frac{1}{2}f''(z_0)(z - z_0)^2 \tag{B.7}$$

From (B.7) we can get an expression for $f'(z)$:

$$f'(z) = u\sqrt{-2f''(z_0)}, \tag{B.8}$$

giving:

$$\lim_{u\to 0} g(u) = \phi(z_0)\sqrt{\frac{-2}{f''(z_0)}}. \tag{B.9}$$

Substituting (B.9) into (B.5) gives:

$$I(\lambda) = \phi(z_0)\sqrt{\frac{-2}{f''(z_0)}}e^{\lambda f(z_0)}\int_{-\infty}^{\infty} e^{-\lambda u^2}du \tag{B.10}$$

We have now deformed the contour, C, such that it passes through the saddle at $u = 0$ and then remains on the real axis where the integrand tends to zero at $\pm\infty$. The integral in (B.10) is now the same as (B.2) which gives our final result:

$$I(\lambda) = \phi(z_0)\sqrt{\frac{-2\pi}{\lambda f''(z_0)}}e^{\lambda f(z_0)} \tag{B.11}$$

B.0.2 Uniform Asymptotic Expansions: Saddle-Pole Coalescence

We now consider integrals of the form (B.1) where $\phi(z)$ has a simple pole at $z = \beta$. We consider β in the neighbourhood of z_0 and allow them to coalesce. In order to get a solution for this, we must use a different comparison integral to that of the

saddle point method as we need to incorporate the pole:

$$I_{comp}(\lambda) = \int_{-\infty}^{\infty} \frac{1}{u - ib} e^{-\lambda u^2} = i\pi e^{\lambda b^2} \text{erfc}\Big[\sqrt{\lambda} b\Big] \tag{B.12}$$

The first few steps in evaluating this integral are very similar to those in the saddle point method. Using the substitution:

$$u^2 = f(z) - f(z_0) \tag{B.13}$$

We map the saddles in (B.1) to those in (B.12) which occur at $u = 0$. Which gives the Jacobian:

$$\frac{\partial u}{\partial z} = \frac{\partial}{\partial z}\Big[\sqrt{f(z) - f(z_0)}\Big] = \frac{f'(z)}{2\sqrt{f(z) - f(z_0)}} = \frac{f'(z)}{2u}. \tag{B.14}$$

We can therefore write (B.1) as:

$$I(\lambda) = e^{\lambda f(z_0)} \int_C q(u) e^{-\lambda u^2} du, \tag{B.15}$$

$$q(u) = 2u \frac{\phi(z)}{f'(z)}, \tag{B.16}$$

where $q(u)$ incorporates the pole at $z = \beta$. In the u-plane, this pole occurs at $u = ib$, where $-b^2 = f(\beta) - f(z_0)$. We now want to extract the pole at $u = ib$ by separating (B.16) in to two parts; one which incorporates the pole and another, regular function, $\psi(u)$, which doesn't have poles at $u = ib$ or $u = 0$.

$$q(u) = \frac{c_{-1}}{u - ib} + \psi(u) \tag{B.17}$$

the constant, c_{-1}, is given by:

$$c_{-1} = \lim_{u \to ib} \big[(u - ib) q(u)\big] = \lim_{z \to \beta} \left[(u - ib)\phi(z) \frac{2u}{f'(z)}\right] = \phi_{-1}, \tag{B.18}$$

where ϕ_{-1} is the residue of $\phi(z)$. We now look at how $\psi(u)$ behaves in the neighbourhood of $u = 0$, we rearrange (B.17) and take the limit as $u \to 0$:

$$\psi(0) = \lim_{u\to 0}\left[q(u) - \frac{c_{-1}}{u - ib}\right] = \lim_{z\to z_0}\left[\phi(z)\frac{2u}{f'(z)} - \frac{\phi_{-1}}{u - ib}\right], \tag{B.19}$$

from (B.8) we have:

$$f'(z) = u\sqrt{-2f''(z_0)}, \tag{B.20}$$

giving:

$$\psi(0) = \lim_{z\to z_0}\left[\phi(z)\frac{2u}{f'(z)} - \frac{\phi_{-1}}{u - ib}\right] = \phi(z_0)\sqrt{\frac{2}{f''(z_0)}} + \frac{\phi_{-1}}{ib}. \tag{B.21}$$

We now have an expression for $q(u)$ in the neighbourhood of $u = 0$:

$$q(u)|_{u\to 0} = \frac{\phi_{-1}}{u - ib} + \phi(z_0)\sqrt{\frac{2}{f''(z_0)}} + \frac{\phi_{-1}}{ib}. \tag{B.22}$$

Substituting (B.22) into (B.15) gives two integrals:

$$I_1(\lambda) = \phi_{-1}\int_{-\infty}^{\infty}\frac{1}{u - ib}e^{-\lambda u^2}du = \phi_{-1}i\pi e^{\lambda b^2}\text{erfc}\Big[\sqrt{\lambda}b\Big] \tag{B.23}$$

$$I_2(\lambda) = \left(\phi(z_0)\sqrt{\frac{2}{f''(z_0)}} + \frac{\phi_{-1}}{ib}\right)\int_{-\infty}^{\infty}e^{-\lambda u^2}du = \sqrt{\frac{\pi}{\lambda}}\left(\phi(z_0)\sqrt{\frac{2}{f''(z_0)}} + \frac{\phi_{-1}}{ib}\right) \tag{B.24}$$

We therefore get our final result for the saddle-pole contribution:

$$I(\lambda) = e^{\lambda f(z_0)}\left[\phi_{-1}i\pi e^{\lambda b^2}\text{erfc}\Big[\sqrt{\lambda}b\Big] + \sqrt{\frac{\pi}{\lambda}}\left(\phi(z_0)\sqrt{\frac{2}{f''(z_0)}} + \frac{\phi_{-1}}{ib}\right)\right] \tag{B.25}$$

Appendix C

The Non-Relativistic Free Particle Propagator

In this appendix, we present the derivation of the non-relativistic propagator (2.62). Whereas, in chapter 2, we derived (2.62) as a limit of the Klein-Gordon propagator: here we use a purely non-relativistic framework.

We begin with equation, (2.20), which gives the integral required to solve in order to determine the propagator of a free particle wavefunction of energy $W(k)$. As we are dealing with a non-relativistic free particle, the energy in this case is:

$$W(k) = \frac{\hbar^2 k^2}{2m} \tag{C.1}$$

Recalling (2.20):

$$\Delta(x,t) = \frac{1}{2\pi}\int_{-\infty}^{\infty} \psi(x,k) \exp\left[-i\frac{W(k)}{\hbar}t\right] dk \tag{C.2}$$

and substituting the free-particle eigenfunction and (C.1) gives:

$$\Delta(x,t) = \frac{1}{2\pi}\int_{-\infty}^{\infty} \exp\left[\left(ikx - i\frac{\hbar k^2}{2m}t\right)\right] dk \tag{C.3}$$

The integral in (C.2) can be solved using the standard integral:

$$\int_{-\infty}^{\infty} e^{-px^2+qx} dx = \frac{\sqrt{\pi}}{p} e^{\frac{q^2}{4p^2}} \tag{C.4}$$

given by (3.323.2) in [54]. Comparing (C.4) and (C.3), the following substitutions can be made to the variables in (C.4):

$$p^2 = \frac{i\hbar t}{2m}, \qquad q = ix, \qquad x = k, \tag{C.5}$$

which allow us to solve the integral in (C.4)

$$\int_{-\infty}^{\infty} \exp\left[\left(ikx - i\frac{\hbar k^2}{2m}t\right)\right] dk = \sqrt{\frac{2m\pi}{i\hbar t}} \exp\left[-\frac{mx^2}{2i\hbar t}\right], \tag{C.6}$$

which gives the propagator as:

$$\Delta(x,t) = \sqrt{\frac{m\pi}{2\pi i\hbar t}} \exp\left[-\frac{mx^2}{2i\hbar t}\right]. \tag{C.7}$$

Lastly, so that we can use (C.7) to derive a time-dependent wavefunction, we off set x by x' to give:

$$\Delta(x-x',t) = \sqrt{\frac{m\pi}{2\pi i\hbar t}} \exp\left[-\frac{m(x-x')^2}{2i\hbar t}\right]; \tag{C.8}$$

the non-relativistic free-particle propagator.

Bibliography

[1] NIST 2010. *NIST Handbook of Mathematical Functions*. http://dlmf.nist.gov: Cambridge University Press.

[2] Y Aharonov. *The Mathematics of Superoscillations*. Rhode Island, United States of America: American Mathematical Society, 2017.

[3] Y Aharonov, D. Z. Alber, and Vaidmen L. "How the Result of a Measurement of a Component of the Spin of a Spin-$\frac{1}{2}$ Particle Can Turn Out to be 100". In: *Physical Review Letters* 109 (1988), pp. 1351–1354.

[4] Y Aharonov, P. G. Bergmann, and J. L. Lebowitz. "Time Symmetry in the Quantum Process of Measurement". In: *Physical Review* 134 (1964), B1410–B1416.

[5] Y. Aharonov and *et al.* "Evolution of Superoscillatory Initial Data in Several Variables in Uniform Electric Field". In: *Journal of Physics A* 50 (2017), p. 185201.

[6] Y Aharonov and *et al.* "How Can an Infra-Red Photon Behave as a Gamma Ray?" In: *Tel-Aviv University Preprint TAUP* (1990), pp. 1847–1890.

[7] Y. Aharonov and *et al.* "On the Cauchy Problem for the Schrödinger Equation with Superoscillatory Initial Data". In: *Journal de Mathématiques Pures et Appliquées* 99 (2013), pp. 165–173.

[8] Y Aharonov and *et al.* "Quantum Random Walks". In: *Physical Review A* 48 (1993), pp. 1687–1690.

[9] Y Aharonov and *et al.* "Some Mathematical Properties of Superoscillations". In: *Journal of Physics A* 44 (2011).

[10] Y Aharonov, S Popescu, and J Tollaksen. "A Time-Symmetric Formulation of Quantum Mechanics". In: *Physics Today* 63 (2011), pp. 27–32.

[11] Y Aharonov and D Rohrlich. *Quantum Paradoxes: Quantum Theory for the Perplexed*. Weinheim: Wiley, 2005.

[12] Y Aharonov and L Vaidman. "Properties of a Quantum System During the Time Inteval Between Two Measurements". In: *Physical Review A* 41 (1990), pp. 11–20.

[13] Y Aharonov et al. "Superpoisitions of time evolutions of a quantum system and a quantum time-translation machine". In: *Physical Review Letters* 64 (1990), pp. 2965–2968.

[14] J Baumgartl and *et al.* "Far Filed Subwavelength Focusing Using Optical Eigenmodes". In: *Applied Physics Letters* 98 (2011), p. 181109.

[15] M. V. Berry. "A Note on Superoscillations Associated with Bessel Beams". In: *Journal of Optics* 15 (2013), 044024 (5pp).

[16] M. V. Berry. "Exact Nonparaxial Transmissions of Subwavelength Detail Using Superoscillations". In: *Journal of the Optical Society of America* 46 (2013), p. 205203.

[17] M. V. Berry. "Superluminal Speed for Relativistic Random Waves". In: *Journal of Physics A* 50 (2012), 22LT01 (7pp).

[18] M. V. Berry. "Waves Near Zeros in Coherence and Quantum Optics". In: *Coherence and Quantum Optics IX (Optical Society of America, Washington DC, 2008)* (2008), pp. 37–41.

[19] M. V. Berry and M. R. Dennis. "Natural Superoscillations in Monochromatic Waves in D Dimensions". In: *Journal of Physics A* 42 (2009), p. 022003.

[20] M. V. Berry and M. R. Dennis. "Phase Singularities in Isotropic Random Waves". In: *Proceedings of the Royal Society of London* 456 (2000), pp. 2059–2079.

[21] M. V. Berry and S Fishman. "Escaping Superoscillations". In: *Journal of Physics A* 51 (2018), 025205 (14pp).

[22] M. V. Berry and S Klein. "Integer, Fractional and Fractal Talbot Effects". In: *Journal of Modern Optics* 43 (1996), pp. 2139 –2164.

[23] M. V. Berry and N Moiseyev. "Superoscillations and Supershifts in Phase Space: Wigner and Husimi Function Interpretations". In: *Journal of Physics A* 45 (2014), 015301 (14pp).

[24] M. V Berry and S Morley-Short. "Representing Superoscillations by Fractals". In: *Journal of Physics A* (2017).

[25] M. V. Berry and P Shukla. "Pointer Supershifts and Superoscillations in Weak Measurements". In: *Journal of Physics A* 45 (2012), 015301 (14pp).

[26] M.V. Berry. "Causal Wave Propagation for Relativistic Massive Particles: Physical Asymptotics in Action". In: *Eurpoean Journal of Physics* 33 (2012), pp. 279–294.

[27] M.V. Berry. "Faster than Fourier". In: *'Quantum Coherence and Reality; in celebration of the 60th Birthday of Yakir Aharonov' (J S Anandan and J L Safko, eds.) World Scientific, Singapore* (1994), pp. 55–65.

[28] M.V. Berry. "Stokes' Phenomenon: Smoothing a Victorian Discontinuity". In: *Publ.Math.of the Institut des Hautes Études scientifique* 69 (1989), pp. 211–221.

[29] M.V. Berry. "Supression of Superoscillations by Noise". In: *Journal of Physics A* 50 (2017), 025003 (9pp).

[30] M.V. Berry and Popescu S. "Evolution of Quantum Superoscillations and Optical Superresolutions without Evanescent Waves". In: *J. Phys A* 39 (2006), pp. 6965–6977.

[31] M.V. Berry and P Sukla. "Geometric phase curvature for random states". In: *Journal of Physics A* 51 (2019), 475101 (13pp).

[32] A Bettini. *Introduction to Elementary Particle Physics, year = 2008, publisher = Cambridge University Press, address = Cambridge, United Kingdom*.

[33] I Bialynicki-Birula and Z Bialynicki-Birula. "Relativistic Electron Wave Packets Carrying Angular Momentum". In: *Phys. Rev. Lett* 118 (2017), pp. 114801–1 –114801–5.

[34] L Brillouin and A Sommerfield. *Wave Propagation and Group Velocity*. New York, USA: Academic, 1960.

[35] J. A. Bucklew and B. E. A. Saleh. "Theorem for High-Resolution High-Contrast Image Synthesis". In: *Journal of the Optical Society of America* 2 (1985), pp. 1233–1236.

[36] R. Buiny and *et al.* "Quantum Harmonic Oscillator With Superoscillatory Initial Datum". In: *Journal of Mathematical Physics* (2014).

[37] M Bussell and P Strange. "Evolution of Superoscillations in the Quantum Mechanical Harmonic Oscillator". In: *European Journal of Physics* 36 (2015), p. 065028.

[38] M. S Calder and A Kempf. "Analysis of Superoscillatory Wavefunctions". In: *Journal of Mathematical Physics* 46 (2005), p. 012101.

[39] G Chen and *et al.* "Planar Binary-Phase Lens for Superoscillatory Optical Hollow Needles". In: *Scientific Reports* 7 (2017), p. 4697.

[40] L Chojnacki and A Kempf. "New Methods For Creating Superoscillations". In: *Journal of Physics A* 49 (2016), p. 505203.

[41] J Colombo F. Ganter and D. C. Struppa. "Evolution of Superoscillations for Schrödinger Equation in a Uniform Magentic Field". In: *Journal of Mathematical Physics* 55 (2017), p. 113511.

[42] "Complex Weak Values in Quantum Meaurement". In: *Physical Review A* 76 (2007), p. 044103.

[43] E.T. Copson. *Asymptotic Expansions*. Cambridge, United Kingdom: Cambridge University Press, 1965.

[44] M. R Dennis, C Hamilton A, and J Courtial. "Superoscillation in Speckle Patterns". In: *Optics Letters* (2008), pp. 2976–2978.

[45] M.R. Dennis and J Lindberg. "Natural Superoscillation of Random Functions in One and More Dimension". In: *Proc. SPIE 7394, Plasmonics: Metallic Nanostructures and Their Optical Properties VII* 33 (2009), pp. 2976–2978.

[46] P. A. M Dirac. "A Theory of Electrons and Protons". In: *Proceedings of the Royal Society A* 126 (1930).

[47] X.N. Dong and *et al.* "Superresolution Far-Field Imaging of Complex Object Using Reduced Superoscillating Ripples". In: *Optica* 4 (2017), pp. 1126–1133.

[48] Rodgers E. T. F and N. I. Zheludev. "Optical Superoscillations: Sub-Wavelength Light Focusing and Supperresolution Imaging". In: *Journal of Optics* 15 (2013), p. 094008.

[49] P. J. S. G Ferreria. "The Energy Expense of Superoscillations". In: *IEEE Transactions on Signal Processing* (2002).

[50] P. J. S. G Ferrira and A Kempf. "Superoscillations: Faster Than The Nyquist Rate". In: *IEEE Transactions on Signal Processing* 54 (2006), pp. 3732–3740.

[51] G.R. Fowles and G.L. Cassiday. *Analytical Mechanics 7th Edition*. Brooks Cole, 2004.

[52] G Torraldo di Franca. "Supergain Antennas and Optical Resolving Power". In: *Nuovo Cimento Suppl.* 9 (1956), pp. 426–435.

[53] J. B. Götte and M. R. Dennis. "Limits of Superweak Amplification to Beam Shifts". In: *Optics Letters* 38 (2013), pp. 2995–2997.

[54] I.S. Gradsteyn and I.M. Ryzhik. *Table of Integrals, Series and Products Seventh Edition*. London, UK: Elsevier, 2007.

[55] A. C. Hamilton and J Courtial. "Metamaterials for Light Rays: Ray Optics Without Wave-Optical Analog in the Ray-Optics Limit". In: *New Journal of Physics* 11 (2009), p. 013042.

[56] J Heading. *An Introduction to Phase-Integral Methods*. New York, USA: Dover, 2013.

[57] Z. S. Hegedus and V Sarafis. "Superresolving Filters in Confocally Scanned Imaging Systems". In: *Journal of the Optical Society of America* 3 (1986), pp. 1892–1896.

[58] F. M. Huang and *et al.* "Nanohole Array as a Lens". In: *Nano Letters* (2008), pp. 2469–2472.

[59] F. M. Huang and M Zheludev. "Focusing of Light By a Nano-Hole Array". In: *Applied Physics Letters* 90 (2007), p. 091119.

[60] N Jin and Rahmat-Samii. "Advances in Particle Swarm Optimization for Antenna Designs: Real-Number, Binary, Single-Objective and Multiobjective Implementations". In: *IEEE Transactions on Antenna Propagation* 55 (2007), pp. 556–567.

[61] T. S. Kao. "Controlling Light Localization With Nanophotonic Metamaterials". In: *PhD Thesis University of Southampton* ().

[62] E Katzav and *et al.* "Yield Statistics of Interpolated Superoscillations". In: *Journal of Physics A* 50 (2016), p. 025001.

[63] E Katzav and M Schwartz. "Yield Optimised Superoscillations". In: *IEEE Transactions on Signal Processing* 61 (2013), pp. 3113–3118.

[64] A Kempf and P. J. S. G Ferrieria. "Unusual Properties of Superoscillating Particles". In: *Journal of Physics A* 37 (2004), pp. 12067–12076.

[65] J Kennedy and R Eberhart. "Particle Swarm Optimisation". In: *IEEE International Conference of Neural Networks Proceedings* (1995), pp. 1942–1948.

[66] A.G Kofman, S Ashab, and F Nori. "Non-Perturbative Theory of Weak Pre and Post Selected Measurements". In: *Physics Reports* 520 (2012), pp. 43–133.

[67] J.F. Koksma and W Westra. "A Causal Alternative to Feynman's Propagator". In: *arXiv:1012.3473* (2010).

[68] V. E. Korepin and *et al.* "Quasiperiodic Tilings: A Generalized Grid Projection Method". In: *Acta Crystallogr. A* (1988), pp. 667–672.

[69] S Kosemeier and *et al.* "Enhanced Toe-Point Resolution Using Optical Eigenmode Optimized Pupil Functions". In: *Journal of Optics* 1 (2011), pp. 257–263.

[70] H. A. Kramers. "Wellenmechanik und halbzahlige quantisierung". In: *Zeitschrift fu-r Physik* 39 (1926), pp. 828–840.

[71] D. G. Lee and P. J. S. G. Ferreria. "Direct Construction of Superoscillations". In: *IEEE Transactions on Signal Processing* 62 (2014), pp. 3125–3134.

[72] D. G. Lee and P. J. S. G. Ferreria. "Superoscillations of Prescribed Amplitude and Derivative". In: *IEEE Transactions on Signal Processing* 62 (2014), pp. 4857–4967.

[73] D. G. Lee and P. J. S. G. Ferreria. "Superoscillations With Optimum Energy Concentration". In: *IEEE Transactions on Signal Processing* 62 (2014), pp. 4857–4967.

[74] D Levine and P. J. Steinheart. "Quasicrystals: A New Class of Ordered Structures". In: *Physical Review Letters* 54 (1984), p. 2477.

[75] D Levine and P. J. Steinheart. "Quasicrystals I: Definition and Structure". In: *Physical Review B* 34 (1986), p. 596.

[76] R.L Liboff. *Introductory Quantum Mechanics, 4th Edition*. Addison Wesley, 1994.

[77] J Lindberg. "Mathematical Concepts of Superresolution". In: *Journal of Optics* 14 (2014), p. 083001.

[78] A. C. Lobo and C. A. Ribeiro. "Weak Values and the Quantum Phase Space". In: *Physical Review A* 80 (2009), p. 012112.

[79] A. W. Lohmann and *et al.* "Fractional Montgommery Effect: A Self Imaging Phenomenon". In: *Journal of the Optical Society of America* 22 (2005), pp. 1500–1508.

[80] K. G. Makris and D Psaltis. "Superoscillatory Diffraction Free Beams". In: *Optics Letters* 36 (2011), pp. 4335 –4337.

[81] M Mazilu and *et al.* "Optical Eigenmodes; Exploiting the Quadratic Nature of the Energy Flux and of Scattering Iinteractions". In: *Optical Express* 19 (2011), pp. 933–945.

[82] W. D. Montgommery. "Self Imaging Object of Infinite Aperture". In: *Journal of the Optical Society of America* 57 (1967), pp. 772–778.

[83] K. M. Nashold and *et al.* "Synthesis of Binary Images From Band-Limited Functions". In: *Journal of the Optical Society of America* 6 (1989), pp. 852–858.

[84] M.E. Peskin and D.V. Schroeder. *An Introduction to Quantum Field Theory*. Colorado, USA: Westview Press, 1995.

[85] K Piche and *et al.* "Experimental Realization of Optical Eigenmode Super-Resolution". In: *Optical Express* 20 (2012), pp. 26424–26433.

[86] W Qiao. "A Simple Model of Aharonov-Berry's Superoscillations". In: *Journal of Physics A* 33 (1996), pp. 2257–2258.

[87] I.H. Redmount and W-H Suen. "Path Intergration in Relativistic Quantum Mechanics". In: *International Journal of Modern Physics A* 08 (1992), pp. 1629–1635.

[88] D. J. Ring and *et al.* "Abberation-Like Cusping Focusing of the Post-Paraxial Talbot Effect". In: *Journal of Optics* 14 (2012), pp. 3438–3445.

[89] J Robinson and R Eberhart. "Particle Swarm Optimisation in Electromagnetics". In: *IEEE Transactions on Antenna Propagation* 52 (2004), pp. 397–407.

[90] E. T. F Rodgers and *et al.* "A Superoscillatory Lens Optical Microscope for Subwavelength Imaging". In: *Nature Materials* 11 (2012), pp. 432–435.

[91] E. T. F. Rogers and *et al.* "Superoscillatory Optical Needle". In: *Applied Physics Letters* 102 (2013), p. 031108.

[92] L.H. Ryder. *Quantum Field Theory, Second Edition*. Cambirdge, United Kingdom: Cambridge University Press, 1996.

[93] T Sales and G Morris. "Axial Superresolution with Phase-Only Pupil Filters". In: *Optical Communications* (1998), pp. 227–230.

[94] V. Savinov. "Subwavelength Focusing of Light by Nanohole arrays". In: *MPhys Thesis, University of Southampton* ().

[95] S. A. Schelkunoff. "A Mathematical Theory of Linear Arrays". In: *The Bell System Technical Journal* 22 (1943), pp. 80–107.

[96] L.S. Schulman. *Techniques and Applications of Path Integration*. New York, USA: Wiley, 1981.

[97] M Schwartz and E Perlsman. "Sensitivity of Yield Optimised Superoscillations". In: *arXiv:1402.3089 [physics.data-an]* (2014).

[98] P Shukla. "Weak Measurements: Typical Weak and Superweak Values". In: *Current Science* (2015), pp. 2039–2043.

[99] A Sommerfield. *Optics: Lectures on Theoretical Physics vol 4*. New York, USA: Academic, 1950.

[100] A. M. Steinberg. "Conditional Probabilitis in Quantum Theory, and the Time Tunneling Controversy". In: *Physical Review A* 51 (1995), pp. 32–42.

[101] G. G. Stokes. "On the Discontinuity of Arbitrary Constants that Appear as Multipliers of Semi-Convergent Series". In: *Acta. Math.* 26 (), pp. 283–287.

[102] P Strange. *Relativistic Quantum Mechanics*. Cambridge, United Kingdom: Cambrige University Press, 1998.

[103] P. Strange. "Relativistic Quantum Revivals". In: *Physical Review Letters* (2010).

[104] B. E. Y Svensson. "Pedagogical Review of Quantum Measurement Theory with an Emphasis on Weak Measurement". In: *Quanta* 2 (2013), pp. 18–41.

[105] B Tamir and R Cohen. "Introduciton to Weak Measurements and Weak Values". In: *Quanta* 2 (2012), pp. 7–17.

[106] B Thaller. *The Dirac Equation*. Berline Heidleberg: Springer Verlang, 1992.

[107] J Tollaksen. "Novel Relationships Between Superoscillations, Weak Values and Modular Relationships". In: *Journal of Physics: Conference Series* 70 (2007), pp. 1–41.

[108] "Typical Weak and Superweak Values". In: *Journal of Physics A* 43 (2010), 354024 (9pp).

[109] R. E. Wagner et al. "Causality and relativistic localization in one-dimensional Hamiltonians". In: *Physics Review A* 83 (2011), pp. 62106–62114.

[110] G. Wentzel. "Eine verallgemeinerung der quantenbedingungen fuer die zwecke der wellenmecha- nik". In: *Zeitschrift fu-r Physik* 38 (1926), pp. 518–529.

[111] A. M. H Wong and G. V. Eleftheriades. "An Optical Supermicroscope for Far-Field, Real Time Imaging Beyond the Diffraction Limit". In: *Scientific Reports* 3 (2013), p. 1715.

[112] A. M. H Wong and G. V. Eleftheriades. "Sub-Wavelength Focusing at the Multi-Wavelength Range Using Superoscillations: An Experimental Demonstration". In: *IEEE Transactions on Antennas and Propagation* 59 (2011), pp. 4766–4776.

[113] A. M. H Wong and G. V. Eleftheriades. "Superdirectivity Based Superoscillatory Wave Design: A Practical Path to Far-Field Sub-Diffraction Imaging". In: *IEEE Transactions on Antennas and Propagation* (2014), pp. 2164–3342.

[114] A. M. H Wong and G. V. Eleftheriades. "Superoscillations Without Sidebands: Power-Efficient Sub-Diffraction Imaging with Propagating Waves". In: *Scientific Reports* 5 (2015), p. 8449.

[115] R Wong. *Asymptotic Apporoximations of Integrals*. Philladelphia, Pennsylvania: Society for Industrial and Applied Mathematics, 2001.

[116] G. H. Yaun and *et al.* "Planar Super-Oscillatory Lens for Sub-Diffraction Optical Needles at Violet Wavelengths". In: *Scientific Reports* 6 (2014), e17036.

[117] A Yoshida and *et al.* "Superfocusing of Optical Beams". In: *Journal of Optics A* 9 (2007), pp. 777–786.

[118] G. H. Yuan and *et al.* "Achromatic Superoscillatory Lenses with Subwavelength Focusing". In: *Light: Science and Applications* (2017).

[119] H-H Zhang et al. "On Analytic Formulas of Feynman Propagators in Position Space". In: *Chinese Physics C* (2010), pp. 1576–1582.

[120] N Zheludev. "What Diffraction Limit?" In: *Nature Materials* 7 (2008), pp. 420–422.

[121] N. I. and Zheludev. "Nanohole Arrays Enable Multiple Point Source Imaging". In: *Laser Focus World* 44 (2008).